TU Delft

BURO HAPPOLD

# Predicting the Best Stability System for High-Rise Steel Buildings by an Artificial Neural Network

Master Thesis

E.G.F. Potijk

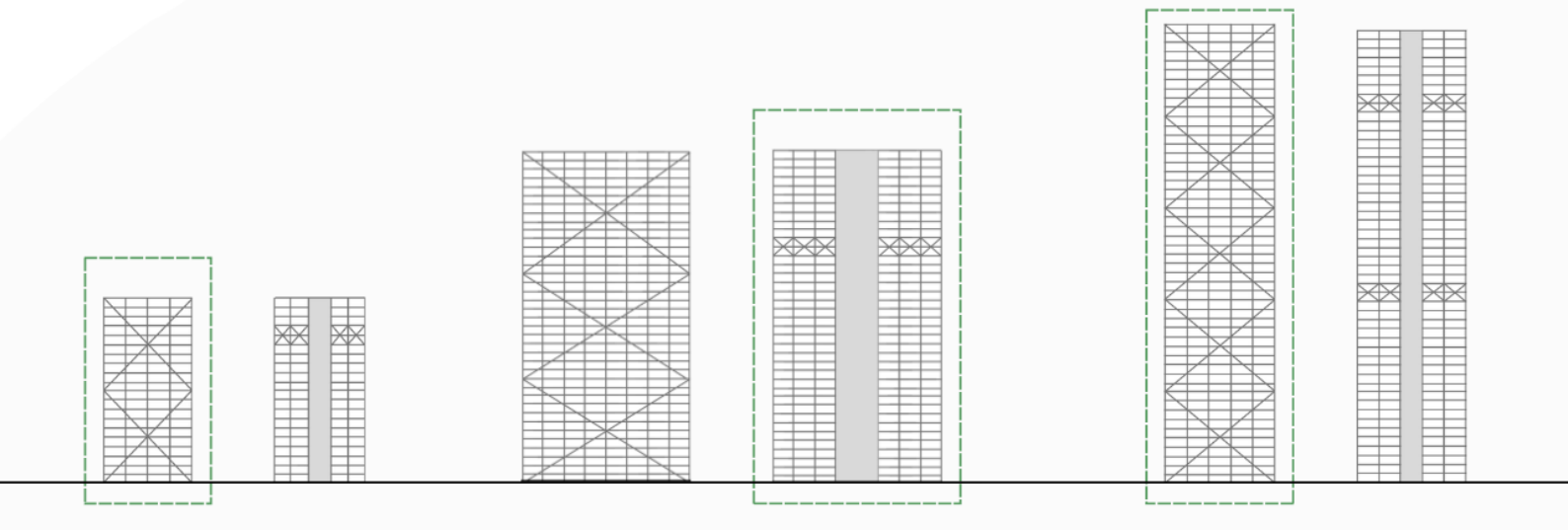

# Predicting the Best Stability System for High-Rise Steel Buildings by an Artificial Neural Network

Master Thesis

by

E.G.F. Potijk

to obtain the degree of Master of Science
at the Delft University of Technology

| | | |
|---|---|---|
| Student Number: | 4715802 | |
| Project Duration: | August, 2023 - May, 2024 | |
| Thesis committee: | dr. ir. P.C.J. Hoogenboom, | TU Delft (chairperson) |
| | dr. ir. F. Kavoura, | TU Delft |
| | ir. A.C.B. Schuurman | TU Delft |
| | ir. T. Uijtenhaak, | Buro Happold |

TU Delft

BURO HAPPOLD

# Preface

Dear reader,

I'm excited to share with you the result of months of hard work – my thesis for my MSc in Civil Engineering. It's a big milestone for me as it marks the end of my student days. My journey as a student started at the Faculty of Civil Engineering, TU Delft with a bachelor's degree in Civil Engineering. After I started my master's degree in Structural Engineering also at the TU Delft, I had a brief one-year break to the Erasmus University in Rotterdam to pursue a management master's degree. But eventually I will finish my student life where it all started as well: at the Faculty of Civil Engineering in Delft. For my master thesis, I was lucky to have had the opportunity to collaborate with Buro Happold on my research.

Over the past few months, I have been diving into the world of machine learning and computational engineering. Sometimes a real challenge, but most of all it has been a real pleasure to learn about this new topic and dive into it. Especially during conversations with my colleagues from Buro Happold as they introduced me to the endless possibilities within machine learning. It has been a joy to combine my passions for parametric design, structural mechanics, and computational design in my research.

I owe great gratitude to those who supported me throughout this fun, but sometimes rather challenging, journey. My supervisor, Tijl Uijtenhaak, provided invaluable guidance during our biweekly meetings. His questions sparked interesting discussions and challenged me to think about every decision. I am thankful for the space to share doubts and questions and the insights gained from our conversations. My thesis committee members, Pierre Hoogenboom, Florentia Kavoura and Marco Schuurman, offered crucial and greatly valuable feedback. I want to thank all of you for our interesting conversations and brainstorm sessions that kept me on track whenever I got lost in the world of machine learning. I could count on them to get me back on track by asking the right questions and by encouraging me to see the bigger picture. All of their support kept me grounded and focused, therefore a big thank you!

Moreover, I am super thankful for my colleagues at Buro Happold. They provided an amazing work environment and spirit and were always ready to discuss ideas and to lend a helping hand. I can not imagine a better place to have written my master's thesis.

I would also like to express my gratitude to my family and friends for their support throughout my thesis journey. Their motivation and encouragement kept me focused and driven. They were always there to ensure some pleasant distraction after the hours I spend on my thesis which was definitely highly appreciated.

In any case, I wish you much reading pleasure!

*Emma Potijk*

# Abstract

Selecting the optimal stability framework for high-rise steel buildings is a critical decision that impact both economic efficiency and sustainability. This decision is not easy since there are many stability frameworks to choose from, such as tube, concrete shear-wall, and outrigger system. Designers and clients aspire to compare multiple structural designs, considering both different frameworks and variations in geometry. Unfortunately, the current process of evaluating multiple designs is time-consuming and relies on the designer's experience and rules of thumb, rather than being driven by data. To address this challenge, predictive models can be used to estimate performance in terms of structural and environmental costs based on the given geometry and framework. However, traditional curve fitting methods often fall short in accurately predicting a complex relationship. In response, this study explores the potential of artificial neural networks to accelerate the decision-making process by predicting the most efficient framework during the early design phase while maintaining sufficient accuracy.

To determine this potential, two parametric models were developed using Rhinoceros software to represent buildings with braced framed tubes and outrigger systems. These models automatically optimised beam and column dimensions by FEM of Karamba, aiming to minimise the mass of these structural elements, across a range of building widths (15 to 60 meters) and heights (48 to 300 meters). The resulting data sets of both braced framed tube and outrigger system reflected the structural and environmental costs for the different designs. Separate neural networks were modelled for each framework. These networks were trained on the different data sets. By comparing predicted structural and environmental costs, the models assisted in the selection between braced framed tubes and outrigger systems.

The artificial neural networks accurately approximated structural and environmental costs for both stability frameworks. The Mean Absolute Percentage Error (MAPE) for the braced framed tube was 14%, while the most accurate alternative curve fit, a third-order polynomial, had a MAPE of 25%. For the outrigger system, the neural network achieved an even lower MAPE of 7%, where the most accurate alternative curve fit, also a third-order polynomial, had a significantly higher error with a MAPE of 31%. The neural networks outperformed traditional curve fitting methods. Additionally, the neural network generated instant results, taking only a second compared to the parametric model's 5 to 30 minutes. However, achieving overall time efficiency with the neural models will require approximately three months when considering both setup time and output generation time. Optimal stability varied based on specific width and height combinations: when looking at environmental costs, the braced framed tube excelled for lower (50-80m) and higher heights (200-300m), while the outrigger system was more efficient for middle heights (80-200m). As the structure's slenderness increased, the braced framed tube regained efficiency for the middle heights.

Impact of the stability framework is defined as the relative contribution of embodied carbon of the stability framework to the total embodied carbon of the structure (including superstructure and floors). The impact of the stability framework ranged from 25% to 57% for the braced framed tube and 33% to 66% for the outrigger system, with the impact increasing with the building's height. The potential gain from selecting the optimal framework, defined as the ratio of the absolute difference in embodied carbon between both frameworks to the total embodied carbon of the worst performing structural framework, ranged from 7% to 18%, with the lowest impact found for the highest height range of 250 to 300 meters.

In conclusion, the research has demonstrated the capability of artificial neural networks to accurately predict the optimal stability system for high-rise steel buildings. Alternative curve fitting methods do not match up to artificial neural networks in terms of accuracy. Whereas, parametric models do not match up to artificial neural networks in terms of analysis speed. Although the results are specific to the braced framed tube and the outrigger system, the proposed methodology offers a framework for comparing stability frameworks in the early-design phase. Additionally, the validated workflow has the opportunity to incorporate data from real-life projects into the input data sets of the neural networks which could bring the predictions in the early-design phase even closer to the reality.

# Contents

# List of Figures

# List of Tables

# 1

# Introduction

## 1.1. Problem statement

In the domain of architectural design and structural engineering, the selection of an optimal stability framework for high-rise buildings has significant influence on both the cost-effectiveness and the sustainability of a building. This selection is not easy since there are a significant number of different stability frameworks to choose from, such as the tube, concrete core, and outrigger systems. Traditional approaches to evaluating stability frameworks often require substantial time investment and heavily rely on the designer's expertise. The desire of the designer or the client to explore multiple designs and evaluate their performance is therefore frequently constrained by time limitations. One common approach to speed up a process is curve fitting. Unfortunately, conventional curve fitting methods (e.g., second and third order regression models) lack accuracy for complex non-linear relationships. As a result, clients and designers face challenges in terms of speed and accuracy when wanting to compare various stability frameworks across different structural dimensions in the early design phase possible leading to inefficient buildings.

To address that challenge, this study explored the potential of artificial neural networks (ANNs). By using a curve fitting method with the ability to capture complex non-linear relationships, artificial neural networks aim to accelerate the decision-making process during the early design phase while maintaining sufficient accuracy. While the application of artificial neural networks has garnered significant attention across different industries, its potential in structural engineering, specifically in prediction of costs, remains relatively unexplored. Bridging this gap is important, as it has potential for redefining the traditional design process, allowing fast exploration of multiple design options and their performance in terms of costs during the early design phase.

## 1.2. Objectives

The primary objective of this study was to design and validate an artificial neural network capable of accurately predicting the performance parameters in terms of costs associated with different stability frameworks (namely braced framed tubes and outrigger systems) for high-rise steel buildings across varying heights and widths. The goal of the neural network is that it serves as a decision-making tool, helping in the selection of the optimal structural system based on either structural or environmental costs in a rapid and accurate way. To achieve this, the research also focused on assembling a sufficient clean data set through parametric models of both stability systems, which could be used to train the artificial neural networks. The goal and the scope of the research leaded to the following main research question of this thesis:

**'How can the performance parameters for different stability frameworks of a high-rise steel building with different volumes be predicted based on its design characteristics in a machine learning approach to accelerate the decision-process?'**

The sub-questions following from the main research question:

1. *What aspects should be considered when designing the stability framework of a high-rise steel building?*

   The design process of a high-rise steel building can require certain structural checks or design constraints considering functionality, stability, stiffness and strength of the design. In this sub-question these aspects were summarized to give an overview on what to take into consideration when developing and designing a high-rise steel building.

2. *What data set and data collection methods are necessary to train a machine learning model to accurately predict performance parameters of high-rise buildings with different volumes?*

   This sub-question examined the requirements for the data that were essential for training the ML tool to make precise predictions of the performance parameters. The quality of the data collection determined the potential of the accuracy of the model and therefore was important to establish correctly.

3. *Can the best stability framework of a high-rise steel building be accurately predicted by means of an artificial neural network?*

   The purpose of this question was to try to establish if it was possible to make a artificial neural network which can accurately predict the best stability framework which is preferably in terms of the performance parameters, namely the structural and environmental costs.

4. *How does the performance of the artificial neural network compare to the performance of other established interpolation techniques?*

   By answering this sub-question, the effectiveness of an artificial neural network was examined in comparison to alternative interpolation methods (first, second and third order regression models). This comparison helped to determine whether the artificial neural network can be seen as advantageous and delivered sufficient performance.

## 1.3. Scope

The primary focus of this research was on high-rise steel buildings, specifically investigating two types of stability systems: the braced framed tube and the outrigger system. The chosen location for these high-rise structures was Rotterdam, the Netherlands. The floor plans of the structures was limited to rectangular floor plans. Other floor plan shapes were not considered within the scope of this study due to time limitations. The structures were evaluated based on two key parameters: the structural costs and the embodied carbon (environmental costs). Regarding the embodied carbon, the focus was on the stages of Cradle-to-Gate (A1-3) in the Life Cycle Assessment (LCA), excluding stages beyond A1-3 from consideration in this research. Factors beyond the mass of structural elements were not accounted for in the cost and embodied carbon assessments. Moreover, the role of the foundation in the overall structure was not taken into account. The influence of the connections on the performance of the structure was also not taken into account. The focus of this research was on steel, and therefore non-steel structural stability frameworks were excluded from this research. The use of artificial neural networks was explored in this research, other machine learning techniques have not been explored in this research.

## 1.4. Approach

The approach of this research was organized into five main tasks:

- **Task 1: Parametric Model Development and Optimisation.**
  In this research, two parametric models were developed for two stability systems: the braced framed tube and the outrigger system. These models underwent validation using analytical and 2D analyses. Next, an FEM optimisation using Karamba was performed where the stiffness and

strength requirements were considered, leading to finding the most optimal cross-section solution of the beams and columns for each structure for different dimensions.

- **Task 2: Data Generation.**
  Data sets for both braced framed tube and outrigger system were produced for the structures. These ranged in height and width, and were derived from the optimised parametric models. These data sets included the mass of all structural elements within the respective structures.

- **Task 3: Artificial Neural Network Development.**
  The generated data sets served as input for the development of artificial neural networks (ANNs). Before training the ANNs, the best configuration of hyperparameters was determined separately for braced framed tube and outrigger system. Once the hyperparameters were established, the ANNs were constructed based on the generated data sets, and the ANN models were trained.

- **Task 4: Prediction and Visualisation.**
  Based on the ANN models, predictions were made regarding the performance of the structures for different volumes (varying heights and widths). These predictions were visualised by graphing the performance of each stability framework over either the varying height or the varying width of the structure.

- **Task 5: ANN Model Validation and Comparison.**
  The accuracy of the ANN models was validated by looking at the loss functions. The effectiveness of the ANN models was compared with other interpolation techniques including the first order, second order and third order regression models. Furthermore, a comparison was made between the performance based on the predictions of the ANN models and the performance of real-life projects.

## 1.5. Report Outline

The structure of the report is illustrated in Figure 1.1. Furthermore, the constituents of each Chapter are also displayed.

**Figure 1.1:** Structure of the report

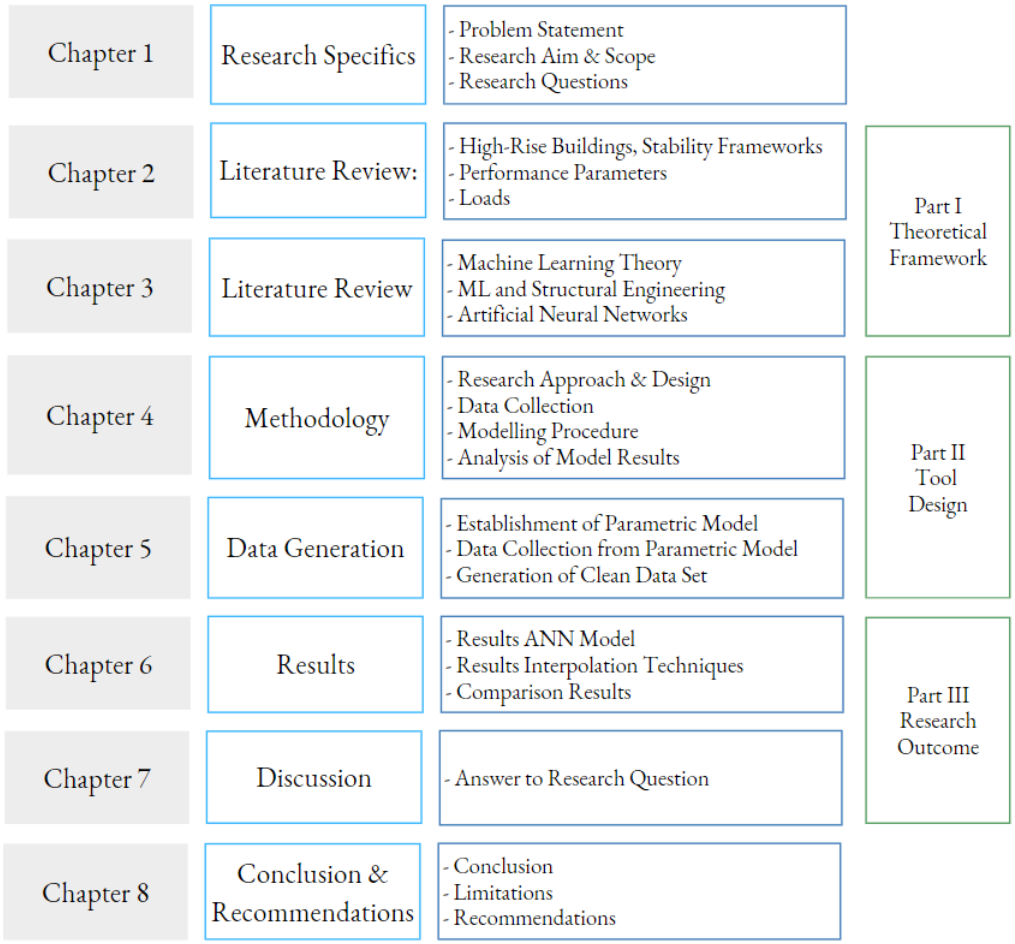

# Part I
# Theoretical Framework

# 2

# High Rise Buildings

This chapter of the literature review of high-rise buildings has two primary objectives. Firstly, it provides an overview of the stability frameworks applicable to high-rise steel buildings and specifies the stability frameworks which are chosen for this research. Secondly, it offers an insight into all the important factors in the design of high-rise structures. The chapter begins with an introduction to high-rise buildings, followed by a division of the feasible stability frameworks for high-rise steel buildings. Subsequently, there is an explanation on the selected stability frameworks for this study. Finally, an overview of the key factors relevant to high-rise building design is presented, each briefly explained. The chapter concludes by summarizing the main findings from the literature review.

This chapter will aim to answer sub-question 1.

1 *What aspects should be considered when designing the stability framework of a high-rise steel building*

## 2.1. Introduction to High-Rise Buildings

A high-rise building in the Netherlands is typically characterized by a total height exceeding 70 meters according to Bouwbesluit [3]. However, the notion of height is relative, and a building's classification cannot be solely based on height alone. Determining whether a structure qualifies as high-rise depends on the contextual surroundings and conditions, making it challenging to establish a precise and universal definition for high-rise buildings. Structurally, the classification of a building as high-rise refers to its sensitivity to lateral forces resulting from wind and earthquakes activities [4]. In essence, a high-rise building is one in which the impact of these lateral forces significantly influences the architectural and engineering design process. The interplay between the building's height and these external forces is leading in shaping the building's structural integrity and design considerations.

The majority of the world's tallest buildings prominently feature a steel structural system [5]. This preference arises from the remarkable strength-to-weight ratio that steel offers, making it a prime choice for such ambitious constructions. Beyond its strength, steel has qualities like convenient assembly and on-site installation, streamlining the construction process. Moreover, steel exhibits cost-effective transport to the construction site and offers an array of strength levels, enhancing its adaptability. Additionally, the availability of a diverse range of sections, due to the easiness of fabricating own sections, further improves the flexibility of steel in high-rise building design.

High-rise structures are exposed to a multitude of diverse loads, stemming from various origins both internal and external. These loads can either be static or dynamic and can be broadly classified by their orientation — either vertical or horizontal. Within the vertical orientation, gravitational forces include the building's self-weight and live loads each contributing to the overall load distribution [4]. For high-rise Conversely, horizontal forces, referred to as lateral loads, consist of the wind pressures and seismic reactions, presenting a challenge to the structural stability [6]. Whereas, the horizontal forces are most critical for high-rise buildings [1]. The challenge of the stability is about the building's ability to

competently counterbalance these lateral forces and the second order effect. This resistance, acquired through deformations and bending, is the base of load-bearing capacity. A schematization of the vertical and horizontal loading of a high-rise building is illustrated in Figure 2.1. The high-rise building is schematized as a cantilever beam, fixed on one side and free on the other side.

**Figure 2.1:** Schematic overview vertical and horizontal loading of a high-rise building

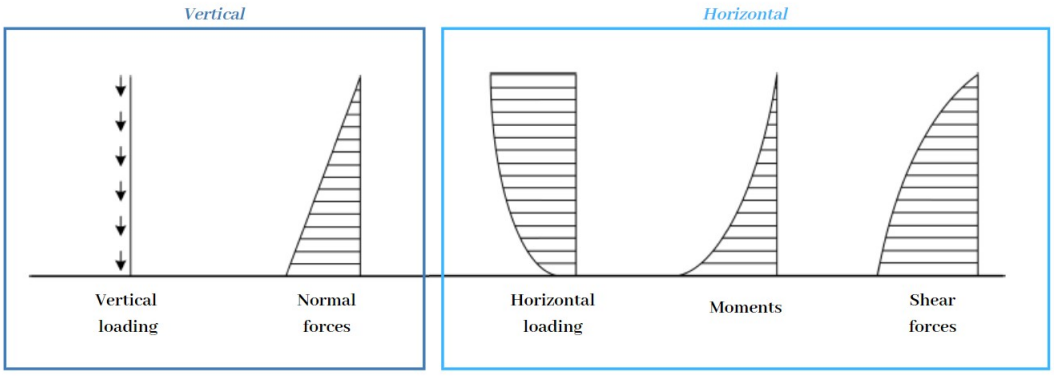


## 2.2. Division of Stability Frameworks

In the pursuit of constructing steel high-rise buildings that can withstand the forces they encounter, a range of stability frameworks has been developed. These frameworks serve as the structural backbone, facilitating the distribution of lateral loads such as wind, seismic forces, and dynamic vibrations. The selection of an appropriate stability framework is necessary, as it directly influences the building's ability to resist deformation, sway, and oscillation. Moreover, the chosen stability framework will ensure the overall safety of the building and preserves aesthetic vision of the architect. Multiple sources are accessible, each displaying a different distribution of stability systems. A few sources will be enumerated, and from among them, two systems will be selected for more in-depth examination for this research. This selection was based on the materials, the applied height constraints and the source of stability of the different systems (interior, exterior or hybrid of both).

According to Gunel and Ilgin (2007), different structural systems are suitable for steel, reinforced concrete, and composite buildings [5]. These systems are categorized based on their source of stability: interior, exterior, or a hybrid of both:

- **Interior system provides stability**
  - *Rigid frame systems.* Rigid framing, specifically moment framing, relies on the fact that the connections between beams and columns have sufficient rigidity to preserve the nearly constant original angles between intersecting parts. In the context of steel structures, achieving rigid framing involves enhancing joint stiffness to ensure the withholding of enough rigidity within the joints.
  - *Braced frame and shear-walled frame systems.* Braced frame systems find application in steel construction. This approach proves remarkably effective and cost-efficient in countering horizontal loads. It aims to enhance the efficiency of a rigid frame by significantly minimising the bending experienced by columns and girders, achieved through the incorporation of supplementary bracing elements. Shear-walled frame systems can be characterized as vertical cantilever beams that withstand lateral wind and seismic loads impacting a structure. These loads are transmitted through the floor diaphragms to the shear walls. Shear-walled frame systems are deployed in both reinforced concrete and composite construction scenarios.
- **Both interior and exterior systems provide stability**
  - *Outrigger systems.* Outrigger systems represent an evolved variation of both braced frame

and shear-walled frame systems, finding application in steel as well as composite constructions. This structural approach involves a central core that incorporates either braced frames or shear walls. Horizontal 'outrigger' trusses or girders then link this core to the outer columns. Additionally, in many instances, external columns are interlinked through an exterior belt girder. When a building is exposed to horizontal loads, the presence of column-restrained outriggers withstands the rotation of the core. This design element helps maintain structural stability during such loading conditions.

- **Exterior system provides stability**
  - *Framed-tube systems.* Framed-tube systems are suitable for steel, reinforced concrete, and composite construction methods. The defining feature of a tube system is the utilisation of closely positioned perimeter columns, interconnected by significant spandrels. This enables the entire building to function comparable to a substantial vertical cantilever, effectively countering overturning moments. The system's efficiency comes from the multitude of robust connections distributed along the perimeter, forming a substantial structural tube.
  - *Braced-tube systems.* Braced-tube systems find applicability in steel, reinforced concrete, and composite buildings. By introducing multi-story diagonal bracings along the tube's façade, the rigidity and efficiency of the framed tube structure can be improved by requiring less material. Consequently, this refined braced-tube configuration becomes suitable for greater heights and permits increased spacing between columns. In steel buildings, steel diagonals or trusses are employed to implement this system.
  - *Bundled-tube systems.* Bundled-tube systems are suitable for steel, reinforced concrete, and composite construction. This approach involves a group of tubes interlinked by shared interior panels, resulting in the creation of a perforated multicell tube structure. the concept of this system is derived from the organization of distinct tubes.

Moreover, R. Nijsse's (2012) classification of stability systems is presented in the schematic overview shown in Figure 2.2 [1]. The stability structures are categorized into frames, cores, outriggers, tubes, and megastructures. The 'megastructure' as defined by Nijsse corresponds to the previously termed 'bundled tube system.' The figure also indicates the maximum heights applicable for each system.

**Figure 2.2:** Stability systems according to R. Nijsse [1]

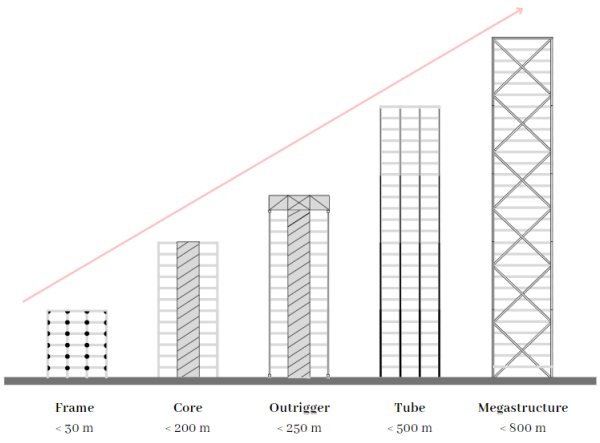


An alternative strategy for arranging stability frameworks in tall buildings is presented by Ali et al. (2007), where also the categorization of interior and exterior systems is applied [2]. The layouts of these systems for both the interior and exterior are presented in Figure 2.3.

**Figure 2.3:** Interior and exterior stability systems according to Ali et al. [2]

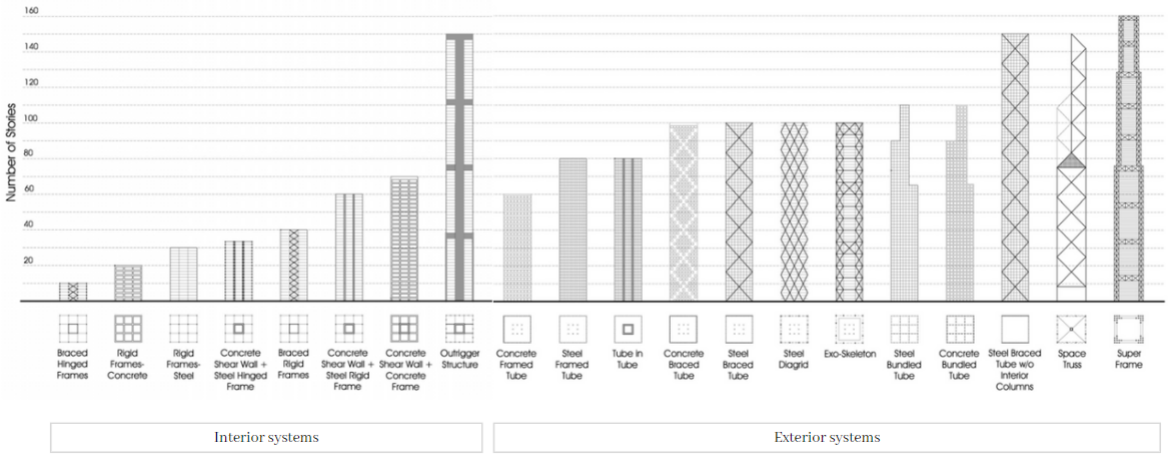


Drawing from the referenced studies that categorize stability systems by Gunel and Ilgin (2007), R. Nijsse (2012), and Ali et al. (2007), two systems have been chosen for examination in this research [5, 1, 2]. This selection process is based on material choice and the designated height range. Given the utilisation of steel as the chosen material, only systems feasible in steel construction are considered. Furthermore, the systems under consideration must be applicable to high-rise buildings within the Netherlands, with a height limit of 300 meters (approximately 100 stories) set as the maximum threshold and a height of 36 meters (approximately 12 stories) set as the minimum threshold. Notably, the tallest building in the Netherlands at present is the Zalmhaventoren, standing at a height of 215 meters [7]. Furthermore, to add interest to the comparison, the decision has been made to evaluate one interior system and one exterior system. This aims to ascertain whether altering the system type has varying effects for different heights and widths of the structure (different volumes of the structure). Consequently, the two stability systems that will be considered for study in this research for high-rise steel buildings are the following:

1. **Outrigger system**
2. **Framed braced tube**

The chosen stability frameworks are illustrated in Figure 2.4, presented by the specified height range. It can be seen that the outrigger system falls under the category of an interior system, while the braced tube is classified as an exterior system.

**Figure 2.4:** Two stability systems chosen for this research based on [2]

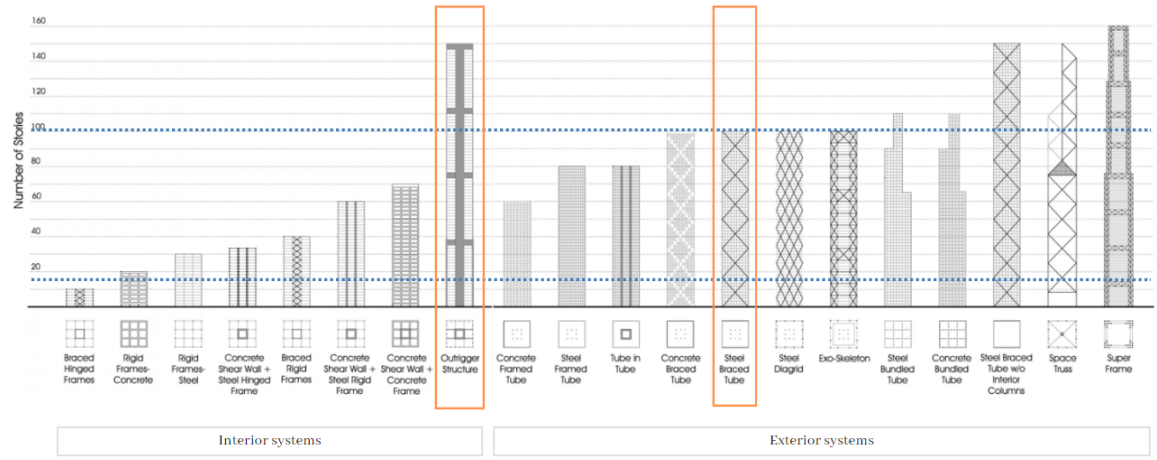


## 2.3. Outrigger Structure

A braced frame featuring outriggers is displayed in figure 2.5, alongside its deflected shape due to lateral loading. This structural configuration consists of a central braced frame with a specific bracing system that connects to two outriggers of equal length. These outriggers are essential in preventing additional rotation of the structure's facade columns. As a result, they generate significant compression and tension forces within these columns, effectively counteracting the horizontal loads applied to the structures.

**Figure 2.5:** Outrigger (based on [8]). a) Model and loads. b) Deflection shape, and axial forces in the external columns.

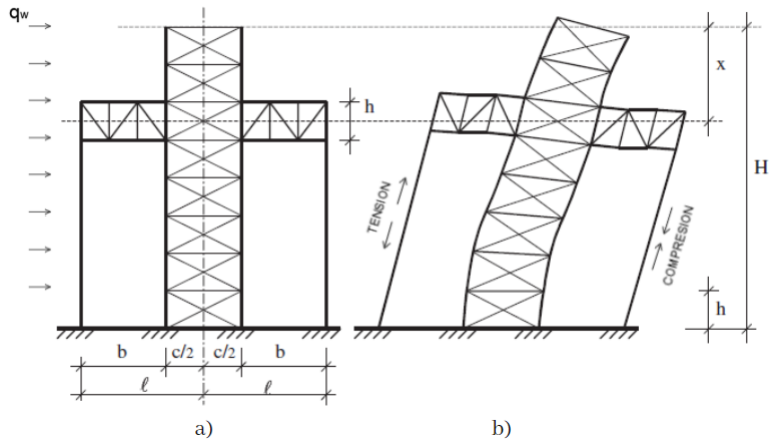


The expression for the restraining moment of the outrigger structure is as follows [8]:

$$M_r = \left\{ \frac{w\left(H^3 - x^3\right)}{6EI_t} + \frac{wx}{\alpha G A_t} \right\} \left\{ \frac{H}{(H-x)S_v + HS_h} \right\} \tag{2.1}$$

The horizontal deflection at the top of the structure can be obtained with the following equation:

$$y_{\text{top}} = \frac{wH^4}{8EI_t} + \frac{wH^2}{2GA_t} - \frac{M_r\left(H^2 - x^2\right)}{2EI_t} - \frac{M_r}{\alpha G A_t} \tag{2.2}$$

The derivation of these formulas can be found in the paper of Hoenderkamp and Bakker (2003) [8]. The right-hand side of equation 2.2 consists of four terms. The first two terms describe the unrestrained horizontal deflections of the braces frame's top, resulting from bending and racking shear under the influence of lateral loading. The third term combines the lateral deflection at the outrigger level, coming from reverse bending to $M_r$, and the additional deflection occurring above the outrigger due to outrigger-level rotation. Finally, the fourth term accounts for horizontal deflection within the braced frame over a single-story height at the outrigger level.

The reduction in deflection for the braced frame is depicted by the final two terms on the right-hand side of Equation 2.2. To maximise this reduction, it can be optimised by taking its derivative with respect to $x$, setting the derivative equal to zero, and solving for $x$. Figure 2.6 illustrates a graphical representation of the optimal outrigger locations as a function of two dimensionless characteristics, $\omega$ and $\beta H$ for a braced frame structure including outriggers. Where $\omega$ can be expressed as:

$$\omega = \frac{S_h}{S_v} \tag{2.3}$$

in which $S_h$ represents the strains in the horizontal and diagonal members and $S_v$ represents the strains in the vertical members. These characteristic structural parameters can be expressed as following:

$$S_v = \frac{H}{EI_t} + \frac{H}{EI_c} \tag{2.4}$$

$$S_h = \frac{1}{\alpha^2}\left\{\frac{b}{24EI_{\mathrm{o}}} + \frac{1}{hGA_{\mathrm{o}}} + \frac{1}{hGA_t}\right\} \tag{2.5}$$

Moreover, the dimensionless characteristic parameter of $\beta H$ can be expressed as:

$$\beta H = H\sqrt{\frac{\alpha GA_t}{EI_t}} \tag{2.6}$$

where $GA_t$ represents the shear stiffness of the braced frame due to racking, $EI_t$ represents the bending stiffness of the braced frame, and $\alpha$ is a dimensionless parameter that can be computed as follows:

$$\alpha = \frac{l}{b} \tag{2.7}$$

Where $l$ is the distance from the exterior column to the centre line of the braced frame and $b$ is the length of the flexible outrigger measured from the facade column to the outrigger-braced frame interface, illustrated in Figure 2.5.

**Figure 2.6:** Optimum location of outriggers [8]

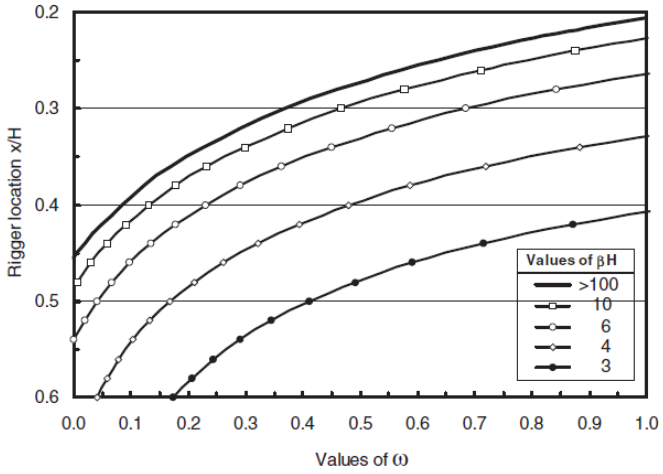


It can be concluded that determining the optimum location for an outrigger in a structure involves complex calculations and depends on various factors. Therefore, for the purpose of the research, a simplification is made of the location of the outrigger by considering only the total height of the structure. Further details wills be explained in Chapter 4.

## 2.4. Framed Tube

As previously mentioned, a key characteristic of a tube system is the strategic placement of closely spaced perimeter columns that are connected by substantial spandrels [5]. The fundamental design principle supporting this architectural approach is to distribute a significant portion of the load-bearing structure along the building's perimeter. This strategy aims to optimise the cross-sectional flexural rigidity of the structure.

Shear lag is a phenomenon that occurs in structural systems like tube systems, where loads are distributed along a perimeter structure [9]. When external forces act on a building, such as wind or seismic loads, these forces are primarily resisted by the outer columns and elements of the building's perimeter. Shear lag arises because not all columns along the perimeter contribute equally to resisting these forces. The columns farther away to the point of load application carry a larger share of the load, while those close to the point of load contribute less. This non-uniform distribution of forces can lead to differences in stress and deformation across the perimeter, potentially resulting in localized weak points or inefficiencies in the structure's response to external loads. The axial stress distribution with and without shear lag of a framed tube due to a lateral load is illustrated in Figure 2.7.

**Figure 2.7:** Axial stress distribution framed tube [9]

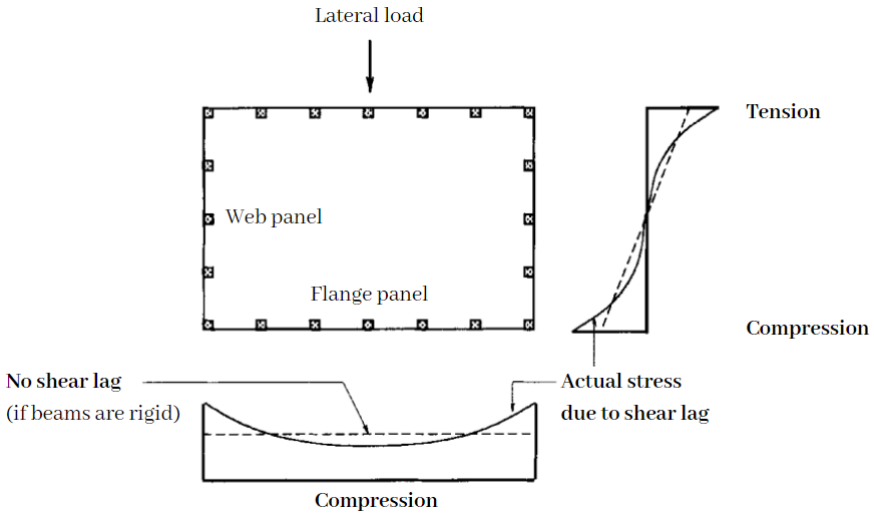


## 2.5. Performance Parameters

The primary objective of this study is to establish an accurate prediction of the structure to facilitate the comparison of various performance parameters across different stability frameworks. Its purpose is to provide a quick performance assessment of the structure during the initial design phase. The performance parameters that will be looked at are costs, environmental impact and flexibility. The focus is therefore not on the structural performance parameters such as deflection, as they are governed by established norms and requirements. The critical criterion is whether the structure operates effectively within the specified tolerance limits, rather than the specific extent of deflection. In essence, the primary focus is on the comparison of the performance of the structure within the established structural norms and requirements.

### 2.5.1. Structural costs

The quantification and comparison of construction costs for the various buildings will be determined. The construction costs typically refers to the expenses related to construction materials (such as concrete, rebar, and structural steel), delivery (from factory to construction site), labor, equipment, and supplementary activities (such as on-site testing). However, this research focuses solely on the costs associated with various construction materials. The total construction costs will be determined by assessing the type and quantity of materials required. Subsequently, the total material costs will be calculated by multiplying the quantity of each material by its respective unit cost. The expression for total costs is presented in Equation 2.8, adapted from Gan et al. [10]:

$$CC_T = \left[ \sum_{i=1}^{I} V_i CC_i + \sum_{j=1}^{J} \rho_j V_j CC_j \right] \cdot A^{-1} \tag{2.8}$$

Where:

$CC_T$ = total construction cost of considered building [€/m$^2$]
$i$ = specific type of concrete
$j$ = specific type of rebar or structural steel
$V_i$ = quantity of concrete *i* [m$^3$]
$CC_i$ = material cost of 1 m$^3$ of concrete *i* [€/m$^3$]
$\rho_j$ = density of rebar or structural steel *j* [kg/m$^3$]
$V_j$ = quantity of rebar or structural steel *j* [m$^3$]
$CC_j$ = material cost of one unit of steel *j* [€/kg]
$A$ = GFA of considered building [m$^2$]

### 2.5.2. Environmental Costs

To quantify the environmental impact in this research, the environmental cost (EC) method was utilised. EC is a Dutch assessment method that consists of ten distinct environmental impact categories and associated formulas [11]. Each impact category is assigned a factor in euros, representing the hypothetical cost (shadow price) needed to mitigate its impact to a sustainable level (see Table 2.9). The environmental impact was computed and analyzed based on the Cradle-to-Gate principle, specifically focusing on the production phase (A1-A3). The stages of life of a building according to EN 15804 is illustrated in Figure 2.8, where also the principle of Cradle-to-Gate can be seen.

**Figure 2.8:** Stages of life cycle of a building accordance with EN 15804

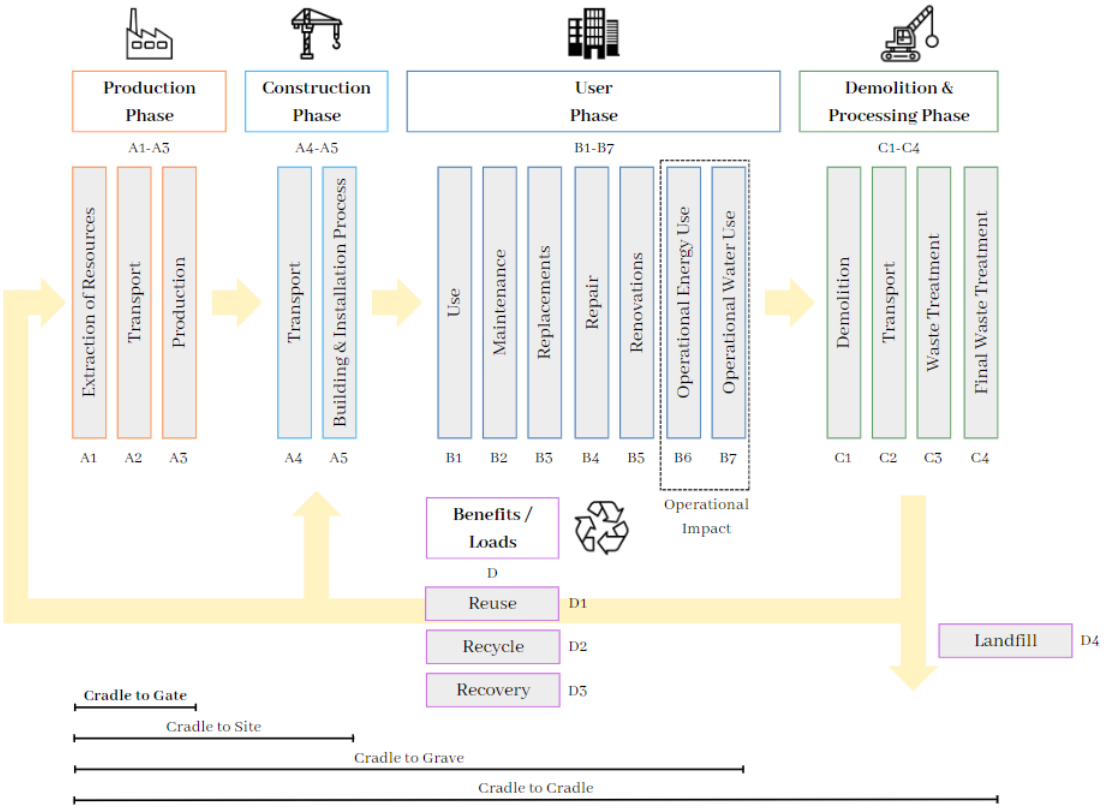


This study the environmental cost of design alternatives is calculated through embodied carbon ($EmCO_2$), which refers to $CO_2$ emissions from material extraction to construction (specifically Cradle to Gate in this research). $EmCO_2$ serves as a benchmark for global warming potential, expressed in Carbon Equivalence ($CO_2eq$). The $CO_2eq$ for each material will be calculated and adjusted by the shadow price of $CO_2eq$, as shown in Table 2.9. The formula for cradle-to-gate emissions and costs follows Gan et al. [12]:

$$EC_{C-G} = \left[ \sum_{i=1}^{I} V_i EF_i + \sum_{j=1}^{J} \rho_j V_j EF_j \right] \cdot SP_{CO_2eq} \cdot A^{-1} \tag{2.9}$$

Where:

$EC_{C-G}$ = total embodied cradle-to-gate carbon cost of considered building [€/$m^2$]
$i$ = specific type of concrete
$j$ = specific type of rebar or structural steel
$V_i$ = quantity of concrete *i* [$m^3$]
$EF_i$ = carbon emission factor per unit volume of concrete *i* [kg$CO_2$eq/$m^3$]
$\rho_j$ = density of rebar or structural steel *j* [kg/$m^3$]
$V_j$ = quantity of rebar or structural steel *j* [$m^3$]
$EF_j$ = carbon emission factor per unit mass of steel material *j* [kg$CO_2$eq/kg]
$SP_{CO_2e}$ = shadow price per kg $CO_2$eq [€/kg$CO_2$eq]
$A$ = GFA of considered building [$m^2$]

The shadow price per kg $CO_2$eq can be referenced in Figure 2.9. The impact of other categories is indirectly considered since for each material the total equivalent $CO_2$ is taken to determine the overall impact of the materials.

**Figure 2.9:** Impact categories and corresponding shadow prices [13]

| **Impact Category** | **Unit** | **Shadow Price / kg Equivalents** [€/kg] |
|---|---|---|
| Abiotic Depletion | kg Sb eq | €0.1600 |
| Global Warming (GWP100) | kg $CO_2$ eq | €0.0500 |
| Ozone Layer Depletion (OCP) | kg CFC-11 eq | €30.0000 |
| Human Toxicity | kg 1,4-DB eq | €0.0900 |
| Fresh Water Aquatic Ecotox | kg 1,4-DB eq | €0.0300 |
| Marine Aquatic Ecotox | kg 1,4-DB eq | €0.0001 |
| Terrestrial Ecotoxicity | kg 1,4-DB eq | €0.0600 |
| Photochemical Oxidation | kg $C_2H_4$ eq | €2.0000 |
| Acidification | kg $SO_2$ eq | €4.0000 |
| Eutrophication | kg $PO_4^{3-}$ eq | €9.0000 |

The emissions in the built environment can be divided into the operational carbon and the embodied carbon. The $CO_2$ emissions resulting from the operation of the built environment are referred to as the operational carbon and is the sum of all the carbon produced over the life time use of the building. The embodied carbon is the carbon footprint of the building before it is built, and consists of the green house gasses emitted during the construction process. The breakdown of the whole life carbon and the embodied carbon for a typical office building is visually shown in Figure 2.10. Notably, 'Construction', on average for a typical office building, accounts for 35% of the embodied carbon. Further dissecting this construction phase reveals that the 'SuperStructure' and 'Substructure' components have the most significant role, collectively contributing to over 60% of the total embodied carbon in a building. It illustrates that by attempting to minimise the embodied carbon or by gaining a clear overview of the embodied carbon of the 'Superstructure' and the 'Substructure', a significant influence on the total embodied carbon of a structure can be achieved.

**Figure 2.10:** Breakdown of embodied carbon typical building

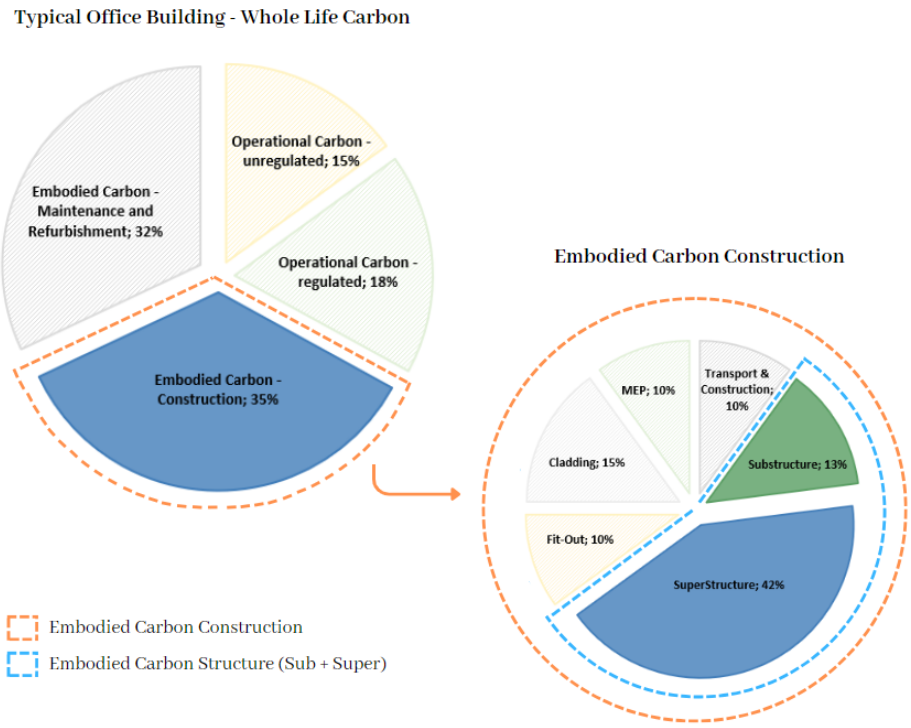


Embodied carbon data sourced from various organizations has been compiled for this study [14] [15] [16]. The environmental impact of different materials and structural elements is assessed using EPDs (European Product Declarations) from multiple organizations. Specifically, the focus is on global warming potential (GWP), recognized as the most significant environmental impact category. Additionally, only stages A1-A3, corresponding to the Production Phase (Cradle to Gate), are considered in this analysis. Therefore, the environmental impact in terms of GWP for stages A1-A3 is detailed in the table, with the figures used for this research provided in Table A.1.

## 2.6. Loads

A high-rise building is exposed to vertical and horizontal loads. In this section in more detail the vertical and horizontal loads will be explained.

### 2.6.1. Vertical Loads

The vertical loads can be categorized into dead loads and variable loads.

- **Dead loads.**
  The total dead weight consists of the summation of the contribution of the structural and the non-structural components. The structural components can be further categorized into the floor structure, the columns and the facade. The self weight of the structural components will automatically be generated and taken into account in the parametric model.

  The non-structural elements are the floor finishing, the ceiling and the mechanical installations. The loads coming from those as follows: 1.2 $kN/m^2$ for floor finishing, 0.15 $kN/m^3$ for the ceiling and 0.1 $kN/m^3$ for mechanical installations [17]. This results in a combined total of 1.45 $kN/m^3$.

- **Variable loads.**
  The amount of variable load is depending on the category of the structure. The overview of the allocation of the five categories can be seen in Eurocode 1 Part 1 (2019) [18]. Category A refers to

variable loads applicable to residential buildings, with a magnitude of 1.75 $kN/m^2$ while category B refers to variable loads for office areas, which is equal to 2.50 $kN/m^2$. The variable load on a floor thus is depending on the building's purpose. The variable load for light-weight partition walls of 1.50 $kN/m^2$ is also taken into account.

### 2.6.2. Horizontal Loads

The lateral force acting on a structure is referred to as the **wind load**, and it can be computed using Equation 2.10 as specified in Eurocode 1 Part 4 (2005) [19]. Only wind loads were considered, as there is no meaningful seismic activity in the area, Rotterdam, of the structure. The process of wind load calculation is comprehensive, with a more detailed breakdown of all the involved parameters provided in Appendix B. In summary, this section presents the primary equations.

$$F_w = c_s c_d \cdot c_f \cdot q_p(z_e) \cdot A_{ref} \tag{2.10}$$

Where:

$c_s c_d$ = structural factor
$c_f$ = force coefficient for the structure
$q_p(z_e)$ = peak velocity pressure ate reference height $z_e$
$A_{ref}$ = reference are of the structure

- **The structural factor** $c_s c_d$ should take into account the effect on wind actions from the non-simultaneous occurrence of peak wind pressures on the surface ($c_s$) together with the effect of the vibrations of the structure due to turbulence ($c_d$). The assumption that $c_s c_d$ equals 1.0 cannot be applied to this research, as it does not align with the conditions applicable to high-rise structures. The value of $c_s c_d$ can be determined with the following expression:

$$c_s c_d = \frac{1 + 2k_p \cdot I_v(z_s) \cdot \sqrt{(B^2 + R^2)}}{1 + 7I_v(z_s)} \tag{2.11}$$

  Where:

  $z_s$ = reference height for determining the structural factor
  $k_p$ = peak factor of the fluctuating part of the load
  $I_v$ = turbulence intensity
  $B^2$ = background factor
  $R^2$ = resonance response factor

- **The force coefficient** $c_f$ of structural elements of rectangular section can be determined with the following expression:

$$c_f = c_{f,0} \cdot \psi_r \cdot \psi_\lambda \tag{2.12}$$

  Where:

  $c_{f,0}$ = force coefficient of rectangular sections
  $\psi_r$ = reduction factor of force coefficient for square sections with rounded corners
  $\psi_\lambda$ = end-effect factor for elements with free-end flow, related to slenderness ratio $\lambda$

- **The peak velocity pressure** $q_p(z)$ can be found with the formula:

$$q_p(z) = (1 + 7I_v(z)) \cdot \frac{1}{2}\rho \cdot v_m^2(z) \tag{2.13}$$

Where:

$\rho$ = wind density
$v_m$ = mean wind speed

The wind speed is depending on the wind zone of the location of the structure. The reference height $z_e$ is depending on the height and width of the building and is illustrated for a high-rise building in Figure 2.11. Moreover, the corresponding velocity pressure profile is illustrated over the height of the building.

**Figure 2.11:** Reference height and velocity pressure profile [19]

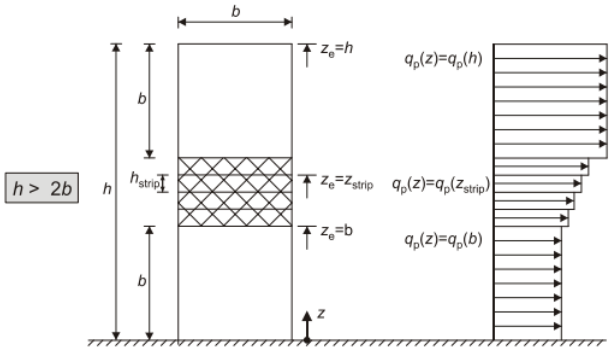


### 2.6.3. Load Combinations

For the design of the structure, different load combinations must be considered. The load combinations and factors that must be considered are summarized in Appendix C. The general formula for the SLS and ULS are presented below. The load combinations for vertical loads in the ultimate limit state is shown in Equation 2.14:

$$\textbf{ULS} = \Sigma(\gamma_{(G,j)} \cdot G_{(k,j)}) + \gamma_{(Q;1)} \cdot Q_{(1;k)} + \Sigma(\gamma_{(Q;i)} \cdot \psi_{(0;i)} \cdot Q_{(i;k)}) \tag{2.14}$$

The load combinations for vertical loads in the service limit state is shown in Equation 2.15:

$$\textbf{SLS} = \Sigma G_{(k,j)} + Q_{(1;k)} + \Sigma(\psi_{(0;i)} \cdot Q_{(i;k)}) \tag{2.15}$$

Where:

$\gamma_{(G,j)}$ = partial factor for permanent action *j*
$G_{(k,j)}$ = characteristic value of permanent action *j*
$\gamma_{(Q;1)}$ = partial factor for leading variable action
$Q_{(1;k)}$ = characteristic value of leading variable load
$\gamma_{(Q;i)}$ = partial factor for variable action *i*
$\psi_{(0;i)}$ = factor for combination value of variable action *i*
$Q_{(i;k)}$ = characteristic value of accompanying variable action *i*

## 2.7. Load-Bearing Floor Systems

This research will examine one type of load-bearing floor systems, namely the hollow core slab floors. This selection is influenced by a study conducted by Lankhorst et al. in 2019, which conducted a life cycle analysis of load-bearing structures in high-rise buildings across Western Europe [11]. While the study considered several materials for the structural components, when looking at the material steel as the structural material, the focus was on the examination of the floor combinations of hollow core slab floors and composite floors. The hollow core slab floor is a floor system that uses the precast concrete

slabs with hollow cores. The slabs feature voids or hollow sections, significantly reducing their weight without compromising strength. The composite floor is a floor system what is a combination of steel with cast-in-situ concrete. The concrete is applied in the compressive layer of the floor and the steel is used to accommodate the tensile forces. For this research the focus will be on the hollow core slab floor. A floor system has various functions, such as the separation of floor levels, insulation of heat and sound, and a structural function. The structural function consist of transferring vertical loads to the floor beams and channeling horizontal loads on the facade to the core.

## 2.8. Foundation

In order to transmit the structural loads of a building to the underlying soil, the installation of a foundation is needed. Foundations can generally be categorized into three main types: shallow foundations, pile foundations, and pile raft foundations [20]. A shallow foundation directly transfers the structural loads to the soil immediately beneath its level. On the other hand, a pile foundation transmits these loads to a deeper layer of sand, while a pile raft foundation uses a combination of both approaches. In the context of high-rise building design in the Netherlands, shallow foundations are typically unsuitable. This limitation comes from the high vertical pressure working on the soil by the structure's own weight. Consequently, high-rise buildings in the Netherlands typically rely on pile foundations for support. The load-bearing capacity and deformation behavior of a pile group is different from that of the behavior of the same piles individually, primarily due to the interaction between the piles and the surrounding soil.

The total deflection at the top of a high-rise building is determined by various structural factors, including flexural rigidity (EI), rotational stiffness (Cr), shear deformation, and second-order effects. The foundation influences the deflection and rotation due to stiffness and fixing the grid of piles at predetermined distances. For this research it has been decided to not include the foundation calculation, since the aim of the research is to compare different stability frameworks. Moreover, since the focus is on high-rise building, the rotational stiffness is having less influence on the total deflection when the height of the building is increasing. Since the influence of the rotational stiffness will have an comparable influence on both stability systems, it inclusion of the foundation will not influence the comparison between the stability systems.

## 2.9. Summary

This literature review focuses on stability frameworks for high-rise steel buildings, emphasizing the design considerations essential for constructing such structures. High-rise buildings, sensitive to lateral forces like wind and earthquakes, rely heavily on the strength and adaptability of steel, making it a preferred material due to its strength-to-weight ratio. The review categorizes stability systems into several frameworks, including rigid frame, braced frame, and outrigger systems, but narrows its focus to outrigger and braced-tube systems based on their suitability for steel construction and applicability within Dutch height restrictions. The analysis includes an evaluation of load-bearing factors, highlighting the predominance of lateral forces in high-rise design. Evaluation of the performance parameters is also provided, including the construction costs and the environmental implication of embodied carbon. the use and application of load-bearing floor systems, particularly hollow core slab floors. The performance parameters of costs and embodied carbon are explained and the calculation of it. Conclusively, the review underlines the importance of selecting appropriate stability frameworks for high-rise steel buildings, considering design, performance parameters, and environmental impacts.

# 3

# Machine Learning

This chapter of the literature review delves deeper into the Machine Learning (ML) theory, serving two main objectives: providing an introductory exploration of ML theory, and secondly, offering an overview of existing studies in the intersection of machine learning and structural engineering. First, an introduction to the essence of ML will be given, followed by an overview of research conducted in the ML and structural engineering domain. Subsequently, an explanation will be given of the Artificial Neural Networks, the chosen tool for this study. The chapter will conclude with a summary of the key findings from the literature review.

This chapter will aim to answer sub-question 2.

2 *What data set and data collection methods are necessary to train a machine learning model to accurately predict performance parameters of high-rise buildings with different volumes?*

## 3.1. Introduction to Machine Learning

The utilisation of artificial intelligence (AI) has been getting increasing attention across various engineering domains [21]. AI-based methodologies have demonstrated their effectiveness in related domains such as robotics [22], manufacturing [23], and medicine [24]; however, they have not yet been fully implemented by structural engineers [25]. A significant sub-field of AI is Machine Learning (ML), which involves the study, design, and creation of algorithms capable of learning from data and subsequently making predictions based on this learned information. Unlike, traditional programming, ML allows computers to acquire knowledge autonomously. Over the past decade, ML methods have seen an increasing adoption in tackling real-world challenges within structural engineering [21]. Nonetheless, substantial room remains for additional integration and utilisation of these methods. Notably, these methods have been applied to a spectrum of tasks, including structural health monitoring (SHM) and damage identification, optimisation, performance evaluation, evaluation of structural reliability and reliability assessment, as well as parameter identification for structural components. This research delves into the spectrum of the task of structural parameter identification, since the aim is to predict the performance parameters for a given volume of a steel high-rise building for different stability systems.

### Classification of Machine Learning

ML can be classified into three categories: supervised, unsupervised, and reinforcement learning [25]. This classification is illustrated in Figure 3.1. Supervised learning is used when both the outcome (also referred to as target or response) and the governing variables of a phenomenon are known. This category of learning can be further divided into regression, where the target is a numerical quantity, and classification, where the target is a label or class. Unsupervised learning, on the other hand, is useful when dealing with unlabeled data. Specifically, it can only be grouped into clustering, where the goal is to identify natural groupings or patterns within the data. Lastly, reinforcement learning applies to algorithms capable of adjusting actions in response to evolving conditions. This type of learning involves making decisions that optimise cumulative rewards over time.

Considering the categorization of various ML types, a selection can be determined for the type to be employed in this research. This choice should be in line with the research objective. The objective is to predict the performance parameters of high-rise buildings where the input is the volume of the high-rise building. The needed data for the ML model will be generated with a parametric model, so both the outcome and the governing variables are known. Moreover, the target is a numerical quantity and therefore it can be concluded that this research falls into the category of **Supervised Learning**, specifically **Regression**.

**Figure 3.1:** Main types of Machine Learning

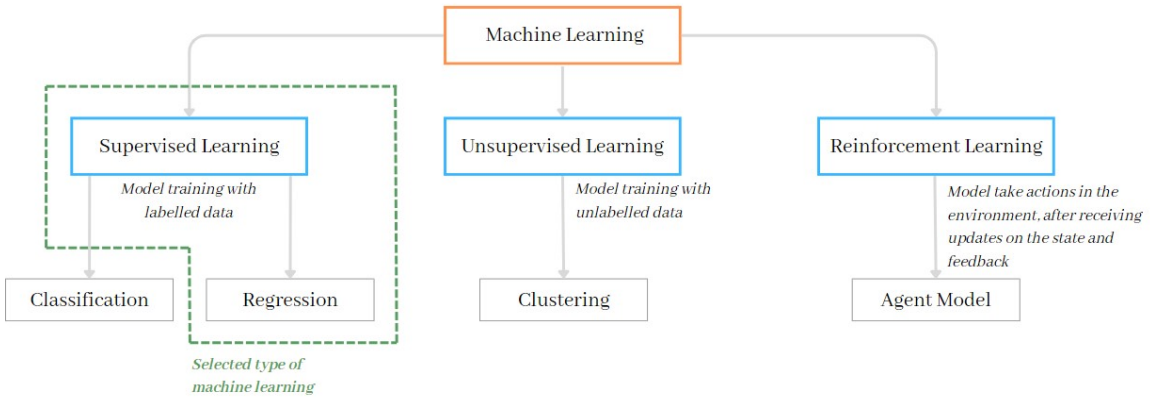


## 3.2. Machine Learning and Structural Engineering

Over the past ten years, there has been a growing trend in the utilisation of ML techniques to address practical challenges in the field of structural engineering [21]. The study of Thai (2022) into the current literature concerning the application of ML methods in the domain of structural engineering revealed five topics [26]:

1. Member
2. Material
3. Damage and Structural Health Monitoring (SHM)
4. Analysis and Design
5. Fire

In order to gain a clearer perspective on the types of subjects that are examined for each topic, a handful of examples are provided within each respective topic. An example within the topic of 'Member' is the prediction of load-carrying capacity of isolated structural members. An example within the topic of 'Material' is the prediction of mechanical property and optimising mix design of concrete. Crack detection and damage assessment of structures is an example within the topic of 'Damage and SHM'. Performing structural analysis to predict the behaviour of structures and optimising their design is an example within the topic of 'Analysis and Design' and predicting fire resistance of structures is an example within the topic of 'Fire'. This research falls within the topic of **Analysis and Design** since a prediction will be made of the performance of a high-rise building.

### 3.2.1. Machine Learning and Performance

Within the domain of Analysis and Design, there are numerous perspectives that can be explored. One particular emphasis is about assessing the performance of a building. Numerous studies have been conducted in the realm of 'Analysis and Design,' specifically targeting the structural performance of buildings. It has been observed that the artificial neural networks (ANN) method has been dominantly used in this domain [26]. So was the optimal design of truss systems examined by Iranmanesh and Kaveh (1999) using neural networks [27]. Kaveh and Servati (2001) employed ANN to formulate

designs for expansive truss structures comprising double-layer grids. Their study consisted of an assessment of the structures' maximum deflection and weight [28]. Papadrakakis et al. (1996) delved into utilising ANN for the purpose of conducting reliability analysis on steel frames [29]. ML has also found utility in the domain of structural analysis by forecasting the deflections and drifts of frames subjected to both gravity and lateral loads. Lee et al. (2001) formulated an ANN model for the analysis of steel-concrete composite bridge girders. This model demonstrated comparisons between the predicted outcomes of deflections, member forces, and ultimate loads and those derived from numerical methods [30]. Another example of a research that is conducted in the domain of ML regarding the analysis and design is from Guan et al. (2021) who created a model based on Random Forest to forecast the drift in steel moment frames [31]. Truong et al. (2022) evaluated different machine learning models including linear regression models, support vector machines, deep learning and tree-based ensemble algorithms for load-carrying capacity assessment of semi-rigid steel structures [32]. Yucel et al. (2019) developed an ANN for the estimation of the optimum tuned mass damper parameters where it was found that the proposed equations were effective for structures subject to seismic input [33].

Another perspective within the domain of Analysis and Design involves predicting the construction cost associated with a building. Research have delved into the utilisation of ANN to enhance the accuracy of building cost estimation [34]. Findings from multiple studies have consistently demonstrated that ANN's outperform traditional regression models in cost estimation of a structure. For example, Kim et al. (2004) conducted a study in which they predicted construction costs using both linear regression and neural networks [34]. The input data included variables such as gross floor area, number of stories, total units, duration, and roof types. Their research revealed that ANN's surpassed the performance of linear regression models in terms of prediction accuracy.

When ANN is being implemented, a surrogate model is created. ANN's are one of the many techniques that can be used to create surrogate models. Surrogate models are statistical models that aim to approximate complex simulation models [35]. Surrogate models serve as statistical representations of the relationship between a set of input variables (e.g. structural properties, loading characteristics) and the response or performance quantities of interest [36]. They are useful for reducing the number of simulations needed for computationally intensive applications. According to Geyer and Singaravel (2018) the main steps to build and use a surrogate model in building design are the following [37]:

1. Build a detailed simulation model
2. Run the model for many different cases to generate a database of results
3. Use the outputs to train and test the meta-model

Surrogate models hold promise as a quick decision-support tool for professionals in the field of construction. Nevertheless, it is crucial to evaluate the quality of the data. Furthermore, although employing surrogate models can reduce computational demands and decrease the time required for simulations and post-processing, it is essential to keep in mind the time required for surrogate model development, as it can significantly impact the design process [37]. Westermann and Evins (2019) found that ANN is the most popular method for surrogate modelling-based optimisation in building design, with energy use, overheating, carbon emissions and total cost as the most common prediction outputs [38].

The preference for ANN over traditional regression analysis in structural engineering arises from its ability to handle the nonlinear relationships between input and output variables during structural design. For instance, the relation between internal forces, displacements, and the size of structural members is nonlinear. This effectiveness in applying ANN to structural engineering is demonstrated in Cheng et al.'s study (2017), where they employed ANN to identify the optimal design parameters for steel columns subjected to axial load [39].

### 3.2.2. Machine Learning and Energy Performance

In the field of ML and structural engineering, and more specifically in the topic of Analysis and Design, another relevant area of exploration involves using surrogate models within ANN for the Building Performance Simulation (BPS) [40]. The focus of this domain is, however, more on the energy performance of a building rather than the structural performance of the building. Leveraging ML in BPS offers a significant advantage: when high-quality measured data is accessible for training the models, the energy consumption can quickly be estimated using these models. The utilisation of ANN surrogate models in

BPS has increased over the recent years, and that can be related to the ability of the positive trade-off between accuracy and computational costs.

The outcomes generated by these models can be categorized into four main domains: energy consumption, comfort metrics, climatic conditions, and environmental performance. Interestingly, the existing literature lacked any applications of high-rise buildings being subjected to such investigations. The predominant focus across these studies was the prediction of performance, rather than the goal of screening, comparisons, optimization, calibration, energy labeling, or control. Furthermore, it was found that the most used approach employed in this context was the utilisation of multilayer feedforward neural networks (MFNN). This is due to their capacity and diversity to develop surrogate models for different case studies and applications, with a high number of inputs and outputs, and diverse relationships between them. An example of a research that demonstrates the effectiveness of an ANN model in the field of energy performance is the study of Li et al. where the building cooling load was effectively predicted for an office building [41].

## 3.3. Artificial Neural Networks

In the domain of ML, Artificial Neural Networks (ANN's) have emerged as a powerful and diverse tool for solving complex problems across various domains [26]. ANN's are computational models inspired by the human brain's neural structure, and their ability to learn and generalise from data has made them essential in numerous applications. This section serves to provide a overview of the foundational concepts of ANN's, setting the stage for the exploration of their application in this research.

The primary objective of an ANN is to forecast output values based on a given set of input values [42]. The strength of an ANN lies in its capacity to make predictions on data it has never encountered during the training phase. To validate this capability, the network's performance must be assessed using a separate set of test samples from the data set that were not part of the training process. This data set is typically divided into two subsets: one for training, and the other for testing. The training samples are employed to train the network, while the testing set is reserved for assessing the network's performance on unseen data. An accurate network demonstrates effective generalisation to previously unseen data.

It's important to note that a longer training process does not necessarily results in better predictions. Overfitting is a common pitfall across all ML algorithms and should be avoided [42]. Overfitting occurs when the ANN achieves exceptional accuracy on the training data at the expense of significantly poorer performance on the testing data and is illustrated in Figure 3.2 [40]. In such cases, the trained network loses its utility since it fails to generalise effectively on unseen data (green square). On the other hand, underfitting is also a challenge and it arises when a model is too simplistic to capture the underlying patterns in the data. In the context of ANN's, this can occur if the network is too shallow or has too few neurons in its layers. An underfit model may perform poorly both on the training and the testing data. Achieving the right balance between overfitting and underfitting is a crucial aspect of training ANN for optimal predictive performance.

**Figure 3.2:** Example of overfitting [40]

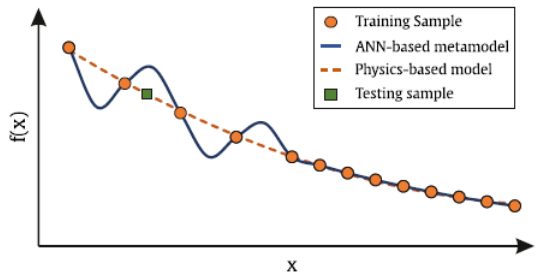


### 3.3.1. Network Architecture

ANN's are approximating functions, and the fundamental concept underlying this ability is known as the Universal Approximation Theorem [43]. This theorem represents the basic idea of this domain of

ANN's, stating that specific types of neural networks can approximate particular functions to a high degree of accuracy. The theorem implies that as long as certain conditions are met, a neural network possess the capacity to learn complex patterns and relationships in data.

Neural networks consist of layers of nodes, including an input layer, one or more hidden layers, and an output layer [42]. Each node functions as an artificial neuron, connecting to the next node and possessing its own weight and threshold value. When the output of a node surpasses its threshold value, it becomes activated and transmits its data to the subsequent layer in the network. Conversely, if the output falls below the threshold, no data is propagated further. A neural network consisting of more than three layers, including both input and output layers, is classified as a deep-learning algorithm. An schematic representation of an ANN is illustrated in Figure 3.3.

Most neural networks operate in a feed-forward manner, meaning information flows in the direction from the input layer to the output layer [43]. There is no feedback loop, and the network does not use its output as input for further processing in the same pass. Backpropagation is the training algorithm most commonly used with feed-forward neural networks. It is not a type of neural network itself but rather an optimization algorithm for training neural networks. It involves calculating the gradient of the loss function (or error function) with respect to the networks weight's and then updated the weights to minimise the loss or error. The section about the training process of the network will go into more detail about that process.

**Figure 3.3:** Schematic illustration of ANN

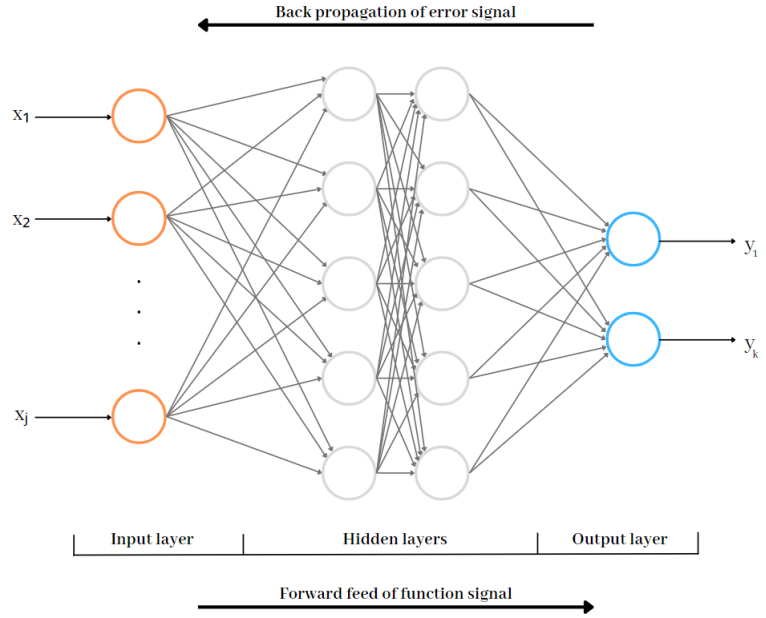


Input values are fed into the neurons within the input layer, where the quantity of neurons aligns with the number of variables or features associated with the problem. Within the input layer, input values do not change in value since there is no activation function present. Therefore, the output value of an input neuron is equal to the value of the actual data input value, where the actual data input values can be written as $\begin{bmatrix} x_1 & x_2 & \dots & x_j \end{bmatrix}$ and the values of the input layers as $\begin{bmatrix} a_1 & a_2 & \dots & a_j \end{bmatrix}$. Therefore it can be stated that $x_i = a_i$. The values of the input layers are subsequently sent to the first hidden layer. The neurons in the hidden layers do modify the incoming data by means of an activation function. This activation function is usually a certain non-linear function which enables the network to predict the non-linear behaviour of the system. The output layer ultimately generates the values that the network aims to predict, $\begin{bmatrix} y_1 & y_2 \end{bmatrix}$. The quantity of the neurons within the output layer corresponds to the number of output parameters targeted for prediction. The neurons within the output layer also apply data modification through the use of an activation function.

### 3.3.2. Mathematical Description

In this section, the mathematical description is given and explained of how a neural network maps output values to a predefined set op input parameters [42]. Figure 3.4 illustrates a single artificial neuron where an input layer is connected to one individual artificial neuron. This neuron accepts inputs from the previous layer, which could be either the input layer or neurons from the previous layer. It receives activation values from the input layer denoted as:

$$a_j = \begin{bmatrix} a_1 & a_2 & \dots & a_j \end{bmatrix} \tag{3.1}$$

Each connection between neurons is associated with a weight, represented as in vector form:

$$w_j = \begin{bmatrix} w_1 \\ w_2 \\ \vdots \\ w_j \end{bmatrix} \tag{3.2}$$

Additionally, there is a bias value $b$, a numerical parameter that contributes flexibility to the ANN. The bias allows a neuron to remain inactive if the weighted sum does not exceed a specific threshold. These three elements are combined to yield the total input $z$ of the neuron, as follows:

$$z = \begin{bmatrix} a_1 & a_2 & \dots & a_j \end{bmatrix} \begin{bmatrix} w_1 \\ w_2 \\ \vdots \\ w_j \end{bmatrix} + b = \sum_{i=1}^{j} (w_i a_i) + b \tag{3.3}$$

The input $z$ is subsequently passed through the activation function $f$, which will be elaborated upon in more detail in a later section. This process ends with the generation of the neuron's final output.

$$y = f(z) = f(\sum_{i=1}^{j} (a_i w_i) + b) \tag{3.4}$$

**Figure 3.4:** An input layer connected to an individual artificial neuron

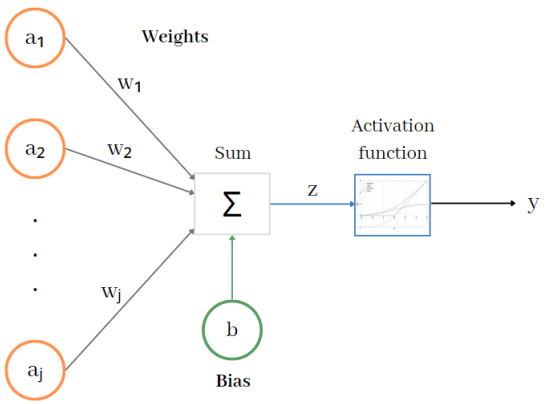


When the layer is comprised of multiple neurons, as opposed to the single-neuron example mentioned earlier, the weights are illustrated in a 2-dimensional matrix $W_{j,k}$, where $j$ corresponds to the number of neurons in the previous layer $(L-1)$ and $k$ represents the number of neurons in the current layer $L$. The resulting weight matrix connecting two layers can be expressed as the following vector:

$$W_{j,k} = \begin{bmatrix} w_{1,1} & w_{1,1} & \dots & w_{1,k} \\ w_{2,1} & w_{2,2} & \dots & w_{2,k} \\ \vdots & \vdots & \ddots & \vdots \\ w_{j,1} & w_{j,2} & \dots & w_{j,k} \end{bmatrix} \tag{3.5}$$

Up to this point, the input data has been depicted only as a vector, representing a single data sample. In practice, neural networks are trained on data sets containing numerous data samples. The actual data set takes the form of $i \times j$ matrix, where $i$ represents the number of data samples, and $j$ corresponds to the number of features or input variables for each sample. This data set is denoted as $X_{i,j}$ and can be written as the following vector:

$$X_{i,j} = \begin{bmatrix} x_{1,1} & x_{1,1} & \dots & x_{1,j} \\ x_{2,1} & x_{2,2} & \dots & x_{2,j} \\ \vdots & \vdots & \ddots & \vdots \\ x_{i,1} & x_{i,2} & \dots & x_{i,j} \end{bmatrix} \tag{3.6}$$

The matrix multiplication between the input data and the weights can be written as following, where $A_{i,k}^{(L)}$ represents the resulting activating matrix. It can be seen that the input $z$ is subsequently passed through the activation function $f(z)$.

$$z^{(L)} = A_{i,j}^{(L-1)} W_{j,k}^{(L)} + B_{i,k}^{(L)} \tag{3.7}$$

$$A_{i,k}^{(L)} = f(z^{(L)}) = f(A_{i,j}^{(L-1)} W_{j,k}^{(L)} + B_{i,k}^{(L)}) \tag{3.8}$$

The activating matrix $A_{i,k}^{(L)}$ is subsequently used as input for the next layer $(L+1)$. This iterative process continues for each layer until the ultimate output is generated from the output layer. The output matrix, denoted as $Y_{i,k}$ consists of $i$ rows, corresponding to the number of data samples, and $k$ columns, aligning with the number of neurons in the output layer, which is equivalent to the number of output parameters. The notation for the different elements are illustrated in the schematic representation of ANN in Figure 3.5.

**Figure 3.5:** Schematic representation of ANN including notation for different elements

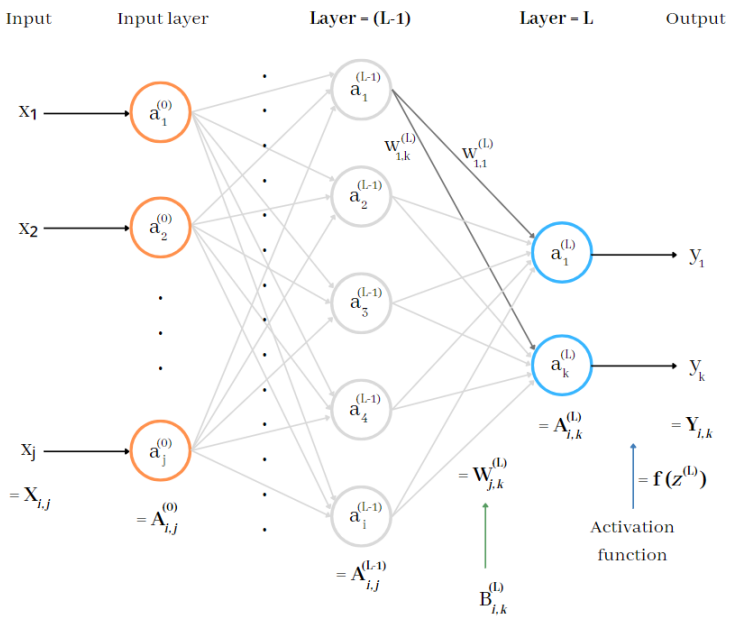

### 3.3.3. Hyperparameters

The criterion for determining the neural network architecture is based on the performance evaluation of several design aspects, the so called hyperparameters [30]. Here's a short explanation of the key hyperparameters that must be defined to achieve an accurate model:

1. **The number of neurons in the hidden layer.**
   The size of the hidden layer is one of the most important considerations when defining an accurate model [44]. Expanding the number of neurons within a layer has the potential to improve the model's ability to capture complex system behavior. However, this isn't always an assured outcome. The number of neurons should be tried to be minimised, given that an increase in number of neurons results in a significant rise in the number of connections. As a consequence, the weight matrices expand, leading to an increase of computational demands for calculating the gradient of the loss function and optimizing weight values. Generally, the number of neurons is increased until there is no improvement in performance anymore.

2. **The number of hidden layers.**
   The number of hidden layers corresponds to the layers positioned between the input and output layers. This concept connects to the Universal Approximation Theorem, which states that a single-layer network with a finite number of neurons in its hidden layer can represent any function [42]. However, achieving this may result in an impractically large number of neurons in the hidden layer, which will hinder effective network training. To be able to efficiently capture the complex behavior of a system while keeping the neuron count manageable, multiple hidden layers can be applied within the network. The optimal number of hidden layers can vary based on the problem's complexity and the data set's size.

3. **The initial connection weights.**
   The conventional approach to network training involves initialising its weights with small random values. If all weights are set to identical values initially, the network can face training challenges [44]. Therefore, when building a model, it is recommended to utilise kernel initializers, which statistically initialise the weights, generating and distributing them as suitable starting values for training.

4. **The initial biases.**
   The probability distribution from which the initial biases are drawn is depending on the hyperparameter of the bias initializer. When building a model, it is recommended to utilise bias initializers, which statistically initialise the biases, generating and distributing them as suitable starting values for training.

5. **The activation function type.**
   The role of the activation function is to introduce non-linearities in the network. Selecting the right activation function holds significant importance, as it can influence the formatting of input data. Available activation functions include the linear function, rectified linear unit (ReLU), hyperbolic tangent (tanh), and logistic sigmoid [43]. For both the hidden layer as for the output layer an activation function has to be chosen. In Figure 3.6 the different activation functions are plotted and to provide an understanding of these activation functions, the functions are shortly explained.

   - **Linear**

   $$f(z) = linear(z) = z \tag{3.9}$$

   The linear activation function, sometimes referred to as the "identity" function (scaled by 1.0) or "no activation," retains the input's weighted sum without altering it, returning the value directly. It is widely used in the output layer for regression problems due to its straightforward

nature, making it the default choice for the output layer for regression problems.

- **ReLU**

$$f(z) = ReLU(z) = max(0, z) \tag{3.10}$$

Rectified Linear Unit (ReLU) neurons are very popular in ANN applications [42]. This activation function is non-linear and has a derivative equal to 1 for $x$ > 0, equal to 0 for $x$ < 0 and undefined at $x$ = 0. The neuron's input is denoted as $z$, which can be calculated by using Equation 3.7. However, a drawback of this function arises when the neuron's input is significantly below zero, rendering the neuron inactive. Sometimes, it remains inactive because the small step sizes in weight adjustments during learning are insufficient to shift the input towards a positive value.

- **Logistic Sigmoid**

$$f(z) = Sigmoid(z) = \frac{e^z}{1 + e^z} \tag{3.11}$$

Prior to the arrival of the ReLU function, the Sigmoid function held the position of being the most widely used activation function in the hidden layers [42]. This function's output consistently falls within the interval (0,1), making it a non-linear function with a well-defined, continuous derivative. Due to the restriction of the sigmoid function's output to the range of 0 to 1, it is primarily employed in the output layer of an ANN. This strategic usage makes sure that the final output is normalized and directly represents the probability of any of the output classes being true.

- **Hyperbolic tangent**

$$f(z) = tanh(z) = \frac{e^z - e^{-z}}{e^z + e^{-z}} \tag{3.12}$$

The Hyperbolic tangent is relatively similar to the Sigmoid function. The function produces an output in (-1, 1) and is a scaled version of the Sigmoid Function. The hyperbolic tangent turns out to be a better choice than Sigmoid in almost every case. The reason for this is that the mean of the activation is closer to zero and the range is twice as large, which makes learning faster by having a higher derivative. However, the same issue as with the Sigmoid function is still observed: if the input becomes large, the slope approaches zero and learning is slowed down. The tanh function is mostly used as activation for the hidden layer, for the same reason as the Sigmoid is.

Both Hyperbolic tangent and Sigmoid have the gradient vanishing problem. That is, for some input regions the gradient is extremely small. This makes training via algorithms, such as gradient descent, inefficient. As a consequence, both the Sigmoid and Hyperbolic tangent functions are not widely used nowadays. The most common activation function for the hidden layer is the ReLU.

**Figure 3.6:** Commonly used activation functions in ANN [43]

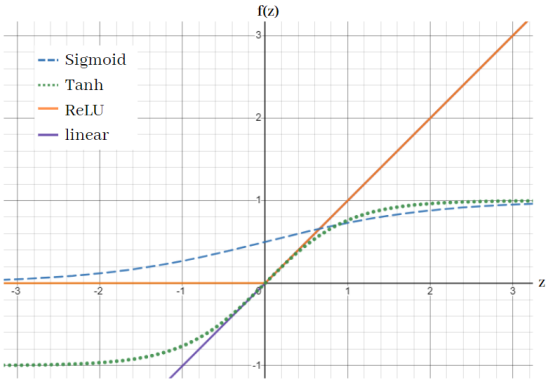


6. **The learning rate.**
   The learning rate, denoted as either $\eta_t$ or $\alpha$, is the step size used during gradient descent optimisation to update the model's weights. It determines the size of weight adjustments during training. The learning rate significantly impact the model's performance, as a lower learning rate may result in slower convergence but a more accurate model. In comparison, a larger learning rate may result in faster convergence but a less accurate model. The significance of this parameter becomes clear when looking at Figure 3.7. As illustrated, a learning rate that is too small results in slow training progress (indicated by the blue short arrows), while a too large learning rate causes training to overshoot the minimum, potentially leading to convergence failure (indicated by the green long arrows).

**Figure 3.7:** Importance of the parameter learning rate for training the ANN [40]

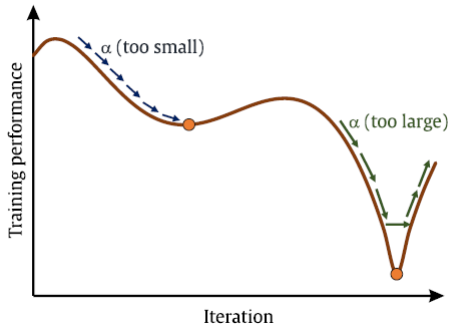


7. **The momentum term.**
   Incorporating a momentum term is a technique used to accelerate the convergence of the gradient-based optimisation techniques [42]. The momentum parameter determines the impact of prior weight adjustments on the current one. This momentum tries to prevent the model from becoming trapped in a local minimum. The value of momentum is between 0 and 1.

8. **Batch size**
   The batch size determines the number of data samples that are processed together in a single forward and backward pass during one iteration of training. It specifies how many training examples are used in each mini-batch to update the model's weight and biases. The choice of batch size can have a significant impact on the training process and the convergence of the model.

9. **Number of training epochs**
   An epoch is one complete pass through the entire training data set. It represents the number of times the model has seen and learned from all the training examples. The number of training

epochs is a critical hyperparameter because it determines how many times the model will update its weights and biases based on the training data. The appropriate number of epochs can vary depending on the complexity of the problem, the size of the data set, and the convergence behavior of the model.

### 3.3.4. Network Setup and Training Process

Before the training process of the model can begin, the network has to be properly set up. This consists of the determination of hyperparameters, which serve as the network's initial settings as just explained in Section 3.3.3. These hyperparameters significantly influence the behaviour and performance of the neural network. The hyperparameters can be optimized by applying an optimization technique.

After setting up the neural network, the training process can start. The training of a neural network is an iterative process aimed at reducing the loss in the produced output values [42]. This error is typically quantified using a loss function or a cost function, which can take various forms. The training procedure for a neural network involves iteratively minimising this loss function. Figure 3.8 presents a flowchart illustrating the general network set-up and training process of an ANN.

**Figure 3.8:** Flowchart network setup and training process of an ANN

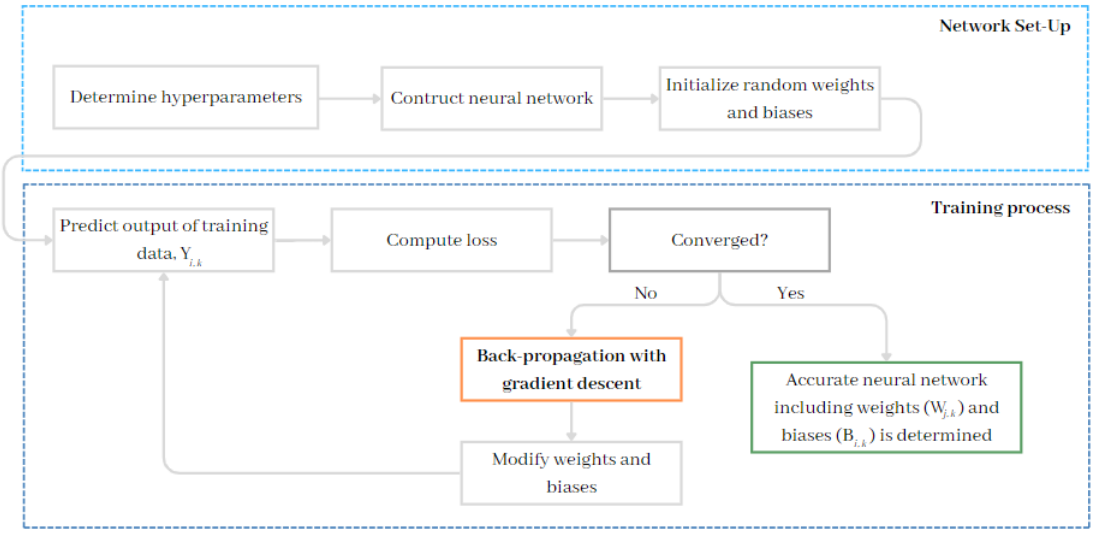


#### Loss Function

One of the steps in the training process involves calculating the loss, which depends on the definition of the applied loss function. The loss function quantifies the error between the predicted values and the true data values. In regression problems, a commonly used loss function is the Mean Squared Error (MSE), as defined in Equation 3.13 [42]. Here, $\hat{y}_i$ represents a single column vector containing predicted values for all training samples corresponding to a specific output variable, while $y_i$ represents the known true output values from the data set. The MSE across all training samples ($n$) is given by:

$$MSE = \sum_{i=1}^{n} \frac{(\hat{y}_i - y_i)^2}{n} \tag{3.13}$$

The value of MSE is always positive, regardless of whether the individual errors are positive or negative. The unit of measurement for the MSE is the square unit associated with the output parameter being predicted. To provide a more intuitive sense of the error magnitude, one can calculate the square root of the MSE, resulting in the Root Mean Squared Error (RMSE). In Equation 3.14 the definition is given of the RMSE.

$$RMSE = \sqrt{MSE} = \sqrt{\sum_{i=1}^{n} \frac{(\hat{y}_i - y_i)^2}{n}} \tag{3.14}$$

Similarly, another commonly used metric to evaluate the performance of regression models is the Mean Absolute Percentage Error (MAPE). Unlike the RMSE, which provides the error in terms of the absolute value of the error, the MAPE gives the relative error in terms of the percentage of the difference between the predicted and actual values. MAPE is calculated as the average of the absolute percentage errors over all instances, as shown in Equation 3.15:

$$MAPE = \frac{1}{n} \sum_{i=1}^{n} \left| \frac{y_i - \hat{y}_i}{y_i} \right| \times 100 \tag{3.15}$$

MAPE provides a measure of the accuracy of the model in predicting future values, and it is particularly useful when dealing with data of varying scales or when interpreting the predictive performance in terms of relative error percentages.

### Optimization techniques

During the process of setting up the neural network and the training process, two instances of optimization techniques come into play. Initially, a technique is selected to optimize the hyperparameters, and subsequently, another technique is chosen to optimize the weights and biases. The choice of an appropriate optimization technique can significantly impact the model's convergence, generalisation, and overall performance.

- **Optimization techniques for determining hyperparameters.**
  There exist mainly three approaches in finding the best hyperparameters [45]:
  - **Grid Search (GS).**
    Grid search is a systematic approach where a set of hyperparameter values (a grid) is defined for each hyperparameter that needs to optimized. It exhaustively explores all possible combinations of hyperparameters from the predefined grid. GS is straightforward and ensures that all specified hyperparameter values are explored. It is useful for relatively small hyperparameter spaces. However, it can be computationally expensive and inefficient for large or continuous hyperparameter spaces since it explores all combinations.
  - **Random Search (RS).**
    Random search, in contrast to GS, randomly samples hyperparameter values from predefined ranges. It randomly selects combinations of hyperparameters for evaluation without the exhaustive nature of GS. RS is more efficient than GS for high-dimensional or continuous hyperparameter spaces. It can find good configurations with fewer evaluations. However, it does not guarantee that all hyperparameter combinations will be explored.
  - **Genetic Algorithm (GA).**
    Genetic algorithms are inspired by the process of natural selection. They evolve a population of potential solutions (hyperparameter configurations) over generations. GA's use selection, crossover (recombination), and mutation operators to generate new hyperparameter configurations. Fitness evaluation guides the selection of the best configurations. GA's are suitable for complex and non-linear hyperparameter spaces, and can discover good configurations efficiently. A disadvantage of GA's is that it may require more computational resources and tuning compared to GS and RS.
- **Optimization techniques for determining weights and biases.**
  The common used methods to optimize the weights and biases in the training process are the gradient descent method and the momentum optimization [42] [46].

– **Gradient Descent Optimization.**
Gradient Descent algorithms are a class of optimizers with the ability to locate local optima within a loss function [47]. These algorithms rely on the gradients, or derivatives, of the loss function concerning the problem variables at each step to establish the appropriate step size and direction. In the domain of ANN, a method called **back-propagation** efficiently and analytically calculates these gradients.

Back-propagation is the process of updating the weights of the network in order to reduce the error prediction. The loss, denoted as $C$, represents a function of all weights and biases in the network. Its gradient, denoted as $\nabla C$, points in the direction of the steepest ascent within the loss function. However, through the process of gradient descent, the model's parameters are systematically adjusted in the opposite direction of the gradient, effectively minimising the loss. This iterative approach forms the core of training neural networks.

The loss gradient vector, $\nabla C$, can be expressed as:

$$\nabla C = \left[\frac{\delta C}{\delta v_1} \quad \frac{\delta C}{\delta v_2} \quad ... \quad \frac{\delta C}{\delta v_n}\right]^T \tag{3.16}$$

Here $v_i$ represents a vector containing all weights and biases. The loss gradient vector indicates the direction in an $n$-dimensional space in which the slope of the loss function is maximised. The update to the vector containing all weights and biases ($v_i$) is calculated as:

$$\Delta v = -\eta \nabla C \tag{3.17}$$

Where $\eta$, known as the learning rate, is a crucial hyperparameter (see Section 3.3.3) that determines the step size used during gradient descent. The change in the loss function can be approximated as:

$$\Delta C \approx \nabla C \cdot \Delta v \tag{3.18}$$

This change quantifies how the loss is expected to decrease after each parameter update.

– **Momentum Optimization.**
In contrast to regular Gradient Descent, which takes small consistent steps down the slope, Momentum Optimization accelerates the descent process significantly [46]. Instead of directly subtracting the gradient of the cost function, multiplied by the learning rate, Momentum Optimization introduces a momentum vector $m$. At each iteration, it subtracts the local gradient from this momentum vector and updates the weights by adding the adjusted momentum vector, see equation 3.19. Unlike the conventional approach where the gradient determines the speed of descent, in Momentum Optimization, the gradient acts as an accelerator rather than just the speed controller. The method considers the previous gradients, allowing the optimization process to get a momentum in a specific direction. To prevent too big momentum, a hyperparameter of the momentum term, denoted as $\beta$, is used. This parameter ensures that the momentum doesn't grow too large and the model doesn't overshoot the optimal solution.

$$\begin{aligned} m &= \beta m - \eta \nabla C \\ \Delta v &= \Delta v + m \end{aligned} \tag{3.19}$$

## 3.4. Genetic Algorithm

Genetic Algorithm (GA) is based on natural evaluation of organisms. As discussed in Section 3.3.4, the GA optimisation technique proves to be suitable technique for identifying optimal hyperparameter settings. It has been briefly noted that GA's are able in handling complex and non-linear hyperparameter spaces, efficiently uncovering effective configurations of the hyperparameters. Consequently,

this research will employ the GA optimisation technique, and the following section will provide a short introduction in the theory behind GA's.

The GA process starts with the population initialisation stage where a population is a collection of individuals [45] [35]. The initial population is typically formed by generating a set of individuals at random. Then, for each successive generation, the following sequence of steps is iteratively carried out:

1. **Evaluation of Fitness.** Each individual's fitness is assessed and connected to the individual.
2. **Selection.** Individuals are chosen to carry over into the next generation.
3. **Variation.** The gene pool undergoes variation to explore new potential solutions.
4. **Repeat.** Continue the process until the one of the specified stopping criteria is satisfied.

The flowchart of the process of GA, including all the different steps, is illustrated in Figure 3.9.

The GA can be stopped when one of the following stopping criterion is satisfied:

- The maximum number of generation is reached.
- The desired level of fitness is reached.
- The fitness of individuals in new generations stops improving (convergence).

**Figure 3.9:** Flowchart genetic algorithm for optimisation hyperparameters

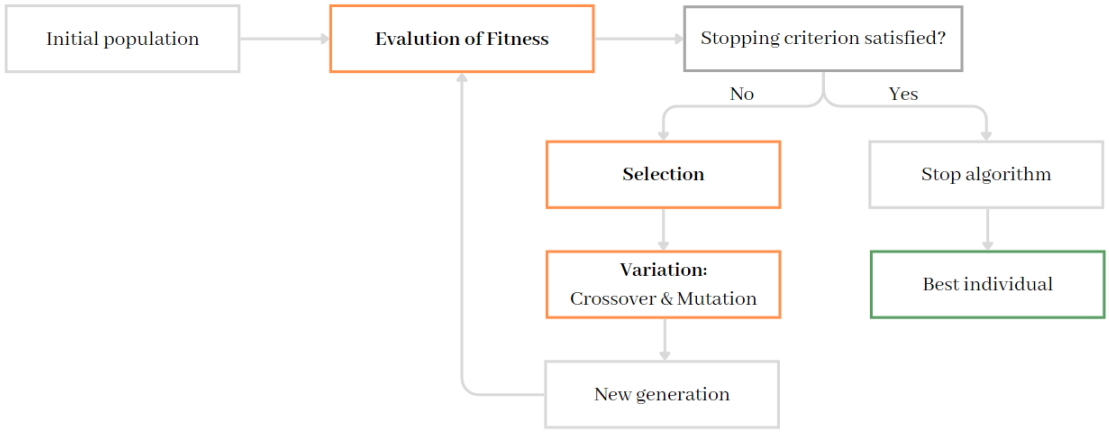


### 3.4.1. Evaluation of Fitness

Each individual within the population is assigned a fitness value, which play a important role in their potential for survival and genetic reproduction in the evolutionary process [35]. An individual's likelihood of surviving and passing on its genetic information to the next generation is directly influenced by its fitness score. The fitness score is computed using a fitness function and will be chosen based on the specific problem. The design and selection of the fitness function depend on problem's requirements. When optimising ML model hyperparameters, an individual's fitness can be measured, for instance, by its prediction accuracy.

### 3.4.2. Selection

In the selection phase, individuals are chosen to become parents for the next generation [35]. The probability of selection is typically proportional to an individual's fitness score. Solutions with higher fitness scores have a higher chance of being selected, simulating the concept of "survival of the fittest" from natural selection. The two most common selection methods are the following:

- **Tournament selection.** Tournament selection is a GA technique where a small group of individuals (the tournament size) is randomly sampled from the population. These individuals compete,

and the one with the highest fitness is chosen as a parent for the next generation. This method helps maintain genetic diversity and promotes the survival of individuals with relatively high fitness.

- **Elitism.** Elitism is a selection strategy in GA's where the best-performing individuals from the current generation are preserved and directly passed to the next generation without undergoing genetic operations like crossover and mutation. This ensures that the top solutions in the population are retained and continue to contribute to subsequent generations.

The selection procedures conducted result in the formation of a new generation, which is called the offspring. When the step of selection is done, this new generation will then undergo genetic variation to explore new potential solutions.

### 3.4.3. Variation

The gene pool undergoes variation to explore new potential solutions and there exist two main methods for variation [35]:

- **Crossover.** Crossover, also known as recombination, involves taking genetic material from two parent individuals selected from the current generation and combining it to create one or more offspring individuals for the next generation. This process mimics genetic recombination in nature, where traits from both parents are mixed to produce genetically diverse offspring. The hyperparameter of the crossover rate (number between 0 and 1) indicates the probability of two parents interchanging their genes.
- **Mutation.** Mutation is a genetic operator that introduces random, small changes into an individual's genetic material. When mutated, the individual will have one or more of its genes altered. The hyperparameter of the mutation rate (number between 0 and 1) indicates the probability of an individual being mutated.

## 3.5. Summary

This literature review examined the application of machine learning theory in structural engineering, focusing on surrogate modeling with Artificial Neural Networks (ANN). The review gave a first introduction of the mechanics of ANN, detailing how input values pass through layers of neurons, each modified by activation functions, to generate predicted values. Training involves iteratively minimising loss functions using metrics like Mean Squared Error (MSE) or Root Mean Squared Error (RMSE) or relative error percentages such as Mean Absolute Percentage Error (MAPE). Optimisation techniques play an important role in neural network setup and training, regarding both hyperparameters and weights/biases. Hyperparameters are the design aspects of the neural network and they significantly influence the model convergence and performance. The optimisation techniques for determining hyperparameters are grid search, random search, and genetic algorithms. Weight and bias optimisation primarily rely on Gradient Descent and Momentum Optimisation methods, adjusting parameters based on loss gradients and momentum vectors, respectively. Optimisation of both the hyperparameters and of the determination of the weights and biases is needed to enable the network to capture complex patterns in data.

# Part II
# Tool Design

# 4

# Methodology

This chapter describes the methodology used to answer the research question *'How can the performance parameters for different stability frameworks of a high-rise steel building with different volumes be predicted based on its design characteristics in a machine learning approach to accelerate the decision-process?'*. To do so, first the general approach is explained to give a framework for the research. Thereafter, different steps that were part of the approach are further elaborated.

## 4.1. Research Design

A methodology was constructed to be able to make the machine learning (ML) tool, more specifically to make the artificial neural network (ANN) model, which was used to make predictions about the performance of the stability framework for the given volume of high-rise steel buildings. The steps that were taken to achieve the goal of this research are summarized in a workflow diagram. The workflow is a rough estimate of the procedure and is shown in Figure 4.1. The goal was to outline a method that enabled an accurate and fast prediction of the performance, in terms of the structural and environmental costs, of a high rise steel building. By determining the costs of different stability frameworks, a decision can be made in the early-design phase regarding the most optimal stability framework for given dimensions.

**Figure 4.1:** Workflow diagram

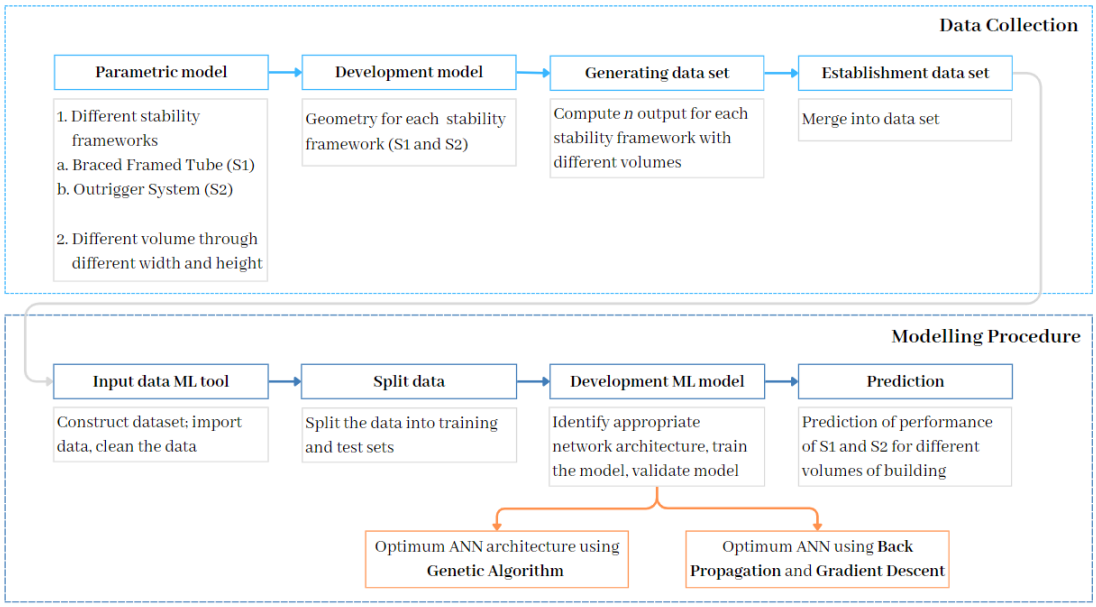

## 4.2. Data Collection

The data collection consisted of the establishment of two parametric models, one for the braced framed tube and one for the outrigger system, to generate input data for training the neural networks. The buildings were modelled in Grasshopper. Moreover, Karamba was used to make structural calculations of the structures. It was chosen to build parametric models of each of the framework since no sufficient available data of real-life high rise buildings and their performance was available. With a parametric model, output data was synthetically produced. In this thesis, simple parametric models were created to represent the high-rise buildings where the height and length of the rectangular floor plan of the building could differ. The chosen stability frameworks of the braced framed tube (S1) and the outrigger system (S2) are presented in Figure 4.2.

**Figure 4.2:** Stability Systems

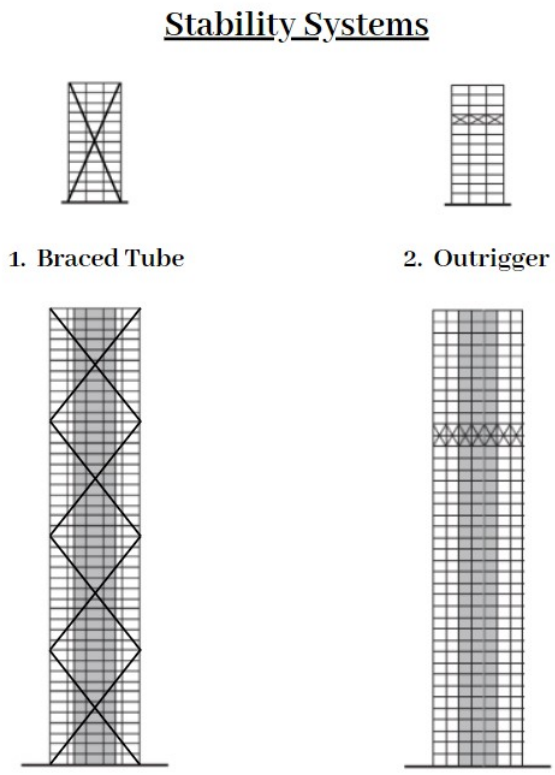


### 4.2.1. Create Parametric Model

The parametric models were made in the software Grasshopper as a plugin in the software Rhinoceros. The modelling and creation of the parametric models can be subdivided into the following steps:

1. **Determination of Input of Model.**
   The variables influencing building performance can be grouped into two main categories: structural variables and performance variables. Structural variables, managed within the Grasshopper (GH) script, refer to variables necessary for constructing the structure's geometry and conducting structural analysis. These variables can further be classified into fluctuating and fixed variables. Fluctuating variables, such as structure width (number of grids) and height (number of floors), fluctuated during data set creation, directly impacting the volume variations. In contrast, fixed variables remained constant during the data set creation. The data set generated by the parametric models provides masses of the structural elements for different geometries of the structures.

   The parameters are necessary for converting the masses of structural elements into structural and environmental costs. This conversion occurred in the Python script after obtaining the data

sets from running the parametric models.

2. **Building Geometry.**
Once the input parameters were established, the geometry was defined and translated into Karamba elements. Structural elements' dimensions differed across the building height to effectively optimise material usage. To be able to do this, different height zones were determined. The distribution of the height zones was depending on the distribution of the wind zones of the structure. A more detailed explanation of the distribution of height zones can be found in Section 5.3.1. Each height zone was customized with an optimised element cross-section, making sure that material efficiency was obtained over the height of the structure in the global analysis.

3. **Determination of Structural Analysis.**
The structural analysis of the structure was done with Karamba, a finite element software, which was depending on the following input:

   - **Joints.** Since this research primarily concentrated on the structural behavior during the early design phase, the connections were not elaborated in detail. However, the structure's stiffness was influenced by the connections' stiffness, making it essential to determine whether a connection was rigid or hinged. The default connection between elements in Karamba is rigid, so it was only needed to model the hinged connections. In Table 4.1 an overview is given of the connection type which were hinged for each stability system. Schematisation of the hinged connections between the elements is given in Figure 4.3 and Figure 4.4.

**Table 4.1:** Overview of connections for the different stability systems

| Element | Connection type | Stability System |
|---|---|---|
| Exterior Beams to Floors | Hinged | S1 and S2 |
| Exterior Beams to Floor Beams | Hinged | S1 and S2 |
| Inner Column to Floor Beams | Hinged | S1 and S2 |
| Exterior Column to Floors | Hinged | S1 and S2 |
| Exterior Column to Outrigger Truss | Hinged | S2 |
| Interior Column to Outrigger Truss | Hinged | S2 |
| Diagionals to Exterior Columns | Hinged | S1 |

**Figure 4.3:** Schematisation of hinged connection between elements of braced framed tube

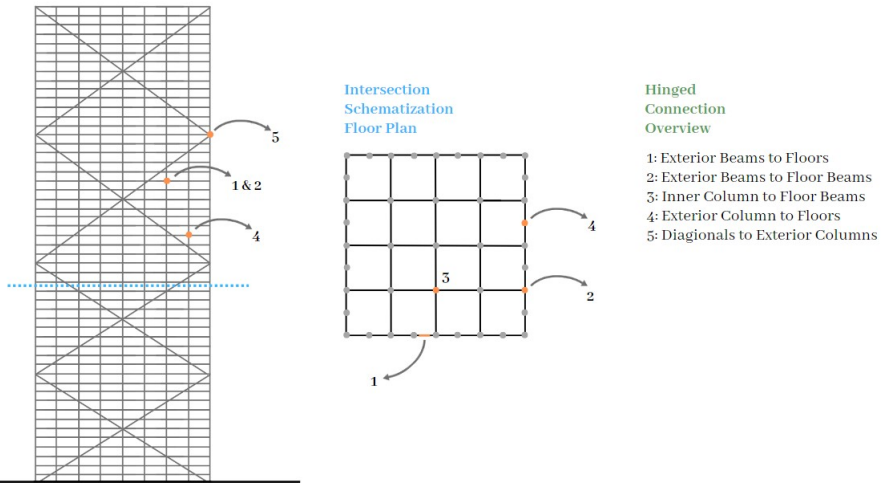

**Figure 4.4:** Schematisation of hinged connection between elements of outrigger system

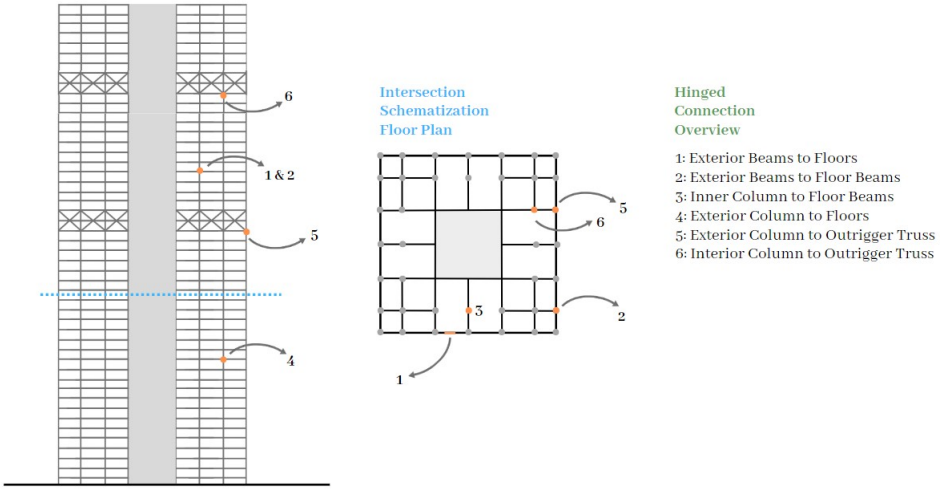


- **Material.** The material of the load-bearing structure was entirely of steel for braced framed tube and a combination of steel and concrete for outrigger system. The steel grade of S355 was chosen and the concrete class of C45/55. The most important material properties of S355 are given in Table 4.2 and of C45/55 (uncracked) in Table 4.3.

**Table 4.2:** Material properties of S355 [48]

| | $\rho$ (kg/m $^3$) | $E$ (MPa) | $G$ (MPa) | $f_y$ (MPa) | $f_u$ (MPa) | $\nu$ (-) |
|---|---|---|---|---|---|---|
| S355 | 7850 | 210000 | 81000 | 355 | 490 | 0.30 |

**Table 4.3:** Material properties of C45/55

| | $\rho$ (kg/m $^3$) | $E_{cm}$ (MPa) | $G$ (MPa) | $f_{ck}$ (MPa) | $f_{cm}$ (MPa) | $\nu$ (-) |
|---|---|---|---|---|---|---|
| C45/55 | 2500 | 36283 | 15118 | 45 | 53 | 0.20 |

- **Load definitions.** The load definitions ware categorized into vertical load, gravity, and horizontal load, with the horizontal load specifically referring to wind load. The magnitude of the horizontal load depended on the different wind zones applied to the structure. These wind zones, represented in Figure 2.11, varied in intensity across the height of the building. A more detailed explanation of the loads and their determination methods is presented in Section 2.6 of the Literature Review. The load combination in the ULS for Consequence Class 3 (CC3) was chosen for during the analysis.
- **Structural elements**. The structural elements included the floors, structural core, exterior columns, exterior diagonals, exterior beams, floor beams, inner columns and the outrigger truss. For the outrigger system, there is an additional distinction between the interior and exterior columns which are connected to the outrigger truss and those that are not. The columns that are connected to the outrigger truss will contribute more to the stability system of the structure, where the columns that are not connected to the outrigger truss will contribute mostly to only the gravity system. Since those columns will have a different function within the structure, they are divided into different subsets to enable a better optimisation. The floors and structural core were converted from a mesh to a shell. The other structural elements were all converted from a line to beam elements.
- **Supports.** The support of the structure was modelled as a fixed support at the bottom points of the structure.

- **Mesh size**. As Karamba is a finite element software, the model's elements were converted into a mesh. The accuracy of the results and the computation time depend on the mesh density. It was therefore necessary to determine the mesh size that will be applied in the model. The mesh size was assumed to be equal to the grid size.

Once these inputs were identified, they were combined into a single component for structural analysis. This process allowed for the calculation of maximum horizontal deflection and the assessment of the utilisation of beam and shell elements under the selected load case. The optimisation consisted of both strength and stiffness requirements, with the maximum utilisation of elements and maximum displacement established as criterion.

4. **Generation of Results.**
Once the parametric model and the desired output data were established, the target output of the structure was generated. The wanted output was the mass of the structural elements for each of the height zone specific. A plug-in tool in Grasshopper called Colibri was used to iterate the parametric model through various geometry variables. This process yielded a data set consisting of the results of the parametric model and the corresponding structural analyses. Table 4.4 provides an overview of the data set's general structure. Each row in this data set represents a list containing input parameter values for a single analysis, alongside the corresponding output values derived from the analysis. The output was the mass of each structural element, denoted as *i*, for each height zone, denoted as *n*. Columns in the table represent specific input or output parameters. The data was stored in a Comma-Separated Values (CSV) file.

**Table 4.4:** General shape of data set

| | Input $x_1$ *Width* | Input $x_2$ *Height* | Output $y_{(i, n)}$ *Mass*$_{(i, n)}$ |
|---|---|---|---|
| Sample 1 | . | . | . |
| Sample 2 | . | . | . |
| ... | . | . | . |
| Sample *m* | . | . | . |

A widely accepted rule of thumb in ML suggests having at least 10 times as many samples as parameters (weights and biases) in the neural network [46]. Applying this rule to this research, where the input data included the building's volume, a total of two input variables was present: one for height and one for the width of the floor plan. The number of output variables was significantly higher as the masses split up regarding different structural elements and different height zones. The total count of output variables was determined by the total number of structural elements and the number of height zones. These structural elements were categorized into two groups: those independent of height zones and those dependent on them. In the case of the braced framed tube, the bracing remained consistent across height zones, whereas for the outrigger system, the outrigger and core structures maintained consistent across heights. For both systems the floor beams are consistent across heights. The structural elements who were dependent on the height zone were the outer columns, inner columns and the outer beams. For the outrigger system, there is an additional division for exterior and interior columns connected to the outrigger and those not connected.. In Table 4.5 an overview is giving on what value these parameters had for the different stability frameworks.

**Table 4.5:** Overview determination of total number of output variables for each system

| | **Braced Framed Tube (S1)** | **Outrigger (S2)** |
|---|---|---|
| # of dependent structural elements | 3 | 5 |
| # of independent structural elements | 2 | 3 |
| # of height zones | 6 | 6 |
| *Total # of output variables* | *3*6+2=20* | *5*6+3=33* |

Taking into account these variables and the specification of one hidden layer with a maximum of 50 neurons, the total number of parameters (P) was estimated using the following equation:

$$\begin{aligned} P &= x_{input;features} \cdot x_{neurons} + x_{neurons} \cdot x_{output;neurons} \\ P_{S1} &= 2 \cdot 50 + 50 \cdot 20 = 1100 \\ P_{S2} &= 2 \cdot 50 + 50 \cdot 33 = 1750 \end{aligned} \tag{4.1}$$

To meet the rule of thumb, the aim was for a data set of around $1110 * 10 = 11100$ samples for braced framed tube and $1750 * 10 = 17500$ for outrigger system. Since this required a substantial data set, it was decided to simplify the desired output to only the total mass of each material. Since the research aimed to determine the overall performance of a structure to compare the two systems, the goal was still met only looking at the total masses. The masses were combined to represent only the total mass of steel and total mass of concrete. In this case, there was only one output neuron for braced framed tube (representing the mass of steel) and two output neurons for outrigger system (representing steel and concrete mass).

$$\begin{aligned} P &= x_{input;features} \cdot x_{neurons} + x_{neurons} \cdot x_{output;neurons} \\ P_{S1} &= 2 \cdot 50 + 50 \cdot 1 = 150 \\ P_{S2} &= 2 \cdot 50 + 50 \cdot 2 = 200 \end{aligned} \tag{4.2}$$

Applying the rule of thumb again, this resulted in a needed data set of 1500 samples for braced framed tube and 2000 samples for outrigger system, which was a more achievable data set size. Since, it was beneficial to understand the mass distribution across different structural elements for various height zones, additional neural networks were established and trained specifically for this purpose. After training, assessing the accuracy of all neural network models allowed for determining their usability and insights, even if they did not meet the rule of thumb beforehand.

Achieving a data set size of considerable size involved automating the Grasshopper script. The plugin of Colibri in GH was utilised to automatically generate through the GH model of braced framed tube and outrigger system by iterating through the input variables and extracted the corresponding outcomes. This approach enabled the generation of substantial data sets for the neural networks. The parametric models for both the braced framed tube and the outrigger system required approximately 72 hours each to run to complete the total data set.

The different steps needed for the creation of the parametric models in GH are summarized in the flowchart in Figure 4.5.

**Figure 4.5:** Flowchart of the creation of the parametric model in Grasshopper

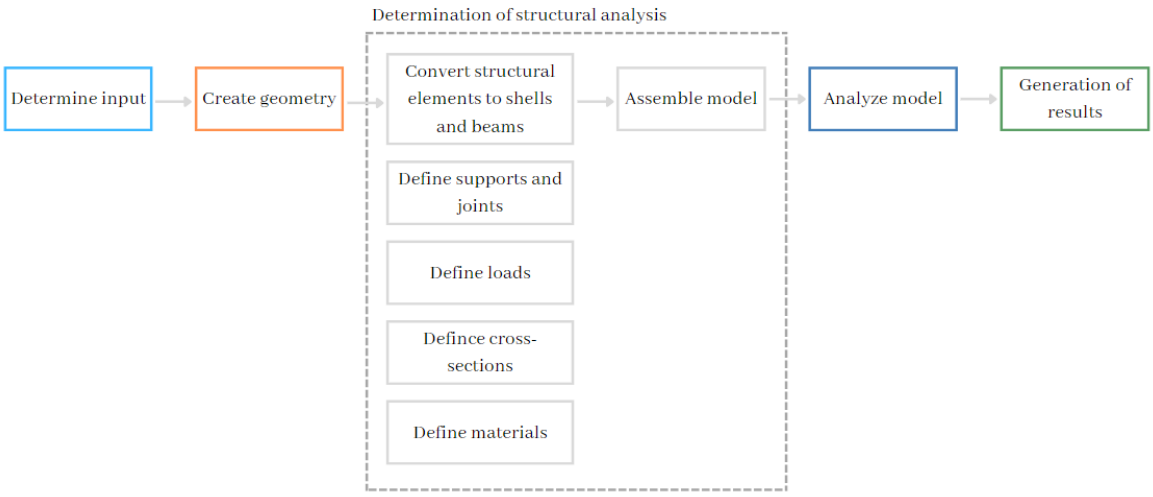

## 4.3. Data Preprocessing

After generating the data sets through the parametric models, it was crucial to preprocess the data to prepare it for use as input for the neural networks. Initially, the data was divided into training and test sets, followed by scaling. It is important to note that data preprocessing was performed separately for each of the four different neural networks. These neural networks consisted of two models for predicting the total mass of both stability frameworks, and two for predicting the mass of each specific structural element within each height zone. An overview of these neural networks is provided in Table 6.3.

| Stability System | ANN Model | Prediction Goal |
|---|---|---|
| Braced Framed Tube | S1-A | Total mass of structure |
| | S1-B | Mass of each structural element within height zones |
| Outrigger System | S2-A | Total mass of structure |
| | S2-B | Mass of each structural element within height zones |

**Table 4.6:** Different ANN models for prediction of the performance of stability systems

### 4.3.1. Split Data

To evaluate the performance of the neural network, the data set was divided into a training data set and a testing data set. During this process, the testing data set was set aside to ensure that the neural network was exclusively trained on the training data set. The purpose of the testing data set was to assess the accuracy of the predictive model on data it had not been exposed to before. This validation was important because the concept of a predictive model is to generalise its predictions across all data points, not just those seen during training. It is common practice to use 80% of the data for training and reserve 20% for testing [46]. Therefore, in this research, 20% of the data was allocated for the testing set and 80% for the training set. However, it was essential to carefully select the test data points. Simply choosing 20% of the data from either end of the data set is not advisable. This approach might lead to clustering of points in specific regions of the design space, potentially biasing the evaluation. A more representative selection method was used to ensure an unbiased and accurate assessment of the neural network's performance. The selection method for this research was the k-fold cross-validation.

### 4.3.2. Scale Data

The input variables were scaled to the same range to prevent poor performance of the neural network due to significant differences in scales along the variables [46]. The two most common and important scaling methods are:

- **Min-Max scaling (normalization).**
  This scaling method scales all data to values within a specified interval, which is almost always the interval of 0 and 1. This is done by subtracting the min value and dividing by the max value minus the min value. The library of Scikit-Learn in Python provides a transformer called $MinMaxScaler$ for this.
- **Standard scaling (standardization).**
  This scaling technique transforms the data into a standard normal distribution. Standardization involves subtracting the mean value, ensuring the standardized values always have a zero mean, and then dividing by the standard deviation, resulting in a distribution with unit variance. Unlike min-max scaling, standardization doesn't constrain values to a specific range, which may be a problem for some models. Neural networks often expect an input value ranging from 0 to 1, and therefore standard scaling may not be the best fit for this research. The advantage of standardization is that it is much less affected by outliers. Scikit-Learn offers a transformer called $StandardScaler$ specifically designed for this standardization process.

To meet the input requirements of the neural networks, which typically expect values within the range of 0 to 1, the research implemented the min-max scaling (normalization) method. Moreover, it should be noted that it was important to fit the scalers to the training data only, not to the full data set (including the test set). Additionally, it was also not necessary to scale the output data, or also referred to as the

target values.

## 4.4. Modelling Procedure

After generating and pre-processing the data set, the subsequent step involved starting the modeling procedure. This modeling process included implementing neural network algorithms and collecting and comparing the results. The modelling procedure consisted of implementing ML algorithms and gathering and contrasting the outcomes. The modelling procedure was done in Python, where Python packages were used for the development of the ML algorithm. The modelling procedure was subdivided in the following tasks:

1. *Import the scaled clean training data.*
2. *Create ANN model.*
3. *Choose hyperparameters.*
4. *Training ANN on data.*
5. *Validate model.*
6. *Make predictions.*

### 4.4.1. Create Artificial Neural Network

The process of training or learning an ANN involved the optimisation of interconnected weights and biases [49]. The widely utilised technique for determining optimal weights and biases in neural networks is the back-propagation algorithm. This technique enhances the network's precision by using a first-order gradient descent approach. The most significant advantage of this approach is its capacity to navigate beyond local minima on the error surface, which will result in solutions that are either optimal or very close to optimally. Thus, in this study, the back-propagation algorithm was the chosen method for the optimisation of interconnected weights and biases. The loss function that was used in this research is the Root Mean Squared Error (RMSE), which is a common loss function for regression problems. A more detailed explanation and the equation of the RMSE can be found in Section 3.3.4 of Chapter 3. The Python library Keras was used for the creation of the neural network and the Python library DEAP was used for the creation of the genetic algorithm (GA) for the determination of the optimal hyperparameters configuration. DEAP, which stands for Distributed Evolutionary Algorithms in Python, is a widely used library designed for the implementation of genetic algorithms. The Python library Scikit-Learn was used for the scaling of the data as mentioned in Section 4.3.

### 4.4.2. Choose Hyperparameters

The ability of an ANN to adapt to the data is depending on both its network architecture and the specific set of hyperparameters chosen. Selecting the appropriate hyperparameters is crucial and time-consuming. Because the network's ultimate performance can only be assessed after training, evaluating numerous hyperparameter combinations can become a time-intensive limitation. Consequently, finding an efficient method to determine the optimal hyperparameters becomes essential. As previously mentioned in the Section 3.3.4 of Chapter 3, there are multiple optimisation techniques for determining the hyperparameters. The three main optimisation techniques are Grid Search, Random Search and Genetic Algorithm. The method applied in this research for finding the optimal set of hyperparameters was the Genetic Algorithm.

Table 4.7 displays the hyperparameters used for optimisation. While there are several hyperparameters available for adjustment in an ANN, this research concentrated on four specific parameters: the number of neurons within the hidden layer, the kernel initializer, the bias initializer and the learning rate. The remaining hyperparameters were maintained as fixed variables for the purposes of this study. A short explanation of the chosen fixed parameters is given below. A more detailed explanation of the theory of each of the hyperparameters can be found in Section 3.3.3 of Chapter 3.

- The **number of neurons in the input layer** was depending on the number of input variables of the model, which included the height of the structure and the length of the floor plan, and therefore was equal to two for all the ANN models.

- The **number of neurons in the output layer** corresponded to the desired output of the model, specifically the performance parameters in this research for each of the structural elements, and therefore was equal to 1 for S1-A, 25 for S1-B, 2 for S2-B and 38 for S2-B.
- The **number of hidden layers** was set to be equal to one. This decision was based on the fundamental idea that one layer can handle complex tasks well according to the universal approximation theorem. This approach ensured that the neural network could capture important patterns in the data without unnecessary complications [30].
- For the **activation functions**, ReLU is commonly used in hidden layers, while Linear activation is suitable for the output layer for regression problems [46]. Therefore, for this research the ReLu was chosen for the hidden layers and Linear activation for the output layer.
- The chosen **cost function** for this regression task was Root Mean Square Error (RMSE), a widely used metric for evaluating the accuracy of regression models.
- In the training process, the **number of epochs** was set to a 10,000.
- A smaller **batch size** was taken and was set to be equal to 64 at first [46].
- The selected **optimiser** was momentum optimisation, preferred for its speed compared to the traditional gradient descent, as detailed in the theory Section 3.3.4. Additionally, Adam optimisation was adopted due to its proven effectiveness, ensuring fast convergence to a good solution [46]. To implement Adam optimisation, it was crucial to determine the learning rate hyperparameter, which was identified as one of the parameters to be optimised by GA.

**Table 4.7:** Summary of different ANN characteristics in this study

| Parameter Type | Parameter | Description |
|---|---|---|
| Fix | Neurons in input layer | 2 |
| | Neurons in output layer | 1 (S1-A), 25 (S1-B), 2 (S2-A), 26 (S2-B) |
| | Number of hidden layers | 1 |
| | Hidden layer activation function | ReLU |
| | Output layer activation function | Linear |
| | Cost function | RMSE |
| | Number of epochs | 10.000 |
| | Batch size | 64 |
| | Optimiser | Momentum optimisation (Adam) |
| Variable | Neurons in hidden layer | Varying from 1 to 50 |
| | Kernel initializer | Random uniform, Constant, Zeros |
| | Bias initializer | Random uniform, Constant, Zeros |
| | Learning rate | 0.01 or 0.001 |

### 4.4.3. Training ANN on Data

Once the neural network was constructed, the next step involved fitting the model to the training data. Before initiating the training process, it was essential to provide and clean the training data, and determine the number of training epochs. As mentioned earlier, the term ”epochs” refers to the number of complete passes the model makes through the entire training data set. Each epoch signifies one full cycle during which the model learns from all the provided training examples. Pre-defining a specific number of training epochs can be challenging. Choosing a too low value might lead to underfitting, while a too high number could result in overfitting. Although callback functions are typically used to address this dilemma, they are not applicable due to the utilisation of the Scikit library in Python. Instead, convergence graphs of the validation and training loss was inspected after training to assess if the selected number of epochs was adequate. Throughout the training process, the performance and error of the neural networks were evaluated using two different metrics: loss and validation loss. The loss represents the error computed over predictions for all training samples, while the validation loss quantifies the error across predictions for all testing samples. It is important to note that the neural network’s weights were updated based on the optimisation of the loss value, not the validation loss. The validation loss served only to assess the network’s ability to predict unseen data accurately.

The convergence graph illustrates the training and validation loss (or error) plotted against the number of epochs during the training process of the ANN model. By analyzing the convergence graph, it becomes clear if overfitting or underfitting is occurring. Overfitting is observed when the training loss continues to decrease while the validation loss either increases or remains constant. On the other hand, underfitting is identified when both the training and validation loss remain high and show minimal improvement, plateauing without convergence to a low value. If the convergence graph reveals any signs of overfitting or underfitting, adjustments can be made to the maximum number of epochs. Furthermore, the ANN model with the lowest error was defined as the best model and was saved as the final output.

### 4.4.4. Validation

In this research, two different types of validation were crucial. The first, cross-validation, played a role in the hyperparameter optimisation process. It was used in fine-tuning the hyperparameters to ensure optimal performance. The second type involved validation using the testing data set, which served as the ultimate evaluation and validation step for the selected neural network. This evaluation was based on the hyperparameters derived from the optimisation process. Both the different types of validation are presented in the flowchart in Figure 4.6.

**Figure 4.6:** Flowchart cross-validation and genetic algorithm workflow

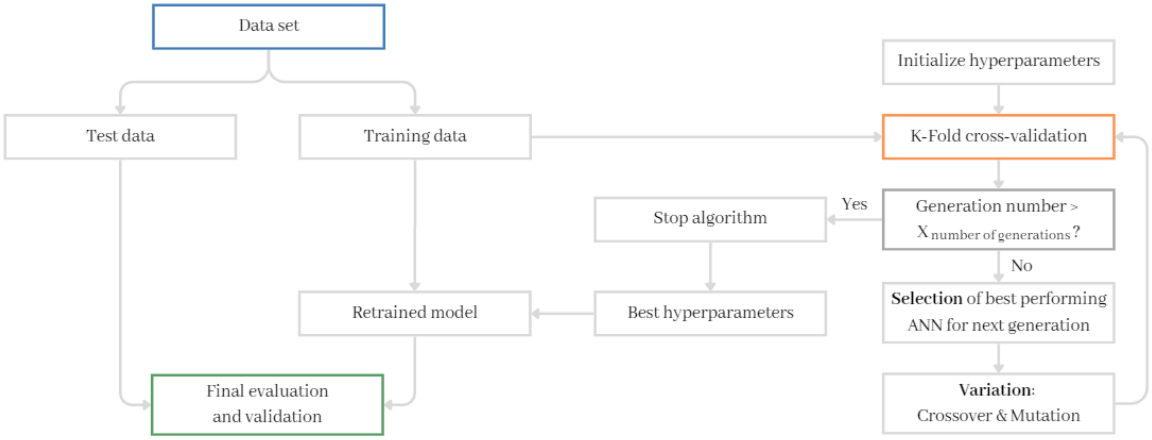


The cross-validation score holds significant importance as it provides insights into the generalisation capabilities of the neural network. This score essentially represents the network's ability to predict values on data it has never encountered before. This study utilised the cross-validation score as a key metric within the genetic algorithm.

The challenge of overfitting on the test set occurs when evaluating different settings, or hyperparameters, within the neural networks. This issue occurs because hyperparameters can be adjusted until the neural network model performs optimally, potentially allowing knowledge about the test set to influence the model. This leakage of information into the model can distort the evaluation results, no longer accurately reflecting the model's generalisation performance. To overcome this problem in this research, a portion of the data set was set aside as a 'validation set'. Training took place on the training set, and evaluation was done on the validation set. If the model performed well, the final evaluation was carried out on the test set. However, dividing the data into three sets significantly reduces the samples available for model learning, and the results can be skewed by a specific random choice for the pair of (train, validation) sets. A solution to this challenge is the implementation of cross-validation (CV). Although a test set is still reserved for final evaluation, the validation set is no longer needed in CV. In the basic k-fold CV approach, the training set is divided into $k$ smaller sets. For each of the $k$ folds:

1. A model is trained used $(k-1)$ of the folds as training data.

2. The resulting model is validated on the remaining part of the data.

The resulting model is validated on the remaining portion of the data. The performance measure reported by k-fold cross-validation is the average of the values computed in this iterative process. In this research, the training data set was divided into five different parts, thus employing a 5-fold cross-validation approach. This strategy ensured a reliable evaluation of the neural network's performance. A visual representation of k-fold cross-validation is presented in Figure 4.7.

**Figure 4.7:** Schematization k-fold cross validation

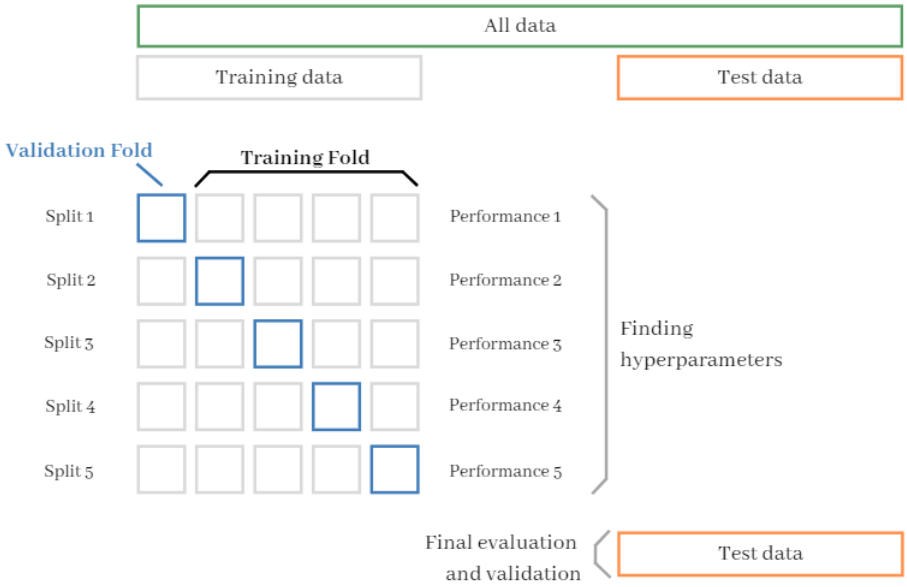


## 4.4.5. Hyperparameter Optimisation using GA

The objective of hyperparameter optimisation was to identify the most effective values for the parameters of the neural network that resulted in the most accurate results. As mentioned earlier, this research implemented the genetic algorithm as the optimisation technique. The fundamental concept involved iterating toward an optimal set of hyperparameters for the ANN models. These iterations, referred to as generations, mimic generations of individuals in biological evolution. The goal was for the fitness of these individuals to improve with each subsequent generation. In the first generation, a variety of random hyperparameter sets (referring to the variable hyperparameters) were generated. These different sets were so called individuals within the context of the GA. Each set of hyperparameters was used to create, train, and validate the neural network. The validation process assigned a specific fitness value to the neural network. The fittest ANN models were selected to survive and pass on their values of the parameters to the next generation.

### Settings for Genetic Algorithm

Before the GA could be runned and the optimised hyperparameters could be found, the settings of the GA had to be set. Moreover, it should be clear which hyperparameters are fixed and which one are variable. As previously presented, table 4.7 provides an overview of both fixed and variable parameters of the neural network. It illustrates that this research focused on optimising four hyperparameters: the neurons in the hidden layer, the kernel initializer, the bias initializer and the learning rate. Given that there are four hyperparameters to optimise, an individual's genotype was represented as a list with four elements. Each element corresponded to a value within the range of possible values for the respective hyperparameter. The genotype essentially captured an individual's properties and was viewed as the set of genes defining that individual.

Before being able to run the GA, there are other settings that needed to be determined. The theory behind these settings is given in Section 3.4 of Chapter 3. An overview of the chosen values for each

of the settings is presented in Table 4.8.

- **Population Size.**
  The population size must be sufficiently large to make sure there is enough diversity in the gene pool. A population that is too small can lead to rapid convergence to a local optimum. However, a larger population size requires evaluating more individuals in each generation. In this study, the evaluation involved a time-consuming 5-fold cross-validation of an ANN. To manage computational time, the population size was limited and set to 100 in this research.
- **Number of Generations.**
  Ensuring convergence requires a sufficient number of generations, but a higher count means evaluating more individuals, leading to increased computational time. In this project, the number of generations was set to be equal to 30.
- **Convergence Limit.**
  The convergence limit was set to prevent exhaustive search, and was set to be equal to three. This parameter dictates that if no improvement was observed for three consecutive iterations, the GA was terminated to prevent exhaustive search.
- **Tournament Size.**
  The size of the selected group of competitors is referred to as the tournament size. It's crucial for this size to be proportionate to the population. If the tournament size matches the population size, the best individual of the generation would dominate every tournament, resulting in offspring with limited genetic diversity. On the other hand, a too small tournament size might allow weaker individuals to pass on their genes. In this research, the tournament size was set to be ten, which was 10% of the population size.
- **Elite portion.**
  To prevent the risk of overlooking the best individuals, elite portion was taken into account. For this research, the elite portion was set to be equal to 0.10, indicating that the top 10% of each generation was guaranteed to pass to the next generation.
- **Crossover Rate and Mutation Rate.**
  The crossover rate indicates the probability of two parents interchanging their genes. And the mutation rate indicates the probability of an individual being mutated. Both values strongly influence the behaviour of the GA. The values of the crossover rate and mutation rate were set to be equal to 0.80 and 0.10, respectively.

**Table 4.8:** Determined values for the settings for GA

| Setting | Value |
|---|---|
| Population size | 100 |
| Number of generations | 30 |
| Convergence limit | 3 |
| Tournament size | 10 |
| Elite portion | 0.10 |
| Crossover rate | 0.80 |
| Mutation rate | 0.10 |

A schematization of how the GA worked to find the best possible configuration of the hyperparameters is presented in Figure 4.8.

**Figure 4.8:** Schematization of the GA for finding the best configuration of the hyperparameters

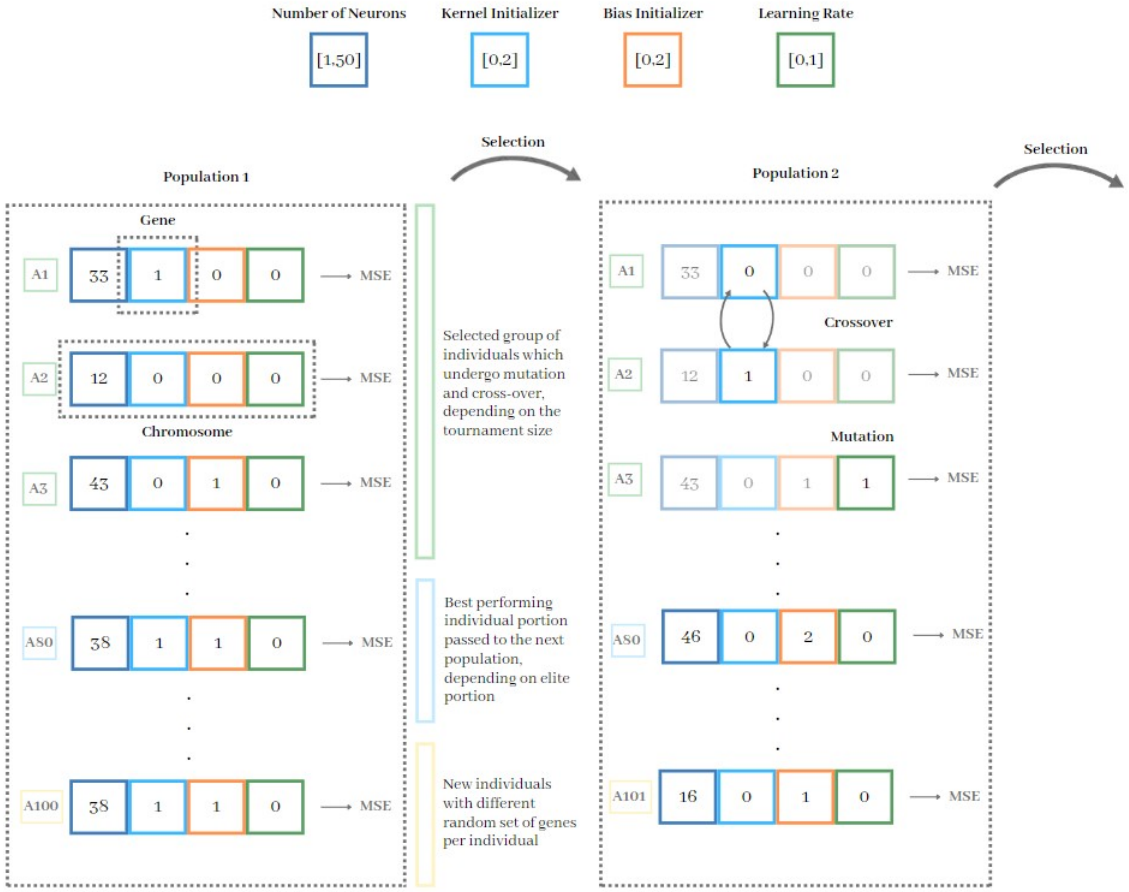


## 4.5. Analysis of Model Results

The results obtained from the modelling procedure were analysed to see if the predictions from the artificial neural network were accurate. A comparison was made between the predictions from the ANN models with the parametric models and other curve fitting models. Moreover, it was checked analytically if the structural requirements are met in terms of stability of the structure in the parametric models. The flowchart illustrating the progression from one step in the modelling procedure to the subsequent analysis of model results can be seen in Figure 4.9.

**Figure 4.9:** Flowchart modelling procedure to next step analysis of model results

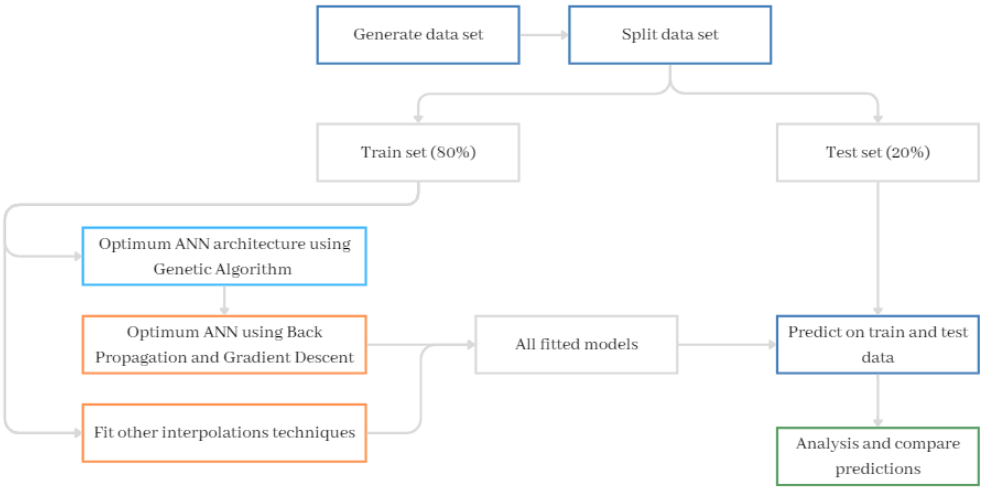


### 4.5.1. Comparison Parametric Model

The predicted output generated by the ANN models was compared to the outcomes of the masses of the parametric model. The parametric model served as the accurate baseline in this research, with a 100% accuracy, as it generated the input data. Next to the accuracy, the needed computational time to generate the outcome of both the parametric model and the ML model was compared.

### 4.5.2. Comparison Other Curve Fitting Methods

The results from the ANN models were compared with the results of other curve fitting methods to assess their respective accuracy's. The ANN model was compared to the curve fitting models of linear regression, second order regression and third order regression.

#### Linear Regression

Linear regression is the most basic form of regression modeling [32]. In its formal representation, the predicted output $y$ is determined through a weighted sum of the input features plus a constant called the bias term (or intercept term), outlined as:

$$y = ax + b \tag{4.3}$$

In this equation, $a$ represents the slope and $b$ represents the intercept term. These factors are deduced by minimising the error between the actual $y$ and the estimated $y'$, which is called the loss function. The loss function, which in this research was equal to the mean squared error (MSE), quantifies this error. In the Python library Scikit-Learn, the class of $LinearRegression$ was used to find the linear relationship between the input and output features [46].

#### Polynomial Regression

Polynomial regression is a technique where a linear model is used to fit nonlinear data by adding powers of each feature as new features, then training a linear model on this extended set of features [46]. Specific forms of polynomial regressions are the second order and third order regression. The general form of the equations for the second and third order are:

$$y_{2nd} = ax^2 + bx + c \tag{4.4}$$

$$y_{3rd} = ax^3 + bx^2 + cx + d \tag{4.5}$$

In this equation, $y$ represents the predicted output, $x$ is the input variable, and $a\ b\ c\ d$ are the coefficients that need to be determined. Polynomial interpolation aims to find the best-fitting nth-order curve that passes through a set of given data points, where the n refers to the polynomial degree. For this research, the Python library Scikit-Learn, the class of $PolynomialFeatures$ was used to find relationships between features.

### 4.5.3. Analyzing the Structural Model

The analysis of the structural model involves the validation process to ensure its reliability. To validate the 3D model in GH, a combination of 2D analyses and analytical calculations was done, see for the elaboration Section 5.5.1. The structure was simplified into a 2D assembly of line members, allowing for easier assessment of its behavior. A reference structure, with predefined dimensions, served as the basis for validation through analytical and 2D analysis methods. In this research, the analytical analysis of individual local members was not included, since the aim of this research was to get an initial feasibility analysis of the design concept in the early design phase rather than a comprehensive final evaluation of the design.

In the analytical analysis, specific formulas known as 'vergeet-me-nietjes' were utilised to determine displacement due to bending in the structural system, focusing primarily on the braced framed tube. The structure was divided into sections corresponding to different wind zones to accurately account for the non-uniform distribution of wind load. Displacement due to shear and the second-order moment generated by self-weight were also considered to ascertain the total displacement of the structure. The results obtained from the analytical analysis were compared against the outputs from the 3D model (parametric model) to evaluate its accuracy and identify any differences. Simultaneously, a 2D analysis was conducted using MatrixFrame software, focusing on both the braced framed tube and outrigger system. Displacement due to bending was calculated, and adjustments were made to incorporate displacement due to shear, particularly for braced framed tube system. The input data derived from previous methodologies, including profile definitions, load definitions, and support definitions, were utilised in the 2D analysis. The outcomes of the 2D analysis were compared with the outputs from the 3D model to assess its performance and reliability.

## 4.6. Summary

This study started by creating data sets for the masses of two stability frameworks: the braced framed tube and the outrigger system. Parametric modelling in Rhinoceros with Grasshopper was used for the creating of the data sets. The cross-sections of the beams and columns of the structures were optimised to minimise the mass. Separate parametric models were developed for each stability framework, resulting in distinct data sets.These data sets served as the foundation for training the ANN models. The data collection phase involved generating both fixed and variable input variables to capture the specifics of high-rise building designs. Subsequently, data preprocessing was conducted, which included dividing the data set into training and testing subsets and normalizing the data to optimise it for efficient training of ANNs. The modeling phase consisted of formulating, training, and validating the ANN model, with the utilisation of a genetic algorithm for hyperparameter optimisation. The training process involved back-propagation for optimising weights and biases, with the Root Mean Squared Error (RMSE) as the loss function. Additionally, the methodology incorporated an evaluation of the ANN's models predictions against those of traditional parametric models and established interpolation methods. Moreover, an analytical verification of the parametric model was performed to ensure the reliability of the parametric model.

# 5

# Data Generation

This chapter outlines the procedures for setting up the parametric models in Rhinoceros, Grasshopper (GH) to generate the data about the masses of the structural elements for structures of various sizes of the braced framed tube (S1) and the outrigger system (S2). It starts with an overview of the roadmap of the data generation process which consisted of six different steps. Afterwards, a more detailed explanation of the different steps of the roadmap is given. First, an overview of input variables is provided, followed by an explanation of assumptions made in the geometry. Then, the chapter details the assumptions and decisions guiding the structural analysis. Subsequently, the chapter considers the specific assumptions and decisions required for the structural analysis. Additionally, an explanation of the results generation process is provided. These outlined steps align with the procedures previously discussed in Chapter 4 of the Methodology, specifically in Section 4.2.1. Any supplementary assumptions, besides those covered in that section, are discussed in this chapter.

It is important to emphasize that the objective of this research was to compare two stability frameworks, making the analysis relative to one another. Consequently, some assumptions could be made, as precision to the exact value was not mandatory for the comparative study. However, it was essential that these assumptions remained consistent across the two different stability frameworks. This made sure that a fair comparison was made among them.

## 5.1. Data Generation Process Overview

Figure 5.1 presents a roadmap outlining the different stages required to generate essential data for training the ANN models. Each step is further broken down into a list of its component parts. The purpose of this roadmap was to provide a preliminary overview of the necessary tasks without requiring an in-depth examination of the GH model for the parametric model and the Python code for the ANN model. An overview of the total GH script is provided in Appendix D.

**Figure 5.1:** Detailed flowchart of the different steps for the generation of data and results

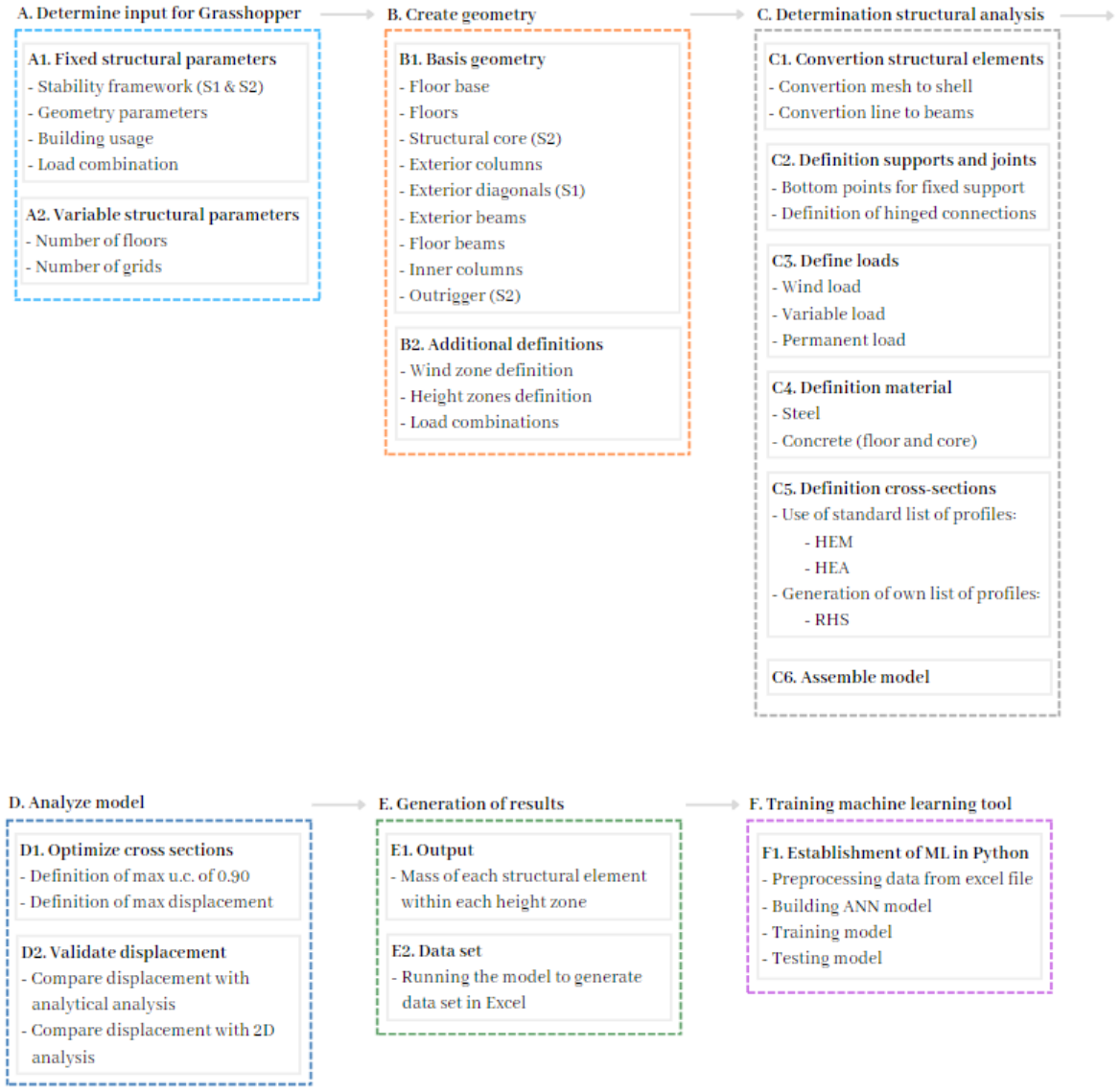


## 5.2. Determination Input for Grasshopper Model

Figure 5.2 provides an overview of the location of the first part, A: Determine input, within the GH script. This section specifically introduced several parameter types related to the structural parameters. Structural parameters were categorized into fixed and variable parameters for both structural system. Fixed structural parameters included components such as stability framework, geometry parameters, building usage, and load combinations. On the other hand, the variable structural parameters influenced the volume of the building.

**Figure 5.2:** Overview Grasshopper script for part A. Determine input


Table 5.2 presents an overview of the model's input structural parameters, which were categorized into fixed and variable parameters. Fixed variables refer to values established before data generation. While these variables were initially self-selected, they could be altered to create a new data set by incorporating different factors. For instance, adjustments may be made if there was a change in the building's function or a modification in the grid size. On the other hand, variable parameters were those that under went variation during the data set generation process. It can be seen that there were only two such variables: the number of floors and the number of grids. Together, these parameters contributed to defining the building's overall volume.

**Table 5.1:** Summary of structural input parameters for the Grasshopper model

| Type | | Parameter | Description |
|---|---|---|---|
| Fixed | *General* | Stability framework | S1: Braced framed tube<br>S2: Outrigger system |
| | | Height floor to floor | 3 m |
| | | Floor thickness | 220 mm |
| | | Building usage | Office space |
| | | Load combination | ULS |
| | *S1 Specific* | Grid size | 1.8 m |
| | | Min angle of bracing | 30° |
| | | Max angle of bracing | 60° |
| | | Max n floors bracing | 30 |
| | *S2 Specific* | Grid size | 3.6 m |
| | | Ratio for location rigger (i = 1) | 0.7 |
| | | Location rigger on nth floor (i > 1) | 20 |
| | | Max range floor beam | 8 m |
| Variable | *General* | Number of floors | Varying from 16 to 100 |
| | *S1 Specific* | Number of grids | Varying from 4 to 32 |
| | *S2 Specific* | Number of grids | Varying from 2 to 16 |

**Table 5.2:** Summary of structural input parameters for the Grasshopper model

## 5.3. Building Geometry

Details regarding additional assumptions made during the establishment of the structure in the second step of Building Geometry, such as the distribution of height zones, bracing definition, structural core definition, and floor plan determination are provided. Figure 5.3 illustrates the specific section in the script where the second part was executed. The visualisation from the GH script of the results of building the geometry is presented in Figure 5.4 for the braced framed tube and in Figure 5.5 for the outrigger system.

**Figure 5.3:** Overview Grasshopper script for part B. Create geometry

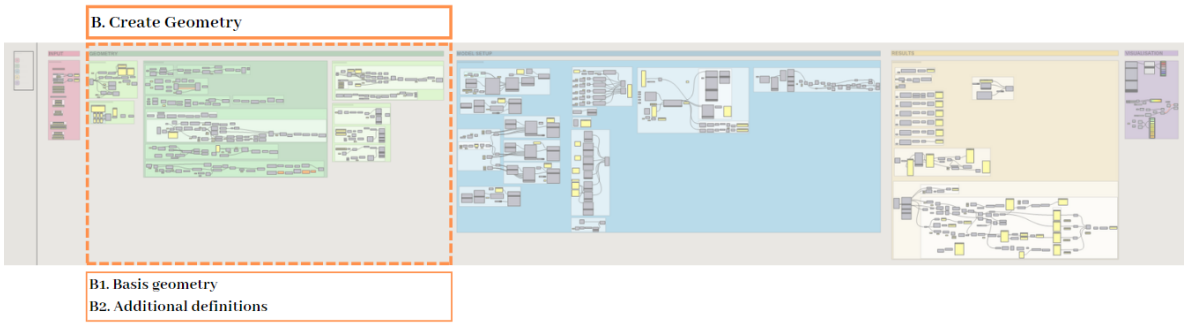


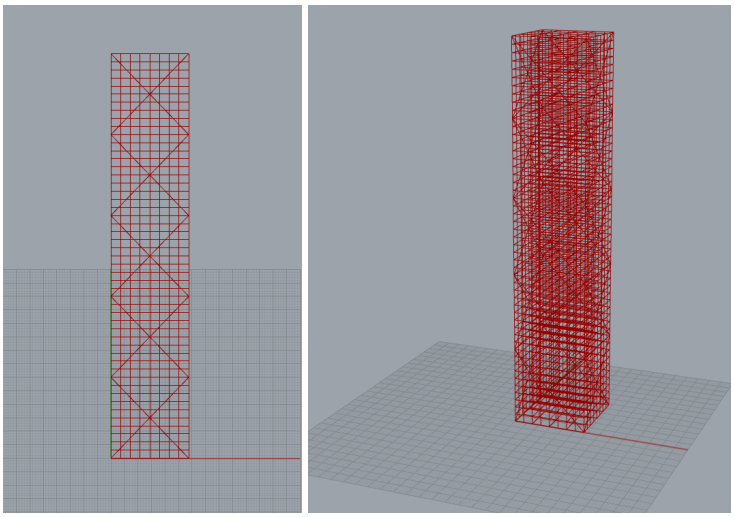

**(a)** Front view of S1 **(b)** 3D Perspective of S1

**Figure 5.4:** Visualisation of geometry of S1 for w = 28.8 m and h = 150 m

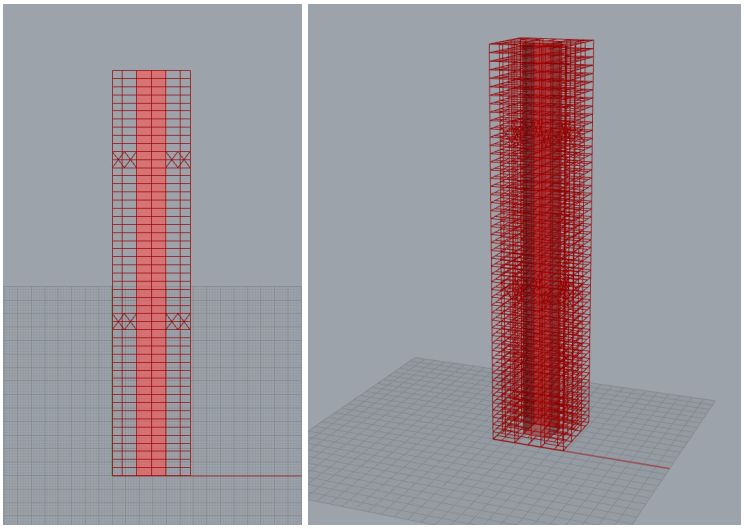

**(a)** Front view of S2 **(b)** 3D Perspective of S2

**Figure 5.5:** Visualisation of geometry of S2 for w = 28.8 m and h = 150 m

### 5.3.1. Height Zones

As previously noted, for effective cross-section optimisation of the load-bearing structure, the building was divided into distinct height zones. This segmentation ensured efficient material optimisation. The division of the structure into zones was based on the classification of wind zones according to the Eurocode [19]. The reference height $z_e$ of the wind zones depends on the height and width of the building. A more detailed explanation of the division of the different wind zones acting on a structure can be found in Section 2. If the height of the building was more than twice the width of the building, three wind zones were identified. The first wind zone, and consequently the first height zone, was equal to one time the width of the building. The third wind zone, and therefore the last height zone (viewed from the top of the building going downwards), was also equal to one time the width of the building. The second wind zone referred to the middle part of the building, and the wind velocity increased in that zone. For the division of the height zones, the second wind zone was divided by an $n$-fold of the width of the structure, similar to what was done for the first and last height zones. In cases where a precise equal distribution of the second wind zone in *n* folds of the width of the structure was not feasible, the height zones closer to the ground level consisted of a higher number of floor zones. The maximum division of the second wind zone was set at four; therefore, the maximum number of height zones was capped at six. Figure 5.6 illustrates examples of the distribution of these height zones for varying total numbers of floors.

**Figure 5.6:** Examples of the distribution of height zones over different heights of the structure

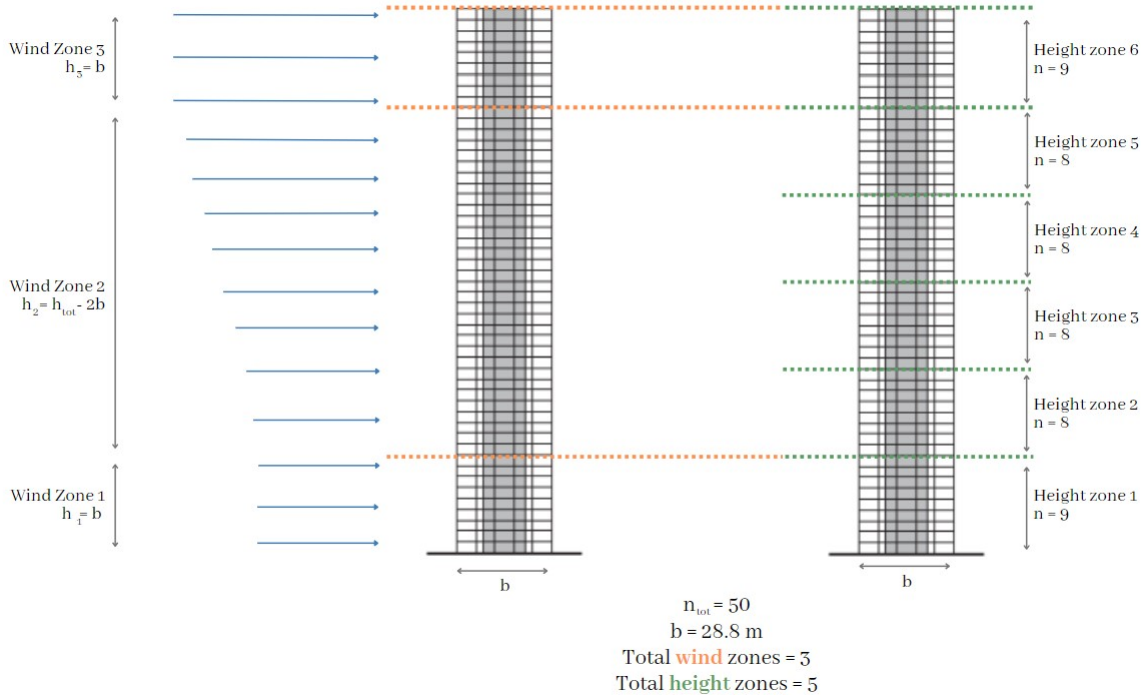


## 5.3.2. Bracing Definition

The bracing configuration on the outer perimeter of the braced framed tube is critical for structural integrity. This configuration is determined by the maximum and minimum angles of the diagonals, as informed by literature on optimal diagonal angles. Baradaran et al. (2019) recommended an optimal angle range for mega bracing systems in steel frames to be between 30 to 60 degrees, varying with the number of stories [50]. They found the most effective angle for mega bracing to be between 36 to 42 degrees, considering the frame height and span. The broader range of 30 to 60 degrees was chosen for this research to allow for a wider variety of bracing configurations. It ensured that there was a higher possibility of the structure to be feasible, since the bracing was required to be evenly distributed across the total height.

## 5.3.3. Structural Core

The structural core was only taken into account for the stability framework of the outrigger system and was not taken into account for the braced framed tube. The dimensions of the structural core were established by examining the ratio observed in the structural cores of various real-life high-rise buildings. The core-to-total area ratio was determined for four different high-rise structures and plotted against their respective total heights. This ratio was calculated as the core's proportion relative to the entire floor plan area. Figure 5.7 displays the plotted results. By analyzing these real-life projects, assumptions were made regarding the relationship between the core ratio and different heights. A fitted line was derived to represent this relationship, enabling the calculation of core lengths for varying heights and floor plans. The final step involved determining how many times the grid size evenly divided the total length. The resulting number, rounded to the nearest even whole number, became the ultimate dimension for the building's core. To maintain symmetry, this number was rounded to the nearest even value, since the total length of the structure was a multiple of an even number of grids. This was done to ensure that the remaining dimensions from the core to the outer perimeter on both sides was evenly distributed in multiples of the grid size.

**Figure 5.7:** Ratio of the structural core of different real-life projects

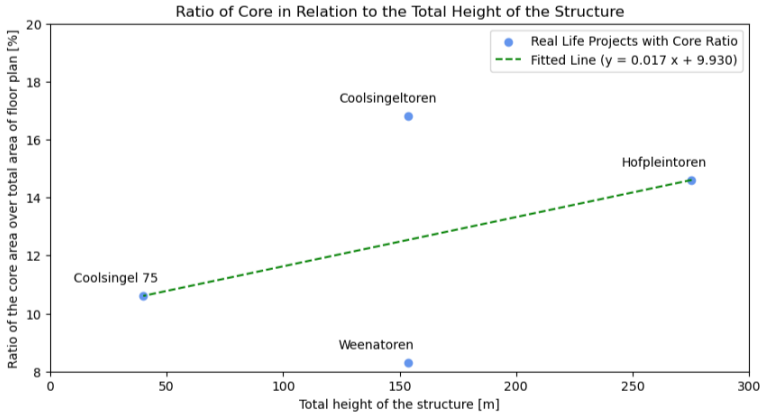


### 5.3.4. Floor Plan Determination

The floor plan varied between the different stability frameworks of braced framed tube and outrigger systems due to the presence or absence of a core. In both systems, the floor beams played a crucial role in transferring vertical forces from the floors to either the core (if present) or the exterior columns. For the outrigger system, the beams connected the stabilizing core and the moment frame. Figure 5.8 provides a schematic overview of the floor plan of 28.8 m for both stability frameworks, including the location of inner and outer columns. To facilitate incremental core size adjustments, the grid size for the outrigger system was intentionally chosen to be twice as small (grid = 1.8 m) as that of the braced framed tube (grid = 3.6 m). This design decision ensured that core dimensions could increase more gradually, avoiding significant changes in the core dimensions.

**Figure 5.8:** Schematic representation of the floor plan distribution

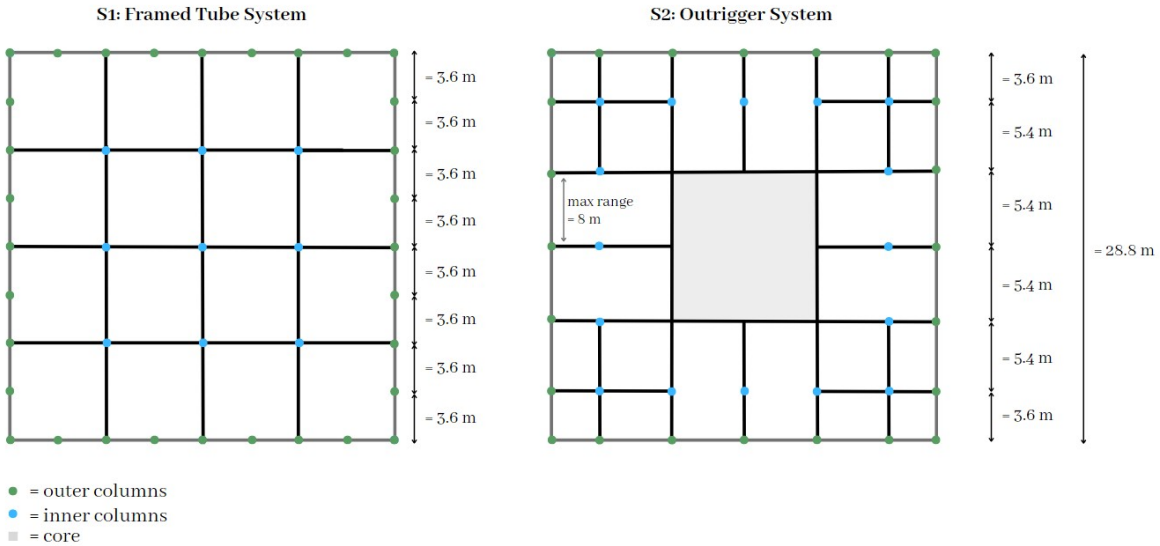


## 5.4. Determination of Structural Analysis

In this section, an elaboration is made on additional assumptions essential for the structural analysis. These assumptions relate to the definition of the wind load on the structure and the conversion of the structural elements to either shell or beam elements. Figure 5.9 illustrates the specific section in the script where this part was executed.

**Figure 5.9:** Overview Grasshopper script for part C. Determination structural analysis

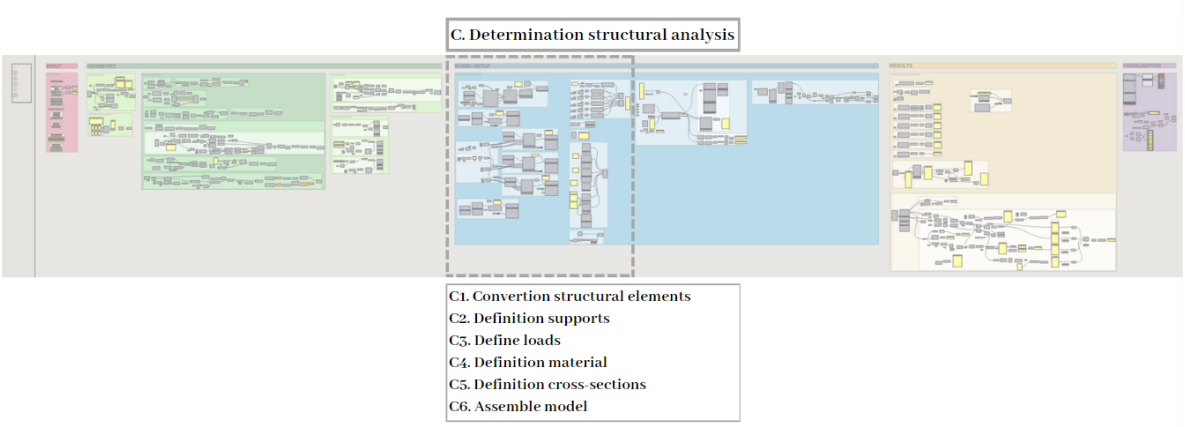


## 5.4.1. Load Definition: Wind Load

To be able to determine the wind load working on the structure, it was necessary to establish the peak velocity pressure, $q_p(z_e)$. The calculation of $q_p(z_e)$ for a building involved certain assumptions about its height. The $q_p(z_e)$ was influenced by the building's reference height, and to be able to determine the $q_p(z_e)$ over a changing height, a relationship between structure height and $q_p(z_e)$ was needed to be stated. This relationship was incorporated into GH, enabling the calculation of $q_p(z_e)$ for varying building heights. The $q_p(z_e)$ of Area II, urban for the Netherlands was taken [51]. The relationship between the $q_p(z_e)$ and the height of a building is presented in Figure 5.10. The established assumed relation between the variables was derived in Python by determining the best possible logarithm function and is presented in Equation 5.1. Furthermore, it was assumed that in the case of three wind zones, the $q_p(z_e)$ in the middle wind zone was subdivided into working heights equal to the floor-to-floor height of the structure. The distribution of the velocity pressure over the height of the building is presented in Figure 5.11.

$$q_p(z_e) = max(0.58, 0.39 \cdot z_e^{0.29}) \tag{5.1}$$

**Figure 5.10:** Change of wind velocity pressure for different heights based on Area II (urban)

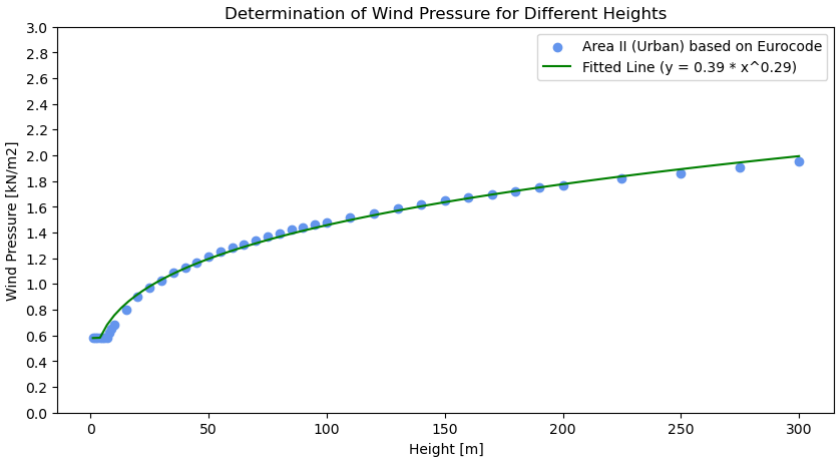

**Figure 5.11:** Assumed velocity pressure distribution over the height of the building

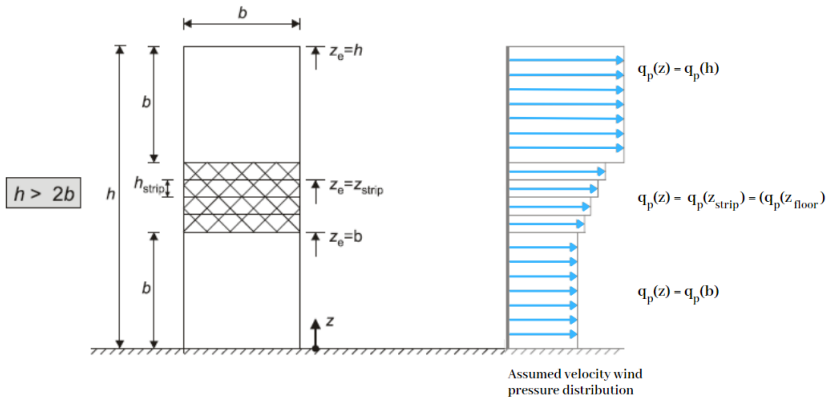


The structural factor $c_s c_d$ was assumed to be 1.1 but was included as a variable parameter, allowing for adjustments to asses its sensitivity if wanted. Given the symmetric rectangular shape of the floor plan, the force coefficient was set at 2.1. This determination was based on $c_{f,0}$ on being 2.1, as the width and length were identical. Additionally, $\psi_r$ is 1.0, reflecting the absence of rounded corners, and $\psi_{lapda}$ was also 1.0, as the research assumed no reduction was needed for the end-effect factor. A more detailed explanation of the assumptions can be found in Appendix B. The wind pressure, derived from the peak velocity pressure and the force coefficient, was represented as a line load on each storey working on one side of the structure.

### 5.4.2. Elements

Each stability framework, both braced framed tube and outrigger system, consisted of a different set of structural elements. Common to both frameworks were the floors, exterior columns, exterior beams, floor beams, and inner columns. However, the braced framed tube consisted also of exterior bracings, while the outrigger system incorporated the outrigger beams and the structural core. Moreover, for the outrigger system there was an distinction made between the columns (both interior and exterior) which were connected to the outrigger truss and which were not. Tables 5.3 and 5.4 provide an overview of the input parameters essential for the structural analysis of each element within the respective systems. For the outrigger system, the distinction between the subsets of the columns connected to the outrigger truss and not connected to the outrigger truss is not presented in the Table since the input range for both columns were equal.

| **Braced Framed Tube System (S1)** | | | | |
|---|---|---|---|---|
| *Element* | *Input model* | *Material type* | *Cross sections* | *Max. Reachable Section* |
| Floors | Mesh to shell | Concrete | Hollow core slab | (-) |
| Exterior columns | Line to beams | Steel | RHS | RHS2000 |
| Exterior diagonals | Line to beams | Steel | RHS | RHS2000 |
| Exterior beams | Line to beams | Steel | HEA | HEA1000 |
| Floor beams | Line to beams | Steel | HEA | HEA1000 |
| Inner columns | Line to beams | Steel | RHS | RHS1000 |

**Table 5.3:** Overview input braced tube (S1) for structural analysis for each element

| **Outrigger System (S2)** | | | | |
|---|---|---|---|---|
| *Element* | *Input model* | *Material type* | *Cross sections* | Max. Reachable Section |
| Floors | Mesh to shell | Concrete | Hollow core slab | (-) |
| Core | Mesh to shell | Concrete | t = 300 mm | (-) |
| Exterior columns | Line to beams | Steel | RHS | RHS2000 |
| Exterior beams | Line to beams | Steel | HEA | HEA1000 |
| Floor beams | Line to beams | Steel | HEA | HEA1000 |
| Inner columns | Line to beams | Steel | RHS | RHS2000 |
| Outrigger truss | Line to beams | Steel | RHS | RHS1000 |

**Table 5.4:** Overview input outrigger (S2) for structural analysis for each element

## 5.5. Analyze Model

The analysis of the parametric model was divided into two parts: optimising the GH model by adjusting the cross-sections for various height zones and validating the GH model. The first part was incorporated into the GH script and was executed there, while the second part involved an analytical analysis that was independent of the GH script. Figure 5.12 illustrates the specific section in the script where the optimisation of cross-sections took place.

**Figure 5.12:** Overview Grasshopper script for part D. Analyze model

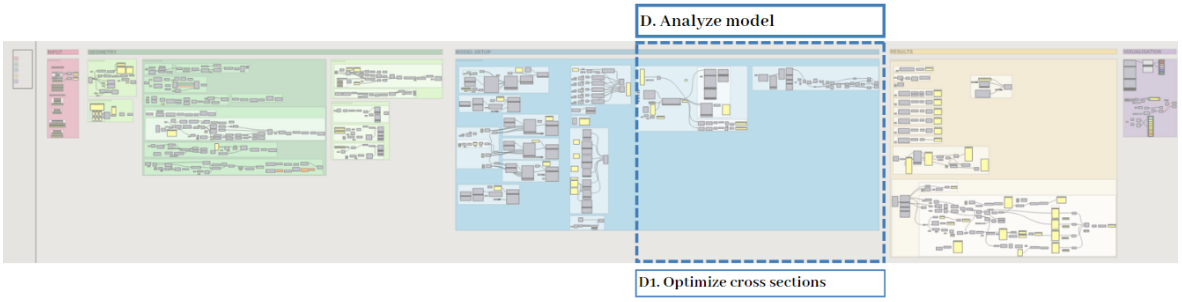


### 5.5.1. Validation of Model

The validation of the 3D model in Grasshopper involved both 2D analysis and analytical calculations. The 3D structure was simplified to a 2D model of line members with moment-resistant and/or pinned connections. A reference structure, with a floor plan measuring 28.8 by 28.8 meters and a height of 150 meters, was chosen for validation of the 3D model through both analytical and 2D analysis methods. This analytical calculation relied on a simplified model of the structure, using formulas known as 'vergeet-me-nietjes' for determining the displacement due to bending. The simplified representation of the structure with the acting wind load is presented in Figure 5.13. The overall displacement of the structure was determined by the combined effects of bending and shear, with the total displacement being the sum of the displacements resulting from these effects. These calculations were used to validate the displacement output from the 3D model by comparing it with the calculated displacement of the building. The displacement output from the 3D model is presented in Figure 5.14. The detailed elaboration of the analytical and 2D analysis for the reference model is provided in Appendix E.

**Figure 5.13:** Simplified representation of the structural system with wind load

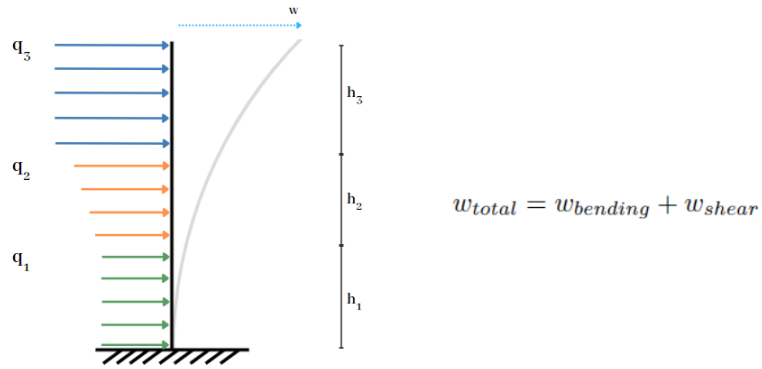


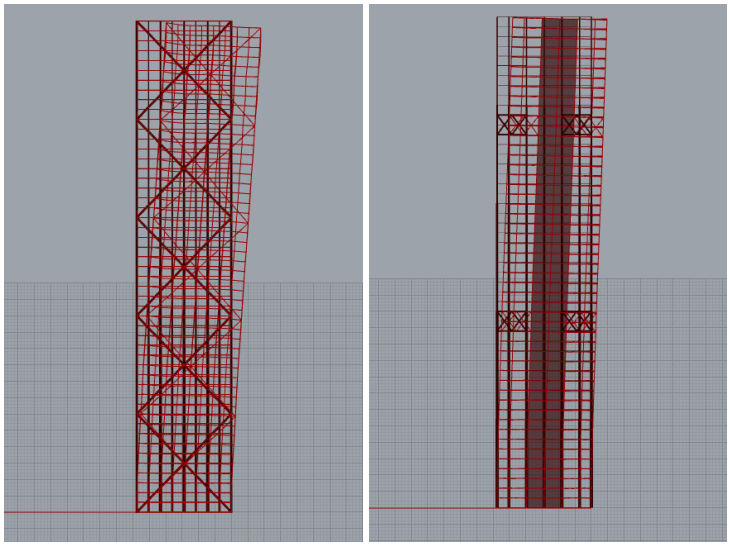

**(a)** Deformation of S1 **(b)** Deformation of S2

**Figure 5.14:** Visualisation of deformation of S1 and S2 for w = 28.8 m and h = 150 m, deformation scale is set at 20

For modeling and developing simplified methods of analysis for lateral load-resisting systems in tall buildings, some simplifications were implemented. These simplifications were applicable in both the analytical as the 2D analysis for the validation of the 3D model. Firstly, it was assumed that all structural elements behaved in a linear elastically, and the principle of superposition could be applied. Secondly, floor structures were considered to have infinite flexural stiffness in their own plane, and the contributions from out-of-plane bending stiffnesses of floors could be neglected. This way the floor did not deform in its own plane but it translated and rotated as a single element in a horizontal plane. Additionally, the foundation was assumed to have infinite rigidity [8].

For both the analytical and the 2D analysis it was necessary to determine the input geometry which would represent the simplified structural system. In Figure 5.15 a visual schematization is presented of the determination of the input geometry for the braced tube system. The formula for determining the moment of inertia of the simplified structural system of the tube is also presented in Figure 5.15. The average thickness of the building's facade was distributed across its entire width, allowing an assumption of the overall average thickness. This was achieved by determining the thickness of the facade columns and the bracing which were present at the intersection of the structure. Subsequently, the thickness was spread out over the total length of the facade to ensure a uniform and average thickness along the perimeter.

**Figure 5.15:** Determination of input geometry for analytical and 2D analysis of the braced framed tube

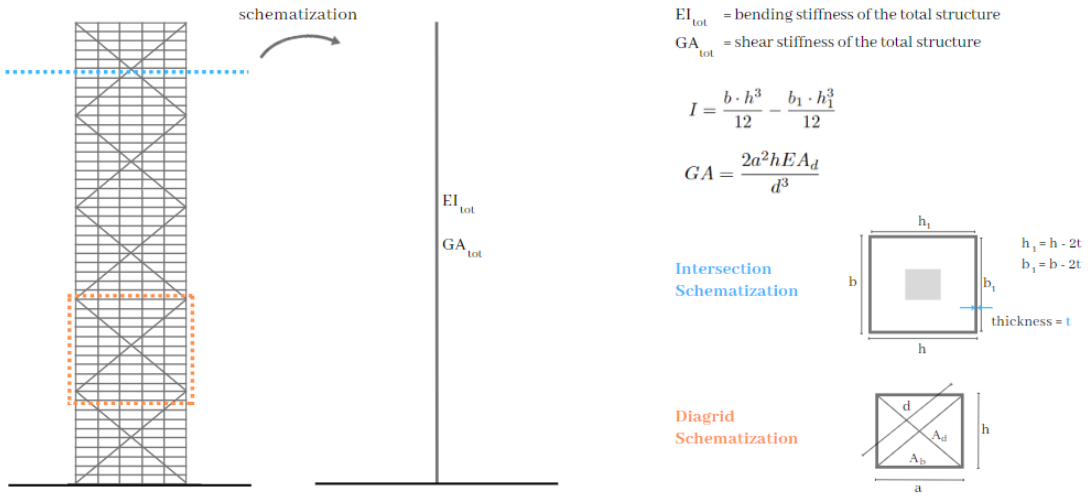


The schematization of the outrigger system for the determination of the input for the 2D analysis is presented in Figure 5.16.

**Figure 5.16:** Determination of input geometry for 2D analysis of the outrigger system

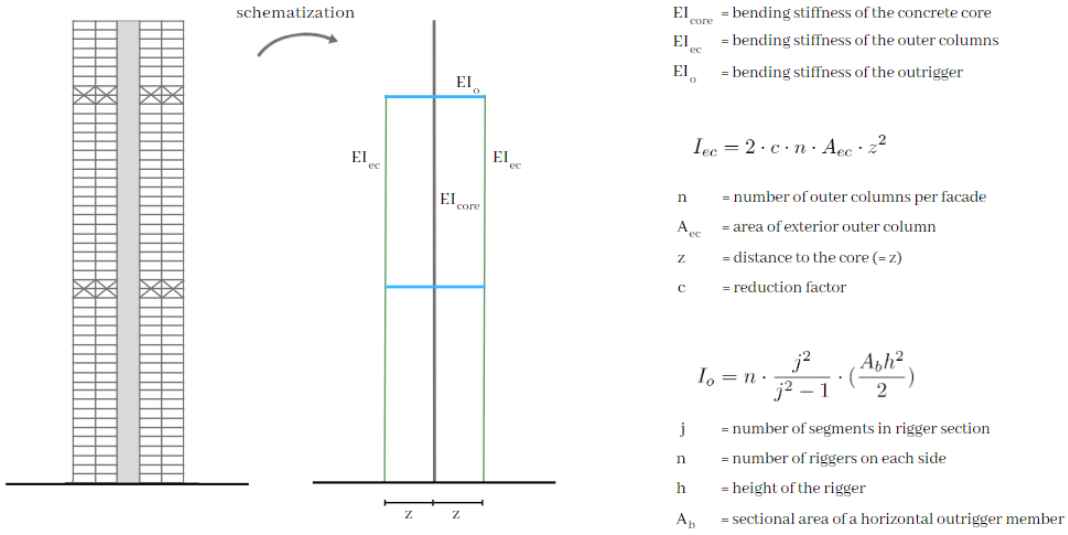


## Analytical Analysis

An analytical analysis was only conducted on the structural system of the braced framed tube, as the outrigger system could not be simplified using the 'vergeet-me-nietjes'. The specific 'vergeet-me-nietjes' utilised to represent the displacement due to bending of the simplified structural system of the braced tube are provided in Figure 5.17.

**Figure 5.17:** Visual representation of the 'vergeet-me-nietjes' for deflection due to bending

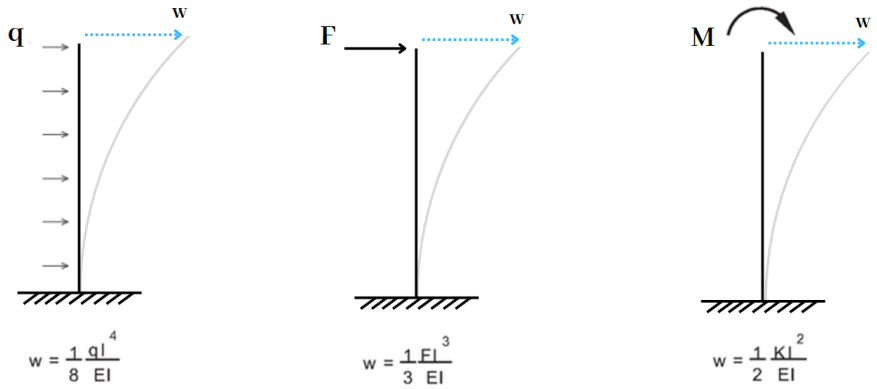


Since the wind load was not uniformly distributed over the height of the building, resulting in multiple wind zones due to the building's height, it became necessary to divide the structure into three different sections to be able to use the 'vergeet-me-nietjes'. Each section represented the structure within a specific wind zone. The comprehensive calculation, illustrating the division of the structure into different wind zones, with different values of $q_w$, and presenting the total deflection due to bending, is presented in Appendix E.

Next to the displacement due to bending, it was necessary to determine the displacement due to shear to get the total deflection. The displacement due to shear was calculated based on the following formula:

$$w_{shear} = \frac{q_w l^2}{2GA_{frame}} \tag{5.2}$$

Where $l$ represents the total height of the structure and $q_w$ the wind load. To complete this formula, the actual increasing wind force $q_w$ was transformed into a constant wind force, which resulted in an equivalent total moment on the structure as the original increasing wind force.

After determining the total displacement, the next step was to consider the second-order moment generated by the self-weight of the building. The total displacement, inclusive of the second-order moment, was calculated using the following formulas:

$$w_{2,total} = w_{1,total} * N \tag{5.3}$$

$$N = \frac{n}{n-1} \tag{5.4}$$

Where $n$ represents the ratio between Euler's critical load ($F_{cr}$) and the working axial force ($F_{Ed}$). Euler's critical load was calculated based on Equation 5.5. The axial force depended on the total own weight of the structure.

$$F_{cr} = \frac{\pi^2 EI}{l_k^2} \tag{5.5}$$

Where:

$l_k$ = buckling length of the structure [m]
$EI$ = total $EI$ of the structure [Nm$^2$]

The results of the analytical calculation of determining Euler's critical load ($F_{cr}$) and the magnification factor for the second order moment effect ($N$) are presented in Table 5.5.

| **Stability System** | **Euler's critical load** | **Factor $N$** |
|---|---|---|
| | [kN] | [-] |
| Braced Framed Tube | 11.5 * $10^6$ | 1.018 |
| Outrigger System | 12.2 * $10^6$ | 1.021 |

**Table 5.5:** Results of calculation of critical load factor and second-order moment ratio

The final outcome of the deflection based on the analytical analysis of the braced framed tube is presented in Table 5.6. The analytical calculation regarding the deflection of the outrigger system was not done regarding the complex calculation.

| **Stability System** | **3D Model** | **Analytical Model** | **Difference** |
|---|---|---|---|
| | [cm] | [cm] | [%] |
| Braced Framed Tube | 30.0 | 29.8 | 0.8 |

**Table 5.6:** Comparison outcome displacement 3D model and analytical model

2D Analysis

The 2D analysis was executed using the MatrixFrame software. The geometry input was derived from the previously mentioned methods for determining the area and moment of inertia, representing the simplified structural system. The 2D analysis was conducted for both the braced tube and the outrigger system. MatrixFrame calculated the displacement without taking into account shear, it considered only the displacement due to bending. Therefore, to enable a comparison with the 3D model output, the outcome of the 2D analysis was combined with the calculated displacement due to shear based on the analytical analysis. It was important to note that this adjustment was only applied to the braced tube, as the displacement due to shear has an insignificant impact on the total displacement for the outrigger system. The input data for profile definitions, load definitions, and support definitions used in the reference structure for both the braced tube and the outrigger are provided in Appendix E. The results of the 2D analysis are presented in Table 5.7.

| **Stability System** | **3D Model** | **2D Model** | **Difference** |
|---|---|---|---|
| | [cm] | [cm] | [%] |
| Braced Framed Tube | 30.0 | 29.2 | 2.9 |
| Outrigger System | 21.0 | 21.2 | 0.9 |

**Table 5.7:** Comparison outcome displacement 3D model and 2D model

## 5.6. Generation of Results

After completing the structural and parametric model analyses, the next phase involves generating results. The desired output from the Grasshopper (GH) script is the mass of each structural element within specific height zones. These masses serve as the basis for determining the performance parameters of construction and environmental costs. The first step in generating the masses will be performed in GH (see Figure 5.18). Subsequently, the masses will be converted into performance parameters in Python.

**Figure 5.18:** Overview Grasshopper script for part E. Generation of Results


Visualisations of the structural analysis results for the braced framed tube and outrigger structures are presented in Figure 5.19 till Figure 5.24. These visualisations used color to represent the utilisation of the elements, where red indicated compression and blue represented tension. The intensity of the color corresponded to the degree of utilisation, darker colors signified higher utilisation. Notably, for the braced framed tube and the outrigger system, it was not possible to find a feasible structure for such height-to-width ratio. These examples provide insight into all the analyses performed. Structural analysis was performed for all structures within the range of widths from 7.2 to 57.6 m and heights from 48 to 300 m.

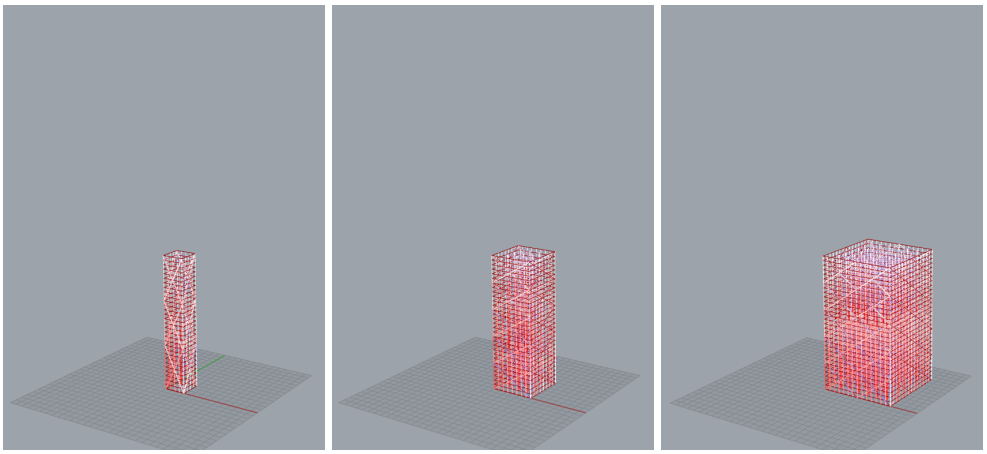

**(a)** S1: w = 14.4 m and h = 90 m **(b)** S1: w = 28.8 m and h = 90 m **(c)** S1: w = 50.4 m and h = 90 m

**Figure 5.19:** Visualisation of 3D analysis of S1 with height = 90 m

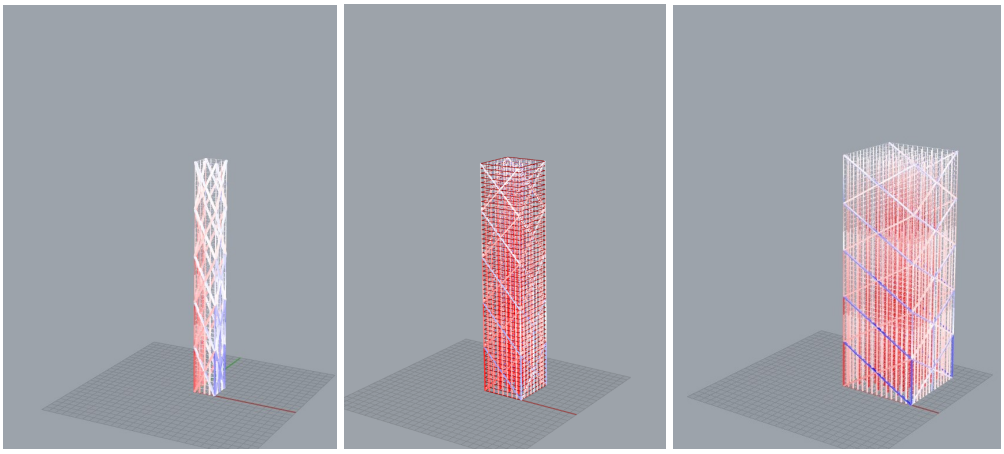

**(a)** S1: w = 14.4 m and h = 150 m **(b)** S1: w = 28.8 m and h = 150 m **(c)** S1: w = 50.4 m and h = 150 m

**Figure 5.20:** Visualisation of 3D analysis of S1 with height = 150 m

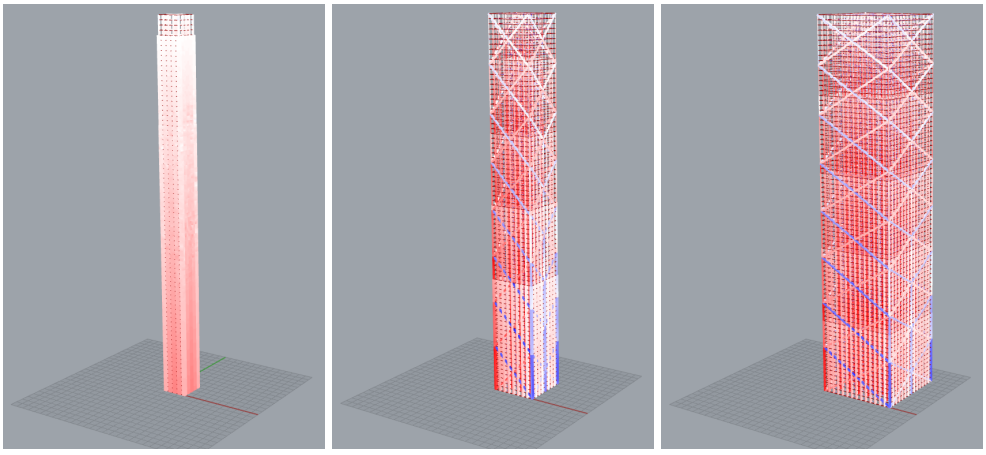

**(a)** S1: w = 14.4 m and h = 240 m **(b)** S1: w = 28.8 m and h = 240 m **(c)** S1: w = 50.4 m and h = 240 m

**Figure 5.21:** Visualisation of 3D analysis of S1 with height = 240 m

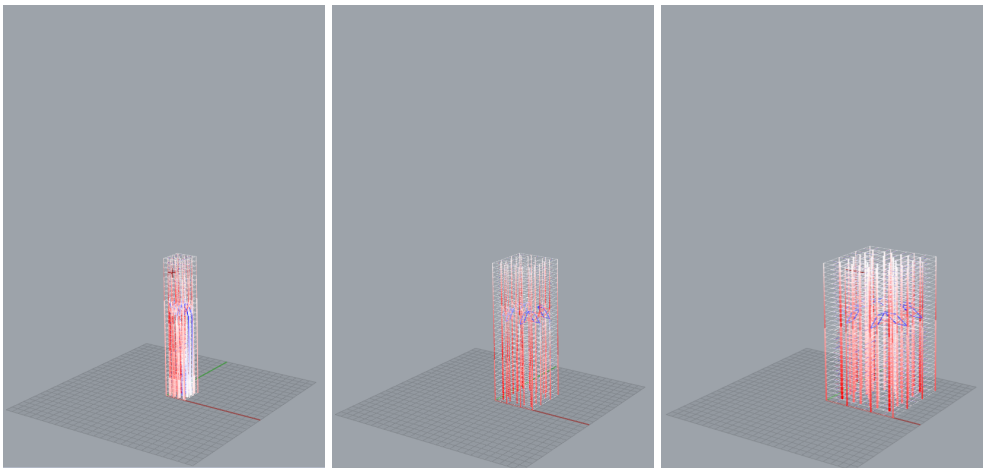

**(a)** S2: w = 14.4 m and h = 90 m **(b)** S2: w = 28.8 m and h = 90 m **(c)** S2: w = 50.4 m and h = 90 m

**Figure 5.22:** Visualisation of 3D analysis of S2 with height = 90 m

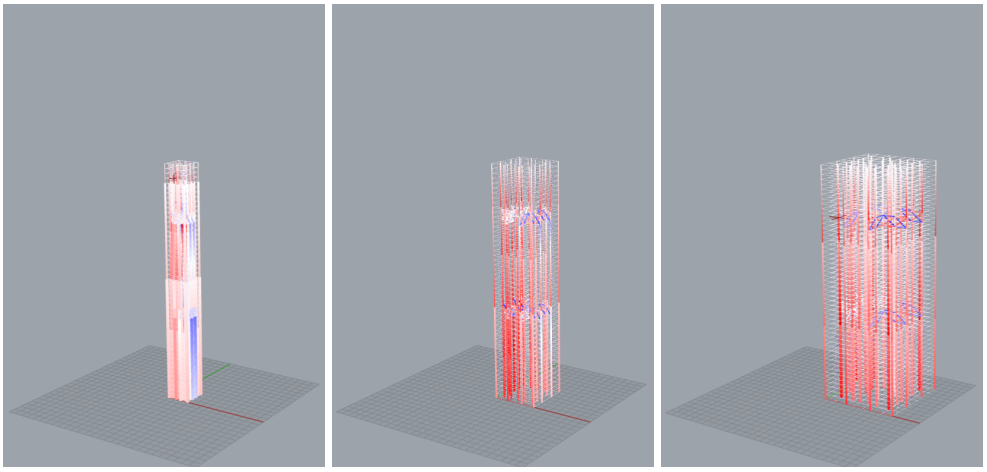

**(a)** S2: w = 14.4 m and h = 150 m **(b)** S2: w = 28.8 m and h = 150 m **(c)** S2: w = 50.4 m and h = 150 m

**Figure 5.23:** Visualisation of 3D analysis of S2 with height = 150 m

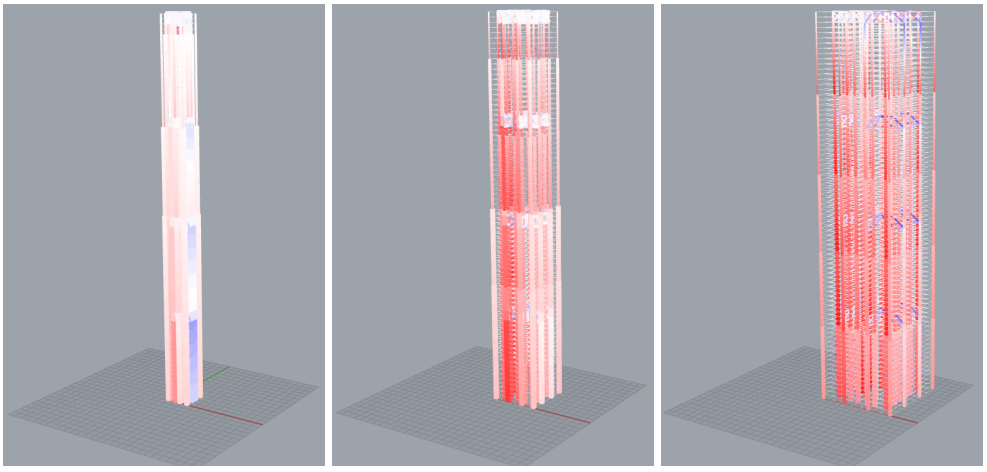

**(a)** S2: w = 14.4 m and h = 240 m **(b)** S2: w = 28.8 m and h = 240 m **(c)** S2: w = 50.4 m and h = 240 m

**Figure 5.24:** Visualisation of 3D analysis of S2 with height = 240 m

### 5.6.1. Optimisation Requirements

The mass of each structural element within each height zone is depended on the cross-section and the material of the element. To obtain the correct cross-section for each structural element, an optimisation process was conducted within GH. This optimisation considered both the strength and stiffness of the structure. For strength considerations, the maximum utilisation was set to 0.90 to ensure the structure possessed sufficient strength. Additionally, the maximum displacement was set to ensure adequate stiffness. Typically, the maximum displacement requirement is provided for load combinations in Serviceability Limit State (SLS), while strength is based on load combinations in Ultimate Limit State (ULS). Consequently, the maximum displacement was set at a factor ($f_{u,ULS}$) higher than what was possible in SLS, allowing for the examination of both strength and stiffness in ULS. This assisted the progress of optimisation of the cross-section in the structure based on both factors. Equations 5.6, 5.7, and 5.8 provide an overview of how the factor can be determined and how to calculate the displacement requirement in ULS:

$$f_{u,ULS} = \frac{\gamma_{W,ULS} \cdot \gamma_{W,SLS} + \gamma_{2nd,ULS} \cdot \gamma_{2nd,SLS} \cdot n_{2,\delta}}{1 + n_{2,\delta}} \tag{5.6}$$

$$u_{max,SLS} = \frac{h}{500} \tag{5.7}$$

$$u_{max,ULS} = u_{max,SLS} \cdot f_{u,ULS} = \frac{f_{u,ULS} \cdot h}{500} \tag{5.8}$$

The calculated values for the additional conversion factor ($f_{u,ULS}$) used to determine the maximum displacement in the ULS are presented in Table 5.8. A more detailed calculation of this conversion factor is provided in Appendix E. The factor is based on the geometry of the base structure, which has a width of 28.8 meters and a height of 150 meters. For simplification, this factor is assumed to be equal for all different geometries of the structures of the braced framed tube and the outrigger system.

| **Stability System** | $n_{2,\delta}$ [-] | $f_{u,ULS}$ [-] |
|---|---|---|
| Braced Framed Tube | 1.02 | 1.40 |
| Outrigger System | 1.02 | 1.40 |

**Table 5.8:** Calculated values of the conversion factor to go from SLS to ULS

### 5.6.2. Performance Variables

To derive the performance parameters in terms of the structural and environmental costs of the structure, it was essential to multiply the output of the GH in the form of the specific masses of materials and elements by the corresponding factors of the performance variables. The factors for the determination of the structural and environmental costs are illustrated in Table 5.9. The conversion of the masses of the elements to the performance parameters of costs was done in Python, and was thus external of the GH script.

The cost per kilogram of hollow core slab was calculated by dividing the price per square meter of hollow core slab, €110/m$^2$, by the mass per unit area of the hollow core, corresponding to a height (h) of 320 mm, which equaled 429 kg/m$^2$ [15]. Similarly, the cost per kilogram of reinforced prefab concrete was computed by dividing the price of reinforced concrete, set at €850 per cubic meter, by the specific weight of reinforced concrete, set at 2500 kg/m$^3$ [52].

| **Material** | **Specifications** | **Costs Weight** [€/kg] | **$CO_2$e Weight** [kg$CO_2$e/kg] | **Source** |
|---|---|---|---|---|
| Steel | Structural, hot rolled, S355 | 3.50 | 1.12 | [16] |
| Concrete | Precast, C45/55, hollow core, h=320mm | 0.256 | 0.155 | [14] [15] |
| | Precast, C45/55, reinforced 150 kg/m$^3$ | 0.340 | 0.238 | [52] |

**Table 5.9:** Factors per material for costs and embodied carbon

## 5.7. Training Machine Learning Tool

After generating a data set of the desired output, the modeling and training of the artificial neural networks started. This process took place externally to the GH script and was implemented using Python. The scripts for building and training the neural networks in Python can be found in Appendix H. The decision was made to develop two distinct neural network models to effectively predict and present the results for each stability system (S1 and S2). The neural network models were designed to predict the total mass of the structures. This prediction formed the foundation for calculating total structural and environmental costs, both of which relied solely on the mass of materials in this research. However, the data set from the parametric models provided masses for each structural element within specific height zones. To determine the total mass of each material, the masses of all structural elements made from

the same material were summed. Additionally, separate neural networks were modelled to predict the mass of each structural element within each height zone, corresponding to the input data set. It was decided not to use the outputs of these neural networks to derive the total mass prediction by summing up all the outputs of each prediction of the structural elements for each height zone. Instead, separate neural networks were developed specifically for predicting the total mass. This approach aimed to prevent the accumulation of errors and inaccuracies from individual mass predictions. Consistently, this methodology was applied to both braced framed tube and outrigger system, resulting in the construction of four distinct neural networks (two neural networks for each structural system). In Table 6.3 of Chapter 4 an outline is given of the four different neural network models with their prediction target. The aim of the additional two neural networks, with the division of the elements, was to gain additional insights into which elements of the structure have the highest contribution to the total mass of the structure.

## 5.8. Summary

This chapter presented the steps that were taken for the generation of the data sets of both the braced framed tube and the outrigger system using a parametric model in GH. It outlined a six-step roadmap for the data generation process, from defining input variables to generating results for structural element masses. The research aimed to facilitate a relative analysis between braced framed tube and outrigger system, ensuring consistent assumptions for a fair comparison. The process included detailing fixed and variable structural parameters, assumptions for building geometry based on wind zones, and structural analysis considerations, particularly for wind load calculations. Moreover, an approach was given on how the GH model was validated in terms of analytical and 2D analysis, ensuring its reliability for further analysis. Result generation focused on optimising the mass of structural elements within height zones, which were then used to calculate the performance parameters of costs and embodied carbon. Furthermore, the reasoning for developing and training four different neural network models was explained in detail, explaining the approach towards accurate predictions by prevention of error accumulation.

# Part III
# Research Outcome

# 6

# Results

This chapter will focus on the elaboration of the insights that can be derived from the artificial neural network models with the input data sets generated by the parametric models. This chapter will aim to answer sub-questions 3 and 4.

3 *Can the stability framework of a high-rise steel building be accurately predicted by means of a machine learning tool?*

4 *How does the performance of the machine learning tool compare to the performance of other established interpolation techniques and to analytical calculations?*

As outlined in Chapter 4, the research process consisted of two primary phases: 'Data Collection' and 'Modelling Procedure', as presented in Figure 4.1. This chapter starts with the outcomes of the initial phase, with the focus on the data collection from the parametric models. After visualising and analyzing the results of the 'Data Collection' phase, the next step involved analyzing the results of the 'Modelling Procedure'. An analysis of the output of the constructed neural networks is presented. Subsequently, the errors associated with this output is discussed and explained. Additionally, the computational time required for both the parametric models and the neural network is explored. Finally, the contribution of the stability framework to the overall structure is assessed.

## 6.1. Results Data Collection

The raw data sets from the parametric model of the braced framed tube (S1) and the outrigger system (S2) were first cleaned and converted. This involved calculating the performance parameters, in terms of structural and environmental costs, based on the mass provided in the raw data sets for both structural forms. The structural cost was determined using Equation 2.8, while the environmental costs was computed using Equation 2.9, both of which are elaborated upon in Chapter 2. Following data conversion and cleaning, the data sets were visualised to illustrate the correlation between the performance parameters and the structure's geometry.

### Visualisation over Height

Figure 6.1 and Figure 6.2 present scatter plots of structural and environmental costs over the height of the structure, respectively. The width of the structure is represented by the changing transparency of color. In the scatter plots, it was observed that costs per gross floor area ($m^2$GFA) increased with increasing height, and costs per $m^2$GFA also increased with decreasing width.

**Figure 6.1:** Structural costs per $m^2$GFA for different dimensions of width and height, S1 and S2

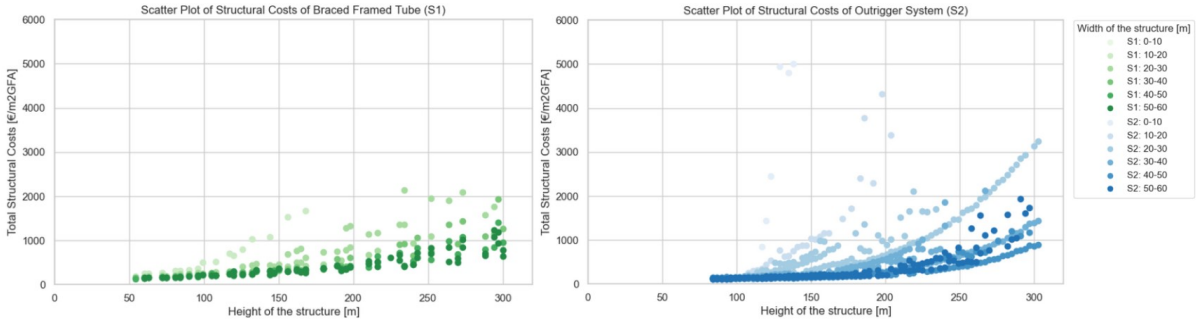


**Figure 6.2:** Environmental costs per $m^2$GFA for different dimensions of width and height, S1 and S2

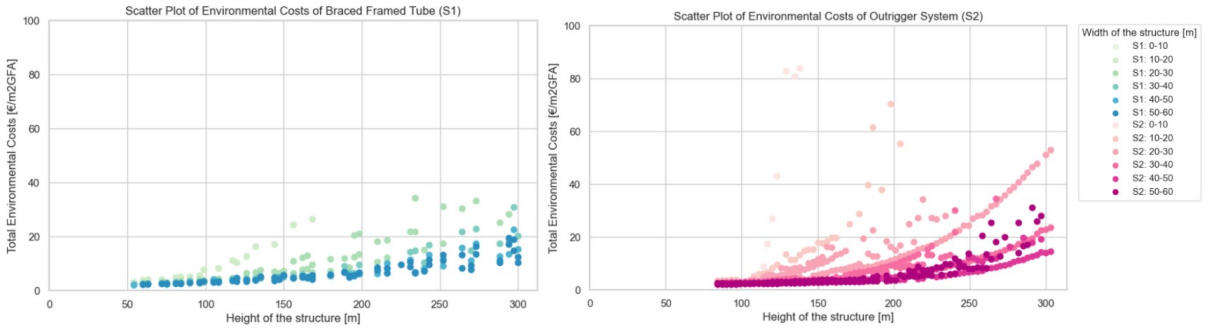


In the stability system of the braced framed tube, there were no structures within the 0-10 meter width range. This absence could be due to two main factors: either there was no feasible bracing configuration within the allowable range of bracing angles, or the stiffness requirements for these dimensions could not be met. The slenderness (height-to-width ratio) was significant for these dimensions, making it challenging to find suitable dimensions within the predetermined cross-section of ranges in the parametric model to still meet the stiffness requirements. A similar trend occurred for the outrigger system, but the highest reachable slenderness was slightly higher. However, costs increased exponentially with such significant slenderness. A zoomed-in graph provides a clearer comparison (see Figure 6.3), and Table 6.1 shows the highest slenderness values for both systems.

| **Stability System** | **Highest Slenderness** |
|---|---|
| | [-] |
| *Braced Framed Tube* | 11.67 |
| *Outrigger System* | 12.50 |

**Table 6.1:** Maximum achieved slenderness of both stability systems, S1 and S2

**Figure 6.3:** Zoomed-In: Costs per $m^2$GFA for different dimensions of width and height, S1 and S2

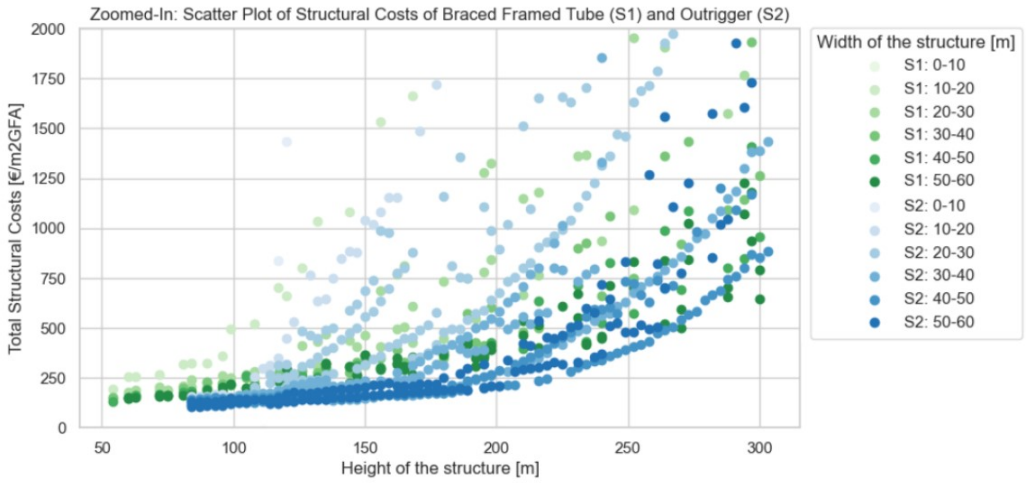


Figure 6.4 illustrates the relationship between total structural costs and total environmental costs per $m^2$GFA for both structural systems: the braced framed tube and the outrigger system. Both systems showed nearly identical slopes in their structural - environmental costs relationship, with a slope of approximately 62 €/$m^2$ of environmental costs. This implied that for every additional unit of environmental costs per square meter, the associated increase in structural costs was consistent for both systems. This correlation is logical, as both costs depended solely on the quantity of materials used, which in turn was proportional to the structural element's mass. Comparing the two stability systems, the observations can be done that the highest total costs of the braced framed tube is much lower than the highest reachable total costs of the outrigger system. This observation was also already seen in previous figures (Figure 6.1 and Figure 6.2), where the outrigger system had higher maximum structural and environmental costs compared to the braced framed tube.

**Figure 6.4:** Construction cost versus the environmental costs per $m^2$GFA for different structural forms

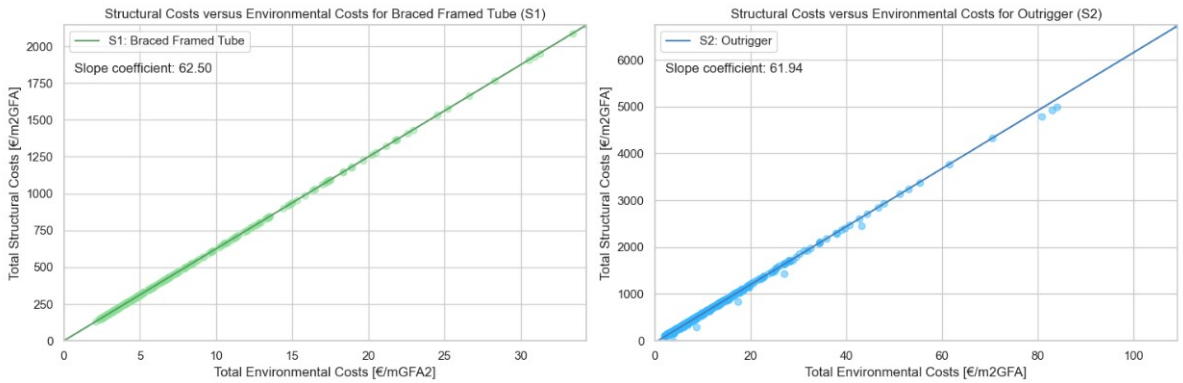


## Visualisation over Constant Width or Height

Additionally, the performance visualisation of stability frameworks was conducted, this time by maintaining one variable constant, either the height or the width. This isolation helped in capturing the behavior when one variable remained consistent. Figure 6.5 illustrates the scatter plot of both braced framed tube and outrigger system with a fixed width of 28.8 meters (matching the width of the validation structure utilised for the 2D and analytical analyses). Notably, the performance of both braced framed tube and outrigger system appeared quite similar. Likewise, Figure 6.6 showcases the performance, in terms of both structural and environmental costs, across varying width plans while the height was

held constant at 150 meters (also aligned with the validation structure). Once more, the performance of both stability systems showed significant similarity.

**Figure 6.5:** Performance versus the height of structure (S1 and S2) for a constant width of 28.8 m

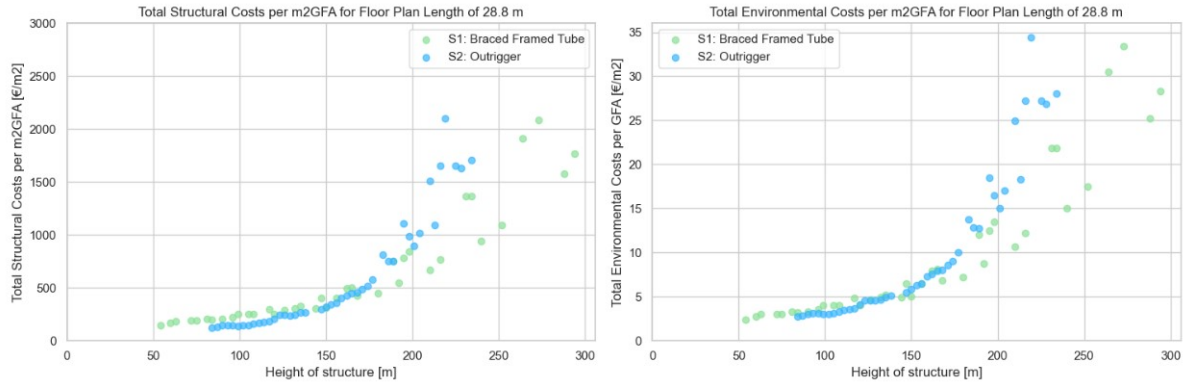


**Figure 6.6:** Performance versus the width of structure (S1 and S2) for a constant height of 150 m

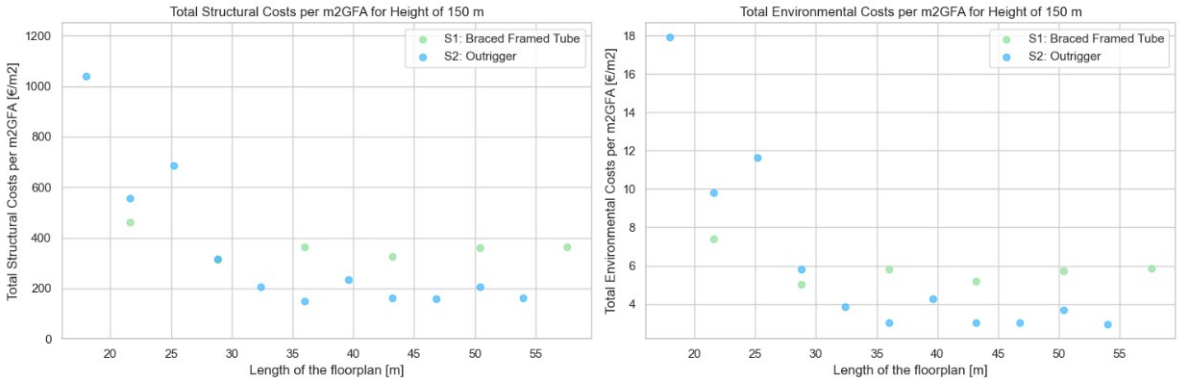


*Comparison with Literature*

Based on the consistent slope of the relationship between structural costs and environmental costs (as shown in Figure 6.4), it can be stated that the relative change in output for structural costs is directly related to environmental costs. Moreover, when comparing the stability frameworks of the braced framed tube and the outrigger system, the choice between embodied carbon and environmental costs does not change the relative comparison. The fundamental environmental impact of a structure remains constant, regardless of whether the focus is on raw carbon emissions (embodied carbon) or the associated financial costs (environmental costs). By multiplying the raw carbon emissions by the shadow price of $CO_2$ the environmental costs can be determined.

To validate the comparison between the two stability frameworks based on the data sets obtained from the parametric models, an analysis was conducted using existing literature. Lankorst et al. (2019) studied load-bearing structures, specifically focusing on their embodied carbon [11]. The findings from Lankhorst et al. align with the parametric models for structures at 150 and 250 meters in height. However, for a 200-meter structure, the parametric model suggests that the braced framed tube has the lowest embodied carbon, whereas Lankorst et al. found the outrigger system to be better. The comparison between the models is presented in Table 6.2.

| Height [m] | Width [m] | | Optimal Stability Framework |
|---|---|---|---|
| 150 | 30.0 | *Lankhorst* | both Outrigger and Braced Tube |
| | 28.8 | *Parametric Model* | both Outrigger and Braced Tube |
| 200 | 31.5 | *Lankhorst* | Outrigger |
| | 28.8 | *Parametric Model* | Braced Tube |
| 250 | 33.0 | *Lankhorst* | Outrigger |
| | 36.0 | *Parametric Model* | Outrigger |

**Table 6.2:** Comparison findings from parametric model with study of Lankhorst (2019)

### Visualisation over Volume

In addition to visualising the performance in terms of costs over the height of the structure, a visualisation for different volumes of the structure is provided to explore the relationship between costs and varying volume. The total volume of the structure was calculated based on its two input variables: the height and the width of the floor plan. The volume was obtained by multiplying the total area of the symmetrically squared floor plan by the number of floors of the structure and the floor-to-floor height.

Figure 6.7 illustrates the visualisation of structural costs per $m^2$GFA over the volume of the structure. Notably, there were some data points within outrigger system data set that exhibited significant structural costs despite having very low volume. These data points correspond to structures with significant slenderness, where the width was substantially smaller than the height of the structure. Meeting stiffness requirements for such structures was a significant challenge. In contrast, less of such outliers were observed in the data set of the braced framed tube. This difference can be attributed to two reasons: either a feasible bracing configuration could not be found, or the stiffness requirements could not be met for dimensions and slenderness similar to those of the outliers in the outrigger data set. To provide a clearer understanding of the relationship between stability systems, these outliers were excluded from the zoomed-in graph, as presented in Figure 6.8.

**Figure 6.7:** Costs per $m^2$GFA versus volume of structure

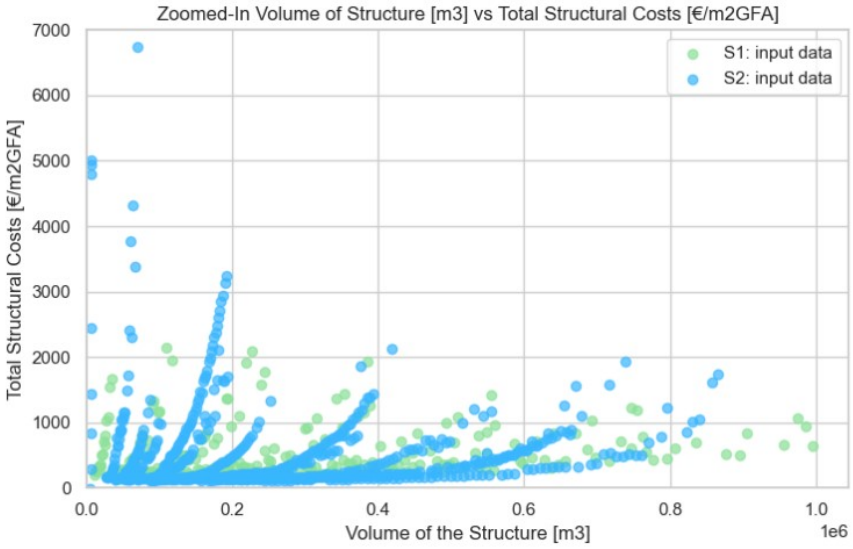

**Figure 6.8:** Zoomed-In: Costs per $m^2$GFA versus volume of structure

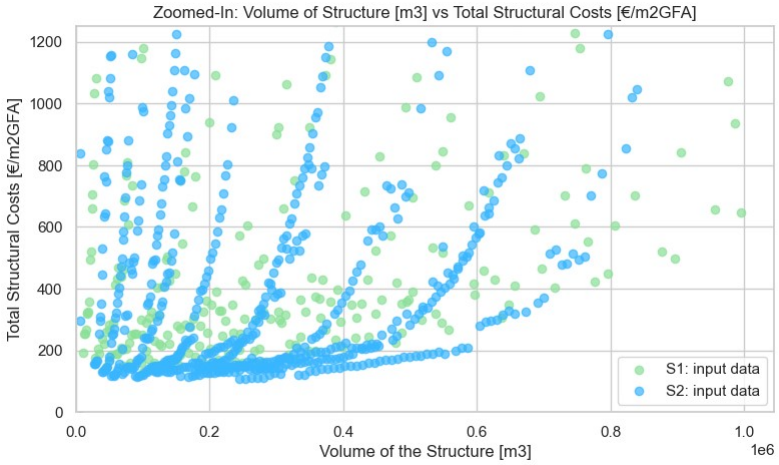


## 6.2. Results Modelling Procedure

After visualising the results obtained from the parameters models in the 'Data Collection' phase, the next step involved investigating the feasibility of prediction the correlation between the structure's dimensions and the performance parameters. The detailed steps of the 'Modelling Procedure' were thoroughly outlined in Chapter 4, where the workflow was explained (see Figure 4.9 in Chapter 4). The presentation of results follows this workflow, and an overview of which results is presented and where in the flowchart they occur is provided in Figure 6.9.

**Figure 6.9:** Flowchart modelling procedure to next step analysis of model results

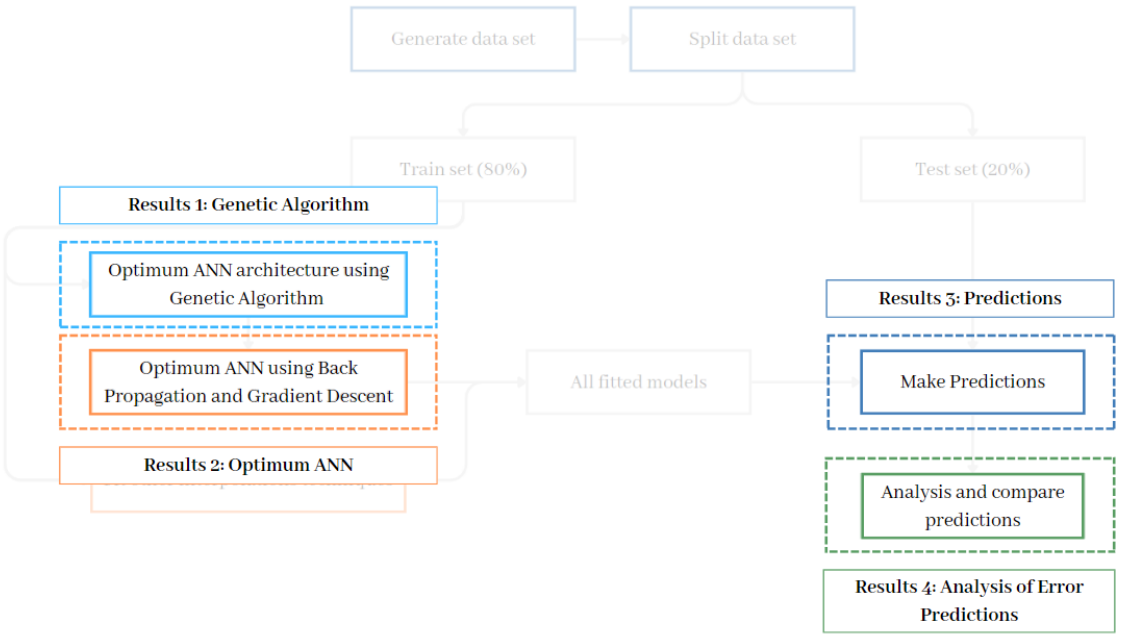


After cleaning and processing the data sets, and successfully training the artificial neural networks, predictions can be made using the ANN models. To add to the relevance of the results and gain insights into the elements with the most impact on the performance in terms of costs, the data sets have been divided to illustrate different perspectives. The prediction of the overall costs of each structural element

is provided based on the S1-A and the S2-A models, along with the performance of each structural element within each height zone, based on the S1-B and S2-B models. By segregating the structural elements in the data set, the contribution of the stability system (both gravity and the stability system) to the overall structure can eb determined. An overview of the different artificial neural networks is provided in Table 6.3.

| Stability System | ANN Model | Prediction Goal |
|---|---|---|
| Braced Framed Tube | S1-A | Total mass of structure |
| | S1-B | Mass of each structural element within height zones |
| Outrigger System | S2-A | Total mass of structure |
| | S2-B | Mass of each structural element within height zones |

**Table 6.3:** Different ANN models for prediction of the performance of stability systems

The research aimed to identify the most advantageous stability framework in terms of structural or environmental costs relative to the given volume of the structure. Therefore, the comparison focused solely on the structural forms. Consequently, the costs of the floors, specifically the hollow core slabs, are not factored into this comparison. This decision was based on the fact that the thickness of the hollow core slab remained constant across different geometries, resulting in consistent mass per squared meter (per $m^2$GFA). As both structural and environmental costs were determined solely by the quantity of mass, they remained constant across different geometries of the structures. Hence, predicting these values of the impact of the floors was unnecessary, as they would remain unchanged. Given their equality across the structural forms, including them in the comparison would not provide additional value.

### 6.2.1. Genetic Algorithm

The Genetic Algorithm (GA) was utilised to optimise hyperparameters across all four ANN models (see Table 6.3. These hyperparameters included the number of neurons in the hidden layer, kernel initializer option, bias initializer option, and learning rate option, as outlined in Table 6.4. The GA iterated through various combinations of these options, aiming to minimise the Mean Squared Error (MSE), serving as the fitness function, on the validation set. This function evaluated each solution's performance based on its hyperparameter configuration, quantifying the difference between predicted and actual values (MSE).

| | Output | Description |
|---|---|---|
| *Number of Neurons* | [1,50] | Range from 1 till 50 |
| *Kernel Initializer* | [0,2] | [Random Uniform, Constant, Zeros] |
| *Bias Initializer* | [0,2] | [Random Uniform, Constant, Zeros] |
| *Learning Rate* | [0,1] | [0.001, 0.01] |

**Table 6.4:** GA configuration parameters

The results obtained give an overview of the GA's optimisation process and its ability to identify the best solution for each ANN model. Specifically, the GA was executed individually for each ANN model to determine the most suitable hyperparameters. Figure 6.10 presents the outcomes of these GA iterations, showing the objective function values (MSE) at different iterations. The x-axis represents the iteration number, while the y-axis indicates the objective function value, with a blue line illustrating its fluctuations across iterations. It can be seen that, for all ANN models, the GA was terminated prematurely due to reaching the convergence limit of three iterations. Table 6.5 provides a summary of the results concerning the best solution uncovered by the GA for each ANN model, along with the corresponding objective function value. The GA successfully identified optimal hyperparameter configurations for all ANN models.

| Hyperparameter | ANN S1-A | ANN S2-A | ANN S1-B | ANN S2-B |
|---|---|---|---|---|
| *Number of Neurons* | 13 | 42 | 47 | 47 |
| *Kernel Initializer* | Zeros | Random Uniform | Random Uniform | Constant |
| *Bias Initializer* | Constant | Random Uniform | Constant | Constant |
| *Learning Rate* | 0.001 | 0.01 | 0.01 | 0.01 |
| *MSE* | 692 | 467 | 85 | 460 |

**Table 6.5:** GA of best configuration for each ANN model

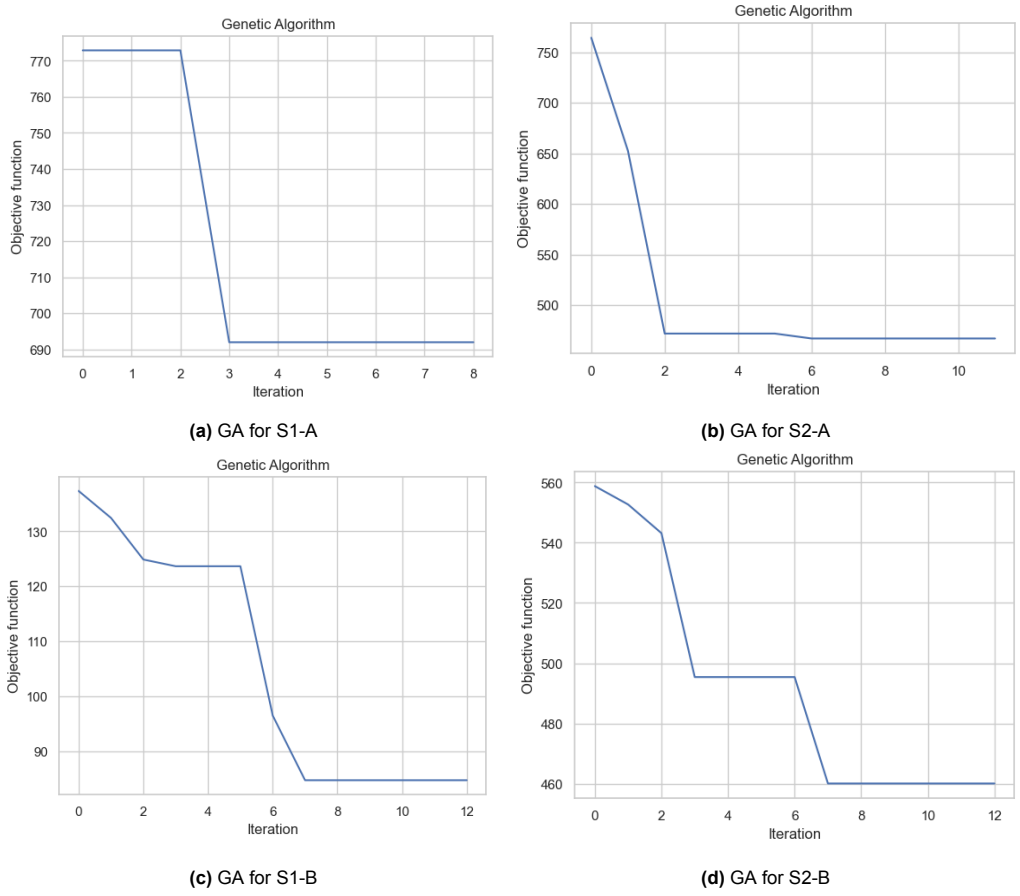


**(a)** GA for S1-A

**(b)** GA for S2-A

**(c)** GA for S1-B

**(d)** GA for S2-B

**Figure 6.10:** GA for finding the best configuration of hyperparameters for all ANN models

### 6.2.2. Optimum ANN

The convergence plots offer a visual representation of the training and validation loss throughout the iterative process, known as epochs. The convergence plots provide insights into whether the ANN model has reached a stable state during training, indicating progress towards finding an optimal configuration of weights and biases. Convergence in this context refers to the point at which the training and validation loss stabilize, indicating that the model has effectively learned the underlying patterns in the data. The training loss measures the model's performance on the training data during each epoch, while the validation loss evaluates its generalization performance on a separate data set. Initially, a decrease in the validation loss is expected, reflecting the model's capacity to generalize. However, if the model begins to overfit the training data by memorizing noise, the validation loss may show an increase, even as the training loss continues to decrease. The term ”loss” here refers to the Mean Squared Error (MSE) loss function used during the training phase. The primary goal during training is to minimise this loss, as a lower MSE indicates that the model's predictions closely align with the actual values, indicating better performance. It was determined that setting the maximum number of epochs for all the models to 10,000 was sufficient to reach a stabilized point for the loss.

Figure 6.11 presents the convergence plot for the braced framed tube (S1-A), presenting both training and validation loss over epochs. The left graph provides a comprehensive view, while the right graph offers a zoomed-in perspective. The observations regarding the convergence plot of the braced framed tube are briefly mentioned in Table 6.6. Figure 6.12 displays the convergence plot of the outrigger's ANN model (S2-A), exhibiting similar trends to the convergence plot of the braced framed tube's ANN model (S1-A). The observations are also presented in Table 6.6.

| **Aspect** | **Braced Framed Tube ANN S1-A** | **Outrigger System ANN S2-A** |
|---|---|---|
| Initial training | Rapid decline in both training and validation loss | Rapid decline in both training and validation loss |
| Change in Behaviour | Beyond 100 epochs slower rate of decline for both losses | Beyond 80 epochs slower rate of decline for both losses |
| Stable State | Around 300 epochs losses remained relatively constant | Around 600 epochs losses remained relatively constant |
| Validation vs. Training | Validation loss slightly higher than training loss | Validation loss slightly higher than training loss |
| Overfitting Check | Validation loss constant, absence of overfitting | Validation loss constant, absence of overfitting |
| Optimal Configuration | Found within range of max. number of epochs | Found within range of max. number of epochs |

**Table 6.6:** Observations convergence graphs of S1-A and S2-A

**Figure 6.11:** Convergence plot of ANN for S1-A

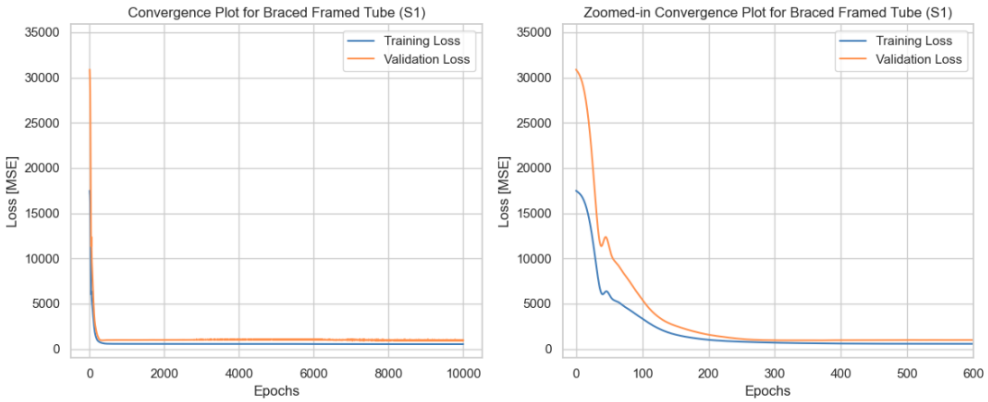

**Figure 6.12:** Convergence plot of ANN for S2-A

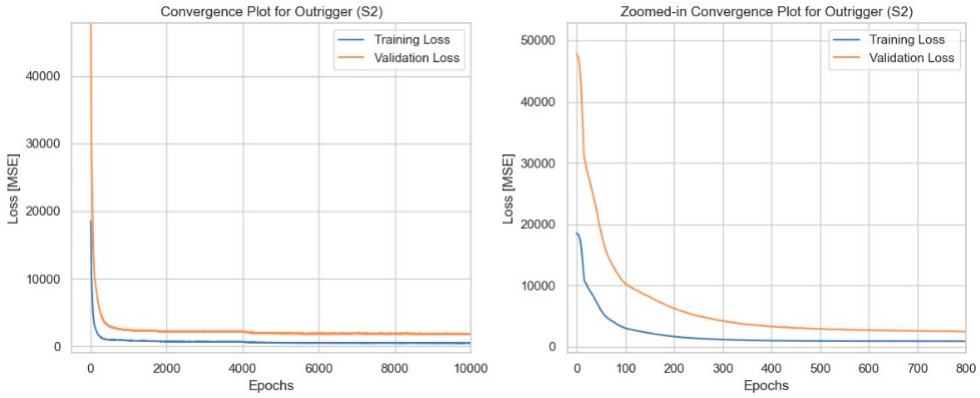


The convergence plots for S1-B and S2-B are presented in Figure 6.13 and Figure 6.14, respectively. Similar trends to the other convergence plots were observed, with no signs of overfitting or underfitting. It can be concluded that both models reached a stable state, indicating that S1-B and S2-B likely found the optimal configuration of weights and biases within the specified number of epochs of 10,000 for both systems.

**Figure 6.13:** Convergence plot of ANN for S1-B

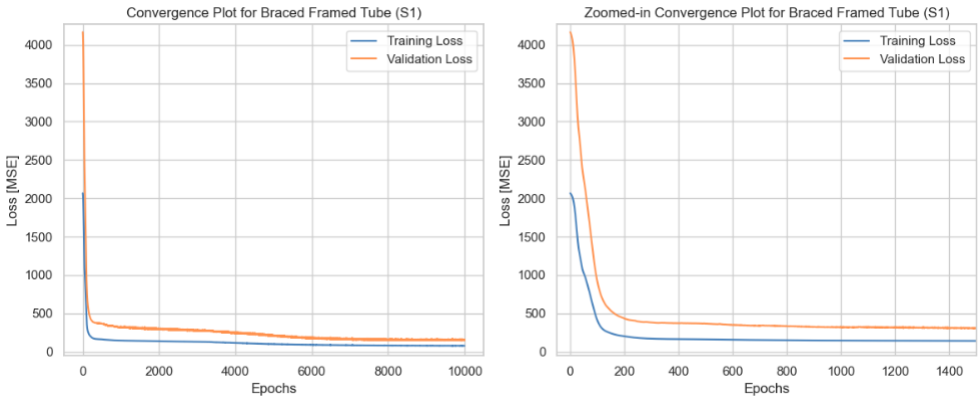


**Figure 6.14:** Convergence plot of ANN for S2-B

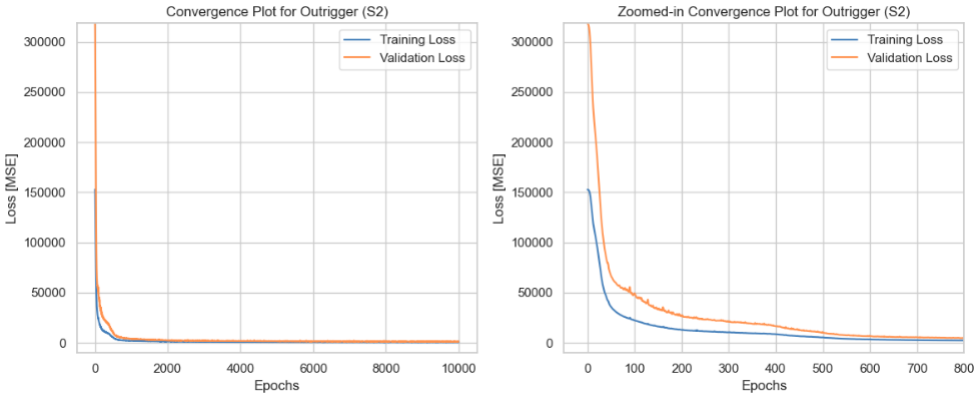

### 6.2.3. Predictions

#### Prediction: Total Structure

After modeling and training the ANN model of braced framed tube and outrigger system, predictions can be made regarding the total masses of the materials of the structure. Based on these predictions, performance parameters such as structural and environmental costs was determined. Since the impact in terms of costs relied solely on the mass predictions, their accuracy was equal. Consequently, for the error analysis, only one of the performance parameters is illustrated (see Section 6.2.4). Figure 6.15 presents the results of the prediction, where input was provided via a slider. The tool automatically generated predictions of performance, compared stability forms, and concluded which stability framework was the most cost-effective in either terms of structural or environmental costs.

**Figure 6.15:** Prediction of performance for both structural forms for specific input data

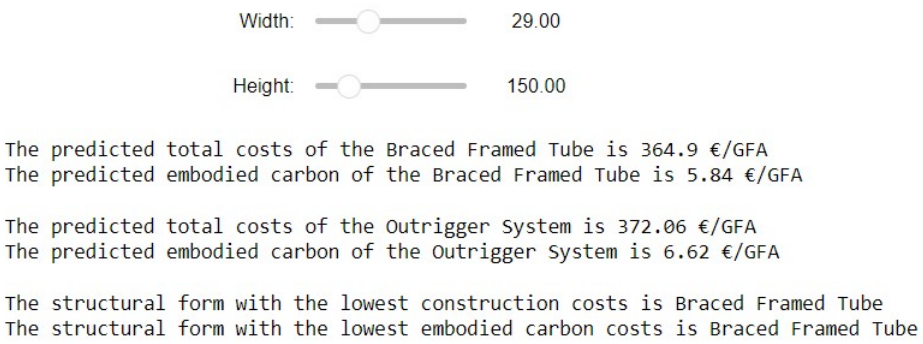


Moreover, to better illustrate the performance of different stability forms, an interactive tool was developed. This tool automatically graphed performance for different input variables, to be able to make a comparison of both structural forms based on the same geometry. The initial step involved selecting one of the two geometry variables, either height or width, as the constant parameter. Subsequently, by choosing one variable as constant, the changing parameter was plotted on the x-axis. This visualisation enabled representation of both total structural and environmental costs over the changing variable. By promptly graphing the performance prediction, the behavior of both structural forms for different geometries became visible. The interactive tool of the total structural costs is presented in Figure 6.16. The graph also includes upper and lower bands for the predictions, illustrating the potential maximum error range. Notably, the RMSE consistently increased in absolute value as the total costs increased. For lower values, the range of error was relatively small, but it expanded as the total costs increased, indicating a widening bandwidth. Additionally, Figure 6.18 highlights the presence of the threshold of the braced framed tube and the outrigger system regarding the maximum reachable slenderness, where after surpassing the upper limit of the slenderness the graph comes to a halt. It can be seen that the maximum reachable slenderness of the outrigger system is slightly higher than the slenderness of the braced framed tube, but the costs increase significantly for such high height-to-width ratios.

**Figure 6.16:** Interactive tool for prediction of performance for both structural forms, width=29m

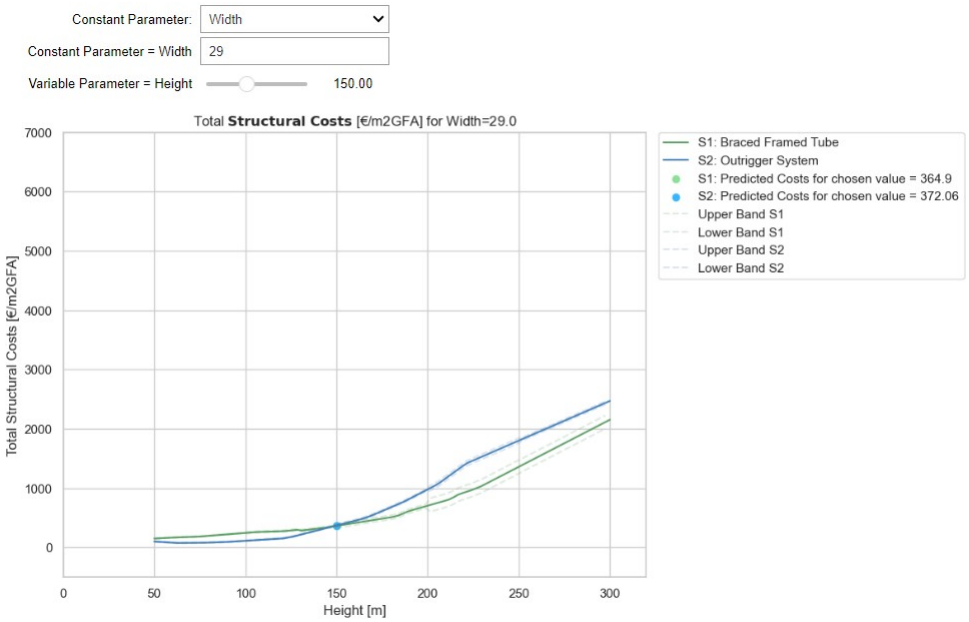


**Figure 6.17:** Interactive tool for prediction of performance for both structural forms, width=20m

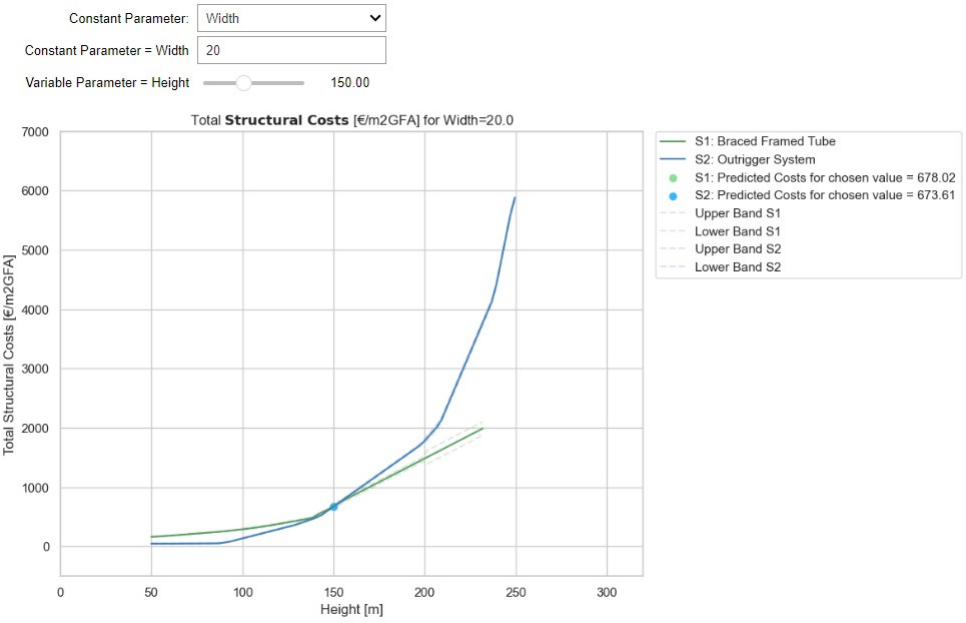

**Figure 6.18:** Interactive tool for prediction of performance for both structural forms, width=45m

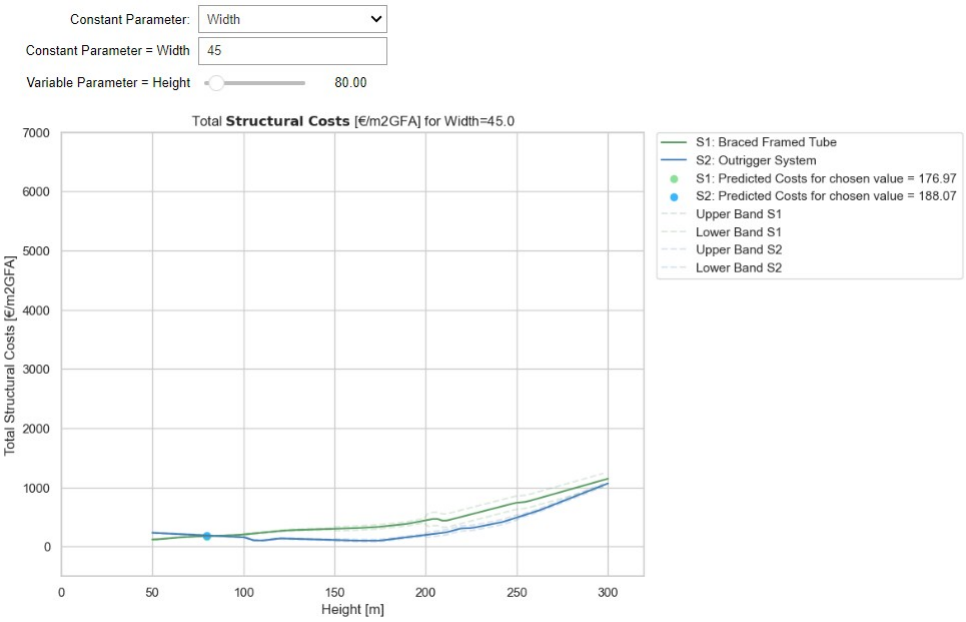


Considering the mass predictions, both structural and environmental costs were determined. Since they rely on the same mass predictions, their accuracy was equivalent. Consequently, for the error analysis, only one of the performance parameters is presented. The predictive accuracy of the models was assessed by comparing their output with the actual data derived from the parametric model. This comparison was crucial for evaluating whether the model could effectively capture the relationship and behavior of structures across varying dimensions. To illustrate this, the relationship between the actual and predicted values, specifically for models S1-A and S2-A, is demonstrated in Figures 6.19 and 6.20. These figures revealed that the ANN models closely mirrored the actual data, indicating their accuracy in capturing the underlying structural behavior. For instance, one figure shows the comparison for a structure width of 28.8 meters, while another figure presents the analysis for a width of 42.2 meters, based on the ANN predictions and actual input data. The magnitude of prediction errors and their implications is discussed in greater detail in Subsection 6.2.4.

**Figure 6.19:** Comparison predictions of S1-A with input data with width of 28.8 meters

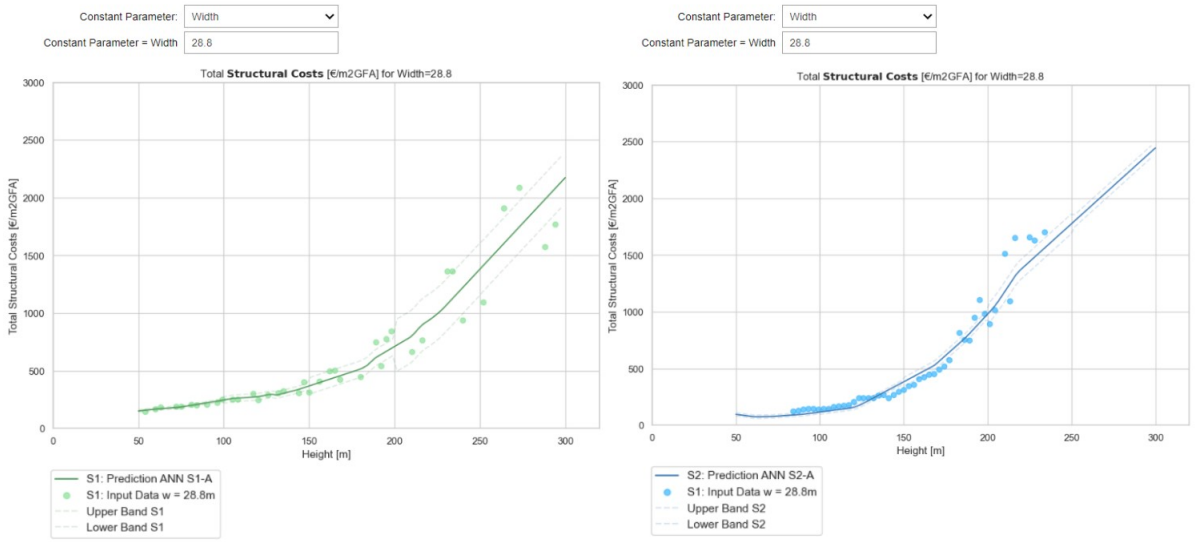

**Figure 6.20:** Comparison predictions of S2-A with input data with width of 43.2 meters

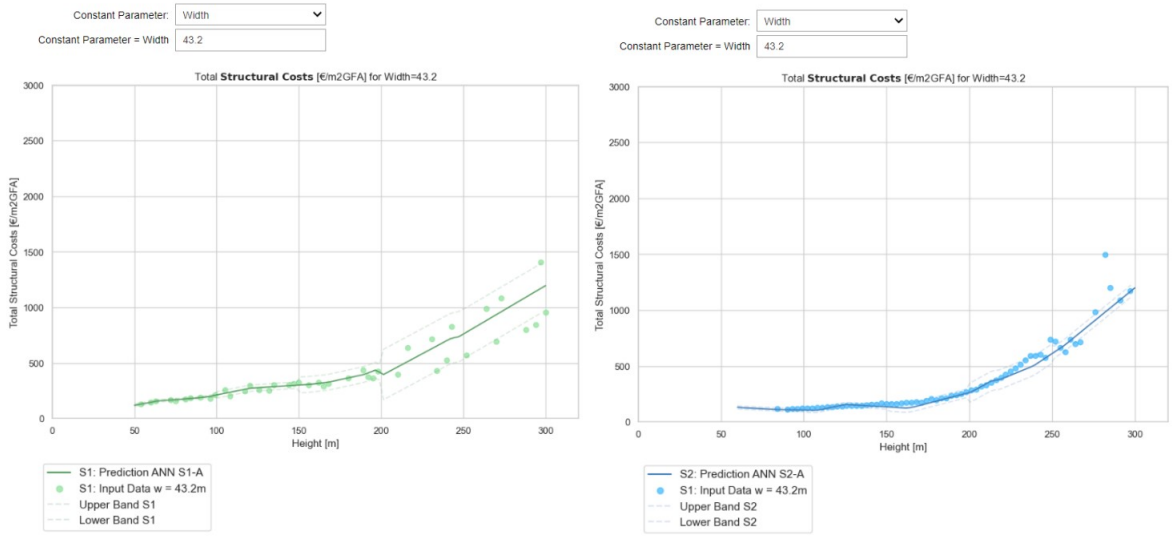


### Prediction: Element Split

The outcomes of the ANN models of S1-B and S2-B are plotted for both structural and environmental costs for each specific structural element. This approach allowed for the identification of areas with the highest costs. The distinction is made between the structural elements part of the stability and gravity system. Within the stability framework, different structural elements play varying roles in the overall impacts. These roles and contributions differ between the two systems of the braced framed tube and the outrigger system. Table 6.7 provides an overview of how these elements contribute to either stability (horizontal force) or gravity (vertical force). The inner columns connected to the outrigger have two purposes: contributing to both the stability and gravity systems. In slender structures, their contribution to stability becomes more governing. An assumption is made regarding the mass distribution of the inner columns connecting to the outrigger truss. The mass of inner columns connected to the outrigger, contributing to the gravity system, is equal to the total mass of inner columns not connected to the outrigger truss (since the latter only contribute to the gravity system). The remaining mass of the inner columns connected to the outrigger contributes to the stability system

Figure 6.23 illustrates the breakdown of performance parameters for the braced framed tube, while Figure 6.24 presents the breakdown for the outrigger system. Both figures display the structural costs predictions for a structure with a height of 150 meters and a width of 29 meters. The tool was designed to be interactive, enabling users to adjust the width and height of the structure. This enabled the automatic generation of new graphical representations, illustrating costs based on the updated input parameters. The costs of the floor system (hollow core slab) was included to visualise the total costs of the gravity system to the stability system of the framework. The contribution in terms of costs from both gravity and stability system and the stability system's ratio are presented.

| Stability System | Framework | Structural Element | Ratio |
|---|---|---|---|
| *Braced Framed Tube* | Stability Framework | Outer columns | Fully |
| | | Bracing diagonals | Fully |
| | Gravity Framework | Floor beams | Fully |
| | | Outer beams | Fully |
| | | Floor system | Fully |
| | | Inner columns | Fully |
| *Outrigger System* | Stability Framework | Outrigger system | Fully |
| | | Core | Fully |
| | | Outer columns connected to outrigger | Fully |
| | | Inner columns connected to outrigger | Partly |
| | Gravity Framework | Floor beams | Fully |
| | | Outer beams | Fully |
| | | Floor system | Fully |
| | | Outer columns not connected to outrigger | Fully |
| | | Inner columns not connected to outrigger | Fully |
| | | Inner columns connected to outrigger | Partly |

**Table 6.7:** Overview of contribution of each structural element to either gravity or stability

**Figure 6.21:** Prediction of parameters prediction; element split S1

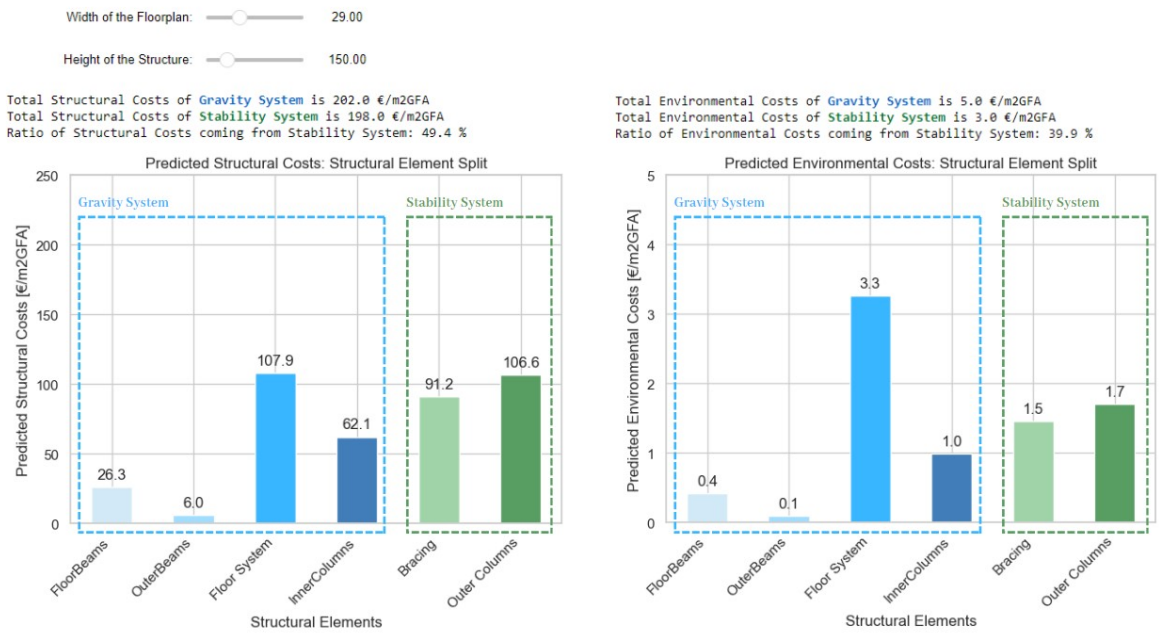

**Figure 6.22:** Prediction of performance parameters; element split S2

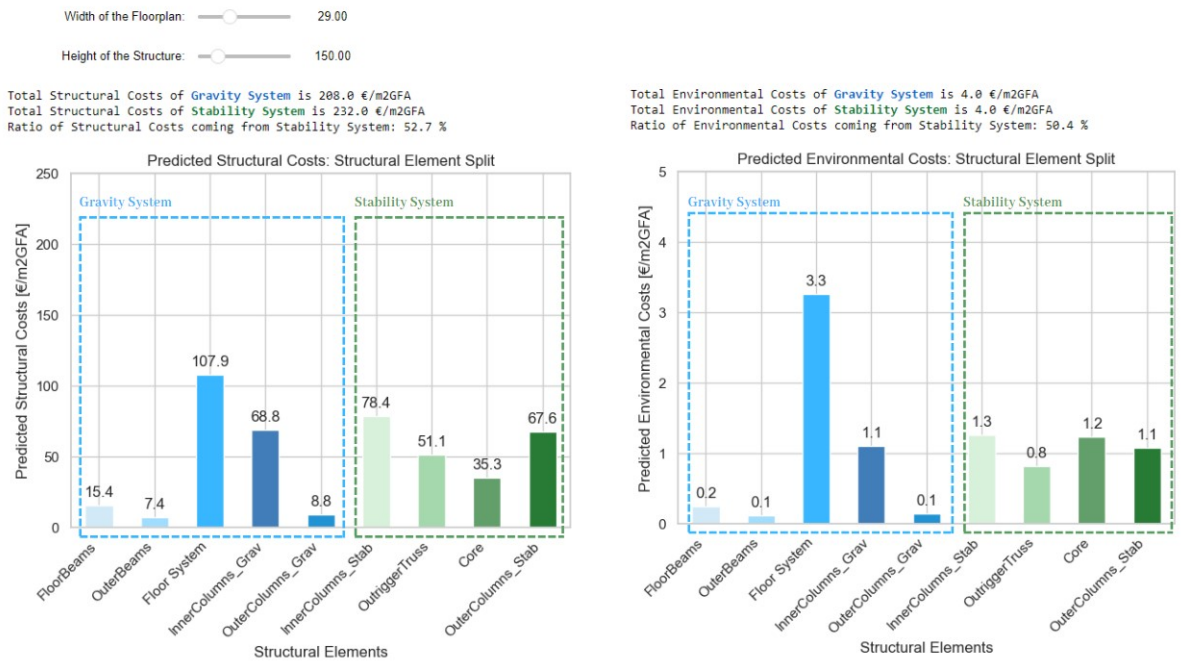


The Root Mean Squared Error (RMSE) and Mean Absolute Percentage Error (MAPE) values for the various elements are presented in Table 6.8 for S1-B and Table 6.9 for S2-B. The RMSE quantifies the error in terms of kg per $m^2$GFA, representing the absolute value of the error. On the other hand, the MAPE expresses the relative error as a percentage of the difference between the predicted and actual values. Using the MAPE metric is particularly useful for assessing the accuracy of these neural networks because it presents the error in relative error percentage. Since the average masses of the structural elements are far apart, making the RMSE relative to the mass and expressing it in terms of the MAPE provides a good way to understand accuracy and compare it across different structural elements.

| **Structural Element** | **RMSE** [kg/$m^2$GFA] | **MAPE** [%] |
|---|---|---|
| *Outer Beams* | 0.68 | 25 |
| *Outer Columns* | 32.83 | 30 |
| *Floor Beams* | 0.60 | 5 |
| *Inner Columns* | 6.12 | 18 |
| *Bracing* | 10.32 | 18 |

**Table 6.8:** RMSE and MAPE of ANN model S1-B for each structural element

| Structural Element | RMSE [kg/m$^2$GFA] | MAPE [%] |
|---|---|---|
| *Outer Beams* | 1.40 | 9 |
| *Outer Columns conn. Truss* | 16.90 | 29 |
| *Outer Columns not conn. Truss* | 1.23 | 21 |
| *Floor Beams* | 1.34 | 22 |
| *Inner Columns conn. Truss* | 31.94 | 43 |
| *Inner Columns not conn. Truss* | 5.61 | 25 |
| *Outrigger Truss* | 15.20 | 23 |
| *Core* | 7.22 | 7 |

**Table 6.9:** RMSE and MAPE of ANN model S2-B for each structural element

### Prediction: Element and Height Zone Split

Furthermore, an overview of the impact of each distinct height zone was determined, based on the output of the ANN model S1-B and ANN model S2-B. This approach allowed for clear visibility into the contribution of each structural element within its respective height zone to the total structural and environmental costs. Figures 6.23 and 6.24 illustrate the division of elements and height zones for both the braced framed tube and the outrigger. The findings align with the expectation that lower height zones require more mass, as they experience greater gravitational forces from the mass above. Consequently, higher mass corresponds to higher costs. Similar to the element split, this tool was designed to be interactive, allowing for adjustments to the width and height inputs. This prompts the automatic generation of new visualisations illustrating the predicted performance of the structure divided over the elements within the specific height zone.

**Figure 6.23:** Prediction of parameters prediction; element and height zone split S1

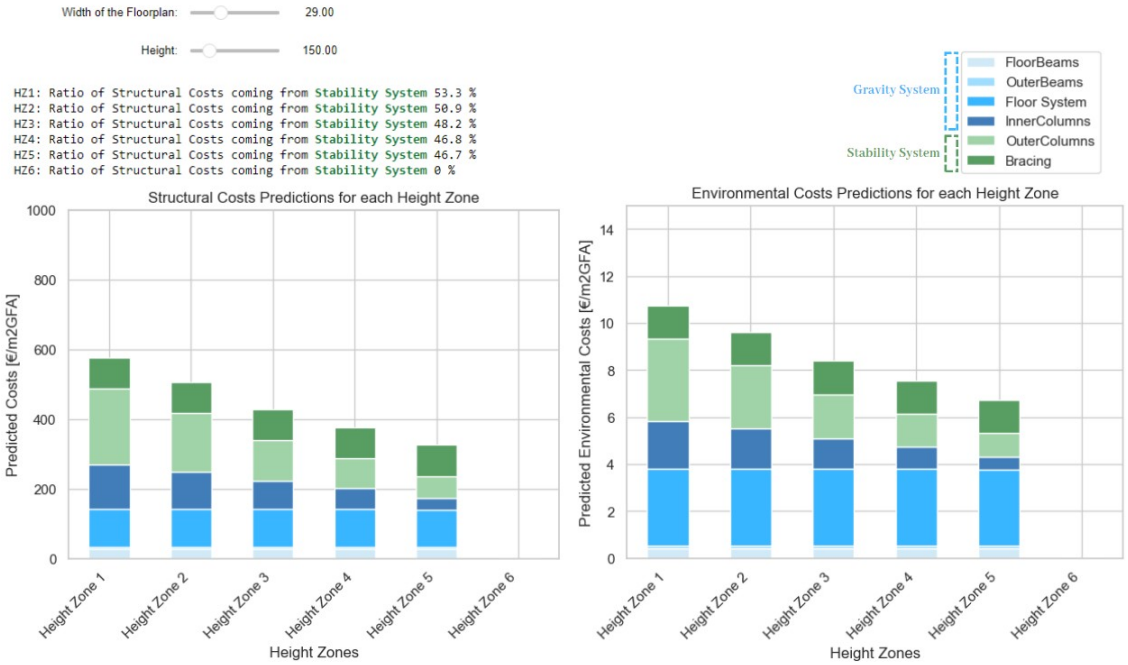

**Figure 6.24:** Prediction of performance parameters; element and height zone split S2

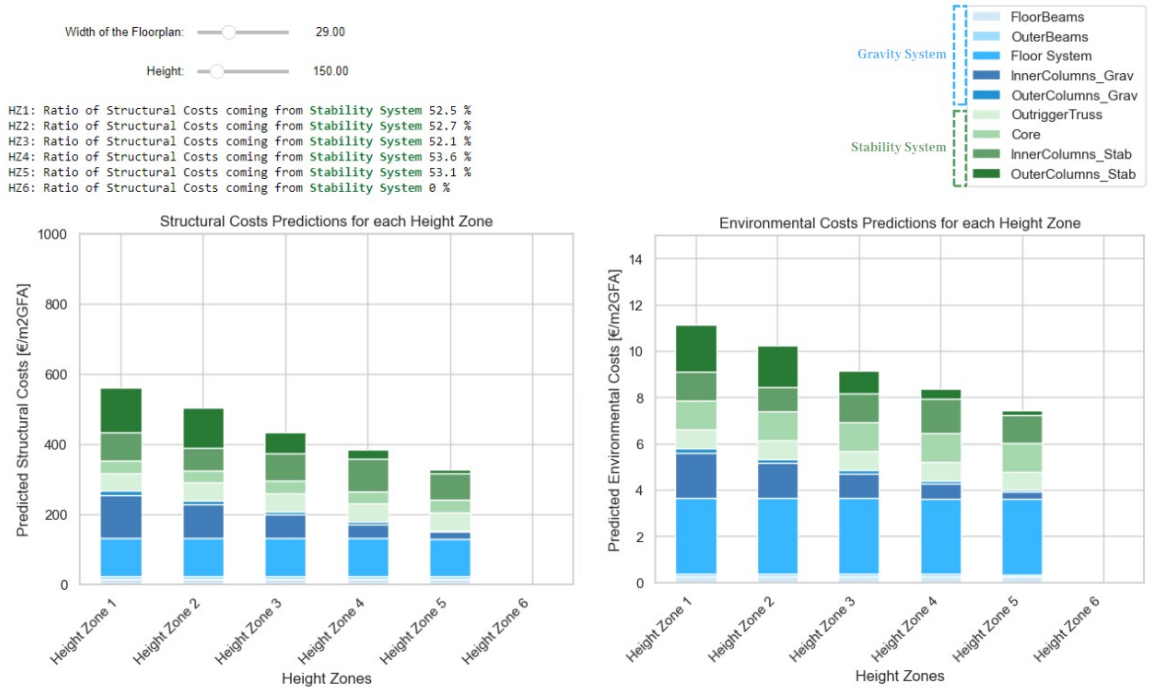


The RMSE and MAPE was calculated for each structural element within each height zone. Tables F.1 and F.2 in Appendix F provide a comprehensive overview of all RMSE and MAPE values for structural elements within each height zone. For the S1-B model, the MAPE ranged from 5% to 35%, indiciting significant variability in the predictions. The mean MAPE across all elements was 23%. The variability in MAPE may be attributed to the large number of desired outputs and the relatively small data set size. For the S2-B model, the MAPE range was even broader, falling between 2% and 53%. The mean MAPE across all elements was equal to 35%.

### 6.2.4. Analysis of Error Predictions

Given that the primary research question is related to the feasibility of developing an ANN model to predict the best performing stability framework across various volumes, the analysis of prediction errors was solely conducted for the ANN models of S1-A and S2-A. The artificial neural network models of S1-A and S2-A align directly with the main aim of this study. While the ANN models of S1-B and S2-B were included to demonstrate potential value outputs, the scope of this research restricted the further analysis of errors for those ANN models. Therefore, the error analysis and comparison with other interpolation techniques was only performed for ANN models S1-A and S2-A.

The relative performance of the ANN was assessed by comparing its prediction error with that of other curve fitting models. This comparison involved examining the distribution of percentage differences between actual and predicted values, also called the relative error, for both the the braced framed tube and the outrigger system. The ANN models were compared to three different curve fitting models: linear regression, second order polynomial regression, and third order polynomial regression. By contrasting the performance of the ANN with that of performance of the curve fitting methods, insights into its relative effectiveness were gained.

#### Evaluation for Braced Framed Tube (S1-A)

First, the values of RMSE and MAPE were calculated to get an impression of the performance of the different models. These values are detailed in Table 6.10, the errors are determined based on the total height range of 50 to 300 meters. It is important to note that the unit of RMSE corresponded to the unit of the output data, which in this case was the mass of the structure, measured in kg/m$^2$GFA. To contextualize the magnitude of the RMSE, attention can be given to the 25th and 75th percentiles and

the mean of the mass of the braced framed tube. Specifically, the 25th percentile of the total mass of braced framed tube was 70.3 kg/m$^2$GFA, the 75th percentile was 190.3 kg/m$^2$GFA, with a mean mass of the structure of 146.2 kg/m$^2$GFA. The results showed that the ANN model outperformed the other models with the lowest MAPE among the four models, standing at 14%, compared to 49% for linear regression, 38% for the second order, and 25% for the third order.

| **Curve Fitting Models** | **RMSE** [kg/m$^2$GFA] | **MAPE** [%] |
|---|---|---|
| ANN | 38.9 | 14 |
| First Order | 55.3 | 49 |
| Second Order | 44.3 | 38 |
| Third Order | 40.3 | 25 |

**Table 6.10:** Overview of RMSE for braced framed tube (S1)

Furthermore, the results of the RMSE for different height subsets of the braced framed tube was examined to understand the variation in accuracy across varying heights, see Table 6.11. The findings revealed that the RMSE increased as the height of the structures increased. Additionally, considering the increase of total mass of the structures as the height of the structures increased, the MAPE was examined. The MAPE also showed an upward trend with increasing heights. Specifically, within the height range of 50 to 100 meters, a MAPE of 5.9% was observed, while for the subset of heights between 250 and 300 meters, the MAPE reached 23.5%.

| **Height Subset** | **RMSE** [kg/m$^2$GFA] | **MAPE** [%] |
|---|---|---|
| 50 - 100 m | 11.2 | 5.9 |
| 100 - 150 m | 27.3 | 8.0 |
| 150 - 200 m | 68.8 | 11.2 |
| 200 - 250 m | 216.4 | 23.8 |
| 250 - 300 m | 223.8 | 23.5 |

**Table 6.11:** Overview of RMSE and MAPE over different height subsets of S1

The probability density of the different models was also generated to provide a more visual representation of the performance of the models. The mean ($\mu$) and the standard deviation ($\sigma$) provide information about the central tendency and distribution of the percentage differences for each regression model. Probability density functions represent the likelihood of different outcomes occurring within a given range. They provide insights into the variability and reliability of predictions, showing how frequently different levels of error occur. The calculated parameters are summarized in Table 6.12. Figure 6.25 illustrates the distribution of relative error for each regression model based on the parameters for the braced framed tube.

| **Curve Fitting Models** | $\mu$ [%] | $\sigma$ [%] | Total PD $\pm$ 15% [-] |
|---|---|---|---|
| ANN | 3.52 | 17.0 | 0.62 |
| First Order | -15.72 | 80.1 | 0.14 |
| Second Order | 5.99 | 59.4 | 0.20 |
| Third Order | 3.87 | 26.7 | 0.39 |

**Table 6.12:** Overview of parameters of the probability density functions for S1

**Figure 6.25:** Distribution of percentage differences of braced framed tube (S1) for different regression models

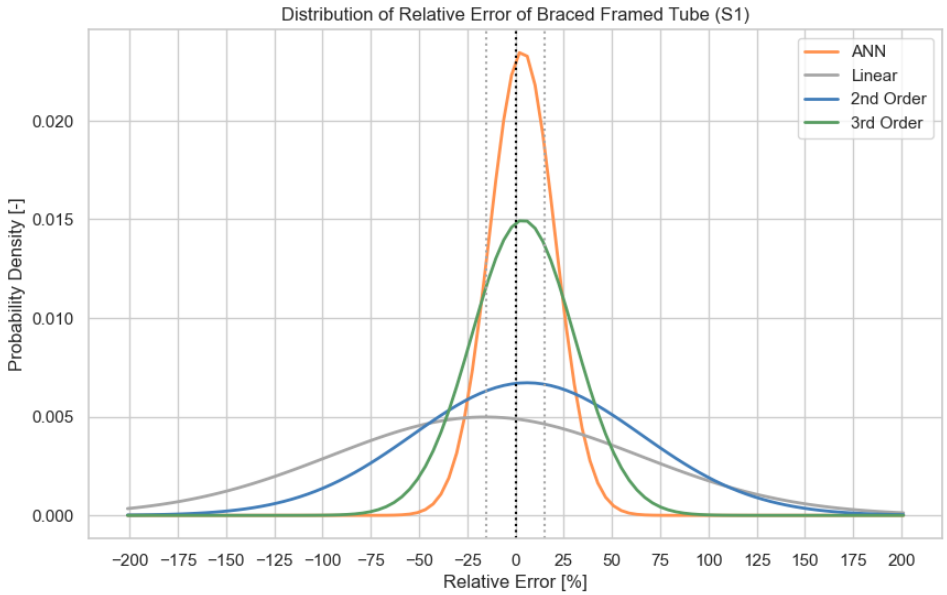


From the Table 6.12 and the Figure 6.25, several insights can be drawn the performance of the regression models in predicting the system's mass.

- **ANN Model**
  The ANN model showed a slightly positive mean ($\mu$ = 3.52%), indicating a tendency to overestimate the actual values. The moderate standard deviation ($\sigma$ = 17.0%) illustrated the relatively high accuracy of the ANN model. The probability that the relative error is within the ranges of -15% and +15% was equal to 62%.
- **First Order Model**
  In contrast to the ANN model, the linear regression model showed a significant negative mean ($\mu$ = -15.72%), suggesting a significant underestimation of the actual values. Additionally, the substantial standard deviation ($\sigma$ = 80.1%) indicated significant variability in predictions, resulting in not accurate estimations. Moreover, the probability of the relative error of the predictions being within $\pm$ 15% was merely 14 %.
- **Second Order Model**
  The second order regression model demonstrated a positive mean of ($\mu$ = 5.99%), indicating a tendency to overestimate the actual values. Moreover, the substantial standard deviation ($\sigma$ = 59.4%) suggested high variability in the predictions. Similarly to the first order, was the probability that the relative error is within $\pm$ 15% low, and is equal to 20% for the second order.
- **Third Order Model**
  The third order model demonstrated a mean ($\mu$ = 3.87%), implying a tendency towards overestimation. The standard deviation ($\sigma$ = 26.7%) suggested relatively high variability in predictions, exceeding that of the ANN model. The probability of third order predictions falling within the range of $\pm$ 15% was 39%, which was better than the first and second order but inferior to the ANN.

*Evaluation of Performance in terms of Structural Costs*
In addition to assessing the accuracy of predictions for the mass of structures, an evaluation of the performance of the curve fitting models in predicting structural and environmental costs was performed. Scatter plots were used to visualise the relationship between predicted and actual values for structural costs across four regression models: ANN, linear regression, second-order regression, and third-order regression. Figure 6.26 presents the scatter plots for the braced framed tube. The x-axes represents the actual costs (€/m$^2$GFA), and the y-axes represents the predicted costs based on the same input

data. The scatter plots include training data (blue circles), test data (purple circles), and a reference line (“True value”) indicating perfect prediction. The main observations are presented in Table 6.13.

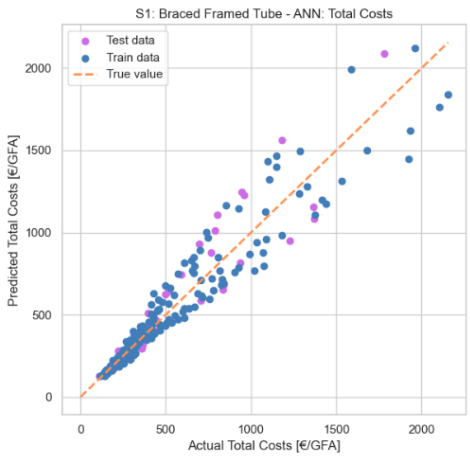


**(a)** Actual vs prediction values ANN


**(b)** Actual vs prediction values Linear Regression

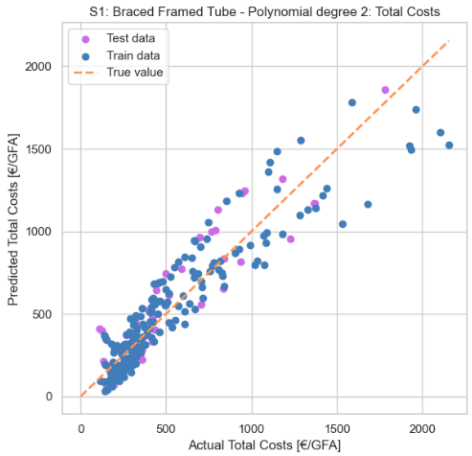


**(c)** Actual vs prediction values 2nd Order Regression

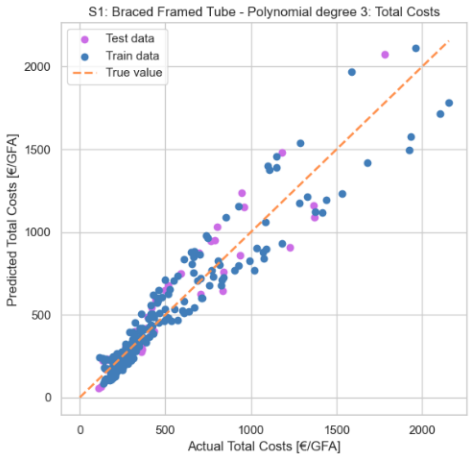


**(d)** Actual vs prediction values 3rd Order Regression

**Figure 6.26:** Actual vs prediction values of structural costs for S1 with different regression models

| ***S1: Braced Framed Tube*** | | **Observation** |
|---|---|---|
| **Curve Fitting Models** | *ANN* | Significantly high accuracy at low costs, but accuracy decreasing with increasing of costs values. |
| | *First Order* | Tendency for underestimation at lowest costs, followed by slight overestimation at middle costs, and significant underestimation at highest costs. |
| | *Second Order* | Relative accurate at lower costs, but accuracy decreasing with increasing of costs. |
| | *Third Order* | Closely resembled the trend of ANN and second order, but less accurate at lower costs than ANN. |
| **General** | | Accuracy of the ANN is the best. |
| | | The observed behavior in the scatter plots aligned with the insights from the probability density distribution. |

**Table 6.13:** Observations from the scatter plot of different regression models for S1

### Evaluation for Outrigger (S2-A)

In line with the methodology applied to the braced framed tube, the RMSE and MAPE were computed for the outrigger system, and the resulting values are listed in Table 6.14. To contextualize the RMSE values, percentiles of the total mass of the outrigger system were determined: the 25th and 75th percentiles and the mean, corresponding to 120.8 kg/m$^2$GFA, 295.2 kg/m$^2$m$^2$GFA and 250.2 kg/GFA respectively.

| **Curve Fitting Models** | **RMSE** [kg/m$^2$GFA] | **MAPE** [%] |
|---|---|---|
| ANN | 29.1 | 7 |
| First Order | 62.9 | 67 |
| Second Order | 52.9 | 41 |
| Third Order | 52.3 | 31 |

**Table 6.14:** Overview of RMSE of percentage difference for S2

Furthermore, the results of the RMSE and MAPE for different height subsets of the outrigger system was again examined to understand the variation in accuracy across varying heights, see Table 6.15. For the outrigger system, the MAPE pattern varied with height: it initially decreased as structures got taller, but for the highest two height subsets, it increased again. The highest accuracy (5.7%) occurred for structures between 150 and 200 meters. The lowest accuracy was observed for the lowest height subset, likely due to the low total mass, which made the error-to-mass ratio relatively higher.

| **Height Subset** | **RMSE** [kg/m$^2$GFA] | **MAPE** [%] |
|---|---|---|
| 50 - 100 m | 14.7 | 9.2 |
| 100 - 150 m | 20.1 | 6.4 |
| 150 - 200 m | 38.6 | 5.7 |
| 200 - 250 m | 86.9 | 7.7 |
| 250 - 300 m | 53.3 | 6.7 |

**Table 6.15:** Overview of RMSE and MAPE over different height subsets of S2

The ANN model for the outrigger system exhibited the highest level of accuracy among the tested interpolation techniques, with an RMSE of 29.1 kg/m$^2$GFA, indicating a relatively low deviation of predictions from actual values. This accuracy was further underscored when looking at the MAPE which is equal to 7%. In contrast, the linear regression model showed a significantly higher RMSE of 62.9 kg/m$^2$GFA and a MAPE of 67% and could therefore be considered as not accurate. Similarly, the second order regression and third order regression models demonstrated RMSE values of 52.9 kg/m$^2$GFA and 52.3 kg/m$^2$GFA, respectively. Despite these lower RMSE values, suggesting relatively better prediction accuracy compared to the linear regression model, they still fell short to be able to make an accurate prediction. In summary, the ANN model provided the most accurate predictions among the tested curve fitting models for the outrigger system.

In addition to analyzing the probability density functions for the braced framed tube, the probability density functions for the outrigger system was also examined. The mean ($\mu$) and standard deviation ($\sigma$) for the four regression models were observed, reproducing the process of the braced framed tube. The parameter values are presented in 6.16 and the distribution of percentage differences for each of the regression models based on those parameters is presented in Figure 6.27.

| **Curve Fitting Models** | $\mu$ [%] | $\sigma$ [%] | Total PD $\pm$ 15% [-] |
|---|---|---|---|
| ANN | -1.03 | 9.5 | 0.89 |
| First Order | 20.03 | 77.0 | 0.08 |
| Second Order | 6.41 | 48.7 | 0.19 |
| Third Order | 2.54 | 35.5 | 0.34 |

**Table 6.16:** Overview of parameters of the probability density functions for Outrigger (S2)

**Figure 6.27:** Distribution of percentage differences of S2 for different regression models

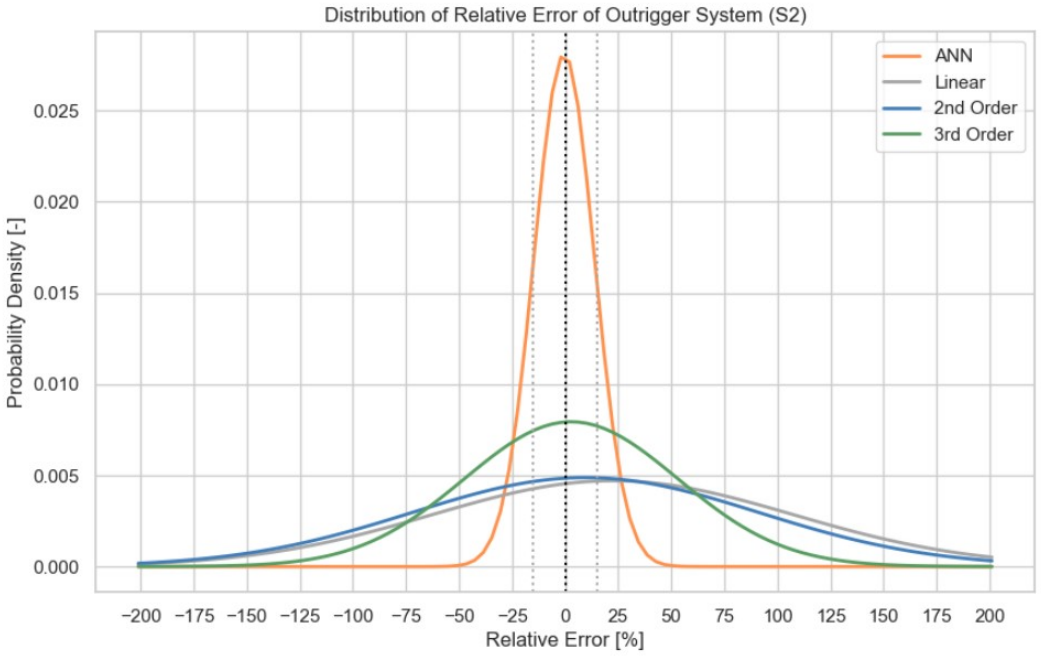


From the Table 6.12 and the Figure 6.25, several insights can be done regarding the performance of the regression models in predicting the system's mass.

- **ANN Model**
  The ANN model for the outrigger exhibited a slightly negative mean $\mu$ = -1.03%), indicating a very small tendency to slightly underestimate the actual values. The standard deviation ($\sigma$ = 9.5%) suggested slight variability in predictions. The probability that the relative error of the predictions falls within the range of -15% and +15% is significant and equal to 89%.
- **First Order Model**
  In contrast to the ANN model, the linear regression model showed a significantly higher positive mean ($\mu$ = 20.03%), suggesting a substantial overestimation of the actual values. Additionally, the large standard deviation ($\sigma$ = 77.0%) indicated considerable variability in predictions, resulting in inaccurate estimations. Moreover, the probability of the relative error of the predictions being within $\pm$ 15% was merely 8%, indicating that the accuracy of the first order regression model should be considered to be insufficient
- **Second Order Model**
  The second order regression model exhibited a positive mean ($\mu$ = 6.41%), indicating a tendency to slighty overestimate the actual values. Furthermore, the standard deviation ($\sigma$ = 48.7%) suggested high variability in the predictions. The probability of the relative error of the predictions being within $\pm$ 15% was only 19%, indicating that the accuracy of the second order regression model should be considered to be insufficient.

- **Third Order Model**
  The third order regression model showed a slight positive mean ($\mu$ = 2.54%), implying a small tendency towards overestimation of results. The standard deviation ($\sigma$ = 35.5%), however, suggested significant high variability in predictions. The probability of third order regression predictions falling within the range of $\pm$ 15% was 34%, which made the third order model the most accurate model compared to the first and second order curve fitting models.

*Evaluation of Performance in terms of Costs*

The predictive performance of total costs for outrigger system is presented in Figure 6.28. This figure showcases scatter plots comparing predicted cost values against actual values for each regression model. The main observations from the scatter plots are presented in Table 6.17.

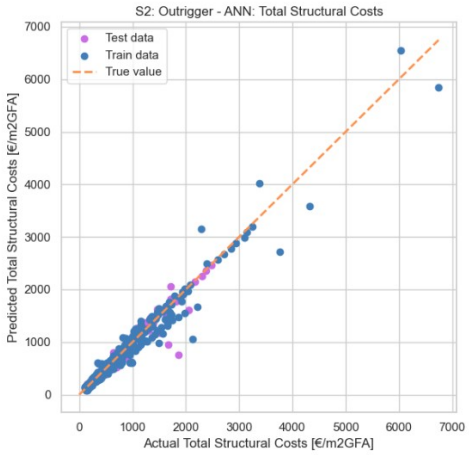


**(a)** Actual vs prediction values ANN

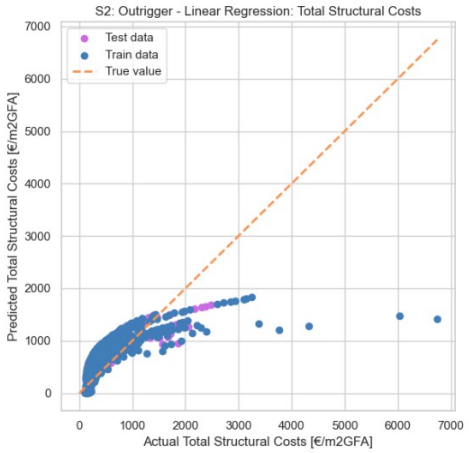


**(b)** Actual vs prediction values Linear Regression

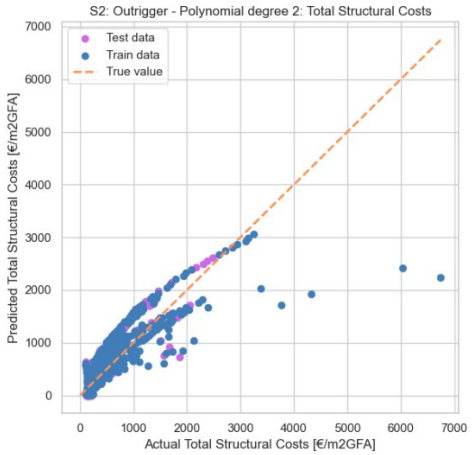


**(c)** Actual vs prediction values 2nd Order Regression

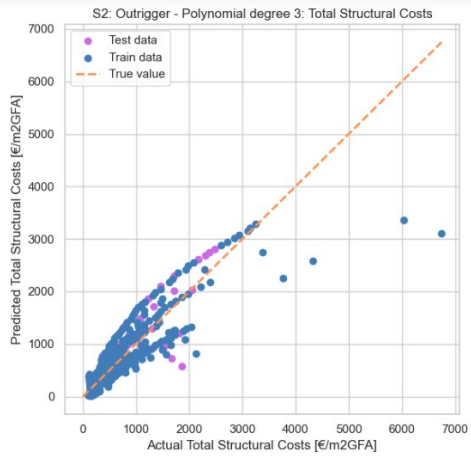


**(d)** Actual vs prediction values 3rd Order Regression

**Figure 6.28:** Actual vs prediction values of construction costs for S2 with different regression models

| *S2: Outrigger System* | | **Observation** |
|---|---|---|
| **Curve Fitting Models** | *ANN* | The ANN model has a significant high accuracy. Accuracy decreased slightly as total costs increased. |
| | *First Order* | Tendency for overestimation at lower costs values, and significant underestimation at higher cost values. |
| | *Second Order* | Similar trend as for the first order but to a lesser extent. |
| | *Third Order* | Same trend as second order and first order, but to a lesser extent. |
| **General** | | Accuracy of the ANN is significantly the best. |
| | | The observed behavior in the scatter plots aligned with the insights from the probability density distribution. |

**Table 6.17:** Observations from the scatter plot of different regression models for S2

#### Difference Accuracy Braced Framed Tube and Outrigger

The difference in accuracy in terms of the RMSE between the braced framed tube (RMSE = 38.9 kg/m$^2$GFA) and the outrigger system (RMSE = 29.1 kg/m$^2$GFA) can be attributed to the difference in sample size. The data set for the braced framed tube consisted of 246 samples, whereas the outrigger system data set consisted of 654 samples. Generally, a larger data set allows for more accurate training of neural network models. Additionally, the higher difference in accuracy when comparing the values of the MAPE for the braced framed tube (MAPE = 14%) and the outrigger system (MAPE = 7%) can be better understood by examining the definition of the MAPE. The MAPE is determined by comparing the predicted total mass to the actual total mass. Notably, the outrigger system has, on average, a higher mass due to its combination of concrete and steel, whereas the braced framed tube system consists solely of steel. The average total mass of the braced framed tube was found to be 146.2 kg/m$^2$GFA and the average total mass of the outrigger system was 250.2 kg/m$^2$GFA. Consequently, even if both systems have the same RMSE value, the MAPE will be lower for the outrigger system. This outcome results from the higher total mass, leading to a smaller error-to-mass ratio and, consequently, a relatively lower MAPE.

### 6.2.5. Computational Time

The total computational time required to capture the final output can be divided into two phases: the initial computational time for model creation and the ongoing time required for result generation. The initial computational time for model creation is a one-time investment, while the time required for result generation is occurring for each iteration. To assess whether the artificial neural network models save computational time, both aspects have been examined for either the neural networks as well for the parametric model.

#### Time for Model Creation

The artificial neural network models required a significant initial investment in terms of time since it was built based on data sets generated by parametric models. So besides modelling the neural networks, also the parametric models had to be modelled. The total initial time required for the creation of the neural networks, before outputs can be generated, was determined by looking at the different tasks outlined in the section of Approach in Chapter 1. An overview of the computational efforts for each of the tasks, which can be understated as the tasks required in the initial investment and creation of the needed models, is presented in Table 6.18. Additionally, the total initial computational time for the parametric model is included in the table, which only consisted of the first task as no further data generation or model creation is needed. There was no time for the model creation when looking at the analytical method, regarding the traditional way of calculating a structure.

| Method | | Explanation | Time | Total Time | Prerequisite |
|---|---|---|---|---|---|
| **ANN Model** | *Task 1* | Parametric model development | 2 weeks | 4 weeks | Familiar with software GH |
| | *Task 2* | Data generation | 1 week | | (-) |
| | *Task 3* | ANN development | 1 week | | Familiar with ML |
| **Parametric Model** | *Task 1* | Parametric model development | 2 weeks | 2 weeks | Familiar with software GH |
| **Analytical** | (-) | No model creation needed | (-) | (-) | (-) |

**Table 6.18:** Overview of time for model creation for ANN and parametric model

### Time for Output Generation

The additional initial computational time required for the neural networks compared to the parametric model needed to be compensated to justify their creation. The time saved with neural networks was in the final phase of the result generation. After training the neural networks, it only took a second to produce an output, significantly faster than with parametric models. In contrast, running the parametric models required between 5 to 30 minutes for both braced framed tube and outrigger system to generate a single output, depending on the scale of the structure. Comparing multiple structures with varying volumes for both stability frameworks could easily extend this time to several hours. Utilising neural networks for comparison significantly reduced this required time, as generating an output took less than a second. Outputs were immediately provided by the neural networks.

| Method | | Explanation | Time |
|---|---|---|---|
| **ANN Model** | *Task 4* | Prediction and visualization | 1 second per iteration |
| **Parametric Model** | *Task 2* | Prediction and visualisation | 5 - 30 minutes per iteration |
| **Analytical** | *Task 1* | Calculation of model | 0.5 week per iteration |

**Table 6.19:** Overview of time for output generation for ANN and parametric model

The break-even point for the number of iterations, where after it became more advantageous for the ANN models, was reached at 120, illustrated in Figure 6.29. This was based on an average durations of 20 minutes per iteration for the parametric model. To provide a more clear perspective, an average of three to four iterations are needed per structure for different geometry variations. This is only considering the structural point of view, however other disciplines such as building physics, cities, facade design and sustainability can also benefit from generating multiple models per project. Therefore, the 120 iterations will be reached after approximately 5 projects if two stability frameworks are compared in the design phase and three disciplines are involved ($120/(3 * 4 * 2) = 5$). For further context, a engineering company, such as Buro Happold, can be considered, which is assumed to handle around 20 high-rise buildings projects per year. Consequently, it can be concluded that it will take around 3 months before the neural network becomes less time-consuming in terms of total computational time. Moreover, a significant advantage of the neural networks is that, during this period, the actual data from real-life projects can be reused as input for the neural network. Over time, the neural networks can capture and learn from real-life data, a capability that the parametric model lacks.

**Figure 6.29:** Initial and output generation time (total computational time) for different methods

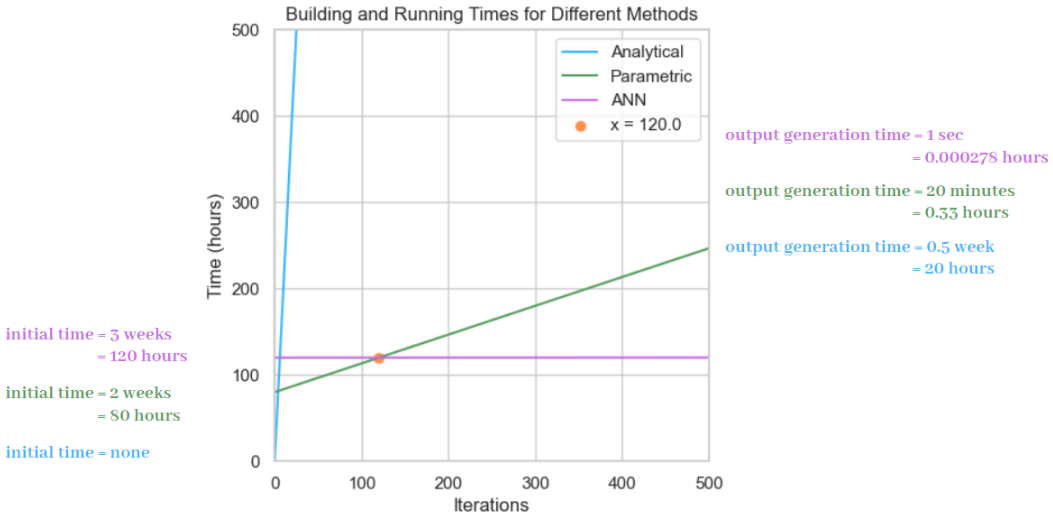


## 6.3. Impact of Stability Framework

The impact of the stability framework was assessed in terms of its contribution of embodied carbon to the total embodied carbon of the structure, including both superstructure (the main-load bearing elements) and the floors. The embodied carbon refers to the raw carbon emission from the structure during the considered life-cycle. The embodied carbon is one step prior to the environmental costs since the environmental costs are calculated based on multiplying the embodied carbon with the shadow price per kg $CO_2$-equivalent. The total embodied carbon is defined as both the embodied carbon coming from the gravity framework and the stability framework. Table 6.7 from Section 6.2.3 gives an overview of the division for the braced framed tube and outrigger system which structural elements are part of the stability or gravity system.

The embodied carbon from the total structure was determined based on the output from the parametric models, with width ranges of 15 to 60 meters and height ranges of 48 to 300 meters. The data from the parametric models was used since the accuracy of the neural networks S1-B and S2-B was considered to be not sufficient enough since the MAPE of S1-B ranged from 5% to 35% and MAPE of S2-B ranged from 2% to 53%. The data from the parametric models was categorized into subsets, each representing a height difference of 50 meters. The results are visualized using box plots, with the median value provided, see Figure 6.30 for braced framed tube and Figure 6.31 for the outrigger system. The median percentage contribution of the stability framework for braced framed tube ranged from 25% to 57%, and for outrigger system, it varied between 33% and 66%. This data illustrated the significant role of the stability framework for both systems in the total impact of the structure, which included both the stability and the gravity framework. Moreover, it can be seen that the relative impact of the stability framework, compared to the impact of the gravity framework, was increasing with the height of the structure. This trend was expected, as the stability requirement of a structure becomes more governing as the slenderness of the building is increasing.

**Figure 6.30:** Box plot of share of EmCO2 of stability framework S1 relative to total EmCO2

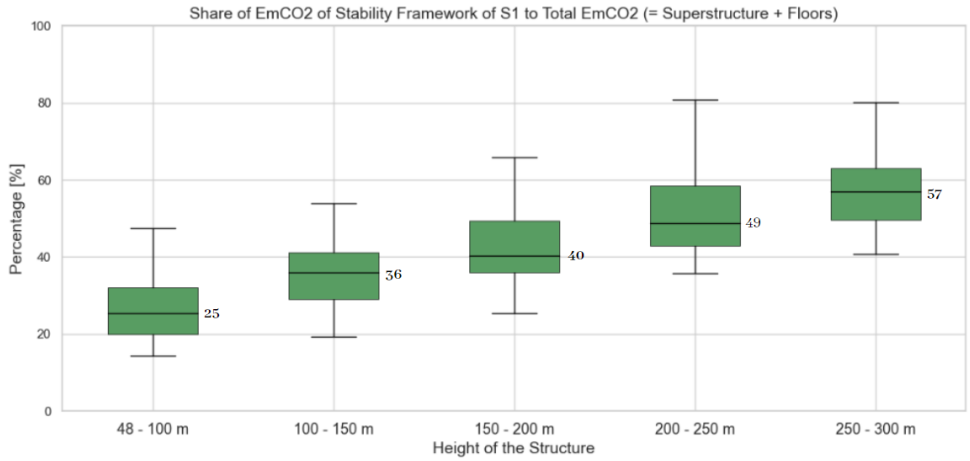


**Figure 6.31:** Box plot of share of EmCO2 of stability framework S2 relative to total EmCO2

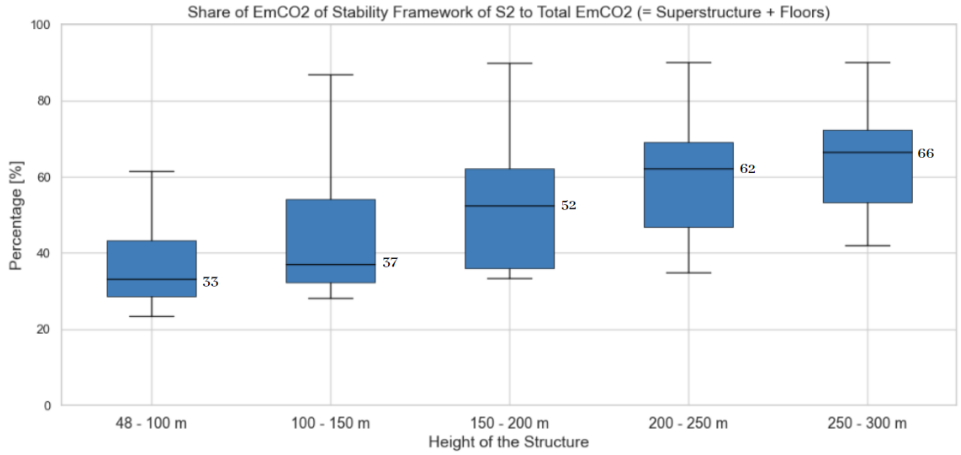


### 6.3.1. Impact of Choosing the Best Performing Framework

In addition, the impact of selecting the optimal stability framework, either braced framed tube or outrigger system, and the potential gains from such a choice was examined. This was achieved by calculating the absolute difference in embodied carbon between both systems for each specific input data based on the predictions from the neural networks, which ranged again from 15 to 60 meters in width and 48 to 300 meters in height. Next, the ratio between the absolute difference in embodied carbon and the total embodied carbon of the worst performing structure was determined. This ratio highlighted the potential benefits of choosing the best performing stability framework. This ratio is visualised in Figure 6.32 using box plots. The total embodied carbon was based on the summation of the superstructure and the floor system. Looking at the ratios, they ranged from 7% to 18%. For lower heights, the difference between both systems was already observed to be small, see for example Figure 6.18. However, due to the relatively low total impact, even minor gains were significant in lower subsets. As the structure height increased, the difference between stability systems expanded more rapidly than the total impact of the structure, resulting in slightly higher percentage gains for middle subsets. For the tallest structures (250 to 300 meters), the relative gain decreased, which can be explained due to a higher relative increase of the total impact than of the relative increase of the difference between both systems. It should be noted that only the values of gains were considered when both stability frameworks were feasible. Since the braced framed tube could not exceed a slenderness of 11, the outrigger system was capped for the structures with slenderness exceeding 11.

**Figure 6.32:** Box plot of potential gain of best performing stability system in terms of embodied carbon

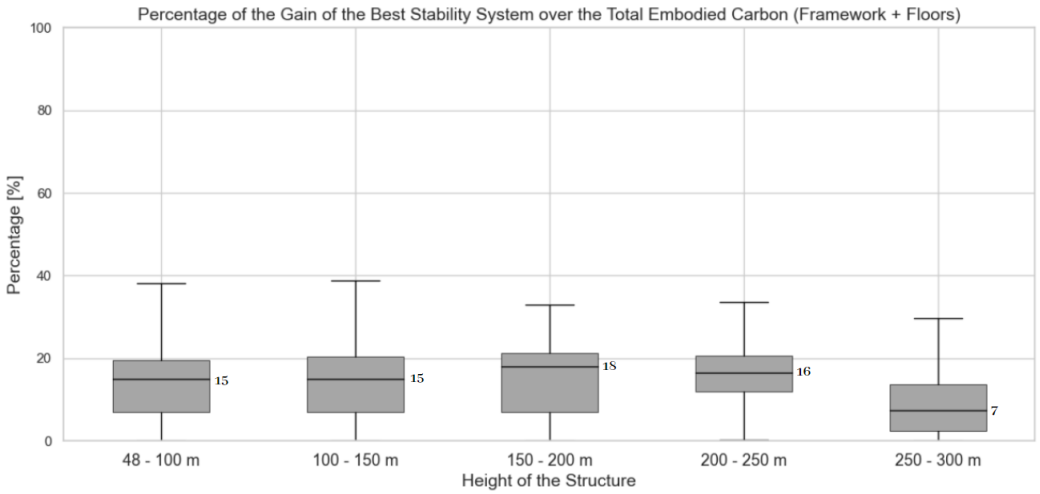


## 6.4. Comparison with Literature

In this research, the performance of stability frameworks (braced framed tube and outrigger system) was investigated using data sets of optimised structures from both frameworks. The predicted values based on the neural networks were compared with real-world projects. It was found that there is limited literature about the impact of high-rise structures, which is the emphasis of this research. Values regarding the impact of high-rise buildings were found in studies by Rock, M. and Sorensen, A. (2022), Oldfield (2012), and Trabucco (2016) [53] [54] [55].

To enable meaningful comparisons, it was essential that values found in literature aligned with the scope of the neural networks. Thus, the focus was on the Cradle-to-Gate (A1-3) life cycle assessment stages. Furthermore, only the lateral-load bearing structures and floors were considered, while aspects such as foundations, envelopes, internal components, services, and appliances, which were not factored into the neural networks, were excluded from the comparison. The results of the comparison between the found values in the literature and the predicted values based on the neural networks are presented in Table 6.20.

- **Study A: Rock (2022)**
  In a comprehensive study conducted by Rock, M. and Sorensen, A. (2022) (referred to as Study A), 769 life cycle assessment (LCA) studies on buildings from five different EU countries were compiled [53]. Among these, only one building met the criteria for a steel frame and could be quantified as a high-rise building. This building consists of 27 storeys and had a total GFA of 64,762 $m^2$. Study A captured an embodied carbon impact of 161 $kgCO_2eq/m^2GFA$. The impact of the embodied carbon was defined as the load-bearing system including the floors. The comparison between real-life projects and the neural network is detailed in Appendix G in Section G.1.

  The neural network of the braced framed tube, based on the same input parameters as the real-life project, predicted a value of 117 $kgCO_2eq/m^2GFA$, reflecting a decrease of 28%. The difference can be attributed to the different stability systems. The prediction was made based on a braced framed tube, whereas the actual stability framework of the building is a steel frame.

- **Study B: Oldfield (2012)**
  In a 2012 study by Oldfield (referred to as Study B), a LCA was conducted on the 41-story office building, known as 30 St. Mary Axe, in London [54]. This building stands at 180 meters tall and has a gross floor area (GFA) of 64,469 $m^2$. The study calculated the building's embodied carbon at 226 $kgCO_2eq/m^2GFA$, taking into account only the structural superstructure and floor system

from stages A1 to A3. A more detailed explanation of the conversion of the embodied carbon value from the study for comparison is presented in Appendix G in Section G.1.

For comparison, a 180-meter braced framed tube structure was examined, where the GFA is higher due to the neural network being based on a lower floor-to-floor height of 3 meters, resulting in more storeys and thus a higher GFA, equal to 64,469 $m^2$. The neural network predicted an embodied carbon value of 285 $kgCO_2eq/m^2GFA$, which is higher than the obtained impact of St. Mary Axe from Study B. The difference may be attributed to the varying architectural designs, as the neural network was based on a fully rectangular structure, unlike the shape of St. Mary Axe. Moreover, another possible reason for the difference can be the different wind load requirements in England relative to wind load requirements of the Netherlands were the neural network is based on.

- **Study C: Trabucco (2016)**
  A third comparison was conducted with the 60-story models from the research of the Council of Tall Buildings and Urban Habitat (CTBUH), by Trabucco [55]. These models have a GFA of 141,600 $m^2$ and are 246 meters in height. Two models were particularly highlighted for comparison: the steel diagrid system and the concrete core with steel frame system. The all-steel diagrid model by Trabucco has an embodied carbon impact of 285 $kgCO_2eq/m^2GFA$, while the 246-meter steel braced framed tube model from this research was predicted to have an impact of 269 $kgCO_2eq/m^2GFA$.

  Similarly, the impact of Trabucco's concrete core with steel frame model is 236 $kgCO_2eq/m^2GFA$, compared to the outrigger system of this research, which was predicted at 252 $kgCO_2eq/m^2GFA$. The observed differences could be attributed to the difference in stability framework, as the concrete core and steel frame represent a different approach compared to the outrigger system. Trabucco's concrete core and steel frame model was selected for comparison as it most closely resembled the stability framework of the outrigger system.

- **Study D: MIT (2024)**
  Furthermore, a comparison was done between the study of MIT Building Technology Program and the Circular Engineering for Architecture (CEA) lab (referred to as Study D) and the neural networks based on the same input data, detailed in Section G.2 of Appendix G [56]. Study D conducted comparisons based on subsets of buildings categorized by the number of stories and floor area, utilising box plots to illustrate statistical measurements. For structures ranging from 11 to 50 stories, the neural networks consistently predicted lower embodied carbon values. However, comparisons for structures with 51 to 100 stories showed significant differences due to the small sample size in the database of Study C and the inclusion of economically and environmentally unfavorable high-slenderness structures in the ANN models. Similar trends were observed in comparisons based on different floor areas.

  To address outliers caused by high-slenderness structures in the neural network's data set, an upper limit on slenderness (set at 11) was implemented for comparison. The revised comparisons still showed significant differences, but it was concluded that setting an upper limit on slenderness in the neural network's data set helped align predictions more closely with real-life scenarios. For structures ranging from 11 to 50 stories it was found that the relative difference of the median was equal to -64%, for the subset 51 to 100 stories the relative difference of the medias was equal to -43%. Similarly, in floor area subsets ranging from 1000 to 10,000 $m^2$, 10,000 to 100,000 $m^2$, and above 100,000 $m^2$, the relative differences in median values were found to be -57%, -63%, and -47%, respectively.

  The significant difference between Study D and the neural networks might be because Study D's data set included all sorts of materials and building types, including concrete. In contrast, the neural network was trained only on the primary material of steel. Comparing Study D to the neural networks was challenging due to the lack of transparency in Study D's data compilation. It could not be seen which buildings and structures the subsets consisted of, and therefore a meaningful comparison was difficult to make.

| **Study** | **System** | **Height** [m] | **Width** [m] | | **GFA** [$m^2$] | **Em$CO_2$** [$kgCO_2eq/m^2GFA$] |
|---|---|---|---|---|---|---|
| A | Steel Frame | 81 | 49 | *Study* | 64762 | 161 |
| | | | | *ANN: S1* | 64762 | 117 |
| B | Steel Diagrid | 180 | 40 | *Study* | 64469 | 285 |
| | | | | *ANN: S1* | 96000 | 226 |
| C | Steel Diagrid | 246 | 49 | *Study* | 141600 | 285 |
| | | | | *ANN: S1* | 196882 | 269 |
| C | Concrete Core + Steel Frame | 246 | 49 | *Study* | 141600 | 236 |
| | | | | *ANN: S2* | 196882 | 252 |

**Table 6.20:** Comparison calculated impact from literature with predicted impact of ANN

# 7

# Discussion

In this chapter, the focus lies within answering the main question by exploring the ability of predicting the best stability framework, in terms of either structural or environmental costs, based on the input geometry of the structure. The analysis consist of examining the outcomes of the 'Data Collection' phase and the subsequent 'Modelling Procedure' step. Their alignment with the Theoretical Framework is assessed to address the main research question, which is restated below:

**'How can the performance parameters for different stability frameworks of a high-rise steel building with different volumes be predicted based on its design characteristics in a machine learning approach to accelerate the decision process?'**

To address the main research question, the results from both the parametric models as from the artificial neural network (ANN) models are discussed. The results regarding the development and the optimisation of the ANN models are examined. Lastly, the performance of the ANN models regarding other curve fitting methods in terms of accuracy is discussed. The discussion concludes by reflecting on the influence of those insights on the decision-making processes when designing a structure.

### Analysis of Parametric Model

The findings from the parametric models of both braced framed tube and outrigger system demonstrated that the relationship between performance in terms of costs of the structure and the input geometry behaved similarly for both stability systems. As buildings increased in height, structural and environmental costs per $m^2$ Gross Floor Area ($m^2$GFA) also rose. The performance in terms of costs (both structural and environmental) was calculated based solely on the mass of the structural elements. The graph representing the costs of the braced framed tube and the outrigger system over an increasing height or width did not reveal a clear relationship or offer a robust comparison. A non-linear relationship was shown, where the relationship for the outrigger system was more complex than for the braced framed tube. For the braced framed tube the maximum reachable slenderness (height-to-width ratio) was found to be 11.67 and for the outrigger system to be 12.50. Higher slenderness was not feasible within the cross-section ranges predetermined in the parametric models. For both system, it failed to meet stiffness requirements beyond the maximum slenderness ratio. The visualisation of data sets showed a parallel relationship between structural and environmental costs for both systems. The approximate slope was 62 €/$m^2$ over the total height range of 50 to 300 meters. Changes in environmental costs had proportional structural cost adjustments across both stability systems.

### Analysis of ANN Model Development and Optimisation

The results of the analysis of the neural networks can be separated into the results regarding the neural network model development and the optimisation of the neural networks.

- **Model Development.**
  The neural networks of both stability frameworks were developed and trained based on the obtained data sets from the parametric models. These parametric models provided data sets containing the total mass of structures, where column and beam dimensions were optimised for

minimal mass. The neural networks were trained based on this total mass information, resulting in predictions for the overall mass of the structure. Additionally, separate neural networks were created to predict the mass of individual structural elements within the overall structure. These element-specific networks were trained using the masses of each component. However, rather than summing up the predicted masses of individual elements to obtain the total structure mass, it was decided to avoid error accumulation by keeping these predictions separate.

- **Model Optimisation.**
  - **Genetic Algorithm.**
    It was found that genetic algorithm was a sufficient method to use for the optimisation of the hyperparameter configurations for the ANN models. For all the four ANN models, the genetic algorithm was able to find the best configuration of the hyperparameters for each specific neural network. Different configurations were found for each of the four ANN models, aligning with literature recommendations that the optimal ANN architecture is specific to each data set and model.
  - **Optimum ANN.**
    The results showed that the use of Back Propagation and Gradient Descent were sufficient methods for training the ANN models. By analyzing training and validation loss over 10,000 epochs for both stability systems, optimal weights and biases were identified. The convergence graphs indicated stable model states without underfitting or overfitting.

### Analysis of Accuracy of ANN Model

The objective of the neural network of the braced framed tube was to predict the total mass of the steel, where the masses are convertible to structural and environmental costs. The objective of the neural network of the outrigger system was to predict the combined total mass of the steel and concrete. The results from the neural networks, presented in Table 7.1, indicated that the neural networks of both braced framed tube and outrigger system gave sufficient accuracy in approximation of the data bases; RMSE of 14% and 7% respectively. The assessment was based on two key metrics: Root Mean Squared Error (RMSE) and Mean Absolute Percentage Error (MAPE).

| | | | **Braced Framed Tube** | **Outrigger System** |
|---|---|---|---|---|
| | | | **S1-A** | **S2-A** |
| *Objective* | Prediction of mass | | Steel | Steel<br>Concrete |
| *Results* | Sample size | [-] | 246 | 654 |
| | RMSE | [kg/m$^2$GFA] | 38.9 | 29.1 |
| | MAPE | [%] | 14 | 7 |

**Table 7.1:** Overview of the objective and results of the neural networks

The neural network of the braced framed tube considered only one variable (steel mass), where the neural network of the outrigger system accounted for both steel and concrete mass (due to the concrete core as part of the stability framework). Despite the additional complexity in modeling the outrigger system, a higher accuracy was found for the outrigger system compared to the braced framed tube. A possible reason is the larger sample size of the outrigger system (n = 654) compensating for its modeling difficulty compared to braced framed tube (n = 246).

### Comparison of ANN Model with other Regression Models

The accuracy and predictive performance of the neural networks were compared with other curve fitting models, including first order, second order, and third order, to evaluate their relative effectiveness. The accuracy of the neural networks of both the braced framed tube and the outrigger system was found

to be the most precise model compared to all the other curve fitting models, see Table 7.2. The results showed the superiority of the neural networks by the quantification of lower RMSE and MAPE values, and visually confirmed through scatter plots comparing actual versus predicted values (Chapter 6 for Section 6.2.4).

| **Metric** | **Curve Fitting Methods** | **Braced Framed Tube** | **Outrigger System** |
|---|---|---|---|
| | | **S1-A** | **S2-A** |
| *MAPE [%]* | First Order | 49 | 67 |
| | Second Order | 38 | 41 |
| | Third Order | 25 | 31 |
| | Artificial Neural Network | 14 | 7 |

**Table 7.2:** Overview of accuracy of different curve fitting methods

### Analysis of Results based on ANN Model

The results showed that the best performing framework was a function of specific width and height combination. For each specific combination of width and height, a different optimal stability framework was found, looking at either structural or environmental costs. An overview of the best stability framework in terms of structural costs is presented in Table 7.3 and in terms of environmental costs is presented in Table 7.4.

| | | Width [m] | | | | |
|---|---|---|---|---|---|---|
| | | 10 | 20 | 30 | 40 | 50 |
| Height [m] | 50 | *Braced Tube* | Outrigger | Outrigger | Outrigger | *Braced Tube* |
| | 100 | *Braced Tube* | Outrigger | Outrigger | Outrigger | Outrigger |
| | 150 | (-) | Outrigger | Outrigger | Outrigger | Outrigger |
| | 200 | (-) | *Braced Tube* | *Braced Tube* | *Braced Tube* | Outrigger |
| | 250 | (-) | (-) | *Braced Tube* | Outrigger | *Braced Tube* |
| | 300 | (-) | (-) | *Braced Tube* | *Braced Tube* | *Braced Tube* |

**Table 7.3:** Overview of best framework in terms of structural costs based on ANN models

| | | Width [m] | | | | |
|---|---|---|---|---|---|---|
| | | 10 | 20 | 30 | 40 | 50 |
| Height [m] | 50 | *Braced Tube* | Outrigger | *Braced Tube* | *Braced Tube* | *Braced Tube* |
| | 100 | *Braced Tube* | Outrigger | Outrigger | Outrigger | Outrigger |
| | 150 | (-) | *Braced Tube* | *Braced Tube* | Outrigger | Outrigger |
| | 200 | (-) | *Braced Tube* | *Braced Tube* | *Braced Tube* | Outrigger |
| | 250 | (-) | (-) | *Braced Tube* | *Braced Tube* | *Braced Tube* |
| | 300 | (-) | (-) | *Braced Tube* | *Braced Tube* | *Braced Tube* |

**Table 7.4:** Overview of best framework in terms of environmental costs based on ANN models

### Impact of Stability Framework

The impact of the stability framework is defined as the contribution in terms of embodied carbon to the overall embodied carbon of a structure, which includes both the superstructure and floors. Embodied carbon is one step prior to environmental costs, since the value is not yet multiplied with the shadow price of $CO_2$-equivalent. Specifically, the stability framework's role is to provide lateral stability to the building. For the braced framed tube system, the stability framework's relative impact ranged from 25% to 57%. For the outrigger system, the relative impact varied between 33% and 66%. The actual percentage depended on the height of the building. As the building height increased, the stability framework's influence on embodied carbon became higher. The substantial impact of the stability framework underscores its importance in determining the overall embodied carbon of a structure. Moreover, it

was found that selecting the optimal stability framework can lead to a potential reduction in embodied carbon. The potential gain ranged from 7% to 18%. This gain is calculated as the ratio between the absolute difference in total embodied carbon between the braced framed tube and the outrigger system, divided by the total embodied carbon of the worst-performing stability framework.

### Accelerating Decision-Making Processes

The parametric model took approximately 5 to 30 minutes per output, depending on the scale of the structure. When evaluating multiple structures with varying volumes, this time extended to several hours. While the parametric model provided valuable results, its output generation time was relatively slow. In contrast, the output generation for the neural networks was merely a second. The neural networks offered a dramatic reduction in output generation time. This speed advantage enabled instant comparisons between the different structural frameworks of the braced framed tube and the outrigger system. However, the setup time for neural networks was longer than that for parametric models. Neural networks were constructed based on data sets generated by the parametric model. Despite this initial setup time, after 120 iterations, the neural networks became more advantageous over the parametric model. For typical structures, three to four iterations of different dimensions of the structure are needed per stability framework when considering the structural point of view. An engineering company handling 20 high-rise building projects annually, with multiple disciplines involved each project, would require approximately 3 months for the neural networks to become less time-consuming. Regarding the possibilities within the neural networks, the results showed the possibility of interpolation between the heights and grid sizes, and was thus not limited by the input data ranges, unlike parametric models. Furthermore, integrating real-life data into the neural network's input data set is possible, enabling predictions in the early design phase to learn from real-life projects and improve accuracy and link to reality.

In summary, the study has shown that an artificial neural network can effectively predict the best stability system for high-rise steel buildings. While the findings are specific to the braced framed tube and outrigger system, the method proposed offers an accurate and fast way to compare stability systems during the initial design stage. This validated approach can be easily adapted to other stability frameworks and shapes by expanding the parametric model, by including different stability systems, different materials and different shapes, and increasing the input data for the artificial neural network models. Additionally, data from real-life projects can be integrated in the input data sets to link the neural network directly to actual data of costs of buildings. The integration of artificial neural network models as predictive models into the design workflow has the potential to improve the efficiency and to promote cost-effective and sustainable design solutions.

# 8

# Conclusion & Recommendations

## 8.1. Conclusion

In the early design phase, designers and clients aspire to compare multiple structural designs, considering both different stability frameworks and variations in geometry. Unfortunately, the current process of evaluating multiple designs is time-consuming. To address this challenge, predictive models can be used to estimate performance in terms of structural and environmental costs based on the given geometry. These models rely on the established relationship between performance and input geometry where the established relationship is depending on the used predictive model. Traditional curve fitting methods, such as polynomial regression models, often fall short in accurately predicting a complex non-linear relationship. Therefore, in this research the potential of artificial neural network was examined as an alternative. It was found that the artificial neural network is able to accurately predict structural and environmental costs based on the input geometry. The artificial neural network outperforms the current design evaluation process in terms of time and outperforms other curve fitting models in terms of accuracy. The conclusions from this research are elaborated below:

- **An artificial neural network gives enough accuracy in approximation of the data base.**
  The artificial neural network for the braced framed tube, which predicted the total mass of steel, demonstrated high accuracy with a Mean Absolute Percentage Error (MAPE) of 14%. Similarly, the neural network model for outrigger system, which predicted the total mass in terms of both steel and concrete, also showed high accuracy with a MAPE of 7%. When looking at the absolute value of the RMSE, a trend was observed where predictions for lower values (heights from 50 to 200 meters) had lower errors in terms of RMSE compared to predictions for higher values (heights from 200 meters). The neural network of the braced framed tube had the small tendency ($\mu$ = 3.5% ) to rather overestimate the costs, whereas the neural network of the outrigger system had rather the very small tendency ($\mu$ = -1.0%) to underestimate.

  *See for a more detailed explanation Chapter 6 for Section 6.2.4.*

- **The artificial neural network significantly outperforms the curve fitting methods in terms of accuracy.**
  The artificial neural network models for both braced framed tube and outrigger system demonstrated lower errors compared to the curve fitting models of the first, second, and third order regression models. For the braced framed tube, the neural network's MAPE was found to be 14%, whereas the most accurate alternative curve fit, the third order, had a MAPE of 25%. For the outrigger system, the neural network's MAPE was 7%, while the most accurate curve fit, again the third order, had a significantly higher error with a MAPE of 31%, indicating its inability to approximate the database effectively.

  *See for a more detailed explanation Chapter 6 for Section 6.2.4.*

- **An artificial neural network is significantly faster in generating results than a parametric model, but needs more model setup time.**
  The artificial neural network model significantly reduced output generation time to just one second per iteration, compared to the parametric model, which took up to 30 minutes. However, the setup time for ANN models was longer because they were constructed based on data sets generated by the parametric models. When considering the total time required for both parametric and neural network approaches, the neural network model became more advantageous after 120 iterations. Typically, three to four iterations are needed per stability framework for different geometry variations. Therefore, when comparing two stability frameworks, it would take approximately five projects or about three months for an engineering company handling 20 high-rise building projects annually with multiple disciplines for the artificial neural network model to become less time-consuming overall.

  *See for a more detailed explanation Chapter 6 for Section 6.2.5.*

- **The best performing framework is a function of specific width and height combination, and differs for structural and environmental costs.**
  The optimal stability framework for structures depends on specific combinations of width and height. When considering structural costs, the outrigger system was more efficient up to a height of 150 meters for a 20-meter width, while the braced framed tube becomes optimal beyond that height. For a 30-meter width, the outrigger system performs better between 50-155 meters, and the braced framed tube dominates between 155-300 meters. Similarly, for widths of 40 meters, the outrigger system is preferable within specific height ranges of 50-190 and 210-255 meters and for widths of 50 meters, the outrigger system is preferable within the ranges of 80-230 meters. The results indicate that the braced framed tube is the optimal stability system for the lowest and highest heights, whereas the outrigger system dominates in the middle section. However, when assessing environmental costs, the braced framed tube was found to more optimal for the middle section of heights. In summary, each specific combination of width and height leads to a different optimal stability framework for either structural or environmental costs.

  *See for a more detailed explanation Chapter 6 for Section 6.2.3 and Chapter 7 for Table 7.3 and Table 7.3.*

- **The relative contribution of embodied carbon from the stability framework ranges from 25% to 57% for braced framed tube and 33% to 66% for outrigger system as part of the total embodied carbon of the structure.**
  The impact is defined as the relative contribution of embodied carbon of a specific part to the total embodied carbon of the structure. The impact of the stability framework, as a part of the total structural framework (superstructure and floors), was found to range from 25% to 57% for the braced framed tube and 33% to 66% for the outrigger system, where the impact increased with the building's height. This significant contribution underscored the influence of the horizontal force (wind load) compared to the vertical force, so the influence of the stability framework to the gravity framework.

  *See for a more detailed explanation Chapter 6 for Section 6.3.*

- **The potential gain in terms of less impact of the best stability framework ranges from 7% to 18%.**
  The potential gain from selecting the optimal framework, defined as the ratio of the absolute difference in embodied carbon between braced framed tube and outrigger system to the total embodied carbon of the structural framework, was found to range from 7% to 18%, where the lowest impact of 7% was found for the highest height range of 250 to 300 meters and the highest impact of 18% was found for the middle height range of 150 to 200 meters.

  *See for a more detailed explanation Chapter 6 for Section 6.3.1.*

## 8.2. Limitations

While this research provided valuable insights, several limitations should be noted:

- **Relative small sample size.** The creation of the data set for training the ANN models required considerable time and resources. Especially for the model of the braced framed tube, the data set was rather small (n = 246), where the data set of the outrigger system was significantly bigger (n = 654). By establishing a bigger data set for the braced framed tube, the ANN model can be trained based on more data points, and therefore will likely reach a higher accuracy. So expand the data set used for training the ANN models to improve the accuracy of the ANN models, with the emphasize on the braced framed tube.

- **Assumption of wind force.** This study assumed a structural factor ($c_s c_d$) of 1.1, which is a parameter in calculating the wind force. The structural factor accounts for the impact of non-simultaneous peak wind pressures on the surface and the structure's vibration due to turbulence. This assumption of a constant value of 1.1 does not hold true under all conditions, as the structural factor can vary based on factors such as the building's design, location, and local weather conditions. Future research could consider a variable structural factor to see the effect on the accuracy of the wind force estimation.

- **Foundation not considered**. The research primarily focused on the load-bearing structure of high-rise buildings, overlooking the foundation's impact on building performance in terms of structural and environmental costs. Future studies could incorporate foundation considerations for a more comprehensive assessment. The influence of including the foundation remains somewhat unpredictable. Lighter structures would require a less substantial foundation, leading to a decreased relative impact. Consequently, the outrigger system (a combination of steel and concrete) might become less favorable compared to the braced framed tube, given the found higher average mass of the outrigger system compared to the braced framed tube . On the other hand, the rotational stiffness of the foundation significantly shapes tall building design. Therefore, it could be argued that the foundation may be relatively consistent across different stability frameworks. Moreover, the building parts of the envelope, internal, services and appliances were also not considered in this research. The contribution of these building parts to the comparison of the stability frameworks can also be investigated.

- **Limited LCA scope.** The life cycle assessment considered only stages A1-3 in this research, leaving out the following stages (A4-D) which would result in a better overview of the environmental impact across the building's entire life cycle.
  - **Exclusion of construction phase: A4-A5.** The impact of transportation is project-specific, closely tied to supplier choices. Predicting the influence of construction remains challenging due to various factors and project-specific considerations. While the construction phase does not significantly affect the overall environmental impact, it is most likely that it will have an equalising effect on the gap in impact between braced framed tube and outrigger system.
  - **Exclusion of demolition phase: C1-C4.** The end-of-life phase was excluded from the scope of this research since demolition of high-rise buildings above 150 meters is rare. In the case that demolition of high-rise buildings would be considered possible and desirable, the highest use of the material steel would most likely become the most favourable due to its high recycling and reuse potential in comparison with concrete. However, it is more desirable to focus on extending the building's lifetime instead of demolition and reconstruction of the building.

- **Assumption structural and environmental costs**. This research assumed that the structural and environmental costs are solely dependent on the mass of the materials used. However, this simplification did not capture the full picture. This assumption is in line with the considered stages of the LCA of A1-3. The total structural and environmental costs of a structure are influenced by a variety of factors besides material quantity. These could include the energy used in material

production and transportation, the costs of different connections between elements, the lifespan and maintenance costs of the materials, and the recycling or disposal impacts at the end of the building's life. All these factors are taken into account when the total LCA is considered, so stages A till D.

- **Rectangular floor plans.** The methodology of this research was limited to rectangular floor plans. Future research could explore the incorporation of diverse floor plan geometry to increase the potential of usability even more for real-life projects.

- **Constant slenderness over building height.** This research focused on structures where the slenderness, or the ratio of the height to width, remained constant throughout the building. The floor plan stayed consistent over the total height of the building. This limitation meant that the findings are not applicable to buildings with varying slenderness or floor plans at different heights.

- **Constant floor system:** The current research considered only one type of floor system, namely the pre-stressed hollow-core slab. This limitation means that other floor systems, such as flat-slab floors and composite floors, are not taken into account. Expanding the scope to include a broader variety of floor systems could improve the scalability and usability of the ANN models.

## 8.3. Recommendations

To further improve the applicability of this research, the following recommendations are proposed:

- **Addition of more performance parameters**. In this research, the ANN models were limited to predicting the masses of structures, as the input was solely based on the masses of the materials. By expanding the input of the ANN models, the predicted output will also expand. The input of the ANN model depends on the data generated from the parametric model. Incorporating performance parameters, such as aspects of building physics like thermal performance and energy efficiency, into the parametric model alongside the masses of the structure, can expand the number of inputs for the ANN models. Consequently, further research can be done if the ANN models will also be capable of accurately predicting the newly incorporated performance parameters, such as thermal performance or energy efficiency.

- **Expand determination of structural and environmental cost.** In this research, the performance parameters of structural and environmental costs were solely based on the mass of the materials. There is potential to expand this approach by including additional aspects that influence the total costs of a structure. For instance, future research could investigate the impact of connections and their complexity on both structural and environmental costs. Additionally, the effect of column length could be considered, such as in cases where columns extend across multiple floors instead of just one. Further research can investigate if this will affect the comparison between the best performing stability frameworks.

- **Inclusion of more building types.** The current research included only two stability frameworks, namely the braced framed tube and the outrigger system. Future research could explore whether the performance of other types of buildings and structures can also be accurately predicted. For instance, stability frameworks such as the frame, tube, and diagrid could be considered. While this study focuses on steel as a material, structures that primarily use cast-in-situ concrete, precast concrete, or timber could also be included for investigation. Further research could examine the potential of incorporating a broader range of materials and investigate the performance of ANN models in predicting the optimal stability framework.

- **Integration of real-life projects.** Future research could explore the impact of incorporating data from actual high-rise building projects into the ANN models. In this study, the data sets utilised for the ANN models are exclusively generated from parametric models, without any real-life data. The effect of integrating such real-life data into the ANN models' input data set requires further

investigation.

- **Dimensions of structural core.** The size of the structural core is determined based on the analysis of four real-life high-rise buildings, which is a small sample size. Moreover, the slenderness of the core was in this research not linked to the slenderness of the building. Linking the slenderness of the core to the slenderness of the structure can improve the determination of the size of the core. The dimensions of the core significantly influence the performance of the outrigger system, as they determine the volume of required concrete. Future research could explore the optimal core dimensions for different structural sizes by increasing the sample size and relating the slenderness of the core with the slenderness of the structure. Moreover, it can be investigated how the core dimensions impact the performance of the outrigger system. This could, in turn, affect the comparison between different stability frameworks.

- **Sensitivity analysis of (shadow) prices.** A sensitivity analysis can be conducted to examine the shadow prices and material prices of concrete and steel. Shadow prices and material prices can fluctuate due to a variety of factors, such as the use of different material suppliers or concrete mix designs. This analysis would investigate whether an increase or decrease in the (shadow) prices of these materials corresponds to a similar change in the gap between the optimal stability framework.

- **Sensitivity analysis of network architecture.** The assumptions regarding the network architecture in this research were that the activation function of the hidden layer was the Rectified Linear Unit (ReLU), and the activation function of the output layer was the Linear function. Future research could investigate whether the accuracy and performance of the ANN models change when the activation function is changed, for example, to the logistic sigmoid or hyperbolic tangent functions. If a different activation function is chosen, it may be necessary to make a change in the optimisation technique. Furthermore, while the optimiser chosen for this research was Adam (a type of momentum optimisation), future studies could investigate whether different optimisers have varying effects on the accuracy and efficiency of the model.

# References


[1] R. Nijsse. *Dictaat Draagconstructies 2*. 2012.

[2] Mir M Ali and Kyoung Sun Moon. “Structural developments in tall buildings: current trends and future prospects”. In: *Architectural science review* 50.3 (2007), pp. 205–223.

[3] Rijksoverheid. *Bouwbesluit*. Available at: https://rijksoverheid.bouwbesluit.com/Inhoud/docs/wet/bb2012/hfd2. 2023.

[4] I. Shakir, M.A. Jasim, and S.S. Weli. “High Rise Buildings: Design, Analysis, and Safety: An Overview”. In: *International Journal of Architectural Engineering Technology* 8 (2021), pp. 1–13.

[5] M. H. Gunel and H.E. Ilgin. “A proposal for the classification of structural systems of tall buildings”. In: *Building and environment* 42.7 (2007), pp. 2667–2675.

[6] C. Sandelin and E. Budajev. *The Stabilization of High-rise Buildings: An Evaluation of the Tubed Mega Frame Concept*. 2013.

[7] *Zalmhaven: Hoogste Woontoren van de Benelux*. https://www.cementonline.nl/zalmhaven-hoogste-woontoren-van-de-benelux. Accessed: 23/08/2023.

[8] JCD Hoenderkamp and MCM Bakker. “Analysis of high-rise braced frames with outriggers”. In: *The structural design of tall and special buildings* 12.4 (2003), pp. 335–350.

[9] Hassan Haji-Kazemi and M Company. “Exact method of analysis of shear lag in framed tube structures”. In: *The structural design of tall buildings* 11.5 (2002), pp. 375–388.

[10] Vincent JL Gan et al. “Sustainability analyses of embodied carbon and construction cost in high-rise buildings using different materials and structural forms”. In: *HKIE Transactions* 24.4 (2017), pp. 216–227.

[11] J. Gerran Lankhorst et al. “Life Cycle Analysis: Load-Bearing Structures Of High-Rise Buildings in Western Europe”. In: *CTBUH Journal Issue III* (2019).

[12] Vincent JL Gan et al. “Developing a CO2-e accounting method for quantification and analysis of embodied carbon in high-rise buildings”. In: *Journal of Cleaner Production* 141 (2017), pp. 825–836.

[13] *Milieu Impact Categorieën*. Accessed on 2023-09-25. URL: https://milieudatabase.nl/nl/milieudata-lca/informatie-voor-lca-opstellers/milieu-impact-categorieen/.

[14] Consolis VBI. “EPD Kanaalplaatvloer 320”. In: (2020).

[15] Consolis VBI. “Productdatablad Kanaalplaatvloer 320”. In: (2024).

[16] SNS / Bouwen met Staal. “EPD Zwaar constructiestaal, 16% hergebruik einde leven”. In: (2022).

[17] Sarkisian M. *Designing tall buildings*. Routledgde, 2016.

[18] Nederlands Normalisatie-instituut. *NEN-EN1991-1-1+C1+C11-NB: National Annex to Eurocode 1: Actions on structures - Part 1-1: General actions - Densities, self-weight, imposed loads for buildings*. 2019.

[19] Nederlands Normalisatie-instituut. *NEN-EN 1991 Part 1-4: General Actions - Wind Actions*. 2005.

[20] Rolf Katzenbach, Steffen Leppla, and Deepankar Choudhury. *Foundation systems for high-rise structures*. CRC press, 2016.

[21] Hadi Salehi and Rigoberto Burgueño. “Emerging artificial intelligence methods in structural engineering”. In: *Engineering structures* 171 (2018), pp. 170–189.

[22] Aaron Smith and Janna Anderson. “AI, Robotics, and the Future of Jobs”. In: (2014).

[23] Guanghui Zhou et al. “Knowledge-driven digital twin manufacturing cell towards intelligent manufacturing”. In: *International Journal of Production Research* 58.4 (2020), pp. 1034–1051.

[24] Gurjit S Randhawa et al. “Machine learning using intrinsic genomic signatures for rapid classification of novel pathogens: COVID-19 case study”. In: *Plos one* 15.4 (2020), e0232391.

[25] Arash Teymori Gharah Tapeh and MZ Naser. “Artificial intelligence, machine learning, and deep learning in structural engineering: a scientometrics review of trends and best practices”. In: *Archives of Computational Methods in Engineering* 30.1 (2023), pp. 115–159.

[26] Huu-Tai Thai. “Machine learning for structural engineering: A state-of-the-art review”. In: *Structures*. Vol. 38. Elsevier. 2022, pp. 448–491.

[27] A Iranmanesh and A Kaveh. “Structural optimization by gradient-based neural networks”. In: *International journal for numerical methods in engineering* 46.2 (1999), pp. 297–311.
[28] A Kaveh and H Servati. “Design of double layer grids using backpropagation neural networks”. In: *Computers & Structures* 79.17 (2001), pp. 1561–1568.
[29] Manolis Papadrakakis, Vissarion Papadopoulos, and Nikos D Lagaros. “Structural reliability analyis of elastic-plastic structures using neural networks and Monte Carlo simulation”. In: *Computer methods in applied mechanics and engineering* 136.1-2 (1996), pp. 145–163.
[30] Seung Chang Lee, Sung Kwon Park, and Byung Hai Lee. “Development of the approximate analytical model for the stub-girder system using neural networks”. In: *Computers & Structures* 79.10 (2001), pp. 1013–1025.
[31] Xingquan Guan et al. “Seismic drift demand estimation for steel moment frame buildings: From mechanics-based to data-driven models”. In: *journal of structural engineering* 147.6 (2021), p. 04021058.
[32] Viet-Hung Truong et al. “Evaluation of machine learning models for load-carrying capacity assessment of semi-rigid steel structures”. In: *Engineering Structures* 273 (2022), p. 115001.
[33] Melda Yucel et al. “Estimation of optimum tuned mass damper parameters via machine learning”. In: *Journal of Building Engineering* 26 (2019), p. 100847.
[34] Gwang-Hee Kim, Sung-Hoon An, and Kyung-In Kang. “Comparison of construction cost estimating models based on regression analysis, neural networks, and case-based reasoning”. In: *Building and environment* 39.10 (2004), pp. 1235–1242.
[35] Iván García Kerdan and David Morillón Gálvez. “Artificial neural network structure optimisation for accurately prediction of exergy, comfort and life cycle cost performance of a low energy building”. In: *Applied Energy* 280 (2020), p. 115862.
[36] Han Sun, Henry V Burton, and Honglan Huang. “Machine learning applications for building structural design and performance assessment: State-of-the-art review”. In: *Journal of Building Engineering* 33 (2021), p. 101816.
[37] Philipp Geyer and Sundaravelpandian Singaravel. “Component-based machine learning for performance prediction in building design”. In: *Applied energy* 228 (2018), pp. 1439–1453.
[38] Paul Westermann and Ralph Evins. “Surrogate modelling for sustainable building design–A review”. In: *Energy and Buildings* 198 (2019), pp. 170–186.
[39] Y Cheng et al. “Optimal design of steel columns with axial load using artificial neural networks”. In: *DEStech Transactions on Engineering and Technology Research,(amme)* (2017).
[40] Nadia D Roman et al. “Application and characterization of metamodels based on artificial neural networks for building performance simulation: A systematic review”. In: *Energy and Buildings* 217 (2020), p. 109972.
[41] Qiong Li et al. “Predicting hourly cooling load in the building: A comparison of support vector machine and different artificial neural networks”. In: *Energy Conversion and Management* 50.1 (2009), pp. 90–96.
[42] Ian Goodfellow, Yoshua Bengio, and Aaron Courville. *Deep Learning*. `http://www.deeplearningbook.org`. MIT Press, 2016.
[43] Seunghye Lee et al. “Background information of deep learning for structural engineering”. In: *Archives of Computational Methods in Engineering* 25 (2018), pp. 121–129.
[44] Jacek Zurada. *Introduction to artificial neural systems*. West Publishing Co., 1992.
[45] Saeid Nikbakht, Cosmin Anitescu, and Timon Rabczuk. “Optimizing the neural network hyperparameters utilizing genetic algorithm”. In: *Journal of Zhejiang University-Science A* 22.6 (2021), pp. 407–426.
[46] Géron Aurélien. *Hands-On Machine Learning with Scikit-Learn Keras, and TensorFlow*. 2nd Edition. 2019.
[47] Michael A Nielsen. *Neural networks and deep learning*. Vol. 25. Determination press San Francisco, CA, USA, 2015.
[48] Eurocode Applied. *Table of design material properties for structural steel*. 2023. URL: `https://eurocodeapplied.com/design/en1993/steel-design-properties` (visited on 10/19/2023).
[49] T.J. Nikose and R.S. Sonparote. “Computing dynamic across-wind response of tall buildings using artificial neural network”. In: *The Journal of Supercomputing* 76 (2020), pp. 3788–3813.
[50] Mohammadreza Baradaran and Morteza Madhkhan. “Determination of optimal configuration for mega bracing systems in steel frames using genetic algorithm”. In: *KSCE Journal of Civil Engineering* 23 (2019), pp. 3616–3627.

[51] L.A.G. Wagemans. *Quick Reference*. 2014.
[52] Livios. *Richtprijzen fundering en beton*. Accessed on: 13-02-2024. 2023. URL: https://www.livios.be/nl/artikel/23105/richtprijzen-fundering-en-beton/.
[53] M. Rock and A. Sorensen. “Towards embodied carbon benchmarks for buildings in Europe”. In: *Build Department of the Built Environment* (2022).
[54] Philip Francis Oldfield. “Tall buildings and sustainability”. PhD thesis. University of Nottingham, 2012.
[55] Dario Trabucco et al. “A Whole LCA of the Sustainable Aspects of Structural Systems in Tall Paper Type”. In: *International Journal of High-Rise Buildings* 5.2 (2016), pp. 71–86.
[56] *deQo – Database of Embodied Quantity Outputs*. Online access through https://www.carbondeqo.com/database/graph. Last accessed on 21/03/2024.
[57] VWN - Vereniging Wapeningsstaal Nederland. “EPD Wapeningsstaal voor toepassing in gewapend betonconstructies”. In: (2021).
[58] Structural Engineer’s Pocket Book. “A brief guide to calculating embodied carbon”. In: (2020).
[59] Nederlands Normalisatie-instituut. *NEN-EN 1990+A1:2006+A1:2006/C2:2019 Eurocode: Grondslagen van het constructief ontwerp*. 2019.
[60] P. Ham and K. Terwel. *Structural Calculations of High Rise Structures*. TU Delft, Apr. 2022.

# A

# Material Data Summary

## A.1. Embodied Carbon Data

The total equivalent of $CO_2$ per kg of prefab reinforced concrete is determined by summing the embodied carbon of precast concrete (unreinforced) with that of the reinforcement bars. The embodied carbon per kg for the reinforcement is computed by multiplying the embodied carbon of reinforcement bars by the ratio of the density of the reinforcement bars to that of reinforced concrete (150 kg/$m_3$ / 2500 kg/$m_3$).

**Table A.1:** Embodied carbon data, all numbers are Cradle to Gate (A1-A3)

| **Material** | **Specifications** | **$CO_2$e Area** [kg$CO_2$e/$m^2$] | **$CO_2$e Weight** [kg$CO_2$e/kg] | **Source** |
|---|---|---|---|---|
| Steel | Structural, hot rolled, S355 | (-) | 1.12 | [16] |
| | Reinforcement bars | (-) | 0.992 | [57] |
| Concrete | Precast, C45/55, hollow core, h=320 mm | 66.43 | 0.155 | [14] [15] |
| | Precast, C40/50, unreinforced | (-) | 0.178 | [58] |
| | Precast, C40/50, reinforced 150 kg/$m^3$ | (-) | 0.238 | |

# B

# Wind Force

The wind force can be calculated using the guidelines outlined in NEN-EN 1991-1-4 [19]. All the equations and information within this section are taken from NEN-EN 1991-1-4 [19]. Equation B.1 represents the expression for calculating wind loads. This appendix provides instructions and assumptions on how to determine the parameters which are present in the equation.

$$F_w = c_s c_d \cdot c_f \cdot q_p(z_e) \cdot A_{ref} \tag{B.1}$$

Where:

$c_s c_d$ = structural factor, see Equation 2.11
$c_f$ = force coefficient for the structure, see Equation B.2
$q_p(z_e)$ = peak velocity pressure at reference height $z_e$, see Equation 5.1
$z_e$ = reference height for external wind action, internal pressure
$A_{ref}$ = reference area of the structure

## B.1. Structural Factor, $c_s c_d$

The structural factor $c_s c_d$ should take into account the effect on wind actions from the non-simultaneous occurrence of peak wind pressures on the surface ($c_s$) together with the effect of the vibrations of the structure due to turbulence ($c_d$). The assumption is made that $c_s c_d$ equals 1.1 for this research.

## B.2. Force Coefficient, $c_f$

The force coefficient ($c_f$) of structural elements of rectangular section can be determined with the following expression:

$$c_f = c_{f,0} \cdot \psi_r \cdot \psi_\lambda \tag{B.2}$$

Where:

$c_{f,o}$ = force coefficient of structures with sharp corners and without free-end flow
$\psi_r$ = reduction factor of force coefficient for square sections with rounded corners
$\psi_\lambda$ = end-effect factor for elements with free-end flow

$c_{f,o}$ = 2.1

The force coefficient of rectangular sections $c_{f,o}$ for this structure is 2.1, given that the width and length of the floor plan are identical, as depicted in Figure B.1. The floor plans of all structures have a symmetrical rectangular profile.

**Figure B.1:** Force coefficients $c_{f,0}$ of rectangular sections with sharp corners and without free-end flow according to NEN-EN 1991-1-4:2005

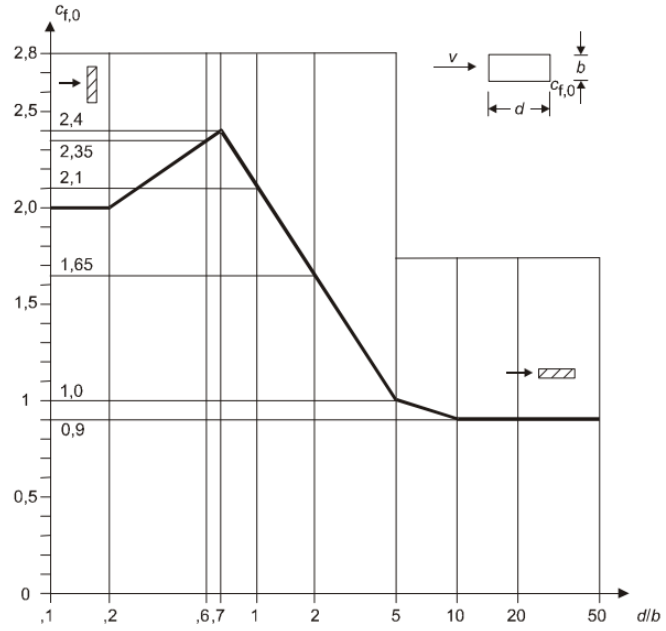


$\psi_r = 1.0$

The reduction factor $\psi_r$ for this structure is set to 1.0 due to the floor plan featuring sharp corners. Consequently, the radius over the width of the floor plan equals zero. The determination of the reduction factor is illustrated in Figure B.2.

**Figure B.2:** Reduction factor according to NEN-EN 1991-1-4:2005

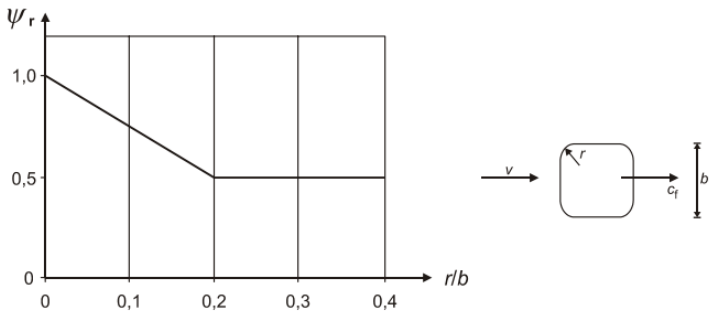


$\psi_\lambda = 1.0$

The end-effect factor $\psi_\lambda$ is presumed to be 1.0, given the emphasis on high-rise buildings of this research. One of the characteristics of high-rise structures is their significant slenderness. A more precise determination of the end-effect factor can be done based on Figure B.3.

**Figure B.3:** End-effect factor $\psi_\lambda$ according to NEN-EN 1991-1-4:2005

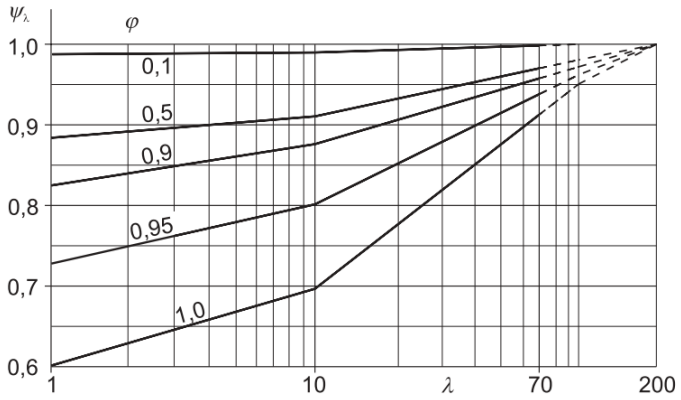


Where the solidity ratio $\phi$ is given by the following expression:

$$\phi = \frac{A}{A_c} \tag{B.3}$$

Where:

$A$ = the sum of the projected areas of the members
$A_c$ = the overall envelope area, $A_c = l \cdot b$

## B.3. Peak Velocity Pressure, $q_p(z)$

The peak velocity pressure will be determined using available data for peak velocity pressure in the Netherlands, specifically in Area II urban. This data can be extracted from the National Annex.

# C

# Structural Loads and Limit States

## C.1. Load Combinations

Eurocodes and national annexes of each country regulate the structural design of European buildings. The limit state design principle is used to evaluate the state of a structure as either satisfactory or unsatisfactory based on whether it meets the limit state design criteria. EN 1990 (Basis of Structural Design) of Eurocode defines two types of limit states that relate to structural safety and usability requirements:

- The Ultimate Limit State (ULS) involves the risk of collapse or other failures that jeopardize personal safety due to instabilities, excessive deformations, or rupture of structural elements.
- The Serviceability Limit State (SLS) refers to deformations that affect a structure's appearance, comfort level, or planned functionality, disrupt its normal use, cause damage, or have long-term effects on its durability.

The structural design process should ensure sufficiently low probability of failure. Therefore, partial safety factors are used for actions and loads. Table C.1 shows the partial safety factors for ULS and SLS considering consequence class 3 for buildings. To take the consequence class into account, the applicable load factors ($\gamma_G$ and $\gamma_{Q;1}$) are multiplied by the factor of 1.1 which results in the values presented in the Table.

| **Design** | **Permanent** | | **Variable** | |
|---|---|---|---|---|
| Load combination | Unfavourable | Favourable | Dominant | Accompanying |
| ULS (1) | 1.5 $G_{\text{k,j,sup}}$ | 0.9 $G_{\text{k,j,inf}}$ | 1.65 $\psi_{0,1}Q_{\text{k,1}}$ | 1.65 $\psi_{0,i}Q_{\text{k,1}}$ with (i > 1) |
| ULS (2) | 1.3 $G_{\text{k,j,sup}}$ | 0.9 $G_{\text{k,j,inf}}$ | 1.65 $Q_{\text{k,1}}$ | 1.65 $\psi_{0,i}Q_{\text{k,1}}$ with (i > 1) |
| SLS | 1.0 $G_{\text{k,j,sup}}$ | 1.0 $G_{\text{k,j,inf}}$ | 1.0 $Q_{\text{k,1}}$ | 1.0 $\psi_{0,i}Q_{\text{k,1}}$ with (i > 1) |

**Table C.1:** Partial safety factors for ULS and SLS

$\psi_0$, $\psi_1$ and $\psi_2$ are the combination factors applied to variable actions to determine their combination value, as per EN 1990 [59]. The factors for Category A: residential spaces and Category B: office spaces can be seen in Table C.2.

| | $\psi_0$ | $\psi_1$ | $\psi_2$ |
|---|---|---|---|
| Category A: residential spaces | 0.4 | 0.5 | 0.3 |
| Category B: office spaces | 0.5 | 0.5 | 0.3 |

**Table C.2:** $\psi$ factors for building according to EN1990 [59]

From NEN-EN1991-1-1 the live load at the floors is set and can be seen in Table C.3. The concentrated force must be applied over an area of 100x100m.

| | $q_k$ kN/m$^2$ | $Q_k$ kN |
|---|---|---|
| Category A: residential spaces | 1.75 | 3.0 |
| Category B: office spaces | 2.5 | 3.0 |
| Category B: light weight partition walls | 1.5 | (-) |

**Table C.3:** Live loads according to NEN-EN1991 [18]

## C.2. Ultimate Limit State

The ULS checks can be divided into checks regarding the stability and the strength of the structure. The equations presented below are based on the reader by P.H. Ham and K.C. Terwel (2017) [60].

### Stability

In the context of the ULS of the stability, the focus is on the slenderness and vertical loading of the structure. Increased slenderness raises the risk of the structure tipping over. To prevent this, the moment generated by wind load and the second-order effect, is compared to the moment resistance caused by the vertical loading. Sufficient capacity must be demonstrated to ensure the building remains stable and in place.

$$M_{\text{vertical}} = \frac{1}{2} \cdot F_{\text{vertical}} \cdot \text{width} \tag{C.1}$$

$$M_{\text{horizontal}} = \frac{1}{2} \cdot F_{\text{horizontal}} \cdot \text{height} \tag{C.2}$$

$$M_{\text{vertical}} > M_{\text{horizontal}} \tag{C.3}$$

### Strength

The strength condition requires a specific compressive strength of the building material. The actual stress should be smaller than the allowable stress.

$$\frac{\gamma_Q \cdot M_{wind}}{W} + \frac{\gamma_G \cdot N_{dead}}{A} < f_{yd} \tag{C.4}$$

The strength requirement is taken into account in the parametric model, where the unity check of 0.90 is applied. When the strength requirement could not be met, the structure was found insufficient.

## C.3. Serviceability Limit State

There are two essential global SLS checks for high-rise buildings: one concerning the maximum allowable lateral deflection and the other focusing on the maximum allowable acceleration, both are determined based on the dynamic behaviour of the structure.

### C.3.1. Deflection

The building's stiffness restricts its lateral deflection due to wind and earthquake loads. The latter are not considered in this research since the location of the structure is in the Netherlands, however they should be taken into account in seismic regions. The maximum allowable total lateral deflection, denoted as $u$, of a building is limited to $h/500$, see Equation C.6. The maximum lateral deflection for inter-storey can also be determined; in this case the stiffness of the foundation is not taken into account, see Equation C.5.

$$\frac{c_d \cdot q_w \cdot h_{storey}^4}{8 \cdot E_{eff} I} < \frac{h_{storey}}{300} \tag{C.5}$$

$$\frac{c_d \cdot q_w \cdot h^4}{8 \cdot E_{eff} I} + \frac{c_d \cdot 2 \cdot M \cdot h}{k \cdot x^2} < \frac{h}{500} \tag{C.6}$$

## C.3.2. Acceleration

The speed at which a building accelerates is constrained by the comfort of its occupants. Too high acceleration can create unsafe or uncomfortable conditions for those inside. Figure C.1 from the Eurocode illustrates the allowable acceleration levels plotted against the structure's natural frequency. The acceleration measured at the building's top may not be greater than this threshold. Line 1 corresponds to office spaces, and line 2 applies to residential spaces. The expression for the natural frequency of a structure can be found in Appendix B, referred to as Equation **??**. The method which is used, is described in the Dutch building code NEN 6702.

**Figure C.1:** Requirement acceleration of a structure according to NEN1991-1-4 [19]

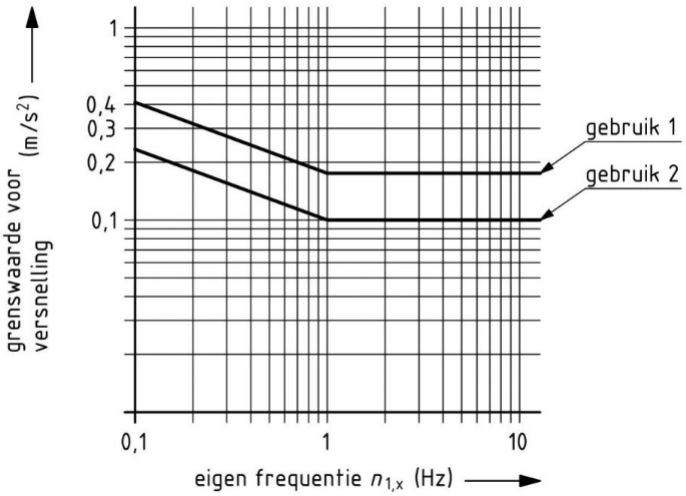


The acceleration at top of the building can be calculated with the following formula:

$$a = 1.6 \cdot \frac{\phi_2 \cdot p_w \cdot C_t \cdot b}{m} \tag{C.7}$$

Where:

$p_w$ = fluctuating part of the wind pressure, see Equation C.9
$C_t$ = shape factor of the structure
$b$ = average width of the structure perpendicular to the wind direction
$\phi_2$ = dynamic factor for vibration caused by wind, see Equation C.8
$m$ = mass of the structure

The dynamic factor which takes the fluctuation of the wind load into account, denoted as $\phi_2$, can be expressed as:

$$\phi_2 = \sqrt{\frac{0.0344 \cdot n_1^{-2/3}}{D \cdot (1 + 0.12 \cdot n_1 \cdot h)(1 + 0.2 \cdot n_1 \cdot b)}} \tag{C.8}$$

Where:

$n_1 =$ natural frequency
$D =$ damping coefficient of the building
$h =$ height of the structure
$b =$ average width of the building perpendicular to the wind direction

The fluctuating part of the wind pressure, denoted as $p_w$ can be expressed as:

$$p_w = 100 \cdot \frac{0.2}{h} \tag{C.9}$$

Where:

$h =$ height of the structure

# D

# Grasshopper Script

**Figure D.1:** Overview GH script: total

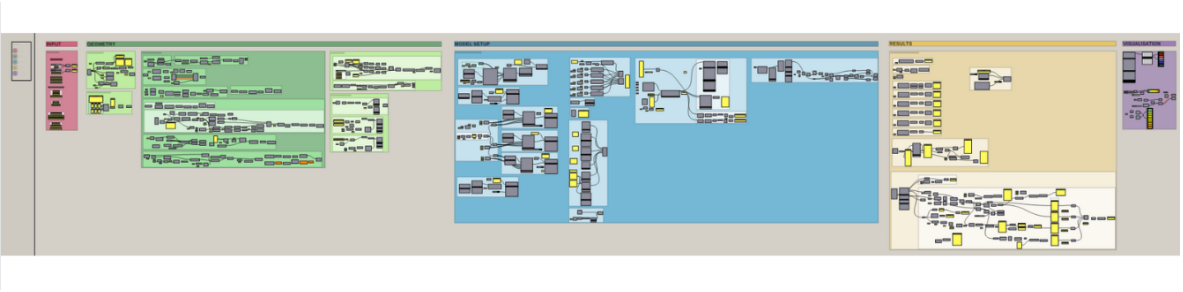

**Figure D.2:** Overview GH script: part A. determine input

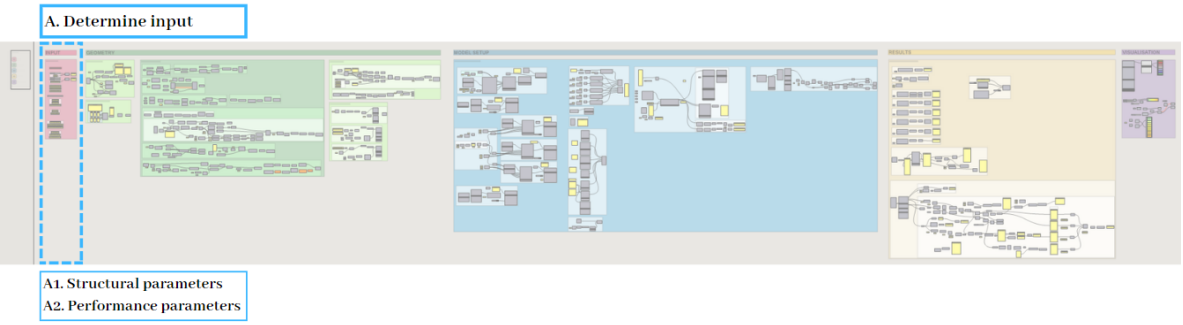


**Figure D.3:** Overview GH script: part B. create geometry

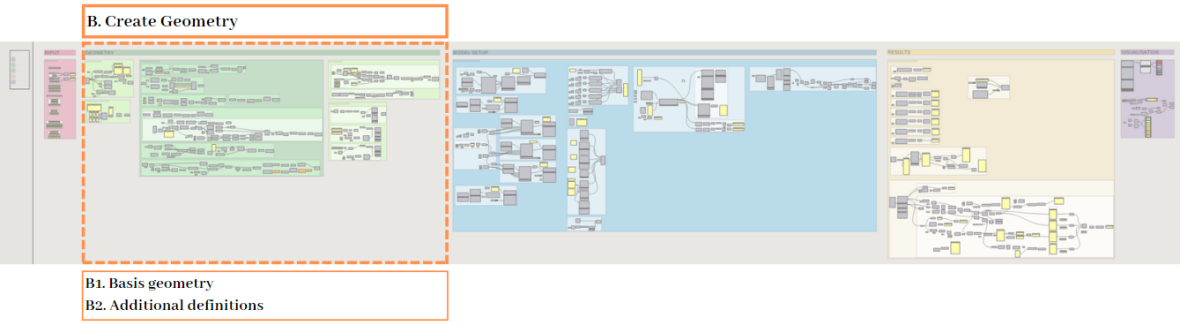

**Figure D.4:** Overview GH script: part C. determination structural analysis

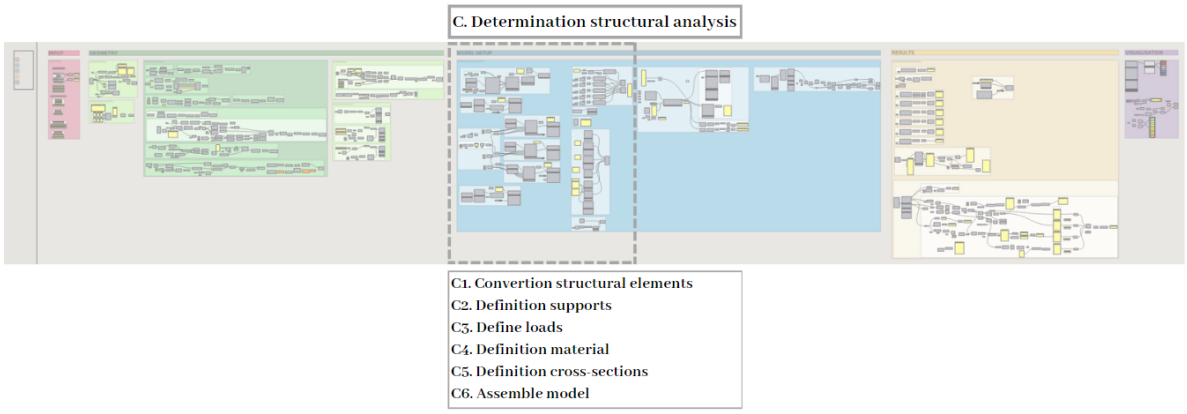


**Figure D.5:** Overview GH script: part D. analyze model

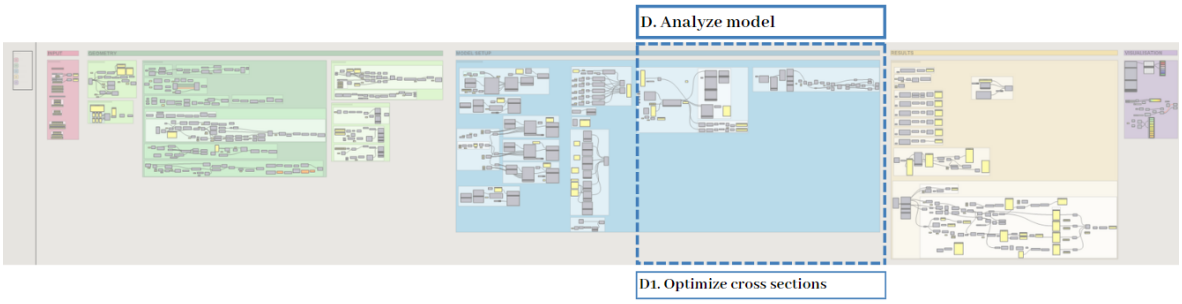


**Figure D.6:** Overview GH script: part E. generation of results

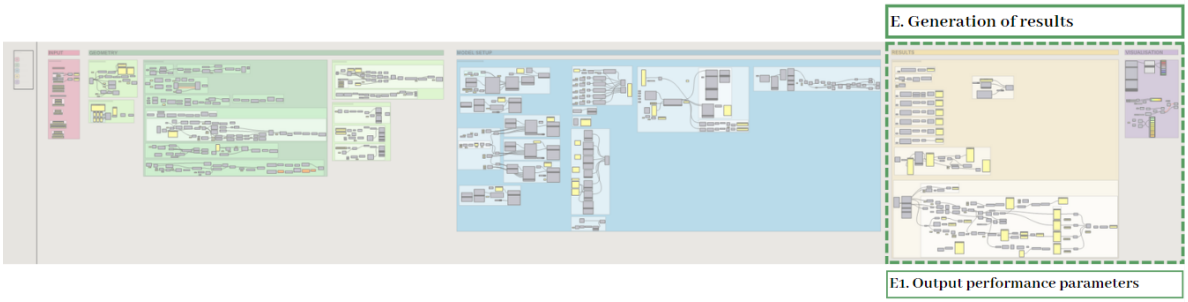

# E

# Validation of 3D Model

The Grasshopper model validation is conducted using Excel. In this validation, the deformation of the reference model is examined. The reference model has a height of 150 meters and a floor plan width of 28.8 meters. As the focus is on deformation, the load combination considered is the Serviceability Limit State (SLS), and no vertical loads, apart from gravity, are applied to the model. The horizontal load is the acting wind force on the structure.

## BRACED TUBE

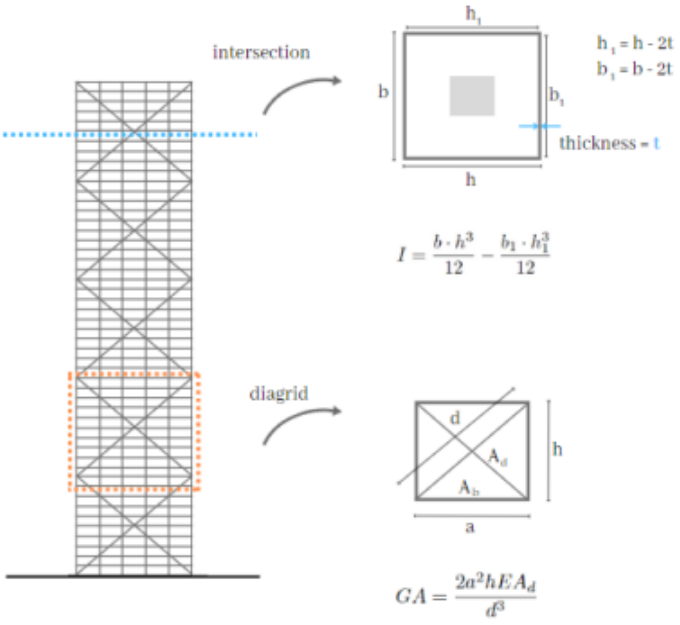


$$I = \frac{b \cdot h^3}{12} - \frac{b_1 \cdot h_1^3}{12}$$

$$GA = \frac{2a^2 h E A_d}{d^3}$$

## CALCULATION MATERIAL PROPERTIES

### Geometry

**Structure**

| | | |
|---|---|---|
| total height | 150 | m |
| E (staal) | 210000 | N/mm2 |
| | 2,1E+11 | N/m2 |
| h | 28,8 | m |
| b | 28,8 | m |

**OuterColumns**

Height Zone #1 : RHS500

| | | |
|---|---|---|
| h | 500 | mm |
| b | 500 | mm |
| A | 34462 | mm2 |
| h | 27 | m |

Height Zone #2 : RHS500

| | | |
|---|---|---|
| h | 500 | mm |
| b | 500 | mm |
| A | 34462 | mm2 |
| h | 33 | m |

| | | |
|---|---|---|
| Height Zone #3 : RHS400 | | |
| h | 400 | mm |
| b | 400 | mm |
| A | 22044 | mm2 |
| h | 33 | m |
| | | |
| Height Zone #4 : RHS300 | | |
| h | 300 | mm |
| b | 300 | mm |
| A | 12386 | mm2 |
| h | 30 | m |
| | | |
| Height Zone #5 : RHS300 | | |
| h | 300 | mm |
| b | 300 | mm |
| A | 12386 | mm2 |
| h | 27 | m |
| | | |
| *Average OuterColumns* | | |
| h | 402,0 | mm |
| b | 402,0 | mm |
| A | 23341,2 | mm2 |
| | | |
| **Diagrid: RHS700** | | |
| h | 600 | mm |
| b | 600 | mm |
| A | 67575 | mm2 |
| | | |
| n diagrid per side | 2 | (-) |
| n column per side | 9 | (-) |
| n columns total | 32 | (-) |
| n diagrid total | 8 | (-) |
| | | |
| t | 11,1764 | mm |
| | 0,0112 | m |
| h1 | 28,778 | m |
| b1 | 28,778 | m |
| I | 177,779 | m4 |
| | 1,78E+14 | mm4 |
| A | 1,287 | m2 |
| | | |
| **Shear stiffness** | | |
| a | 28,8 | m |
| h | 30 | m |
| E | 210000 | N/mm2 |
| | 210000000 | kN/m2 |
| A_d | 67575 | mm2 |
| | 0,067575 | m2 |

| | | |
|---|---|---|
| d | 42 | m |

$$GA = \frac{2a^2 hEA_d}{d^3}$$

| | | |
|---|---|---|
| GA = | 9819363 | kN |
| | 9819363238 | N |

**Stiffness Check**

| | | |
|---|---|---|
| h_tot / 500 | 0,3 | m |
| | 30 | cm |

w2 = w1 * N
total deflection including second order effect

**Second Order Effect**

**Eulerse knikkracht**

$$F_K = \frac{\pi^2 EI}{l_k^2}$$

| | | |
|---|---|---|
| EI | 3,73336E+13 | Nm2 |
| k factor | 1,2 | (-) |
| l | 150 | m |
| Center of gravity | 75 | m |
| l_k | 180 | m |
| F_k | 11372478574 | N |
| | 11372478,57 | kN |

**Eigen gewicht**

| | | |
|---|---|---|
| mass | 20402000 | kg |
| | 200144 | kN |
| F_Ed | 200144 | kN |

**Vergrotingsfactor**

| | | |
|---|---|---|
| n | 56,82 | (-) |
| N = n / (n-1) = | 1,018 | (-) |

| | Braced column | | | Unbraced column | | |
|---|---|---|---|---|---|---|
| Buckled shape | 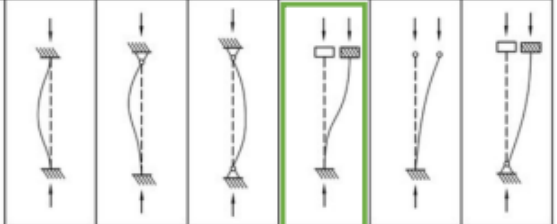 | | | | | |
| Effective length factor (k) | 0.70 | 0.85 | 1.00 | 1.20 | 2.20 | 2.20 |
| Symbols for end restraint conditions | = Rotation fixed, translation fixed | | | = Rotation fixed, translation free | | |
| | = Rotation free, translation fixed | | | = Rotation free, translation free | | |

**CALCULATION WIND LOAD**

**Wind Load**

For calculation see Sheet 'Wind Pressure'

| | | |
|---|---|---|
| Total wind moment | 1103041,038 | kNm |
| arm for total moment | 75 | m |
| Average q wind pressure | 3,4044 | kN/m2 |
| SLS load factor | 1 | (-) |
| ULS load factor | 1,65 | (-) |
| q | 3,404447648 | kN/m2 |
| | 98,04809225 | kN/m |
| | 98048,09225 | N/m |

**CALCULATION DEFLECTION**

**I) Deflection due to bending**

**B3: w based on q-load**

| | | |
|---|---|---|
| w bending | 0,181 | m |
| | **18,06** | cm |

For more details see Sheet 'Deflection Bending Braced Tube'

**II) Deflection due to shear**

$$\delta_{top} = \frac{qH^2}{2GA_{frame}}$$

| | | |
|---|---|---|
| GA | 9819363238 | N |

| | | |
|---|---|---|
| w shear | 0,11 | m |
| | 11,23 | cm |

**III) Total Deflection**

w total = w bending + w shear

**B3: w based on q-load**

| | | |
|---|---|---|
| w total | 0,293 | m |
| | 29,30 | cm |
| w2 total | **29,82** | cm |

**COMPARISON WITH 3D and 2D MODEL**

**3D Model: Rhino / Grasshopper**

| | | |
|---|---|---|
| w_3D (hinged structure) | **30,05** | cm |
| difference: 3D with analytic | **-0,76%** | |

**2D Model: MatrixFrame**

| | | |
|---|---|---|
| w_2D | 17,42 | cm |

For more details see Sheet 'MatrixFrame'
Note: MatrixFrame is only deflection due to bending

| | | |
|---|---|---|
| w_2D including shear | 28,65 | cm |
| w2_2D including shear | **29,17** | cm |
| difference: 3D with 2D | **-2,94%** | |

## ADDITIONAL MORE DETAILED HAND CALCULATION

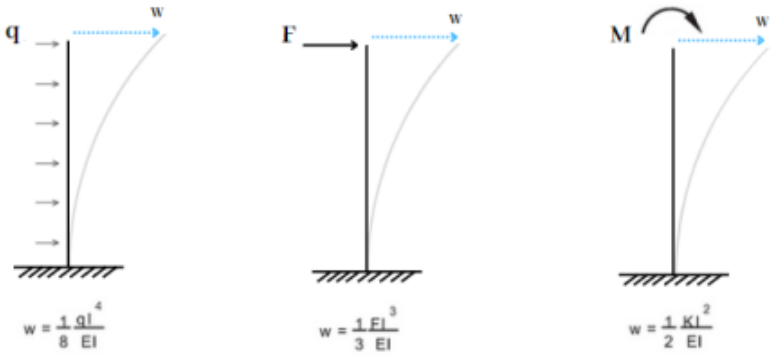


| Parameters | | |
|---|---|---|
| **Zone 1** | | |
| M1_tot | 30687 | kNm |
| h1 | 30 | m |
| q1 | 68,2 | kN/m |
| **Zone 2** | | |
| M2_tot | 384261 | kNm |
| h2 | 90 | m |
| q2 | 94,9 | kN/m |
| F2 | 8539,1 | kN |
| q_constant | 68,2 | kN/m |
| M_constant | 276185 | kNm |
| M_increasing | 108076 | kNm |
| q_increase | 26,69 | kN/m |
| **Zone 3** | | |
| M3_tot | 49898 | kNm |
| h3 | 30 | m |
| q3 | 110,9 | kN/m |
| F3 | 3326,6 | kN |

| Calculation | | |
|---|---|---|
| **Zone 1** | | |
| w1,1 from q | 0,00018 | m |
| φ1,1 from q | 0,00001 | rad |

| | | |
|---|---|---|
| w1,2 from M2 | 0,00463 | m |
| φ1,2 from M2 | 0,00031 | rad |
| | | |
| w1,3 from F2 | 0,00206 | m |
| φ1,3 from F2 | 0,00053 | rad |
| | | |
| w1_tot | 0,00688 | m |
| φ1_tot | 0,00085 | rad |

| **Zone 2** | | |
|---|---|---|
| w2,1 from q_constant | 0,01498 | m |
| φ2,1 from q_constant | 0,00022 | rad |
| | | |
| w2,2 from q_increasing | 0,00586 | m |
| φ2,2 from q_increasing | 0,00009 | rad |
| | | |
| w2,3 from M3 | 0,00541 | m |
| φ2,3 from M3 | 0,00012 | rad |
| | | |
| w2,4 from F2 | 0,02165 | m |
| φ2,4 from F2 | 0,00036 | rad |
| | | |
| w2,5 from φ1 | 0,07639 | m |
| | | |
| w2_tot | 0,12430 | m |
| φ2_tot | 0,00079 | rad |

| **Zone 3** | | |
|---|---|---|
| w3,1 from q | 0,00030 | m |
| | | |
| w3,2 from (φ1 + φ2) | 0,04916 | m |
| | | |
| w3_tot | 0,04946 | m |
| | | |
| w_tot | 0,18 | m |
| | **18,06** | cm |

## OUTRIGGER

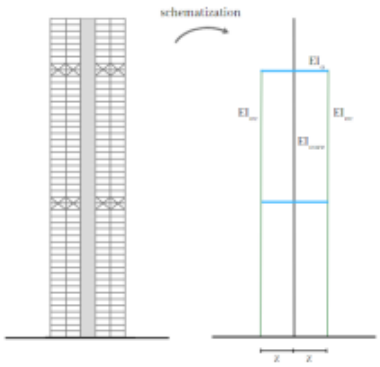


$EI_{core}$ = bending stiffness of the concrete core
$EI_{ec}$ = bending stiffness of the outer columns
$EI_{o}$ = bending stiffness of the outrigger

$$I_{ec} = 2 \cdot c \cdot n \cdot A_{ec} \cdot l^2$$

n = number of outer columns per facade
$A_{ec}$ = area of exterior outer column
l = distance to the core (= z)
c = reduction factor

$$I_o = n \cdot \frac{j^2}{j^2 - 1} \cdot \left(\frac{A_b h^2}{2}\right)$$

j = number of segments in rigger section
n = number of riggers on each side
h = height of the rigger
$A_b$ = sectional area of a horizontal outrigger member

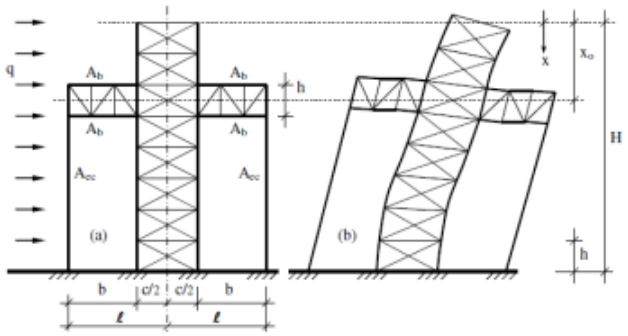


## CALCULATION MATERIAL PROPERTIES

### Geometry

**Basis Structure**

| | | | |
|---|---|---|---|
| total height | 150 | m | |
| h | 28,8 | m | |
| b | 28,8 | m | |

**Material**

| | | | |
|---|---|---|---|
| E (steel) | 210000 | N/mm2 | |
| | 2,1E+11 | N/m2 | |
| Ecm (concrete) C45/55 | 36 | GPa | Concrete is assumed to be |
| reduction factor | 0,67 | (-) | uncracked |
| Ec,eff | 24 | GPa | |
| | 24000 | N/mm2 | |

**Core**

| | | |
|---|---|---|
| h_outer | 10,8 | m |
| b_outer | 10,8 | m |
| t | 400 | mm |
| | 0,4 | m |

| | | |
|---|---|---|
| h_inner | 10 | m |
| b_inner | 10 | m |
| | | |
| I_core | 300,4075 | m4 |
| | 3E+14 | mm4 |
| A_core | 16,64 | m2 |

**ExteriorColumn (ec): RHS1000**

| | | |
|---|---|---|
| h | 1000 | mm |
| b | 1000 | mm |
| A | 137940 | mm2 |
| I | 2,16E+10 | mm4 |
| | | |
| n column per side | 4 | (-) |
| n columns total | 8 | (-) |
| | | |
| c | 0,6 | (-) |
| z = 1/2 b | 14,4 | m |

4 profiles work together with a relatively stiff rigger to provide the structure more stability

$$EI_{ec} = 2EA_{ec}\ell^2$$

| | | |
|---|---|---|
| A ec | 551760 | mm2 |
| | 0,55176 | |
| I ec | 1,37E+14 | mm4 |
| | 137,2955 | m4 |

**Rigger**

| | | |
|---|---|---|
| n total riggers | 2 | (-) |

*Beam: RHS500*

| | | |
|---|---|---|
| h | 500 | mm |
| b | 500 | mm |
| A | 34462 | mm2 |
| I | 1,35E+09 | mm4 |
| n beams | 2 | (-) |
| h | 6 | m |
| n riggers | 2 | (-) |
| j | 5 | (-) |

$$EI_0 = n \cdot \frac{j^2}{j^2 - 1}\left(\frac{EA_b h^2}{2}\right)$$

| | | |
|---|---|---|
| I outrigger | 2,58E+12 | mm4 |
| | 2584,65 | m4 |

*Belt Rigger: RHS500*

| | | |
|---|---|---|
| A | 34462 | mm2 |
| n | 10 | (-) |
| | | |
| A outrigger | 827088 | mm2 |
| | 0,827088 | m2 |

**Stiffness Check**

| | | |
|---|---|---|
| h_tot / 750 | 0,2 | m |
| | 20 | cm |

**Second Order Effect**

**Eulerse knikkracht**

$$F_K = \frac{\pi^2 EI}{l_k^2}$$

| | | |
|---|---|---|
| EI | 4,02E+13 | Nm2 |
| k factor | 1,2 | (-) |
| l | 150 | m |
| Center of gravity | 75 | m |
| l_k | 180 | m |
| F_k | 1,22E+10 | N |
| | 12242425 | kN |

**Eigen gewicht**

| | | |
|---|---|---|
| mass | 25470000 | kg |
| | 249861 | kN |
| F_Ed | 249861 | kN |

**Vergrotingsfactor**

| | | |
|---|---|---|
| n | 49,00 | (-) |
| N = n / (n-1) = | 1,021 | (-) |

**COMPARISON WITH MODEL**

**3D Model: Rhino / Grasshopper**

| | | |
|---|---|---|
| w (hinged structure) | **21,03** | cm |

**2D Model: MatrixFrame**

| | | |
|---|---|---|
| w_2D | 20,78 | cm |

For more details see Sheet 'MatrixFrame'
Note: MatrixFrame is only deflection due to bending

| | | |
|---|---|---|
| w2_2D | 21,21 | cm |
| difference: 3D with 2D | 0,87% | |

## BRACED TUBE

### Input

#### Geometry

| | | |
|---|---|---|
| total height | 150 | m |

#### Profile definitions

| | | |
|---|---|---|
| E (staal) | 2,1E+08 | kN/m2 |
| A | 1,28702 | m2 |
| I | 177,779 | m4 |

| | Label | Oppervl. | Trgh. mom. | E-mod. | Mat. type | Mat. code |
|---|---|---|---|---|---|---|
| ▶ | P4 | 1.2870e+00 | 1.7790e+02 | 2.1000e+08 | Handmatig | Niet gedef. |

#### Load definitions

| Label | Type | Beginwaarde | Eindwaarde | Beginafstand | Eindafstand | Richting | Staaf/Knoop |
|---|---|---|---|---|---|---|---|
| LD1 | q | 68.198 | 68.198 | 0.000 | 30.000 | Z' | S1 |
| LD2 | q | 68.198 | 110.966 | 30.000 | 120.000 | Z' | S1 |
| LD3 | q | 110.966 | 110.966 | 120.000 | L | Z' | S1 |

#### Support definitions

| Label | X | Z | Yr | Hoek Yr | Object | X | Z | Omschrijving |
|---|---|---|---|---|---|---|---|---|
| 01 | Vast | Vast | Vast | | K1 | 0.000 | 0.000 | |
| | | | | | | | | |

### Results

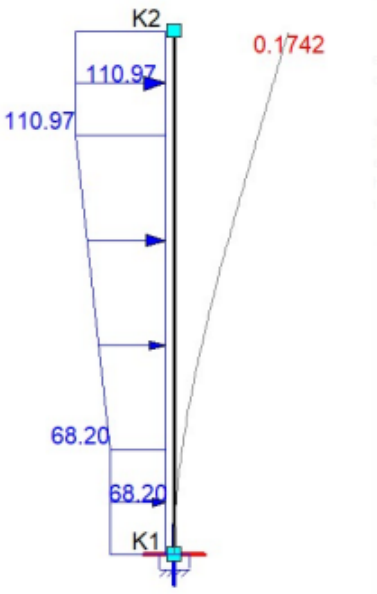


**Deflection**

| | | |
|---|---|---|
| w | 0,1742 | m |
| | 17,42 | cm |

## OUTRIGGER SYSTEM

### Input

#### Geometry

| | | | |
|---|---|---|---|
| total height | 150 | m | |
| place 1st outrigger | 61,5 | m | |
| place 2nd outrigger | 121,5 | m | |

#### Profile definitions

**Core**

| | | | |
|---|---|---|---|
| E (uncracked concrete) | 36000 | N/mm2 | |
| reduction factor | 0,67 | (-) | |
| E (uncracked concrete) | 24120 | N/mm2 | Label = P4 |
| A_tot | 16,64 | m2 | |
| I_tot | 300,407 | m4 | |

**Exterior Columns**

| | | | |
|---|---|---|---|
| E (steel) | 2,1E+08 | kN/m2 | Label = P3 |
| A | 551760 | mm2 | |
| I | 1,4E+14 | mm4 | |

**Rigger**

| | | | |
|---|---|---|---|
| E (steel) | 2,1E+08 | kN/m2 | Label = P1 |
| A | 827088 | mm2 | |
| I | 2,6E+12 | mm4 | |

Profielen

| | Label | Oppervl. | Trgh. mom. | E-mod. | Mat. type | |
|---|---|---|---|---|---|---|
| | P1 | 8.2700e-02 | 2.5840e+03 | 2.1000e+08 | Handmatig | N |
| ▶ | P3 | 5.5000e-01 | 1.3700e+04 | 2.1000e+08 | Handmatig | N |
| | P4 | 1.6640e+01 | 3.0041e+02 | 2.4100e+07 | Handmatig | N |

#### Load definitions

Load is applied on the core of the structure.

| Label | Type | Beginwaarde | Eindwaarde | Beginafstand | Eindafstand | Richting | Staaf/Knoop |
|---|---|---|---|---|---|---|---|
| LD1 | q | 68.198 | 68.198 | 0.000 | 30.000 | Z' | S1 |
| LD2 | q | 68.198 | 110.966 | 30.000 | 120.000 | Z' | S1 |
| LD3 | q | 110.966 | 110.966 | 120.000 | L | Z' | S1 |

#### Support definitions

**Core**

Foundation of the core fully fixed support

**Columns**

Supports of the columns are pinned supports

**Rigger**

Connection rigger and the core is assumed to be fully rigid

Connection of the columns and the rigger are assumed to be hinged

**Results**

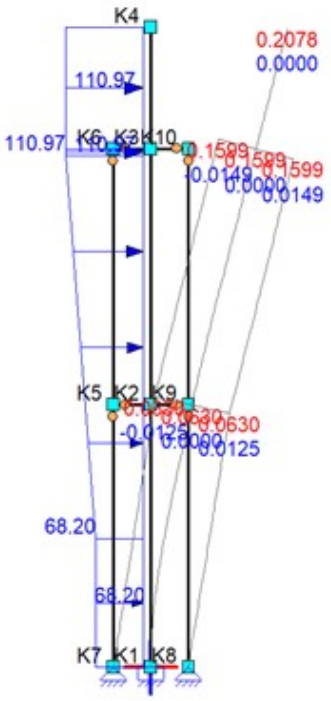


**Deflection**

| | | |
|---|---|---|
| w | 0,2078 | m |
| | 20,78 | cm |

**WIND PRESSURE DETERMINATION**

| | |
|---|---|
| **Width of floorplan [m] =** | 28,8 |
| **Δ height [m] =** | 3 |

| Height [m] | Wind pressure [kN/m2] | Arm [m] | Wind moment [kNm] |
|---|---|---|---|
| 0 | 0 | 0 | 0 |
| 3 | 2,36784 | 1,5 | 306,9 |
| 6 | 2,36784 | 4,5 | 920,6 |
| 9 | 2,36784 | 7,5 | 1534,4 |
| 12 | 2,36784 | 10,5 | 2148,1 |
| 15 | 2,36784 | 13,5 | 2761,8 |
| 18 | 2,36784 | 16,5 | 3375,6 |
| 21 | 2,36784 | 19,5 | 3989,3 |
| 24 | 2,36784 | 22,5 | 4603,1 |
| 27 | 2,36784 | 25,5 | 5216,8 |
| 30 | 2,36784 | 28,5 | 5830,6 |
| 33 | 2,438774 | 31,5 | 6637,4 |
| 36 | 2,504987 | 34,5 | 7466,9 |
| 39 | 2,567173 | 37,5 | 8317,6 |
| 42 | 2,625875 | 40,5 | 9188,5 |
| 45 | 2,681529 | 43,5 | 10078,3 |
| 48 | 2,734490 | 46,5 | 10986,1 |
| 51 | 2,785053 | 49,5 | 11911,1 |
| 54 | 2,833463 | 52,5 | 12852,6 |
| 57 | 2,879929 | 55,5 | 13809,8 |
| 60 | 2,924628 | 58,5 | 14782,2 |
| 63 | 2,967715 | 61,5 | 15769,3 |
| 66 | 3,009323 | 64,5 | 16770,4 |
| 69 | 3,049568 | 67,5 | 17785,1 |
| 72 | 3,088553 | 70,5 | 18813,0 |
| 75 | 3,126369 | 73,5 | 19853,7 |
| 78 | 3,163097 | 76,5 | 20906,8 |
| 81 | 3,198810 | 79,5 | 21972,0 |
| 84 | 3,233573 | 82,5 | 23048,9 |
| 87 | 3,267443 | 85,5 | 24137,3 |
| 90 | 3,300476 | 88,5 | 25236,8 |
| 93 | 3,332718 | 91,5 | 26347,1 |
| 96 | 3,364214 | 94,5 | 27468,1 |
| 99 | 3,395005 | 97,5 | 28599,5 |
| 102 | 3,425126 | 100,5 | 29741,1 |
| 105 | 3,454613 | 103,5 | 30892,5 |
| 108 | 3,483496 | 106,5 | 32053,7 |
| 111 | 3,511804 | 109,5 | 33224,5 |
| 114 | 3,539564 | 112,5 | 34404,6 |
| 117 | 3,566802 | 115,5 | 35593,8 |
| 120 | 3,593539 | 118,5 | 36792,1 |
| 123 | 3,619798 | 121,5 | 37999,2 |
| 126 | 3,852504 | 124,5 | 41440,6 |
| 129 | 3,852504 | 127,5 | 42439,2 |

| | [0] |
|---|---|
| 0 | 2.36784 |
| 1 | 2.36784 |
| 2 | 2.36784 |
| 3 | 2.36784 |
| 4 | 2.36784 |
| 5 | 2.36784 |
| 6 | 2.36784 |
| 7 | 2.36784 |
| 8 | 2.36784 |
| 9 | 2.36784 |
| 10 | 2.438774 |
| 11 | 2.504987 |
| 12 | 2.567173 |
| 13 | 2.625875 |
| 14 | 2.681529 |
| 15 | 2.73449 |
| 16 | 2.785053 |
| 17 | 2.833463 |
| 18 | 2.879929 |
| 19 | 2.924628 |
| 20 | 2.967715 |
| 21 | 3.009323 |
| 22 | 3.049568 |
| 23 | 3.088553 |
| 24 | 3.126369 |
| 25 | 3.163097 |
| 26 | 3.19881 |
| 27 | 3.233573 |
| 28 | 3.267443 |
| 29 | 3.300476 |
| 30 | 3.332718 |
| 31 | 3.364214 |
| 32 | 3.395005 |
| 33 | 3.425126 |
| 34 | 3.454613 |
| 35 | 3.483496 |
| 36 | 3.511804 |
| 37 | 3.539564 |
| 38 | 3.566802 |
| 39 | 3.593539 |
| 40 | 3.619798 |
| 41 | 3.852504 |
| 42 | 3.852504 |
| 43 | 3.852504 |
| 44 | 3.852504 |
| 45 | 3.852504 |
| 46 | 3.852504 |
| 47 | 3.852504 |
| 48 | 3.852504 |
| 49 | 3.852504 |

| | | | |
|---|---|---|---|
| 132 | 3,852504 | 130,5 | 43437,8 |
| 135 | 3,852504 | 133,5 | 44436,3 |
| 138 | 3,852504 | 136,5 | 45434,9 |
| 141 | 3,852504 | 139,5 | 46433,5 |
| 144 | 3,852504 | 142,5 | 47432,0 |
| 147 | 3,852504 | 145,5 | 48430,6 |
| 150 | 3,852504 | 148,5 | 49429,2 |

| | | |
|---|---|---|
| **Total wind moment** | 1103041,038 | kNm |
| **average q wind pressure** | 3,404447648 | kN/m2 |

| | | |
|---|---|---|
| M1_tot | 30687,2064 | kNm |

M2_tot

| Height [m] | Wind pressure [kN/m2] | Arm [m] | Wind moment [kNm} |
|---|---|---|---|
| 3 | 2,438774 | 1,5 | 316,1 |
| 6 | 2,504987 | 4,5 | 973,9 |
| 9 | 2,567173 | 7,5 | 1663,5 |
| 12 | 2,625875 | 10,5 | 2382,2 |
| 15 | 2,681529 | 13,5 | 3127,7 |
| 18 | 2,734490 | 16,5 | 3898,3 |
| 21 | 2,785053 | 19,5 | 4692,3 |
| 24 | 2,833463 | 22,5 | 5508,3 |
| 27 | 2,879929 | 25,5 | 6345,1 |
| 30 | 2,924628 | 28,5 | 7201,6 |
| 33 | 2,967715 | 31,5 | 8076,9 |
| 36 | 3,009323 | 34,5 | 8970,2 |
| 39 | 3,049568 | 37,5 | 9880,6 |
| 42 | 3,088553 | 40,5 | 10807,5 |
| 45 | 3,126369 | 43,5 | 11750,1 |
| 48 | 3,163097 | 46,5 | 12708,1 |
| 51 | 3,198810 | 49,5 | 13680,7 |
| 54 | 3,233573 | 52,5 | 14667,5 |
| 57 | 3,267443 | 55,5 | 15668,0 |
| 60 | 3,300476 | 58,5 | 16681,9 |
| 63 | 3,332718 | 61,5 | 17708,7 |
| 66 | 3,364214 | 64,5 | 18748,1 |
| 69 | 3,395005 | 67,5 | 19799,7 |
| 72 | 3,425126 | 70,5 | 20863,1 |
| 75 | 3,454613 | 73,5 | 21938,2 |
| 78 | 3,483496 | 76,5 | 23024,5 |
| 81 | 3,511804 | 79,5 | 24121,9 |
| 84 | 3,539564 | 82,5 | 25230,0 |
| 87 | 3,566802 | 85,5 | 26348,7 |
| 90 | 3,593539 | 88,5 | 27477,6 |

| | | |
|---|---|---|
| M2_tot | 384261,0 | kNm |

M3_tot

| Height [m] | Wind pressure [kN/m2] | Arm [m] | Wind moment [kNm} |
|---|---|---|---|
| 3 | 3,619798 | 1,5 | 469,1 |
| 6 | 3,852504 | 4,5 | 1497,9 |
| 9 | 3,852504 | 7,5 | 2496,4 |
| 12 | 3,852504 | 10,5 | 3495,0 |
| 15 | 3,852504 | 13,5 | 4493,6 |
| 18 | 3,852504 | 16,5 | 5492,1 |
| 21 | 3,852504 | 19,5 | 6490,7 |
| 24 | 3,852504 | 22,5 | 7489,3 |
| 27 | 3,852504 | 25,5 | 8487,8 |
| 30 | 3,852504 | 28,5 | 9486,4 |

M3_tot 49898,3 kNm

**DETERMINATION FACTOR ULS / SLS**

$$f_{u,ULS} = \frac{\gamma_{W,ULS} \cdot \gamma_{W,SLS} + \gamma_{2nd,ULS} \cdot \gamma_{2nd,SLS} \cdot n_{2,\delta}}{1 + n_{2,\delta}}$$

| | | | | |
|---|---|---|---|---|
| ULS | G | 1,5 | γW,ULS | 1,65 |
| | Qv | 0,825 | γ2nd,ULS | 1,1625 |
| | Qw | 1,65 | | |
| SLS | G | 1 | γW,SLS | 1 |
| | Qw | 1 | γ2nd,SLS | 1 |

$$u_{max,SLS} = \frac{h}{500}$$

$$u_{max,ULS} = u_{max,SLS} \cdot f_{u,ULS} = \frac{f_{u,ULS} \cdot h}{500}$$

**Braced Framed Tube**

| | | |
|---|---|---|
| n2, δ | 1,018 (-) | Second Order Factor, see Sheet 'Braced Tube' |
| fu,ULS | 1,40 (-) | |
| 500 / fu,ULS = | 356 | |
| **u,max, ULS =** | h / 356 | |

**Outrigger System**

| | | |
|---|---|---|
| n2, δ | 1,021 (-) | Second Order Factor, see Sheet 'Outrigger' |
| fu,ULS | 1,40 (-) | |
| 500 / fu,ULS = | 356 | |
| **u,max, ULS =** | h / 356 | |

# F

# Error Analysis of S1-B and S2-B

| **Structural Element** | **RMSE** [kg/m$^2$GFA] | **MAPE** [%] |
|---|---|---|
| *H1: Outer Beams* | 1.14 | 25 |
| *H2: Outer Beams* | 1.15 | 26 |
| *H3: Outer Beams* | 0.52 | 23 |
| *H4: Outer Beams* | 0.46 | 27 |
| *H5: Outer Beams* | 0.35 | 23 |
| *H6: Outer Beams* | 0.45 | 23 |
| *H1: Outer Columns* | 70.02 | 30 |
| *H2: Outer Columns* | 59.12 | 33 |
| *H3: Outer Columns* | 39.79 | 35 |
| *H4: Outer Columns* | 17.10 | 30 |
| *H5: Outer Columns* | 8.28 | 25 |
| *H6: Outer Columns* | 4.41 | 27 |
| *H1: Inner Columns* | 9.69 | 9 |
| *H2: Inner Columns* | 8.82 | 16 |
| *H3: Inner Columns* | 6.28 | 17 |
| *H4: Inner Columns* | 5.32 | 20 |
| *H5: Inner Columns* | 4.01 | 22 |
| *H6: Inner Columns* | 2.04 | 23 |
| *Floor Beams* | 0.59 | 5 |
| *Bracing* | 10.32 | 18 |

**Table F.1:** RMSE and MAPE of ANN S1-B of each element within each height zone

| **Structural Element** | **RMSE** [kg/m$^2$GFA] | **MAPE** [%] |
|---|---|---|
| *H1: Outer Beams* | 0.34 | 2 |
| *H2: Outer Beams* | 1.40 | 10 |
| *H3: Outer Beams* | 1.31 | 9 |
| *H4: Outer Beams* | 0.87 | 13 |
| *H5: Outer Beams* | 0.78 | 12 |
| *H6: Outer Beams* | 0.67 | 8 |
| *H1: Outer Columns conn. Truss* | 31.01 | 27 |
| *H2: Outer Columns conn. Truss* | 32.93 | 34 |
| *H3: Outer Columns conn. Truss* | 96.28 | 37 |
| *H4: Outer Columns conn. Truss* | 65.53 | 33 |
| *H5: Outer Columns conn. Truss* | 46.83 | 28 |
| *H6: Outer Columns conn. Truss* | 10.29 | 13 |
| *H1: Outer Columns not conn. Truss* | 31.01 | 27 |
| *H2: Outer Columns not conn. Truss* | 32.93 | 27 |
| *H3: Outer Columns not conn. Truss* | 96.28 | 28 |
| *H4: Outer Columns not conn. Truss* | 65.53 | 22 |
| *H5: Outer Columns not conn. Truss* | 46.83 | 20 |
| *H6: Outer Columns not conn. Truss* | 10.29 | 9 |
| *H1: Inner Columns conn. Truss* | 60.42 | 53 |
| *H1: Inner Columns conn. Truss* | 46.46 | 48 |
| *H1: Inner Columns conn. Truss* | 40.35 | 47 |
| *H1: Inner Columns conn. Truss* | 49.49 | 49 |
| *H1: Inner Columns conn. Truss* | 61.08 | 38 |
| *H1: Inner Columns conn. Truss* | 7.33 | 23 |
| *H1: Inner Columns not conn. Truss* | 60.42 | 25 |
| *H1: Inner Columns not conn. Truss* | 46.46 | 29 |
| *H1: Inner Columns not conn. Truss* | 40.35 | 28 |
| *H1: Inner Columns not conn. Truss* | 49.49 | 27 |
| *H1: Inner Columns not conn. Truss* | 61.08 | 25 |
| *H1: Inner Columns not conn. Truss* | 7.33 | 14 |
| *Floor Beams* | 1.63 | 9 |
| *Outrigger Truss* | 26.69 | 38 |
| *Core* | 19.18 | 7 |

**Table F.2:** RMSE and MAPE of ANN S2-B of each element within each height zone

# G

# Comparison Literature

## G.1. Adaption of Literature Data

A comparison is made with three different studies found in the literature regarding the embodied carbon impact of high-rise buildings. To ensure a fair comparison, it was necessary to adapt the literature data to match the scope of the ANNs. The scope of the ANN consisted of the load-bearing system, which included the superstructure and upper floors, while the scope of the LCA spanned from stages A1 to A3. The foundation was not considered in this analysis. Table G.1 provides an overview of the data found in the literature before adaptation to the ANN's scope, where study A refers to Rock (2022) [53], study B to Oldfield (2012) [54] and study C to Trabucco (2016) [55].

| **Study** | **System** | **Total GFA** [$m^2$] | **Floors** [-] | **Scope Structure** | **Scope LCA** | **Em$CO_2$** [kg$CO_2$eq/$m^2$GFA] |
|---|---|---|---|---|---|---|
| A | Steel Frame | 64,762 | 27 | All Components | ABC | 1201 |
| B | Steel Diagrid | 64,469 | 41 | Load-bearing System | ABC | 404 |
| C | Steel Diagrid | 141,600 | 60 | Load-bearing System | A1-3 | 285 |
| C | Concrete Core + Steel Frame | 141,600 | 60 | Load-bearing System | A1-3 | 236 |

**Table G.1:** Overview of the found data in the literature

### Study A

The values from Study A needed adjustments to match the structural scope, focusing only on the load-bearing system, and confining the LCA scope to stages A1-A3. The study revealed that the Cradle-to-Gate phase (A1-A3) accounts for an average of 56% of the total life cycle embodied carbon. Additionally, the load-bearing structure (including floors) constitutes an average of 24% of the life cycle's embodied carbon emissions. These established average ratios, 56% for A1-A3 and 24% for the load-bearing structure, were used to calculate the embodied carbon. The structure in Study A was intended for non-residential purposes.

### Study B

For Study B, the values only required adjustments to fit the correct LCA scope. The average impact ratio of stages A1-A3 on the total life cycle, identiefied in Study A, was again utilized for this study's adjustments. This was essential since Study B lacked specific information about the impact ratios of

different life cycle stages, leading to the assumption that the ratio from Study A is also representative for Study B.

Study C
The embodied carbon values identified in Study C were already consistent with the scope of the ANN models used in this research, thus no adjustments were necessary.

The adapted values from the literature are summarized in Table G.2, ensuring that the scope of the structure and the LCA are uniform across all evaluated impacts.

| Study | System | Total GFA [$m^2$] | Floors [-] | Scope Structure | Scope LCA | $EmCO_2$ [$kgCO_2eq/m^2GFA$] |
|---|---|---|---|---|---|---|
| A | Steel Frame | 64,762 | 27 | Load-bearing System | A1-3 | 161 |
| B | Steel Diagrid | 64,469 | 41 | Load-bearing System | A1-3 | 226 |
| C | Steel Diagrid | 141,600 | 60 | Load-bearing System | A1-3 | 285 |
| C | Concrete Core + Steel Frame | 141,600 | 60 | Load-bearing System | A1-3 | 236 |

**Table G.2:** Overview of the adapted data from literature

## G.2. Adaption of Data Base

The MIT Building Technology Program and the Circular Engineering for Architecture (CEA) lab at ETH Zurich have established a data base, known as deQo, of the embodied carbon of a significant number of buildings [56] (referred to as study B). While a graphical overview of the data was provided, direct access to the underlying data sets was not available. The data sets consist of various building types, and the life cycle stages considered align with the scope of this research, specifically stages A1-3. Moreover, the considered building components are also in line with the building components considered in the ANN models, namely only the structural components of a structure, excluding the foundation. The buildings analyzed in both box plots serve an office function, conforming the function of the building usage considered in the data sets of the ANN models. Two comparisons are made, one where the data set is divided into subsets for different number of stories, and one where the data set is divided into subsets for different floor area.

### G.2.1. Illustration of Distribution through Box Plots

The box plots illustrate statistical measurements including the median, the 25th and 75th quartiles, and the minimum and maximum values. The minimum and maximum values are defined as the quartile value plus 1.5 times the interquartile range (IQR). The IQR is a measure of statistical distribution, representing the range between the 25th and 75th percentiles of the data. It provides insight into the spread of the middle 50% of the data, making it a measure of variability. To be able to make a comparison, predictions were generated using the ANN models across width ranges of 15 to 60 meters and height ranges of 48 to 300 meters, corresponding to the input data. These predictions were then grouped into the same subsets as those of the box plots provided by the deQo database. Additionally, box plots were constructed based on these ANN predictions. The box plots, and the corresponding statistical measures, based on the real-life projects within the data base of Study C are compared to the box plots, and statistical measurements, generated based on the ANN models.

- **Distribution over different ranges of number of stories**
  Figure G.1 illustrates the box plots of the distribution of the embodied carbon over a different number of stories for all building types. Given the research's focus on high-rise buildings, box plots based on the ANN models were created only for the last two subsets of the number of

stories, representing buildings with 11 to 50 and 51 to 100 stories, respectively. It's important to note that the number of buildings within the database falling within the subset of 51 to 100 stories was relatively small, with only 10 buildings considered. Consequently, the box plot and statistical measures derived from this subset may not be fully representative due to the small sample size.

An overview comparing the values of embodied carbon between real-life projects in Study C (deQo database) and the predicted values using identical input parameters is provided in Table G.5. The box plots generated by the ANN models, are based on the best performing stability framework, so either S1 or S2. For each specific input the best performing stability framework has been considered and taken into account. Moreover, the contribution of the floors are also taken into account and added to the predictions, to get the full embodied carbon contribution of the structure including the floors. The floors are taken into account since the floors are also considered in the box plots of the results of Study C.

**Figure G.1:** Box plots of distribution of embodied carbon for all building types for different number of stories based on database of embodied quantity outputs [56]

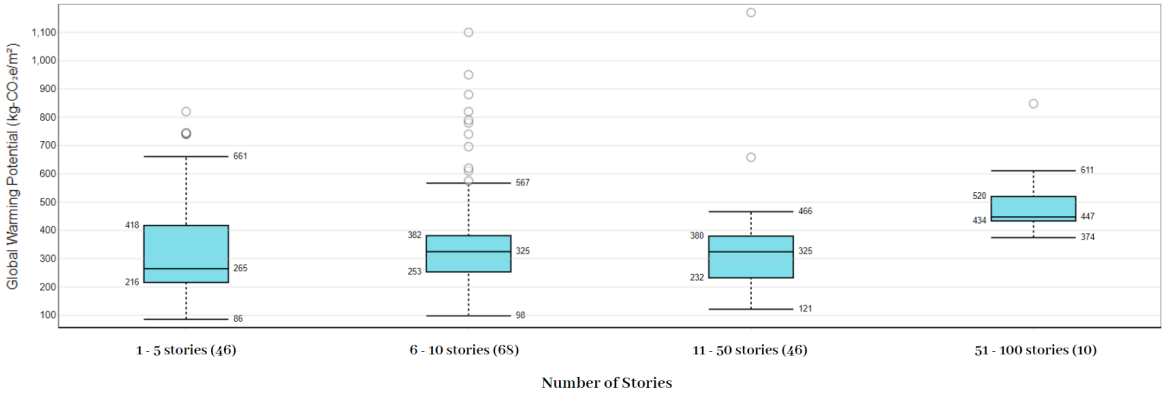


**Figure G.2:** Box plots of distribution of predicted embodied carbon for different number of stories based on ANN models

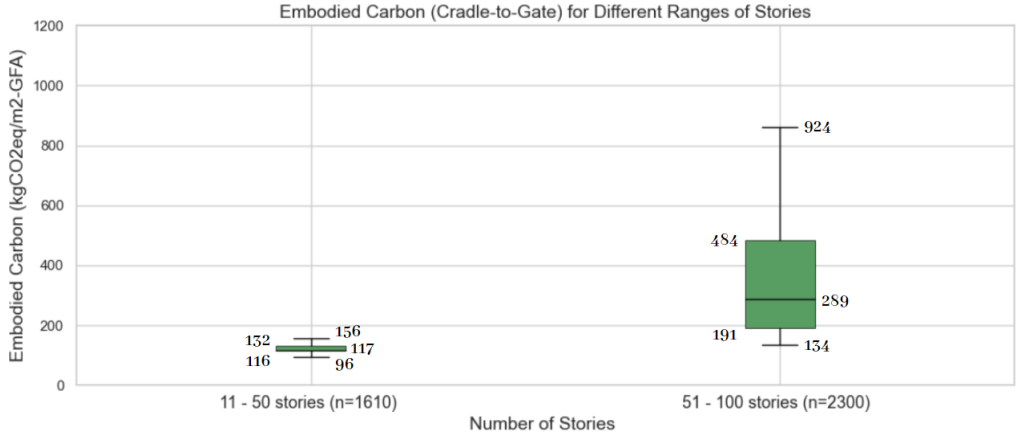

| | **Study C: $EmCO_2$** [$kgCO_2eq/m^2GFA$] | **ANN: $EmCO_2$** [$kgCO_2eq/m^2GFA$] | **$\Delta$ $EmCO_2$** [$kgCO_2eq/m^2GFA$] | **$\Delta$ $EmCO_2$** [%] |
|---|---|---|---|---|
| *11 - 50 Stories* | | | | |
| Min | 121 | 96 | -25 | -21 |
| Q25 | 232 | 116 | -116 | -50 |
| Median | 325 | 117 | -208 | -64 |
| Q75 | 380 | 132 | -248 | -65 |
| Max | 466 | 156 | -310 | -67 |
| *51 - 100 Stories* | | | | |
| Min | 374 | 134 | -240 | -64 |
| Q25 | 434 | 191 | -243 | -56 |
| Median | 447 | 289 | -158 | -35 |
| Q75 | 520 | 484 | -36 | -7 |
| Max | 611 | 924 | +313 | +51 |

**Table G.3:** Overview of the predicted values based on ANN models and the actual values based on study C for different ranges of number of stories

In the comparison of total embodied carbon between the ANN model and actual values for structures ranging from 11 to 50 stories, the ANN model consistently predicts lower values. The relative difference ranges from -21% to -67%, suggesting that the choice of an optimal stability framework can significantly reduce the total embodied carbon. For structures in the range of 51 to 100 stories, the comparison between the data base and the ANN models is significantly different. This could be attributed to the limited number of samples (n=10) in the database for this range, which is not representative for such a large range. The ANN model considered all possible combinations of widths and heights, including structures with significant slenderness. In reality, a structure with such a small width and such a large height (and thus such a significant slenderness) would not be constructed due to economic and environmental considerations. While such examples are absent in real-life projects, they are included in the ANN model's dataset. This difference becomes also visible when comparing statistical measurements. As the cost of the structure increases, the relative difference also increases. This can be attributed to the ANN model's dataset, which included high-slenderness structures that are both economically and environmentally unfavorable and unlikely to be realized in real-life projects.

- **Distribution over different ranges of floor area**
  Figure G.3 presents the box plots of the distribution of the embodied carbon over different floor areas based on the data base of Study B. Figure G.4 presents the box plots based on the predictions of ANN models regarding the division of the data based on different floor areas. The first subset for areas smaller than 1000 $m^2$ was excluded for comparison, as no structure within the ANN model ranges had a floor area smaller than 1000 $m^2$.

**Figure G.3:** Box plots of distribution of embodied carbon for all building types for different floor areas based on database of embodied quantity outputs [56]

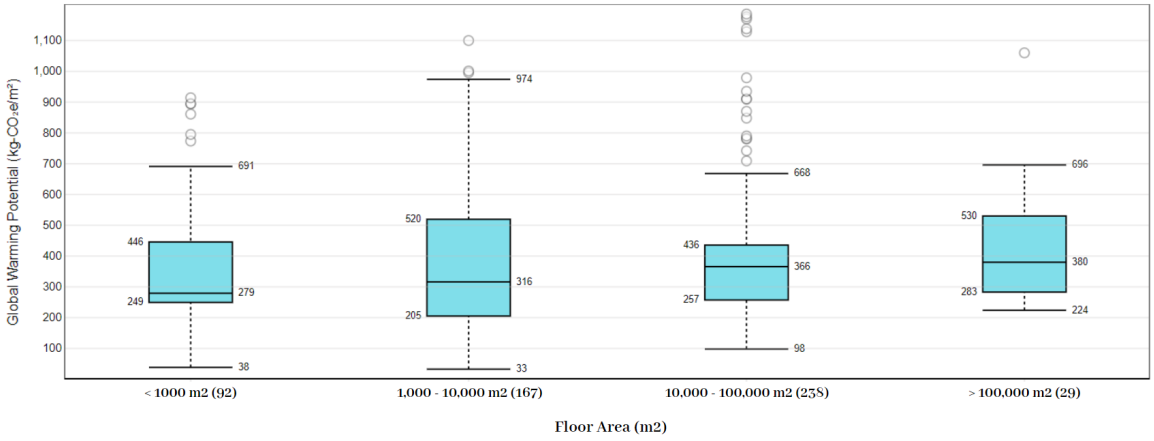


**Figure G.4:** Box plots of distribution of predicted embodied carbon for different floor areas based on ANN models

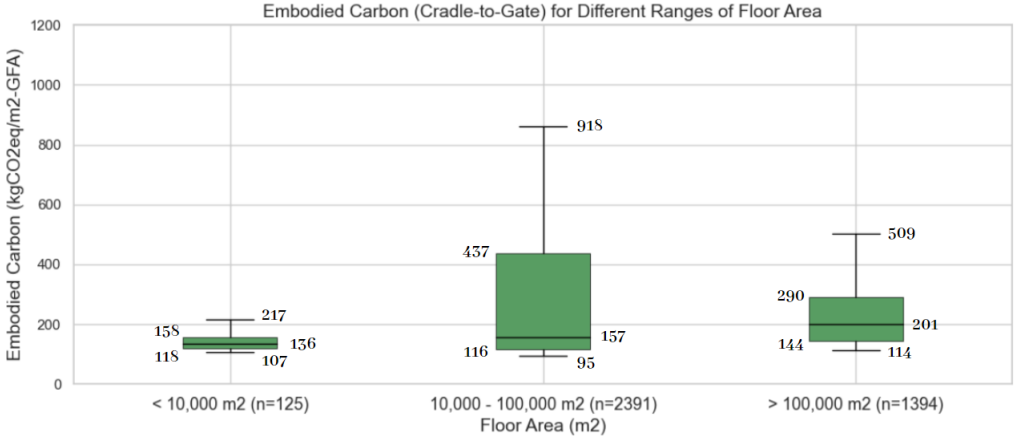

| | **Study B: $EmCO_2$** [$kgCO_2eq/m^2GFA$] | **ANN: $EmCO_2$** [$kgCO_2eq/m^2GFA$] | **$\Delta$ $EmCO_2$** [$kgCO_2eq/m^2GFA$] | **$\Delta$ $EmCO_2$** [%] |
|---|---|---|---|---|
| *1000-10,000 $m^2$* | | | | |
| Min | 33 | 107 | +74 | +224 |
| Q25 | 205 | 118 | -87 | -42 |
| Median | 316 | 136 | -180 | -57 |
| Q75 | 520 | 158 | -362 | -70 |
| Max | 974 | 217 | -757 | -78 |
| *10,000-100,000 $m^2$* | | | | |
| Min | 98 | 95 | -3 | -3 |
| Q25 | 257 | 116 | -141 | -55 |
| Median | 366 | 157 | -209 | -57 |
| Q75 | 436 | 437 | +1 | 0 |
| Max | 668 | 918 | +250 | +37 |
| *> 100,000 $m^2$* | | | | |
| Min | 224 | 114 | -110 | -49 |
| Q25 | 283 | 144 | -139 | -49 |
| Median | 380 | 201 | -179 | -47 |
| Q75 | 530 | 290 | -240 | -45 |
| Max | 696 | 509 | -187 | -27 |

**Table G.4:** Overview of the predicted values based on ANN models and the actual values based on study B for different ranges of floor areas

In the segment covering areas between 1000 to 10,000 $m^2$, the ANN model tends to predict considerably lower values compared to those from Study B, with the exception of the minimum value. This can be attributed to the smallest floor area considered in the ANN model being 3600 $m^2$, based on a width equal to 15 meters and a height equal to 48 meters. This is significantly larger than the subset's minimum value of 1000 $m^2$.

The same trend observed for the subsets of the number of floors is also present for the last two subsets of different floor areas. For the subset of areas between 10,000 to 100,000 $m^2$, the ANN models significantly overestimate the upper quartile and the maximum values compared to the Study B database. For the subset of areas larger than 100,000 $m^2$, only the minimum value is not overestimated by the ANN models. This can be attributed to the ANN model receiving inputs of all possible options within the width and height ranges, thereby generating structures with significant slenderness. The Study C database, which relies solely on real-life projects, is unlikely to include structures with a very small width and a significant height.

### G.2.2. Setting Upper-Limit Slenderness

It was concluded from the comparison between Study C and the predictions based on ANN models that the ANN models included structures with very small widths and significant heights, which resulted in some outliers in the comparison. Therefore, the decision was made to conduct the comparison as well with an upper limit on the slenderness of the structures. This upper limit was set at 11, consistent with the maximum slenderness of a braced framed tube. In reality, structures with such small widths and large heights, resulting in a slenderness greater than 11, would not be economically or environmentally feasible to construct. Consequently, such examples are absent in real-life projects and are therefore excluded from the dataset used by the ANN models.

- **Distribution over different ranges of number of stories**

**Figure G.5:** Box plots of distribution of embodied carbon for all building types for different number of stories based on database of embodied quantity outputs [56]

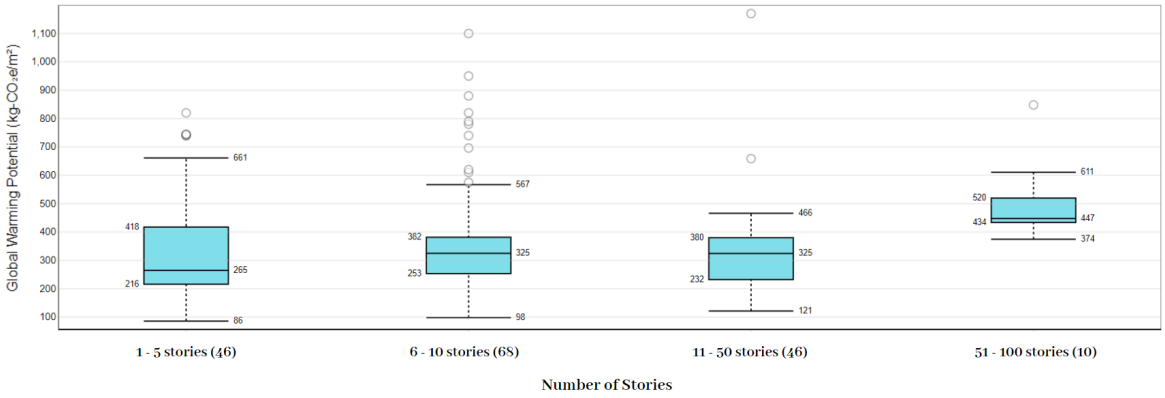


**Figure G.6:** Box plots of distribution of predicted embodied carbon for different number of stories based on ANN models

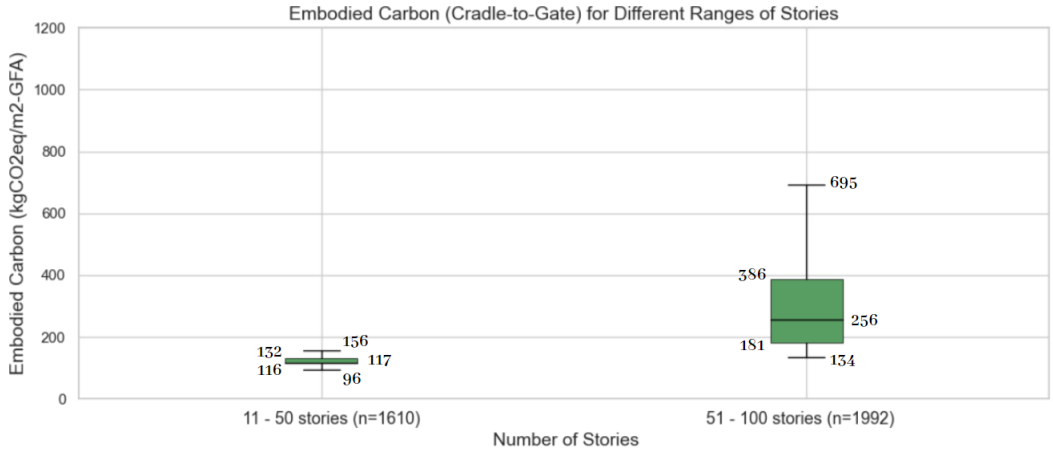


| | **Study B: $EmCO_2$** [$kgCO_2eq/m^2GFA$] | **ANN: $EmCO_2$** [$kgCO_2eq/m^2GFA$] | **$\Delta$ $EmCO_2$** [$kgCO_2eq/m^2GFA$] | **$\Delta$ $EmCO_2$** [%] |
|---|---|---|---|---|
| *11 - 50 Stories* | | | | |
| Min | 121 | 96 | -25 | -21 |
| Q25 | 232 | 116 | -116 | -50 |
| Median | 325 | 117 | -208 | -64 |
| Q75 | 380 | 132 | -248 | -65 |
| Max | 466 | 156 | -310 | -67 |
| *51 - 100 Stories* | | | | |
| Min | 374 | 134 | -240 | -64 |
| Q25 | 434 | 181 | -253 | -58 |
| Median | 447 | 256 | -191 | -43 |
| Q75 | 520 | 386 | -134 | -26 |
| Max | 611 | 695 | +84 | +14 |

**Table G.5:** Overview of the predicted values based on ANN models and the actual values based on study B for different ranges of number of stories

- **Distribution over different ranges of floor area**
  Figure G.7 presents the box plots of the distribution of the embodied carbon over different floor areas based on the data base of Study C. Figure G.8 presents the box plots based on the predictions of ANN models regarding the division of the data based on different floor areas. Again, the first subset for areas smaller than 1000 $m^2$ was excluded for comparison. The structures of the ANN models are limited to having a slenderness smaller than 11.

**Figure G.7:** Box plots of distribution of embodied carbon for all building types for different floor areas based on database of embodied quantity outputs [56]

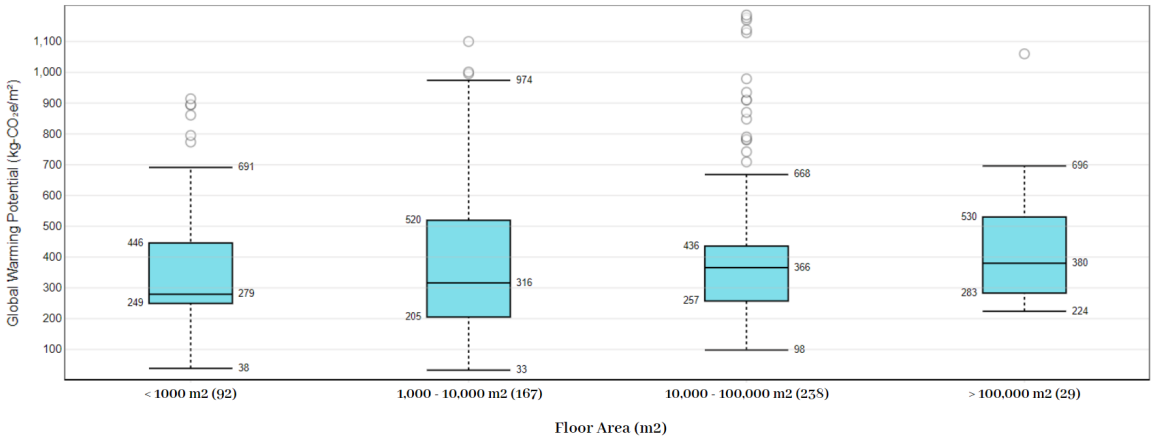


**Figure G.8:** Box plots of distribution of predicted embodied carbon for different floor areas based on ANN models

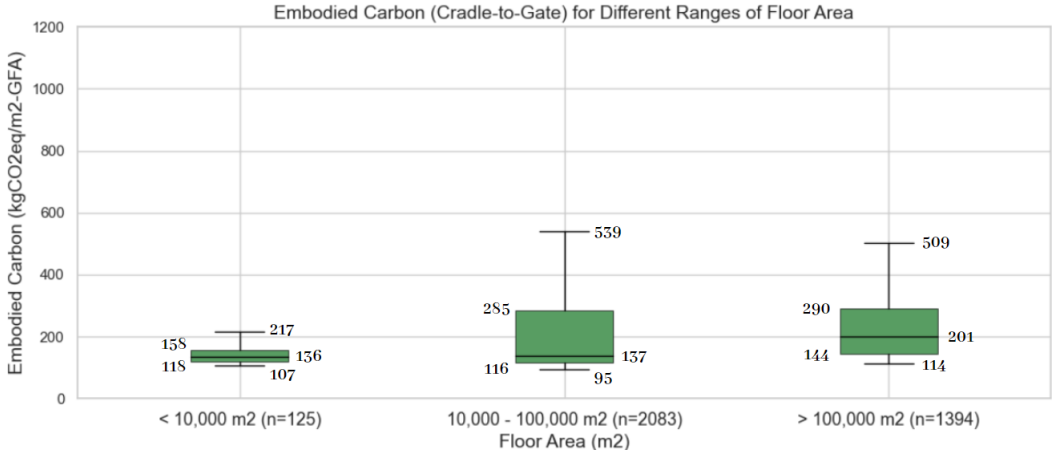

| | **Study B: $EmCO_2$** [$kgCO_2eq/m^2GFA$] | **ANN: $EmCO_2$** [$kgCO_2eq/m^2GFA$] | **$\Delta$ $EmCO_2$** [$kgCO_2eq/m^2GFA$] | **$\Delta$ $EmCO_2$** [%] |
|---|---|---|---|---|
| *1000-10,000 $m^2$* | | | | |
| Min | 33 | 107 | +74 | +224 |
| Q25 | 205 | 118 | -87 | -42 |
| Median | 316 | 136 | -180 | -57 |
| Q75 | 520 | 158 | -362 | -70 |
| Max | 974 | 217 | -757 | -78 |
| *10,000-100,000 $m^2$* | | | | |
| Min | 98 | 95 | -3 | -3 |
| Q25 | 257 | 116 | -141 | -55 |
| Median | 366 | 137 | -229 | -63 |
| Q75 | 436 | 285 | -151 | -35 |
| Max | 668 | 539 | -129 | -19 |
| *> 100,000 $m^2$* | | | | |
| Min | 224 | 114 | -110 | -49 |
| Q25 | 283 | 144 | -139 | -49 |
| Median | 380 | 201 | -179 | -47 |
| Q75 | 530 | 290 | -240 | -45 |
| Max | 696 | 509 | -187 | -27 |

**Table G.6:** Overview of the predicted values based on ANN models and the actual values based on study B for different ranges of floor areas

# H

# Python Script of ANN Model

The Python scripts related to visualizing the output data from parametric models and building the artificial neural networks can be found in the additional document attached to this thesis.